Holocene variability in sea ice, primary productivity and terrigenous input in Baffin Bay-Labrador Sea: A biomarker approach

zur Erlangung des Doktorgrades der Naturwissenschaften

am Fachbereich Geowissenschaften

der Universität Bremen/

Dissertation

vorgelegt von/by

Jeetendra Kumar Saini

Geboren am 08.07.1990 in Kanpur

Gutachter: Prof. Dr. Rüdiger Stein und Prof. Dr. Martin Melles

Universität Bremen

Erklärung

Hiermit erkläre ich an Eides statt, dass ich die vorliegende Arbeit ohne unzulässige Hilfe Dritter und unter Verwendung keiner als der von mir angegebenen Quellen und Hilfsmittel angefertigt habe. Die aus fremden Quellen wörtlich oder inhaltlich übernommenen Informationen sind als solche kenntlich gemacht.

Affirmation

I affirm that I wrote the presented thesis independently and without illicit assistance from third parties, I used no sources other than those indicated nor aids other than those permissible, I appropriately referenced any text or content from other sources.

Bremen, 19th April 2021

Jeetendra Kumar Saini

Colloquium
Bremen, 23. June 2021

"We have run out of excuses and we are running out of time."

Greta Thunberg at COP24 meeting, 12.12.2018, Poland

"Where I live, the sea ice never stops. It's a living thing."

H. G. Wells

Versicherung an Eides Statt / *Affirmation in lieu of an oath*

gem. § 5 Abs. 5 der Promotionsordnung vom 18.06.2018 /according to § 5 (5) of the
Doctoral Degree Rules and Regulations of 18 June, 2018

Ich / I, Jeetendra Saini, Am Alten Hafen 26, 27568 Bremerhaven. 3108161
(Vorname / First *Name*, Name / *Name*, Anschrift / *Address*, ggf. Matr.-Nr. / *student ID no., if applicable)*

versichere an Eides Statt durch meine Unterschrift, dass ich die vorliegende Dissertation selbständig und ohne fremde Hilfe angefertigt und alle Stellen, die ich wörtlich dem Sinne nach aus Veröffentlichungen entnommen habe, als solche kenntlich gemacht habe, mich auch keiner anderen als der angegebenen Literatur oder sonstiger Hilfsmittel bedient habe und die zu Prüfungszwecken beigelegte elektronische Version (PDF) der Dissertation mit der abgegebenen gedruckten Version identisch ist. / *With my signature I affirm in lieu of an oath that I prepared the submitted dissertation independently and without illicit assistance from third parties, that I appropriately referenced any text or content from other sources, that I used only literature and resources listed in the dissertation, and that the electronic (PDF) and printed versions of the dissertation are identical.*

Ich versichere an Eides Statt, dass ich die vorgenannten Angaben nach bestem Wissen und Gewissen gemacht habe und dass die Angaben der Wahrheit entsprechen und ich nichts verschwiegen habe. / *I affirm in lieu of an oath that the information provided herein to the best of my knowledge is true and complete.*

Die Strafbarkeit einer falschen eidesstattlichen Versicherung ist mir bekannt, namentlich die Strafandrohung gemäß § 156 StGB bis zu drei Jahren Freiheitsstrafe oder Geldstrafe bei vorsätzlicher Begehung der Tat bzw. gemäß § 161 Abs. 1 StGB bis zu einem Jahr Freiheitsstrafe oder Geldstrafe bei fahrlässiger Begehung. / *I am aware that a false affidavit is a criminal offence which is punishable by law in accordance with § 156 of the German Criminal Code (StGB) with up to three years imprisonment or a fine in case of intention, or in accordance with § 161 (1) of the German Criminal Code with up to one year imprisonment or a fine in case of negligence.*

Bremerhaven, 19.04.2021   Unterschrift / *Signature*
Ort / *Place*, Datum / *Date*

Table of contents

Abstract

The Arctic reacts very sensitively to natural and anthropogenic climate perturbations due to positive feedback mechanisms of the so-called "Polar Amplification". Sea ice is a very important part of the Arctic climate system, however, since the late 70s, the Arctic sea ice extent has decreased by more than one-third (>40%) than forecasted by climate models. This rapid decline has raised concern about the role of anthropogenic greenhouse gas emissions and natural variability of sea ice in relation to its short and long-term changes. Paleoenvironmental investigations are essential for the development and correction of futuristic climate models. Arctic outflow through Baffin Bay, via the Labrador Sea, acts as a substantial contributor of fresh water to the North Atlantic fuelled by the melt water input from the West Greenland Ice Sheet (GIS). Marine sedimentary archives from this area may thus provide records of sea ice and past ice sheet dynamics in this highly climate-sensitive area. So far, the sea ice variability and long-term changes in the water masses, especially the West Greenland Current, as well as the impact of melt-water discharge from the GIS that occurred since deglaciation, all remain barely documented. Furthermore, it is of particular interest to investigate how climatic and oceanographic changes have affected sea ice, primary productivity conditions and terrigenous input in this north-south transect of eastern Baffin Bay and Labrador Sea margin, where such long-term Holocene records are sparsely documented.

To achieve these objectives biomarkers (sea ice proxy IP_{25}, phytoplankton biomarkers; brassicasterol and dinosterol and terrigenous biomarkers; campesterol and ß-sitosterol) as well as organic geochemical bulk parameters (TOC, TOC/N, $\delta^{13}C_{org}$) were analyzed. The first manuscript provides insights into Holocene variability in sea ice and primary productivity conditions on a ^{14}C-dated sediment core from NE Baffin Bay (Core GeoB19927-3). In the second study, we described and compared past variability in sea ice and primary productivity conditions from a N-S transect along the eastern Baffin Bay (Core GeoB19948-3, Core GeoB19927-3) and Labrador Sea (GeoB19905-1) margin. A third study addresses the variability in terrigenous organic carbon input along this N-S transect during the Holocene covering the last 11.5 ka BP.

In the early Holocene, the conditions in Baffin Bay were characterized by extended (early) spring sea ice cover (SIC), low primary productivity and low (terrigenous) organic carbon

deposition prior to 9.4 ka BP suggesting cold deglacial conditions. This is followed by a period (~9.4-8.8 ka BP) of a variable to marginal SIC, increased primary productivity and high terrigenous input. Thereafter, a short period of increased SIC and reduced productivity was recorded between ~8.8-7.6 ka BP, probably related to the opening of the Nares Strait and subsequently increased Arctic Water influx and decreased WGC strengths, albeit, terrigenous organic matter accumulation rates display a decreasing trend but remained high compared to the mid Holocene level. However, during the early Holocene, prior to 9.1 ka BP, the conditions in the NE Labrador Sea remained predominantly ice-free (in spring/autumn). Very low accumulation rates of marine and terrigenous biomarkers indicate cold conditions related to the ice-proximal environment. Afterwards, between about 9.1-7.6 ka BP, the conditions in the NE Labrador Sea are characterized by high biological production and spring-autumn ice-free conditions corresponding to the onset of Holocene Thermal Maximum (HTM)-like conditions. This is reflected in relatively high accumulation rates of terrigenous biomarkers in this interval possibly related to the enhanced summer melting and relatively high WGC strength in the Labrador Sea area until 7.6 ka BP, which may have promoted long-distance transport of terrigenous matter supply into the area.

A transition towards reoccurring ice-edge (polynya-type) and significantly reduced SIC and primary productivity conditions in Baffin Bay are evident in the mid Holocene (~7.6-3 ka BP). Terrigenous organic carbon flux also decreased significantly in this interval and overall the surface conditions can be characterized as HTM-like conditions. These HTM-like conditions are especially represented in the NE Labrador Sea core during 5.9-3 ka BP as shown by continued spring-autumn ice-free conditions and high biological productivity. Terrigenous biomarkers indicate a decrease in terrigenous sediment delivery, in accordance with the retreated GIS and local glaciers in this period.

In the late Holocene (last ~3 ka BP), the conditions in eastern Baffin Bay are represented by an overall decrease in sea ice and primary productivity conditions, in combination with decreased terrigenous input of organic carbon. Our sea ice proxy PIP_{25} show no correlation to the Neoglacial cooling trend observed elsewhere in Northern Hemisphere, possibly due to the persistent influence of the WGC and interactions with the adjacent fjords. However, the last 3 ka BP (late Holocene) at core GeoB19905-1 from the NE Labrador Sea is characterized by

increased accumulation of terrigenous biomarkers. The accumulation rates of primary productivity biomarkers also show a strong increase during the last about 2 ka BP. This can be explained by increased preservation of organic matter related to a strong increase in the accumulation of poorly-sorted fine-grained sediments due to which organic matter may have become enriched. However, the possibility of diagenetic alterations and stimulated growth by melt water released nutrients (e.g. Fe, silica) linked to the Neoglacial regrowth of local Glaciers cannot be ruled out in the upper-most centimetres of the last 1.4 ka BP.

The results from this transect study provide further insights into the understanding of the influence of melt water discharges and oceanic current variability on sea ice, marine productivity conditions and terrigenous input in this highly sensitive area.

Zusammenfassug

Die Arktis reagiert aufgrund positiver Rückkopplungsmechanismen der sogenannten „Polar Verstärkung" sehr empfindlich auf natürliche und anthropogene Klimastörungen. Meereis ist ein sehr wichtiger Bestandteil des arktischen Klimasystems. Seit Ende der 70er Jahre hat sich die Ausdehnung des arktischen Meereises um mehr als ein Drittel (> 40%) verringert. Dies ist weitaus mehr als Klimamodelle prognostiziert haben. Dieser rasche Rückgang hat sowohl die anthropogene Treibhausgasemissionen als mögliche Verursacher als auch die natürliche Variabilität des Meereises im Verhältnis zu seinen kurz- und langfristigen Veränderungen in den Focus der Forschung gesetzt. Paläoumweltuntersuchungen sind für die Entwicklung und Korrektur von Klimamodellen von wesentlicher Bedeutung. Durch den Schmelzwassereintrag durch den Westgrönländischen Eisschild trägt der Abfluss arktischen Wassers durch die Baffin Bay über die Labradorsee wesentlich zum Süßwasserhaushalt im Nordatlantik bei. Marine Sedimente aus diesem Gebiet können daher Erkenntnisse über Meereis und die Dynamik der Eisdecke in diesem hochklimasensiblen Gebiet liefern. Bisher sind die Veränderungen von Meereisesausdehnung und die langfristigen Veränderungen der Wassermassen, insbesondere des Westgrönlandstroms, sowie die Auswirkungen des Schmelzwassereintrages durch den Grönländischen Eisschild, die seit der Enteisung aufgetreten sind, kaum dokumentiert. Darüber hinaus ist es von besonderem Interesse zu untersuchen, wie sich klimatische und ozeanografische Veränderungen auf das Meereis, die Primärproduktion und den terrigenen Eintrag in der östlichen Baffin Bay und am Rande der Labradorsee ausgewirkt haben.

Um diese Ziele zu erreichen, wurden Biomarker (Meereis-Proxy (IP_{25}), Phytoplankton-Biomarker (Brassicasterol und Dinosterol) sowie terrigene Biomarker (Campesterol und ß-Sitosterol) sowie organische geochemische Bulk-Parameter (TOC, TOC / N, $\delta^{13}C_{org}$) analysiert. Das erste Manuskript bietet Einblicke in die holozäne Variabilität des Meereises und der Primärproduktion eines ^{14}C-datierten Sedimentkerns aus nordöstlichen Baffin Bay (Core GeoB19927-3). In der zweiten Studie haben wir die Variabilität des Meereises und der Primärproduktion im Holozän anhand eines Nord-Süd-Transekts entlang der östlichen Baffin Bay (Core GeoB19948-3, Core GeoB19927-3) und Labradorsee (GeoB19905-1) beschrieben und verglichen. Eine dritte Studie befasst sich mit der Veränderung des organischen Kohlenstoffeintrags entlang dieses Nord-Süd -Transekts während der letzten11,5 ka BP.

Im frühen Holozän (vor 9,4 ka BP) waren die Bedingungen in Baffin Bay durch eine ausgedehnte Frühjahr-Eisbedeckung, eine geringe Primärproduktivität und eine geringe Ablagerung von terrigenem organischen Kohlenstoff gekennzeichnet, dies deutet auf kalte deglaziale Bedingungen hin. Darauf folgt ein Zeitraum (~ 9,4-8,8 ka BP) mit variablen bis marginalen Meereisbedeckung, einer erhöhten Primärproduktivität und hohem terrigenen Eintrag. Zwischen 8,8 und 7,6 ka BP war die Meereisbedeckung größer und Produktivität geringer. Dies steht wahrscheinlich im Zusammenhang mit der Öffnung der Nares-Straße und dem dadurch vermehrten Zufluss von arktischem Wasser und/oder einer verringerten Stärke des Westgrönlandstroms. Obwohl die Akkumulationsraten der terrigenen organischen Substanz einen abnehmender Trend zeigen, bleiben sie im Vergleich zum mittleren Holozän hoch. Während des frühen Holozäns vor 9,1 ka BP herrschten in der nordöstlichen Labradorsee überwiegend eisfreie Bedingungen (im Frühjahr / Herbst) vor. Sehr niedrige Akkumulationsraten von marinen und terrigenen Biomarkern weisen auf kalte Bedingungen durch die eisnahe Umgebung hin. Danach sind die Bedingungen in der nordöstlichen Labradorsee zwischen etwa 9,1 und 7,6 ka BP durch eine hohe biologische Produktion und eisfreie Bedingungen im Frühjahr und Herbst gekennzeichnet, die den Bedingungen des Holozäne Thermal Optimum (HTM) entsprechen. Dies spiegelt sich in relativ hohen Akkumulationsraten terrigener Biomarker in diesem Intervall wider, die möglicherweise mit verstärktem Schmelzen im Sommer und der Stärke des Westgrönlandstroms im Labradorseegebiet zusammenhängen. Letzteres begünstigt möglicherweise den Transport von terrigenem Material über weite Strecke bis hin ins Untersuchungsgebiet.

Ein Übergang von wiederkehrenden Eiskante (Polynya-Typ) und signifikant reduzierter Meereisbedeckung und Primärproduktion ist in der Baffin Bay im mittleren Holozän (~ 7,6-3 ka BP) erkennbar. Der terrigene organische Kohlenstofffluss nahm in diesem Intervall ebenfalls signifikant ab. Insgesamt können die Oberflächenbedingungen als HTM-ähnliche Bedingungen charakterisiert werden. Diese HTM-ähnlichen Bedingungen sind insbesondere im nordöstlichen Labradorsee-Kern zwischen 5,9 und 3 ka BP erkennbar, wie die eisfreien Bedingungen im Frühjahr und Herbst und die hohe biologische Produktivität zeigen. Mit dem Rückzug des Grönländischer Eisschildes und den lokalen Gletschern in diesem Zeitraum weisen die terrigene Biomarker auf eine Abnahme des terrigenen Sedimenteintrages hin.

Im späten Holozän (letzte ~ 3 ka BP) sind die Bedingungen in der östlichen Baffin Bay durch eine allgemeine Abnahme des Meereises und der primären Produktivitätsbedingungen in Kombination mit einem verringerten terrigenen Eintrag von organischem Kohlenstoff dargestellt. Unser Meereis-Proxy PIP_{25} zeigt keine Korrelation mit dem an anderer Stelle auf der Nordhalbkugel beobachteten neoglazialen Abkühlungstrend, möglicherweise aufgrund des anhaltenden Einflusses des Westgrönlandstroms und der Wechselwirkungen mit den benachbarten Fjorden. Die letzten 3 ka (spätes Holozän) im Kern GeoB19905-1 aus der nordöstlichen Labradorsee sind jedoch durch eine erhöhte Akkumulation terrigener Biomarker gekennzeichnet. Die Akkumulationsraten der Biomarkern für die Primärproduktion zeigen ebenfalls einen starken Anstieg während der letzten etwa 2 ka. Dies kann durch eine höhere Erhaltung organischer Substanz erklärt werden, die durch ebenfalls erhöhte Akkumulation schlecht sortierter Sedimente begünstigt wird. Diagenetische Veränderungen und verstärktes Algenwachstum durch freigesetzte Nährstoffe (z.B. Eisen, Silizium) aus dem Schmelzwasser, die mit dem neoglazialen Nachwachsen lokaler Gletscher verbunden sind, kann jedoch im obersten Abschnitt des Kernes (letzten 1,4 ka BP) nicht ausgeschlossen werden.

Die Ergebnisse dieser Studie liefern weitere Einblicke in das Verständnis des Einflusses von Schmelzwasserabflüssen und der Änderungen der Meeresströmung auf das Meereis, die marinen Produktivität und den terrigenen Eintrag in diesem hochempfindlichen Gebiet.

Acknowledgements

Where to begin…there have been so many people, colleagues, friends, family and institutes that have helped shape this PhD thesis to fruition.

I'll start with thanking first of all dear Prof. Dr. Rüdiger Stein and dear Dr. Kirsten Fahl for the continuous and intensive support and acting as my PhD parents. I would like to extend a warm hug to Prof. Dr. Anne de Vernal for making it possible to work at GEOTOP, Montreal, Canada and having such a fruitful time and further support and encouragement.

This PhD project was one of many ArcTrain projects so I gratefully acknowledge the Deutsche Forschungsgemeinschaft (DFG) (GRK 1904) for its funding. I would also like to thank Prof. Dr. Dierk Hebbeln and Prof. Dr. Michael Kucera for external support within the ArcTrain framework and such an excellent organization.

On a personal level, I would like to thank the crew and scientists on the Maria S. Merian MSM44/MSM66 cruise for collecting the cores among some of them presented in this thesis later and my lovely ArcTrain/POLMAR fellow members for such a wonderful time during cuises, excursions and conferences. I'd like to extend a warm hug to Jens Weiser and Lina Madaj for being as you are. On a special note, I also want to thank my office mates Junjie, Henriette, Tanja, Anne, Defang, Jayzee and lab mate Walter Luttmar for such a great time.

I really enjoyed working at AWI because of my colleagues from Marine Geology: Thanks to Julia, Nicole, Kevin, Elena, Thomas, Nicolleta, and many more. On a personal level, I am very grateful to Elif Gizem Ertekin for holding through the 'special' year of 2020 and kisses to family members and friends (Lika, Andy, Saunak, Olga, Julian...) for being there, thanks for everything.

Dear co-authors, I like to give a big thank to all for helping a small PhD student trying to make an impact in science and making this work an interdisciplinary firework.

Last but not least, I would like to acknowledge people around me and myself for staying strong through the amazing/challenging times though full of experiences and believing in that "everything is possible".

List of Abbreviations

AMS	Accelerator Mass Spectromentry
AO	Arctic Oscillation
AWI	Alfred Wegener Institute, Helmholtz Centre for Polar and Marine Research
Atl. W	Atlantic Water
AW	Arctic Water
BSTFA	Bis-trimethylSilyl-TriFluoroacet-Amide
$CaCO_3$	Calcium Carbonate
TOC/N	Ratio of Carbon and Nitrogen
$\delta^{13}C_{org}$	Stable isotopes of organic carbon
$\delta^{18}O$	Stable Oxygen Isotopes
DBD	Dry Bulk Density
DFG	Deutsche Forschungsgemeinschaft
EGC	East Greenland Current
GC-MS	Gas Chromatography - Mass Spectrometry
GIS	Greenland Ice Sheet
HBI	Highly-Branched Isoprenoid
HBI II	Di-unsaturated HBI lipid
HBI III	Tri-unsaturated HBI lipid
IBCAO	International Bathymetric Chart of the Arctic Ocean
IPCC	Intergovernmental Panel on Climate Change
IP_{25}	Ice Proxy with 25 carbon atoms
$IPSO_{25}$	Ice Proxy with 25 carbon atoms for the Southern Ocean
IC	Irminger Current
IRD	Ice Rafted Debris
ka	Thousand years before present
LC	Labrador Current
LIA	Little Ice Age
LIS	Laurentide Ice Sheet
GIS	Greenland Ice Sheet
LGM	Last Glacial Maximum
LSDW	Labrador Sea Deep Water

MAT	Modern Analogue Technique
MCA	Medieval Climate Anomaly
MIZ	Marginal Ice Zone
MRA	Marine Reservoir Age
NAO	North Atlantic Oscillation
NC	Norwegian Current
ODV	Ocean Data View (software)
PIP_{25}	Phytoplankton – IP_{25} sea ice index
POC	Particulate Organic Carbon
RCP	Representative Concentration Pathway
SIM	Selected Ion Mode
SiO_2	Silicon Dioxide
SIC	Sea Ice Cover
SST	Sea Surface Temperature
TIC	Total Ion Current
TLE	Total Lipid Extract
TOC	Total Organic Carbon
TN	Total Nitrogen
TPD	Transpolar Drift
U^{K}_{37}	Alkenone Unstauration Index
UQAM	Université du Québec à Montréal
VPDB	Vienna PeeDee Belemnite
WGC	West Greenland Current
WSC	West Spitsbergen Current
YD	Younger Dryas
7-HND	7-HexylNonaDecane
^{14}C	Radiocarbon

1 Introduction

1.1 The Arctic Ocean–physiography and modern setting

The Arctic Ocean located high in the Northern Hemisphere represents a unique environmental setting. The ocean is almost entirely surrounded by the American and Eurasian continents (Fig. 1.1) and its connection to the other ocean is limited. The deep Fram Strait provides a major pathway for exchanging warm Atlantic Water and cold Polar Water and sea ice between the Arctic and Atlantic Ocean (Rudels et al., 2000), while narrow and shallow Bering Strait imports mainly Pacific Water into the Arctic Ocean without a major outflow of Polar Water into the Pacific Ocean (Jones et al., 2003). Shallow waterways characterize the Canadian Arctic Archipelago, the Barents Sea and limited exchange conditions occur in the Chukchi Sea, the East Siberian Sea, the Laptev Sea, the Kara Sea and Baffin Bay.

The hydrographical structure of the Arctic Ocean waters consists of three main water masses; the upper (surface) Water (~0-200 m), the intermediate (Atlantic) Water (~200-800 m), and the deep Water (>800 m) (Fig. 1.2). The upper layer consists of water masses characterized by cold temperatures and low salinity due to the influence of fresh water input from ice melting and cold atmospheric temperatures related to the polar night of the winter months. The circulation in this surface layer can be broadly characterized by the wind-driven clockwise flowing Beaufort Gyre in the western Arctic and the Transpolar Drift in the eastern Arctic Ocean, mainly responsible for exporting large volume of ice out of the Arctic Ocean (Fig. 1.1) (Gow and Tucker, 1987; Thorndike, 1986). These circulation patterns drive the export of low-salinity surface water alongside sea ice through the Fram Strait and the Canadian Arctic Archipelago (Jakobsson et al., 2004; Jones et al., 2001; Schauer et al., 1997). The change in these circulation patterns strongly affects the sea ice formation as well as the sea ice and fresh water export via the Fram Strait/Canadian Arctic/Baffin Bay (Carmack, 2000). The large Arctic rivers i.e. the Yenisei, Ob and Lena from the Eurasian continent and Mackenzie river from the North American continent export large amount of fresh water, including dissolved nutrients which play a crucial role in controlling sea ice formation (Aagaard and Carmack, 1989) and marginal shelf productivity (see 1.3 and 1.4).
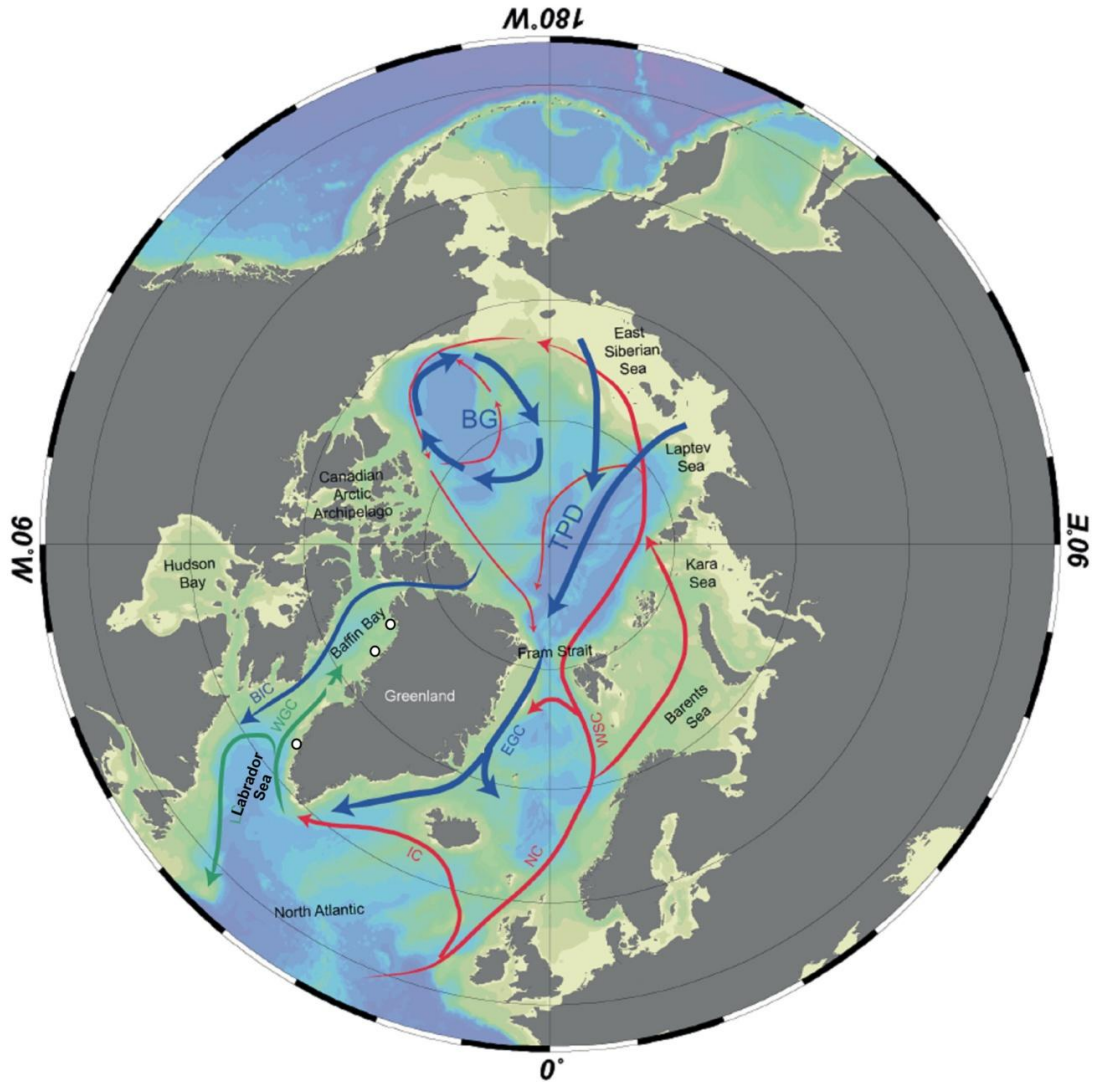
Figure 1.1: Schematic map of the Arctic Ocean showing modern surface circulation and surrounding land masses (adapted after Macdonald et al., 2003). White dots indicate the location of studied sediment cores from Baffin Bay and the Labrador Sea area. Red arrows indicate the inflow of Atlantic Water, and blue arrows refer to the circulation of polar water. The bathymetry is based on the IBCAO V3 grid (Jakobsson, 2002). (WGC = West Greenland Current, IC = Irminger Current, EGC = East Greenland Current, BC = Baffin Current, BG = Beaufort Gyre, TPD = Transpolar drift, NC = Norwegian Current, WSC = West Spitsbergen Current).

Below the upper surface layer, the intermediate layer consists of relatively warm and saline Atlantic Water that flows northward and bifurcates into the Irminger Current (IC) and Norwegian Current (NC) and further into Spitsbergen Current (SC) that continues northwards along the Barents Sea coasts. In the Arctic Ocean, this Atlantic Water submerges beneath the

cold fresh water layer and continues in intermediate depths towards the Siberian continental shelves (Fahrbach et al., 2001; Rudels et al., 2015). The deep Arctic Water submerged beneath the Atlantic layer is dominated by waters of very high salinity formed due to lateral exchange of waters between the Nordic Seas and Arctic shelves during brine formation (Coachman and Aagaard, 1974).
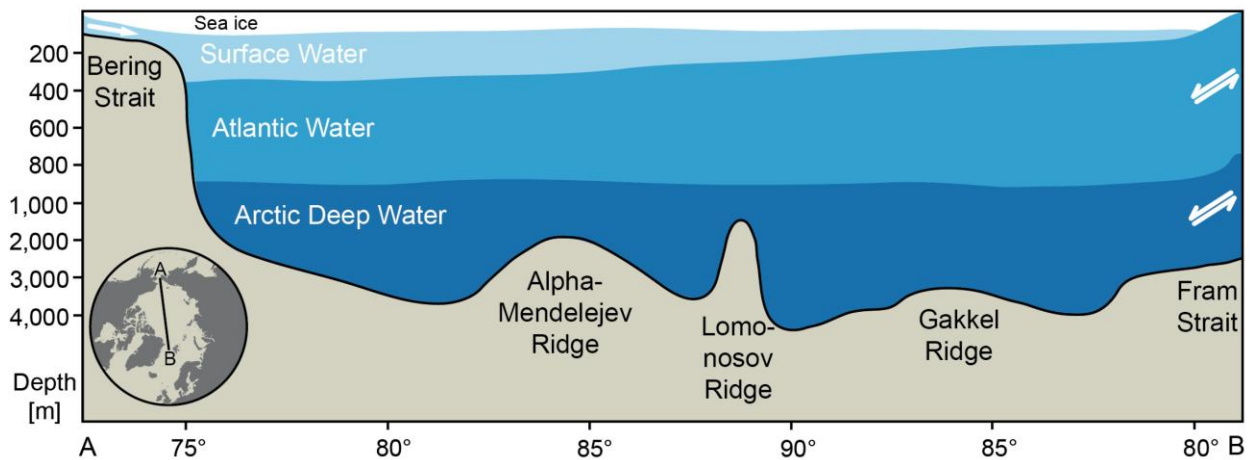
Figure 1.2: Schematic cross-section of the Arctic oceanographic structure along a transect from the Bering Strait to the Fram Strait (Source: Kremer, 2018, modified from MacDonald et al., 2004). Water mass exchange with neighboring oceans is shown as white arrows.

1.2 Sea ice in the Arctic climate system and its modern distribution

Sea ice is an important part of the Arctic climate system. Sea ice reflects much of the incoming solar radiation during the summer (>~80%), thus keeping the Arctic cooler than other tropical/low latitude areas. The sea ice cover limits the exchange of moisture, heat and gas between the ocean and the atmosphere, thus acting as a physical barrier between the ocean and the atmosphere (Fig. 1.3). Sea ice also provides a platform and hunting grounds for megafauna and acts as a barrier for other parts of the ecosystem.

The most defining feature of sea ice in the Arctic is it's seasonal to perennial sea ice cover, following the annual changes in insolation and fresh water discharge and thus pronounced seasonality. New sea ice forms during autumn and continues to grow until March to the maximum extent of ~15 million km^2 (NSIDC, 2020) (Fig. 1.4). Following the return of sunlight,
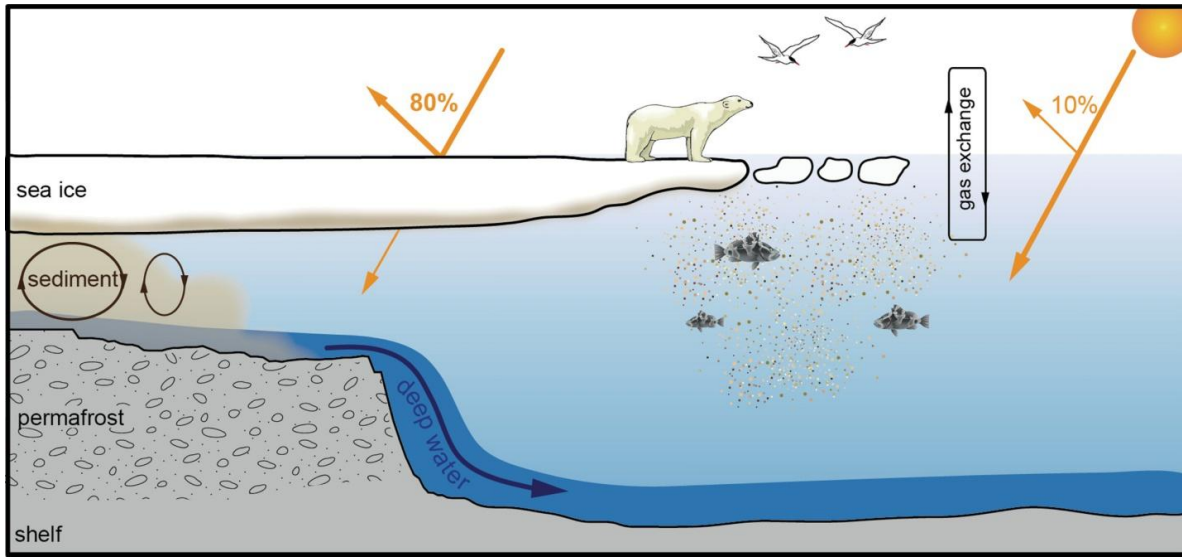
Figure 1.3: Schematic sketch of sea ice-related processes in the Arctic regions (Source: Kremer, 2018a, from MacDonald et al., 2004).

sea ice starts to melt in late spring, reaching the minimum extent around late September with <4-5 million km^2 of sea ice cover (Fig. 1.4) (NSIDC, 2020). Seasonal sea ice that lasts the summer may survive for years and become multiyear (perennial) ice, especially in the central Arctic Ocean with a thickness up to ~3-4 meters (Fig. 1.5, 1.6) (Wadhams, 1992).
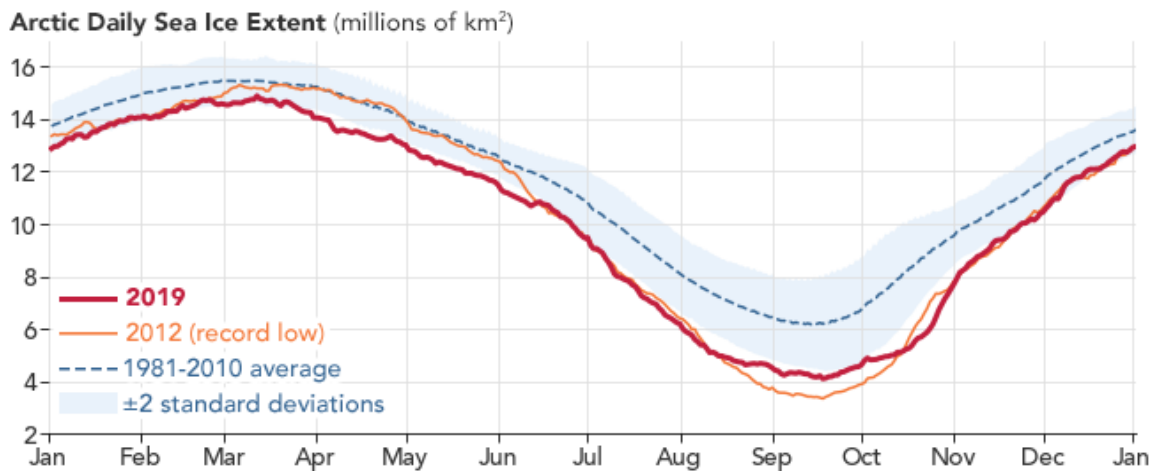
Figure 1.4: Arctic daily sea ice extent from January to December 2019 in comparison with the median between 1981 to 2010 and the record low year 2012 (Source: https://polarportal.dk).

Since the beginning of satellite observations in the late 70s, the Arctic sea ice has decreased rapidly (Stroeve et al., 2007) (Fig. 1.5, 1.6), and this observed decline in sea ice extent exceeds several forecast model predictions for the 21st century (Fig. 1.7). However, models in recent years have explored sea ice in some more detail and are now in much better agreement with the observed rate of sea ice decline (Fig. 1.7), although still imperfect. Since the 70s, the summer sea ice extent has decreased by -8.6% per decade, the fastest rate ever observed after the advent of the industrial era (Kinnard et al., 2011; Stroeve and Notz, 2018) (Fig. 1.7). The absolute sea ice minimum (so far) was reached in September 2012 when sea ice decreased to 3.4 million km^2 (Fig. 1.4). The winter (March) sea ice extent has decreased too, however, at a smaller rate (-2.4% per decade from 1979 to 1999 and -3.4% per decade from 2000 to present) than the summer ice extent (Fig. 1.4, 1.6) (Notz and Stroeve, 2018; Stroeve and Notz, 2018). Based on the current trends (with middle-range CO_2 emission scenario, i.e., 720 ppm), climate models forecast a seasonally ice-free Arctic Ocean in approximately 30 years (Holland et al., 2006; Wang and Overland, 2012) (Fig. 1.7).
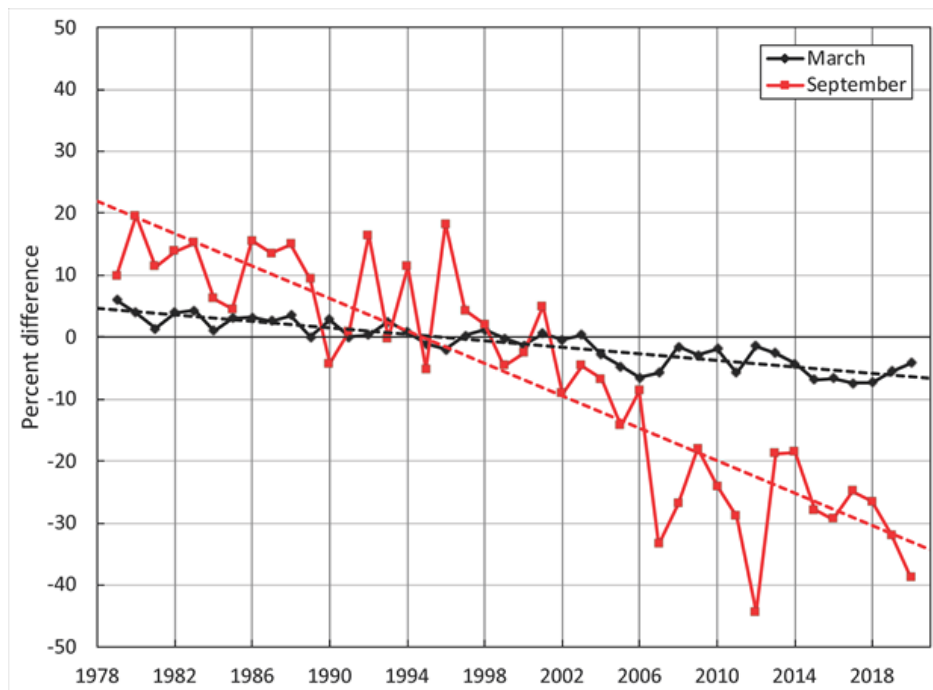
Figure 1.5: Monthly sea ice extent and linear trend (dashed) lines for March (black) and September (red) derived from the satellite measurement from 1979 to 2020 (NSIDC, 2020) showing the SIC decline in the last ~40 years (Arctic Report card, https://arctic.noaa.gov/Report _card).
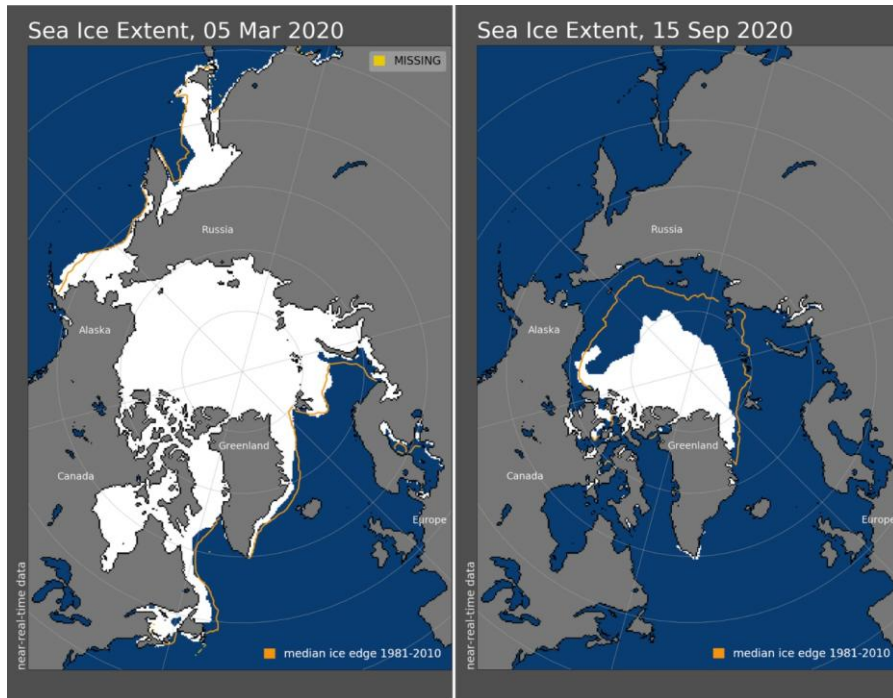
Figure 1.6: Satellite-derived sea ice extent in March and September 2020 relative to the median ice edge extent from 1981 to 2010 (NSIDC, https://nsidc.org, accessed December 2020).
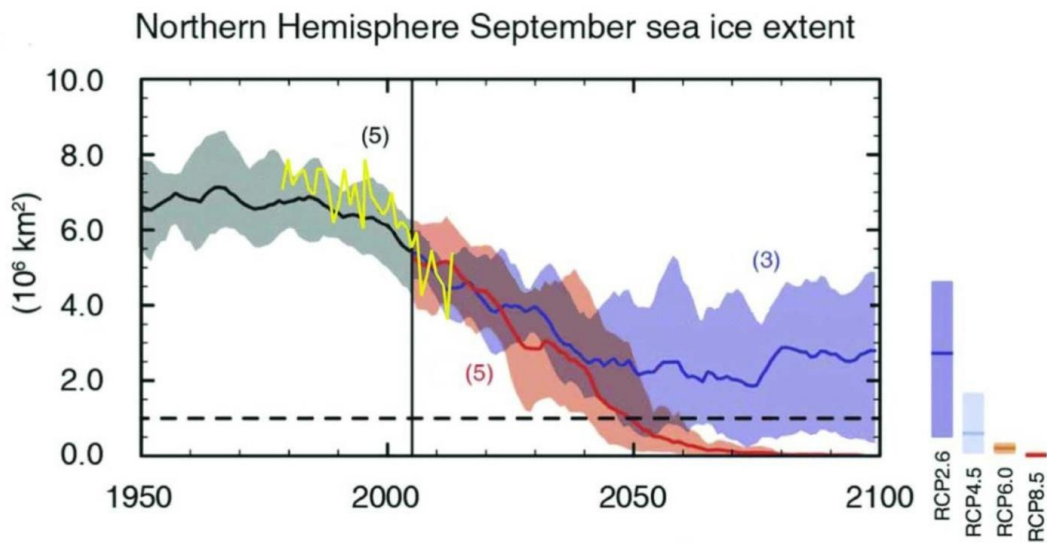
Figure 1.7: The projections of September Arctic sea ice extent for the century based on 5th assessment of IPCC AR5 report that best captures recent sea ice changes until 2013 (yellow curve). A high (red) and very low emissions (blue) scenario are shown as shaded bands with solid as mean. Representative Concentration Pathways of greenhouse gases emissions in relation to the projected radiative forcing in 2100. (Source: USGS website accessed in 2020 and https://arctic.noaa.gov/Report _card).

The extent of sea ice cover is subject to various internal and external forcing mechanisms such as natural versus anthropogenic climate forcing. Sea ice reacts sensitively to atmospheric pressure changes (i.e. changing wind patterns) in the Arctic on decadal time scales, such as the Arctic Oscillation (AO) and North Atlantic Oscillation (NAO) (Hurrell et al., 2001; Kwok et al., 2013; Rigor et al., 2002) (Fig.1.8). Usually, these high latitude counter-clockwise circulation patterns are synchronous and exhibit a positive and negative mode (Darby et al., 2012; Jones et al., 1997). The positive/negative mode is associated with low/high surface pressure and strong/weak zonal winds over the Arctic Region. During a positive AO/NAO mode, the polar vortex remains strong due to low surface pressure in the Arctic, meaning northward shift of the Jet Stream, thus colder air masses are bound around the North Pole. In a negative mode, however, the polar vortex is weak and the Jet stream moves south, transporting cold air masses southwards. The positive mode of the AO/NAO is usually associated with the increased export of sea ice from the Arctic as well as the northwards transport of warm Atlantic Water causing thinning (reduction) of Arctic sea ice (Darby et al., 2012; Dickson et al., 1996; Thompson and Wallace, 1998).
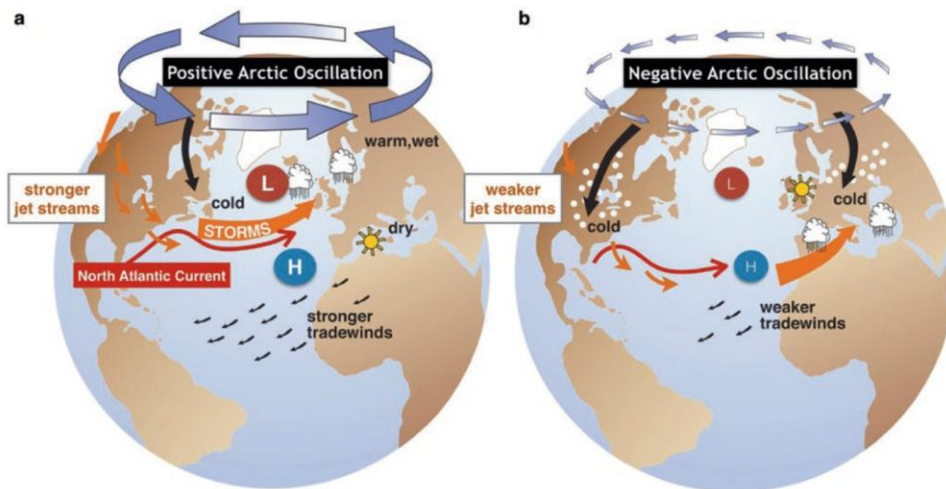
Figure 1.8: Schematic of the Arctic Oscillation (AO) and North Atlantic Oscillation (NAO) and its climatic effects during a) positive mode and b) negative mode (adapted after AMAP, 2017; Campos and Horn, 2018).

Besides the areal loss of sea ice extent, the thickness and volume of ice too, have declined drastically (-3.1 thousand km^3/decade) resulting in the loss of thick multi-year ice, as displayed by a continuous decline in ice volume from 1979 to 2018 derived from satellite measurements

(Fig. 1.9) (Serreze et al., 2007b; Stroeve et al., 2012). The loss of multi-year sea ice is very susceptible to a potential rise in oceanic and atmospheric temperatures in the future too because of ongoing climate change (Comiso, 2012).
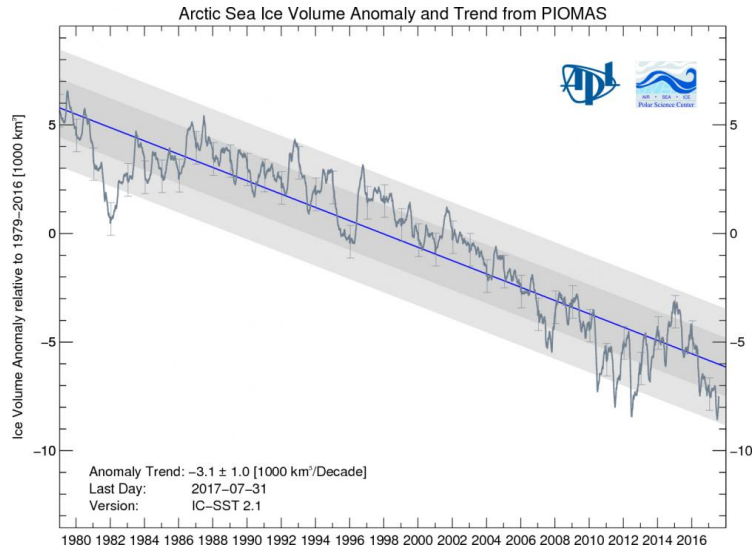
Figure 1.9: Sea ice volume (linear trend 'blue') anomalies in PIOMAS (Zhang and Rothrock, 2003) calculated from a 1979 to 2016 baseline. (Source: http://psc.apl.uw.edu/research/projects/arctic-sea-ice-volume-anomaly/).
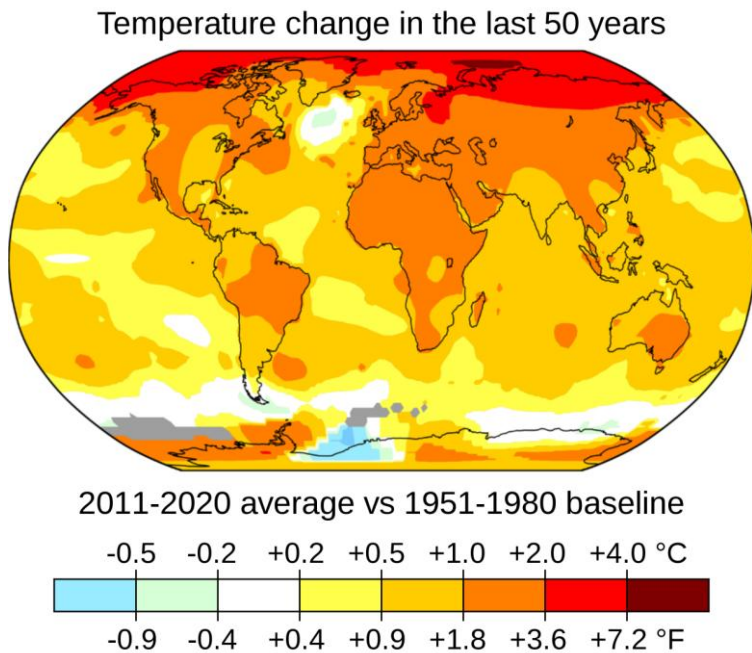
Figure 1.10: Global land and ocean-based temperature anomalies in the last 50 years showing amplified global temperatures together with the Arctic warming twice than the global average. (Source: NASA/ https://en.wikipedia.org/wiki/Climate_change).

One of the most obvious signals of climate change is the rise of global average temperatures in the past several decades (Fig. 1.10). The Arctic region will continue to warm more than twice the global average, a phenomenon called the "Polar Amplification" (Serreze and Barry, 2011) and will probably lead to the ice-free Arctic by the end of 21st century (Fig. 1.7).

Such developments would be disastrous to Arctic flora and fauna as sea ice presents a unique habitat for specialized microbes, fishes, birds and marine mammals (Fig. 1.3). Sea ice thickness controls light conditions and hence controls marine productivity to a great extent (Belchansky and Douglas, 2002; Cremer, 1999). Ice algae and phytoplankton bloom are the foundations of the Arctic food web that influence the organic carbon budget of the Arctic Ocean (Gradinger, 2009). Moreover, when sea ice melts, nutrients and terrigenous organic matter are released to the water column stimulating ocean primary productivity in combination with sunlight (cf. 1.3).

Since the observational and satellite-derived sea ice time series are short and biased by the impact of industrialization since the 18th century, the reconstructions of natural sea ice variations on longer geological time scales are highly relevant. Such reconstructions can greatly improve forecast climate models and clarify unsolved questions regarding the role of sea ice, primary productivity and fate of terrigenous OM in the climate system and its response to natural and/or anthropogenic climate changes.

1.3   Processes controlling the organic carbon cycle in the Arctic Ocean

1.3.1   Primary productivity

Autotrophic algae living in sea ice (ice algae) and water column (phytoplankton) undergo photosynthesis and are usually the main primary producers in the Arctic Ocean. Primary productivity strongly depends on the light and nutrients availability, thus melting and retreat of sea ice during spring/summer/autumn might affect primary production in the Arctic Ocean and its adjacent shelf seas by altering light conditions and stratification (Ardyna et al., 2017; Barber et al., 2015; Leu et al., 2015) (Fig. 1.11). Phytoplankton bloom development is strongly influenced by sea ice conditions and in ice-edge areas the buildup of bloom may be faster than in areas of open waters (Wassmann et al., 2011).
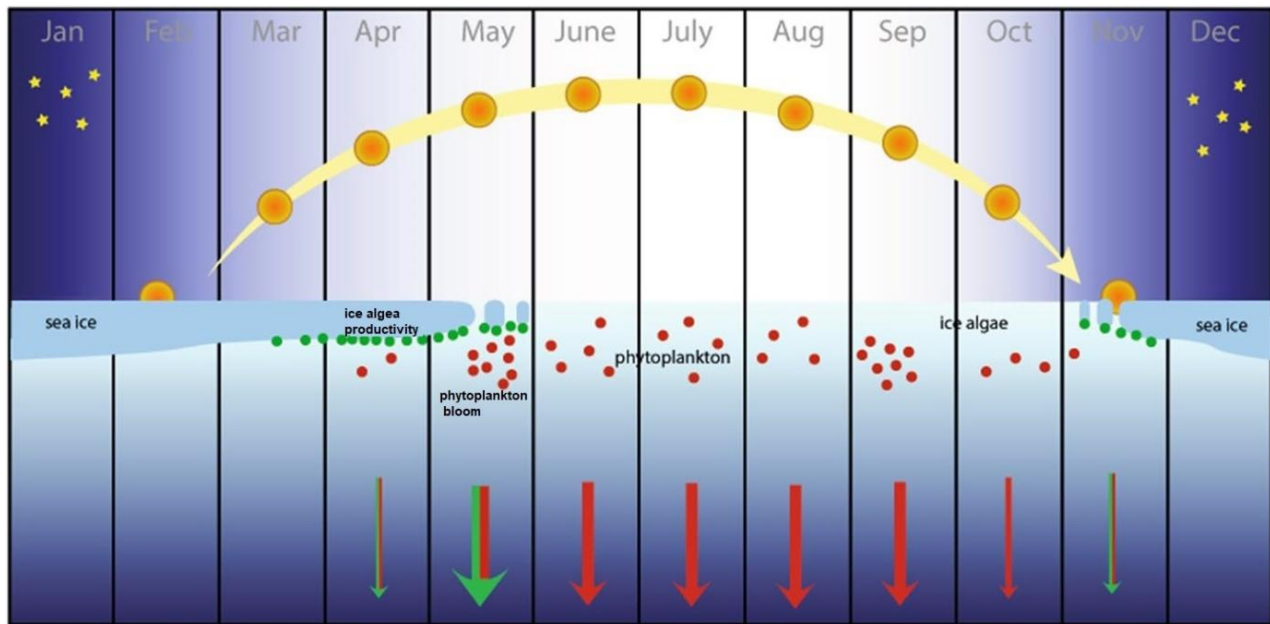
Figure 1.11: Schematic illustration of principal processes during an annual productive cycle in the Arctic Ocean. The development of phytoplankton bloom, ice algae, and seasonal light conditions along the eastern Baffin Bay (Disko Bugt) region in the Arctic (Source: Kolling et al., 2018, modified from Wassmann et al., 2011, 2020).

Climate change and the resulting reduction in ice cover will probably lead to more persistent ice algae blooms and will take a greater share of primary production (Wassmann et al., 2020). Recent studies have further shown that primary production can also occur under lower light conditions and earlier in the seasonal cycle than previously thought (Randelhoff et al., 2020). Also, light availability is not constant in the Arctic regions and varies significantly spatially and temporally. For example, between 67.4 and 72°N, the sun is below the horizon from 1 to 72 days, however, between 72 and 78°N the sun is below the horizon for 112 to 144 days (Fig. 1.12A) (Wassmann et al., 2020). The light forcing, among others, is a key determinant of ice algae and phytoplankton bloom development and therefore drives productivity as a function of latitude. Therefore, inside each longitudinal light window with its variable sea ice cover, the timing and extent of the ice and phytoplankton productivity vary from April to late summers from the south towards higher latitudes (Wassmann et al., 2020) (Fig. 1.12B).
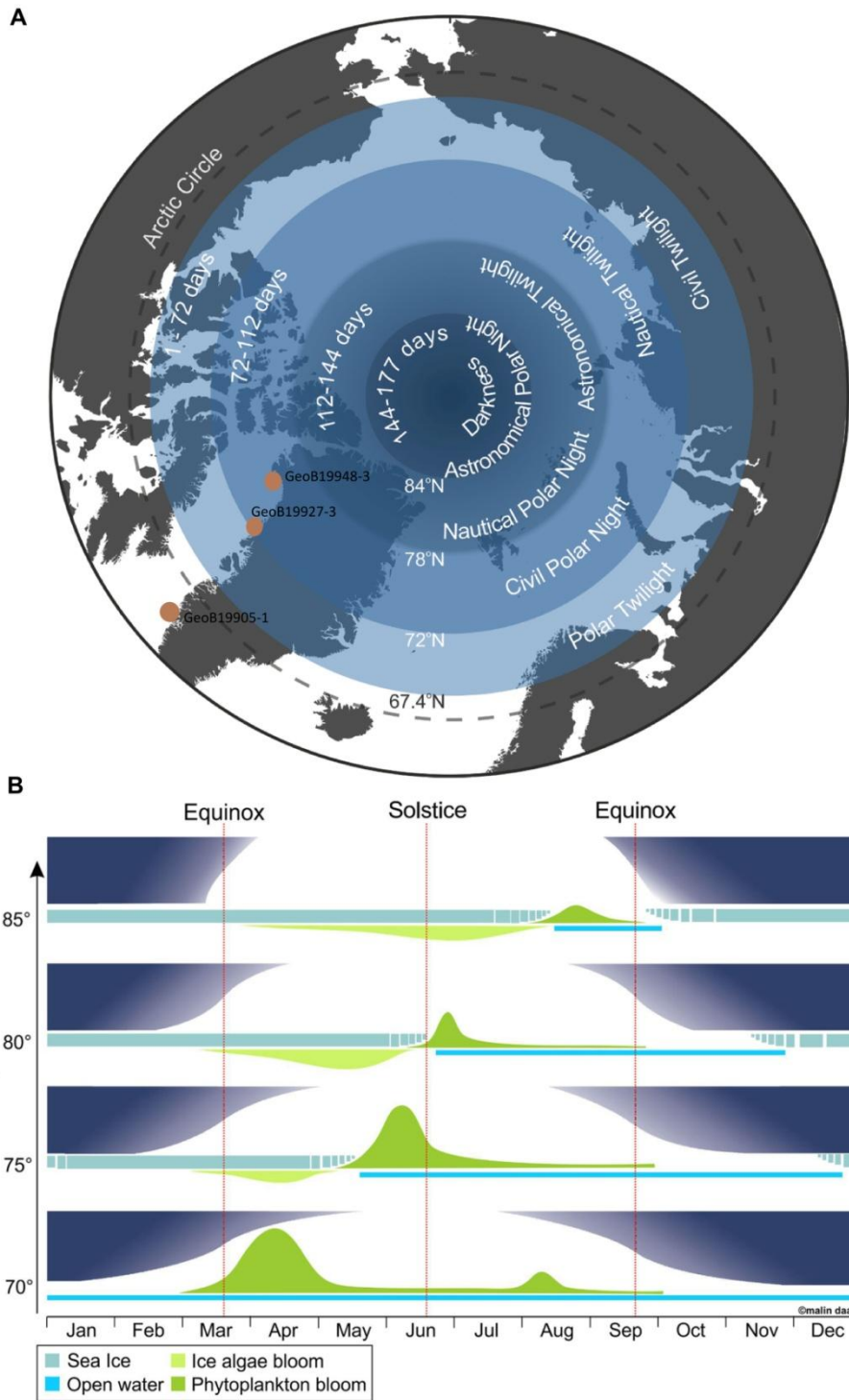
Figure 1.12: (A) Different types of Polar night situations (number of days when the sun is below the horizon) from the Arctic Circle 67.4°N towards almost the North Pole 84°N. (B) Ice algae and phytoplankton bloom conditions as a function of latitude. Note that combined conditions including light, ice and stratification regulates the timing of the bloom development along a particular latitudinal axis. (Source: modified from Wassmann et al., 2020).

11

Recent studies have suggested the overall increase in primary production due to accelerated loss of Arctic sea ice as well as enhanced nutrient supply owing to increased ice-sheet melting over the past several decades (Hill et al., 2018; Lewis et al., 2020; Tremblay et al., 2015). Compared to the average 2003-2019, for example, increased chlorophyll-a concentrations were found in phytoplankton in the Laptev Sea during July and August 2020 (Fig. 1.13). This is probably linked to the very early sea ice loss and exceptionally warm conditions during 2020. A widespread increase in primary productivity is also reported along the SE and SW Greenland, Baffin Bay, Barents Sea, Hudson Bay and Bering Sea regions and is linked to the increases in sea ice losses (Fig. 1.13, 1.14).

The amount and composition of organic carbon preserved in the sedimentary records depend upon factors such as primary production, terrigenous input, transformation processes as well as bulk accumulation rates. Owing to light limitation and sea ice cover, the central Arctic Ocean is characterized by very low primary production (<11 g cm^{-2} a^{-1}) compared to the Arctic marginal seas (30-150 g cm^{-2} a^{-1}) (Fig. 1.14) (Stein, 2008, Stein and MacDonald, 2004a). Baffin Bay is reported to have annual primary productivity in the range of 60-120 g cm^{-2} a^{-1}, assuming a 120-day growth season (Gosselin et al., 1997).
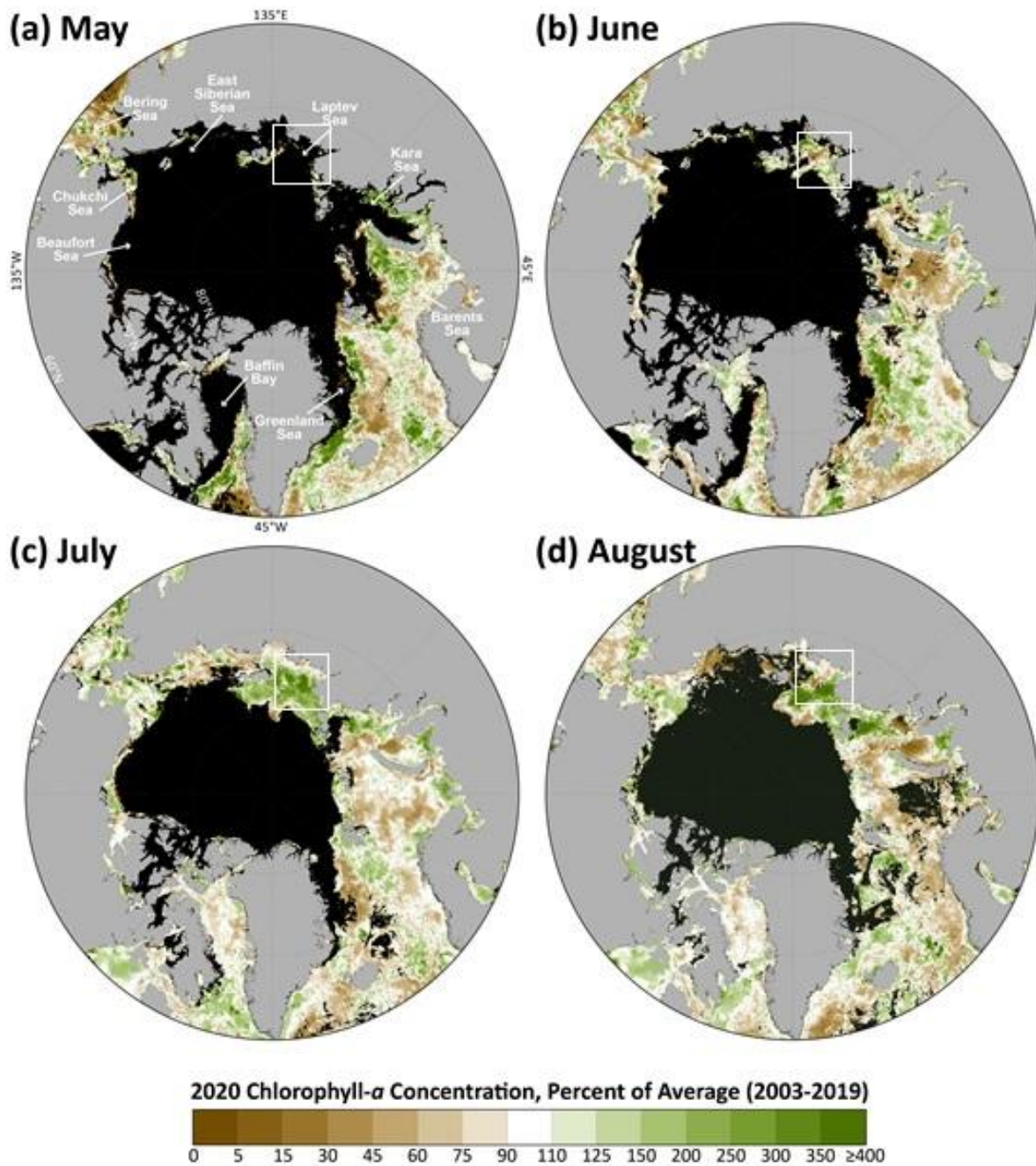
Figure 1.13: Satellite-based mean monthly chlorophyll-a concentration across the pan-Arctic region during 2020, displayed as a percent of the 2003-2019 average for a) May, b) June, c) July, and d) August. Areas shown as black represent regions where no data are available (due to cloud cover or >10% sea ice cover) (Source: http://oceancolor.gsfc.nasa.gov/; DOI: 10.25923/vtdn-2198).
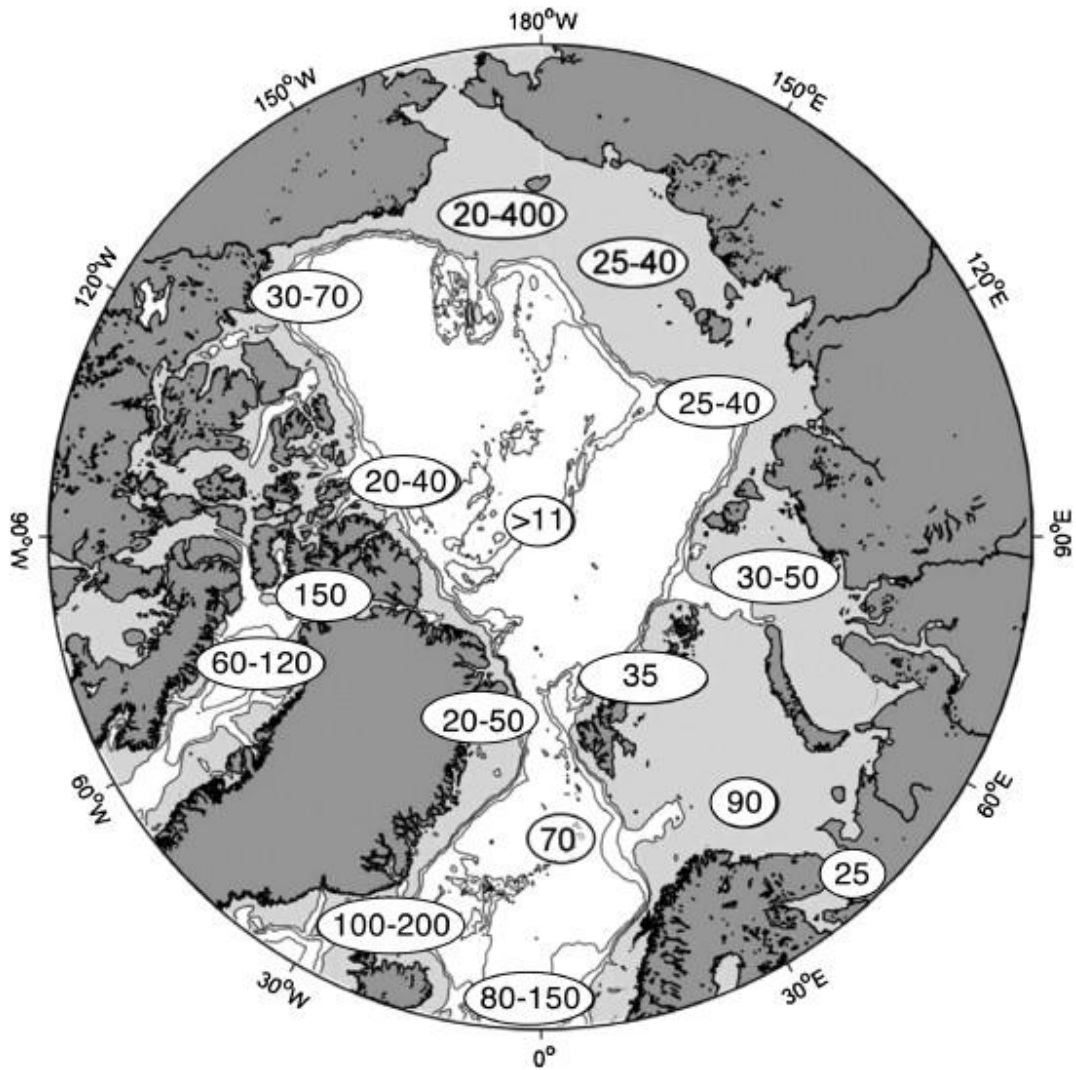
Figure 1.14: Total annual primary productivity (in g cm^{-2} a^{-1}) distribution across the Arctic (Source: Stein, 2008; based on Sakshaug, 2004).

1.3.2 Terrigenous input

Arctic regions act as sensitive filter zones for terrigenous matter input onto the continental shelves via river discharge and coastal erosion (Wegner et al., 2015). This material is distributed further across by ocean currents, sea ice, icebergs and aeolian processes (Fig. 1.15). Over the past several decades, Arctic regions have shown increased export of terrigenous sediments supply mainly due to enhanced annual river discharge, and this may alter the delivery of nutrients and promote primary production in the Arctic Ocean (Retamal et al., 2008). Climate

warming in the eastern Siberian Arctic has caused enhanced transport of large amounts of 'old' terrigenous organic matter, previously stored for a long time in the (thawing) Siberian permafrost, however, the fate of which is still debated (Bröder et al., 2019; Mann et al., 2015; Tesi et al., 2013). A significant part of the remobilized terrigenous organic matter could be degraded on the Arctic shelf and may be released into the atmosphere leading to further positive feedback for global climate warming.
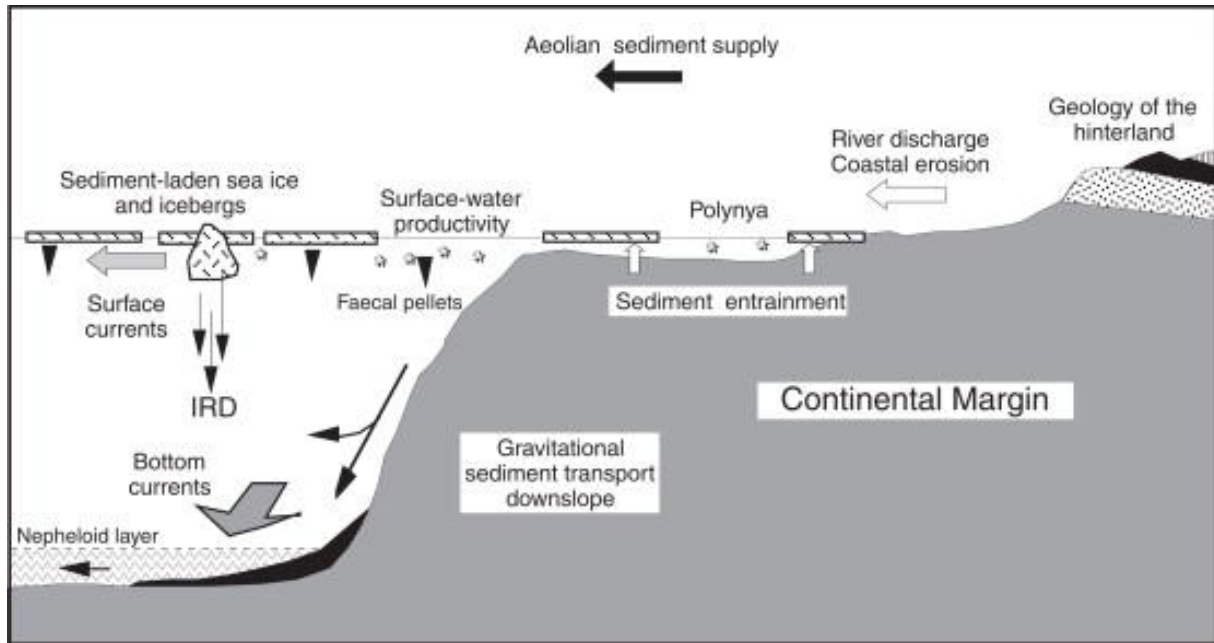
Figure 1.15: General processes controlling terrigenous sediments input in the Arctic Ocean (modified from Stein & Korolov, 1994; Stein, 2008).

The significance of terrigenous organic matter in the contemporaneous ocean and deep-sea sediments is an important, however, yet poorly understood aspect of the global organic carbon cycle (Eglinton and Repeta, 2003). The influence of climate variations, including the supply of riverine, eolian and sea ice exported terrigenous organic matter to the ocean is also not well constrained and the conventional assumption that deposition of terrigenous particles is restricted to the shelf and the upper slope is questionable (Stein and Fahl, 2000; Stein and MacDonald, 2004a; Wagner et al., 2004). During the LGM, thick perennial sea ice cover may have only allowed for minimal sea ice transport, and disintegrating ice sheets during the Deglacial period may have accounted for major transport. During the Holocene, however, the sediments released

from sea ice could have accounted for a major fraction or even dominate the total flux of terrigenous organic matter i.e. in the Arctic Ocean and Greenland Seas (Hebbeln and Wefer, 1991; Stein and MacDonald, 2004a).
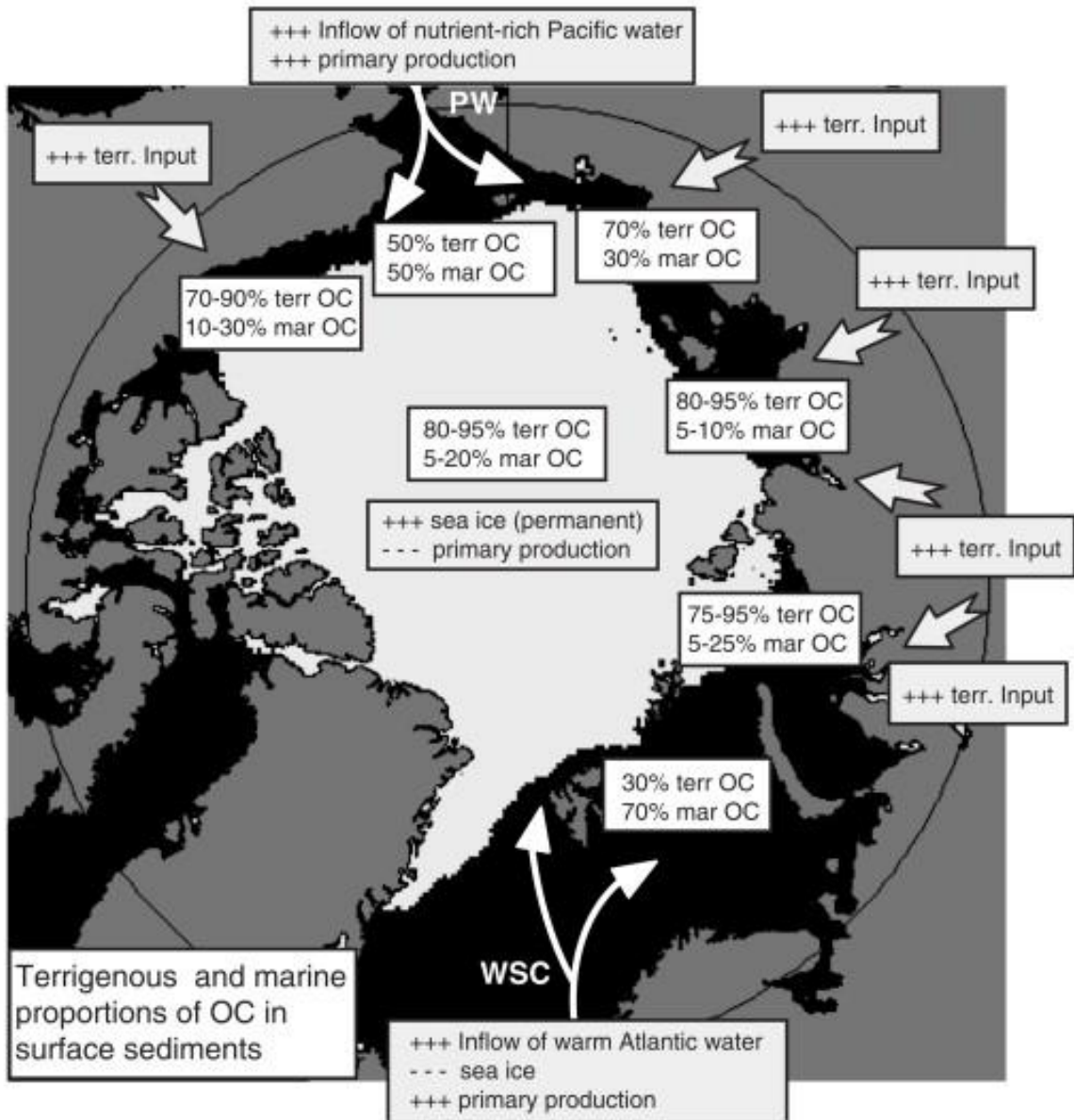
Figure 1.16: Terrigenous (terr OC) and marine organic-carbon (mar OC) distribution (in average percent) across the central Arctic Ocean and its marginal seas. (Source: Stein & Macdonald, 2004a and references therein.

Presently, terrigenous organic carbon dominates the areas close to river mouth discharge i.e., the Laptev Sea, Kara Sea, East Siberian Sea and Mackenzie river delta as well as the central Arctic Ocean, however, marine organic carbon may become significant in areas with high primary production such as in the Barents Seas (Fig. 1.16). However, no significant reliable data are available for Canadian Arctic and Baffin Bay regions.

1.3.3 Preservation

The mechanisms that may control the preservation of organic matter in the ocean sediments are the key to interpreting paleoceanographic signal. Generally, the carbon content of ocean sediments is strongly influenced by the primary production, particulate organic carbon influx to the bottom, transformation processes in the water column, the oxygen content, and the organic matter degradation rate as well as bulk sedimentation rates. Additionally, sediment grain size may also play an important factor in controlling organic carbon concentrations. High fine-grained siliciclastic material deposition may enhance preservation of marine (and terrigenous) organic matter by coagulation processes ("ballast effect"; Iversen and Robert, 2015; Fahl and Stein, 2007; Ittekot et al., 1992). For example, based on study by Fahl and Stein (2007) in the Kara Sea sediments (core BP99-04), the authors reported high accumulation of organic carbon linked to the distinct increase in fine-grained sediments caused by reduced current velocity and reduced river discharge. Here, the increased amount of organic carbon preservation was reported to be predominantly caused by terrigenous source of organic matter (Fahl and Stein, 2007). Furthermore, the understanding of the fate of terregenous organic carbon in marine sediments is quite important, as it is strongly related to the organic matter burial in marine sediments owing to different remineralization capacity of marine and/or terrigenouc organic carbon in the oceanic sediments. Additionally, marine organic matter can be more reactive than terrigenous organic matter, thus might undergo preferential remineralization. Additionally, in the topmost centimeters of the ocean sediments, preservation as well as diagentic alterations may also affect the organic carbon accumulation (cf. Fahl and Stein, 2012; Belt & Müller, 2013). However, these factors are highly variable in different environments of the Arctic Ocean (Stein, 2008) and should be interpreted with caution.

1.4 **Study area and modern setting**

Our principal study area includes Baffin Bay and the NE Labrador Sea located between Greenland and the Canadian Arctic Archipelago (CAA) in the Arctic region (Fig. 1.17A, B). Baffin Bay is a narrow semi-enclosed oceanic basin constrained by Baffin Island to the west, Ellesmere Island, Nares Strait to the north and in the south connected to the Atlantic Ocean via the Labrador Sea and Davis Strait. On the eastern side, Baffin Bay is connected to the Greenland. Baffin Bay stretches from ~67°N to 76°N, covering a total area of ~690,000 km^2. Baffin Bay is connected to the Arctic Ocean via the Nares Strait (~250 m deep) and Canadian Arctic islands in the north, while in the south it is connected to the Labrador Sea and North Atlantic via the Davis Strait (~640 m deep). The surface and subsurface waters in Baffin Bay and the Labrador Sea are characterized by a counter-clockwise gyre due to the interaction of northward-flowing warm high salinity Atlantic Water (Atl.W: 300-800m) transported by the West Greenland Current (WGC) with the southward flowing cold polar sourced Arctic Water (AW: 0-300m) transported via the Baffin Current (BC) (Fig. 1.17C) (Ribergaard et al., 2008; Tang et al., 2004). The WGC is formed by a combination of (1) Atlantic-sourced, relatively warm and saline water from the Irminger Current (IC), (2) polar-sourced cold, low salinity water from the East Greenland Current (EGC) and (3) local melt-water discharge along the SW-Greenland coast (Fig. 1.17) (Tang et al., 2004).

Modern sea ice cover duration (Fig. 1.17B) is longest in the north-western areas of Baffin Bay and shortest in its south-eastern regions, an area strongly influenced by the northward flowing warmer WGC (Tang et al., 2004). Sea ice begins forming in the north around October and covers most of the bay with sea ice by March (Bi et al., 2019). Sea ice reduces in summer and attains its minimum in September in Baffin Bay; however, the eastern Labrador Sea remains generally ice-free year-round due to the strong influence of the WGC (NSIDC, 2020; Tang et al., 2004). Furthermore, an area of around 80,000 km^2 in north-western Baffin Bay (North Water Polynya) is kept open by prevailing north-westerly winds, limiting formation of newly-formed thick sea ice cover, resulting in open-water conditions, high primary productivity and extensive heat loss to the atmosphere (Melling et al., 2010; Dunbar and Dunbar, 1972; Tremblay et al., 2002).
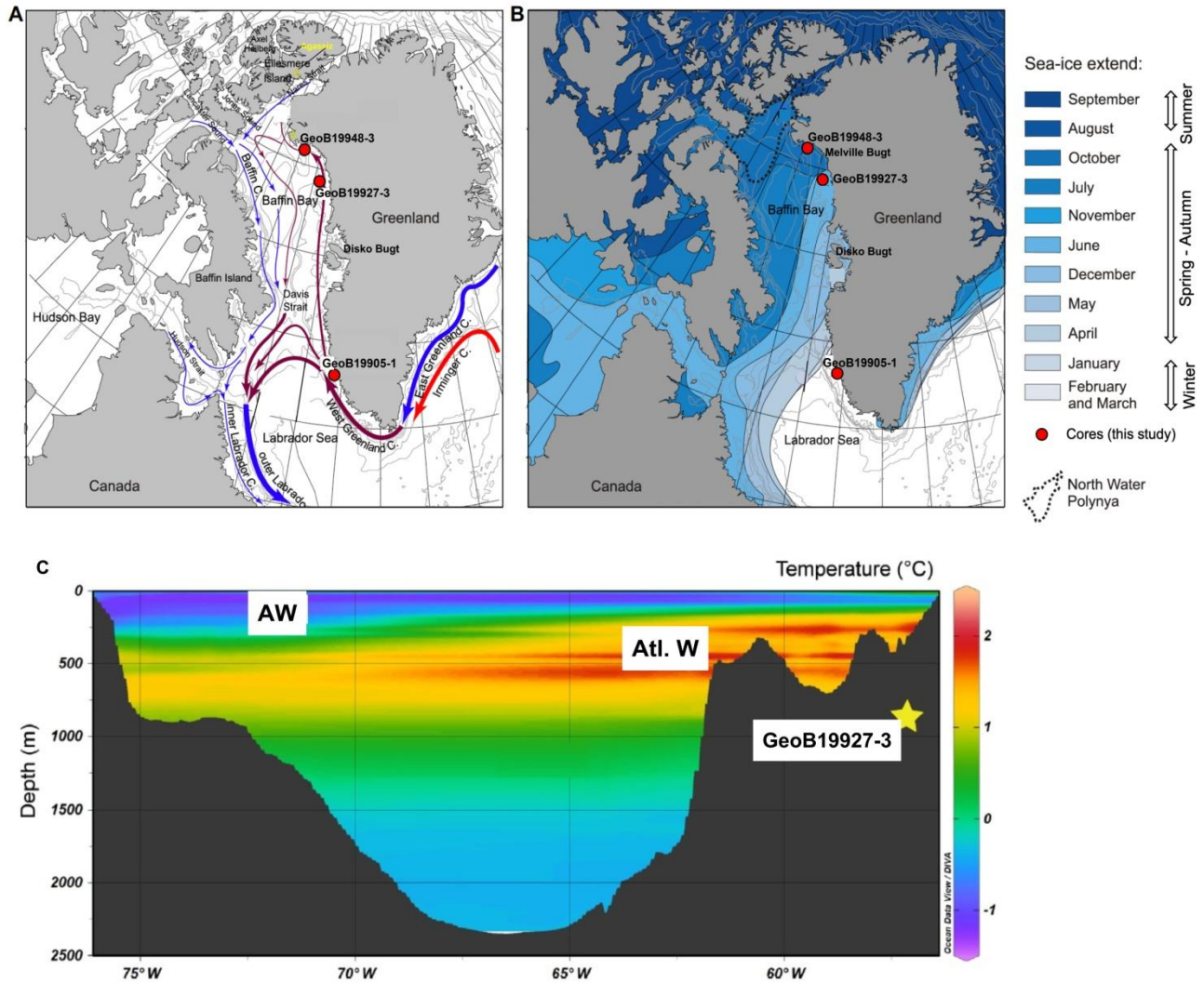
Figure 1.17: A. Map showing the location of sediment cores (GeoB19948-3, GeoB19927-3 and GeoB19905-1) studied herein and surface circulation in Baffin Bay and Labrador Sea areas. The warm surface currents are shown in red and cold polar sourced currents in blue. B. The average maximum extent of the sea ice edge for each month of the year (as per data from NSIDC, 2012), adapted from Seidenkrantz (2013a). C. Water mass profile in the Baffin Bay area along 73°N transect and the star indicates the core site at 932m water depth. The Schematic depth profile of Atlantic Water (Atl. W): 300-800m and Arctic Water (AW): 0-300m is shown according to World Ocean Atlas (Source: modified from Hansen et al., 2020; Locarnini et al., 2013).

Fast-flowing glaciers i.e. Ussing Braeer and Cornerll glaciers from the northwestern GIS and Kangiata nunata sermia, Isortuarssup sermia from the southwestern GIS, are in close proximity (Fig. 1.18) and might influence sediment delivery in this area (Joughin et al., 2010; Rignot and Kanagaratnam, 2006; Wood et al., 2018). The sediments deposited at the seafloor of the eastern

19

margin of Baffin Bay and the Labrador Seas are predominantly derived from glacial erosion of the surrounding landmasses, and high sedimentation rates of 40-140 cm/ka make this area an ideal site for paleoenvironmental studies (St-Onge and St-Onge, 2014).
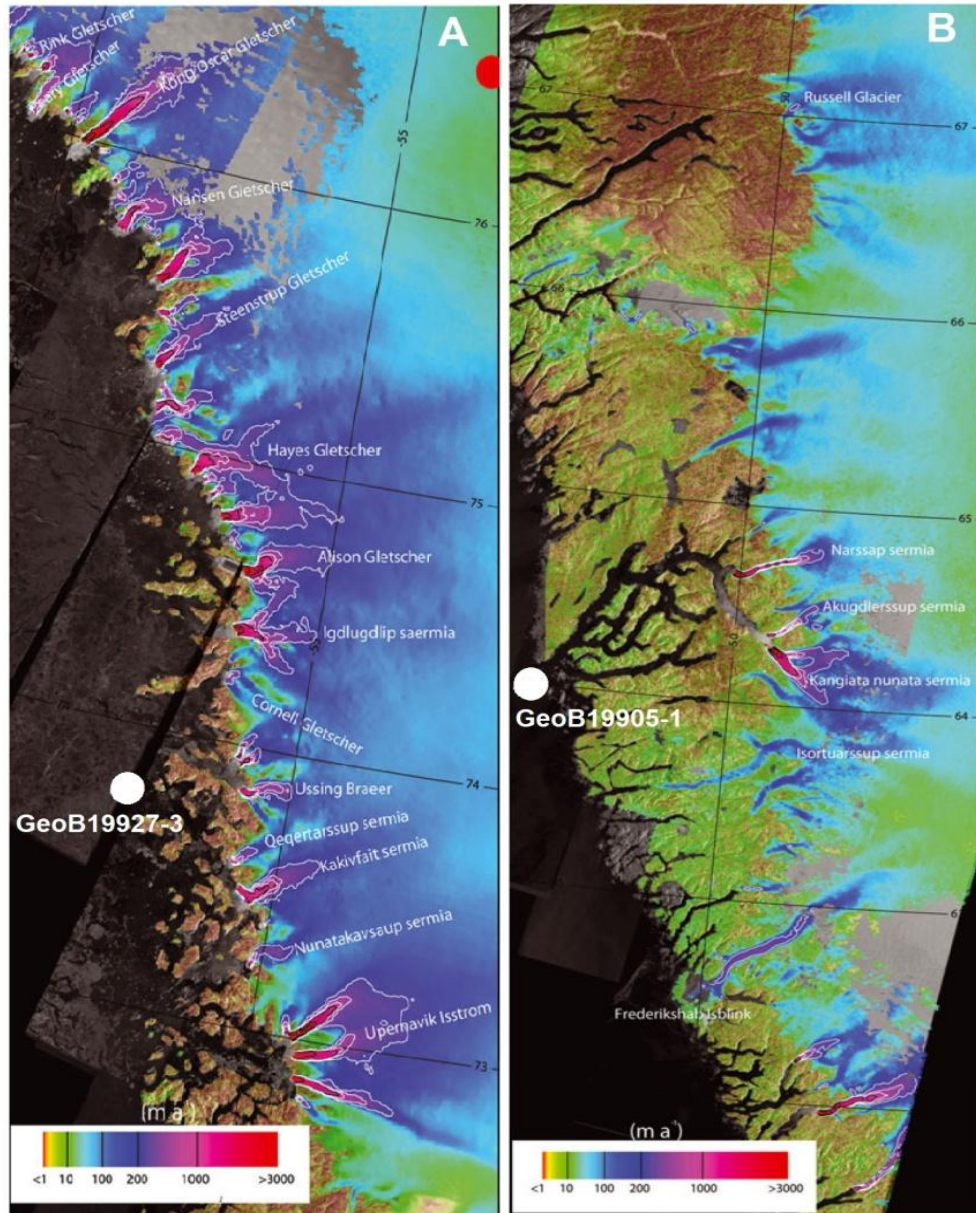
Figure 1.18: Major glaciers around the (A) northwestern and (B) southwestern Greenland Ice Sheet and their coastal flow speed as per year 2005/06, modified from Joughin et al. (2010).

1.5 Quaternary climate evolution
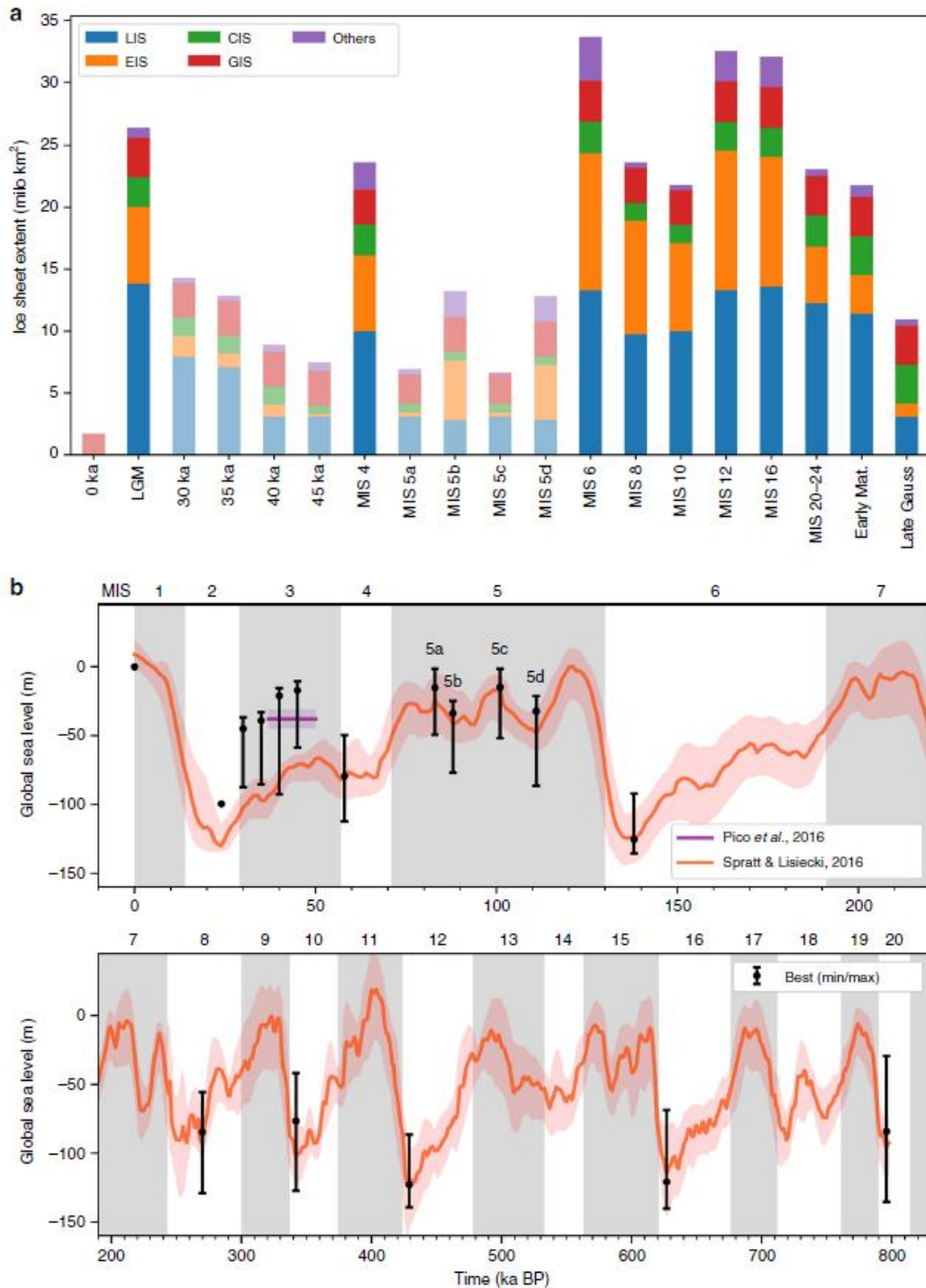
Figure 1.19: Northern Hemispheric ice-sheets variability during the Quaternary period. (a) Bar chart of major ice-sheet extents during the Quaternary period divided into 18 time-slices relative to the present-day extent (0 ka). Low saturation colors indicate comparatively warm intervals, whereas high-saturation colors indicate maximum ice-sheets during full-glacial periods. (b) Relative sea level fluctuations over the past 800 ka relative to the present day (0 ka). (From Batchelor et al., 2019 and references therein).

1.5.1   Glacial-interglacial cycles

In contrast to a significantly warmer period prior to 2.6 Ma, the Quaternary period of the last 2.6 Ma is associated with extreme growth and decay of polar ice sheets and Arctic sea ice became an integral part of the earth's climate system. During the Quaternary, Arctic climate was influenced by glacial-interglacial cycles (Fig. 1.19a) caused by changes in the Earth's orbit ("Milankovitch cycle"; Berger et al., 2005) and is associated with major seesaw type fluctuations in the global sea level (Fig. 1.19b). These cycles have had period of about 20 ka, 40 ka and 100 ka (Bamber, 2016). Since the middle Quaternary (around 800 ka BP), glacial-interglacial cycles tend to have a frequency of about 100 ka (so-called "eccentricity" cycle) (Lisiecki and Raymo, 2005). Over the last 450 ka, glacials have lasted about 70 ka to 90 ka, whereas interglacials lasts approximately 10 ka (Philander, 2008). Abrupt warming at the end of glacial periods tends to occur much faster than the increase in solar insolation possibly due to several feedback mechanisms, including ice-albedo and CO_2 release into the atmosphere. Sea level fall and rise with each glacial (cold) and the interglacial (warm) period leading to animal, plants and human migration. When the ice ages began, ice sheets spread from the high latitudinal areas and covered much of North America, Eurasia and the Barents Seas in the northern hemisphere. During the glacials, the GIS was supposedly larger than present, extending out to continental margins (Bamber et al., 2015). Additionally, using terrestrial and modeling studies, Batchelor et al. (2019) hypothesized Northern Hemispheric ice-sheet extent prior to the LGM in 17 time-slices of 5 ka intervals for major marine isotopic stages (MIS) corresponding to cool and warm intervals (Fig. 1.19a, 1.20).

During the last 800 ka, large parts of North America and Europe were covered with ice sheets in glacial times corresponding to MIS 20 to MIS 2 (LGM) (Fig. 1.19). In the Canadian Arctic and Greenland, ice sheet extended further onto the shelf areas, while in northern Eurasia, ice advanced onto the Barents Sea and Kara Sea ice shelves (Svendsen et al., 2004). However, NE Russia may have still remained ice-free (Gualtieri et al., 2003). During the most recent and best constrained glacial cycle (MIS 2-5d; Fig. 1.20d-m), the ice-sheet advanced in continental interiors of NE Asia and eastern Europe earlier in the last glacial cycle, whereas western Europe (EIS) and Laurentide ice-sheets (LIS) attained their maximum extent towards the end of the
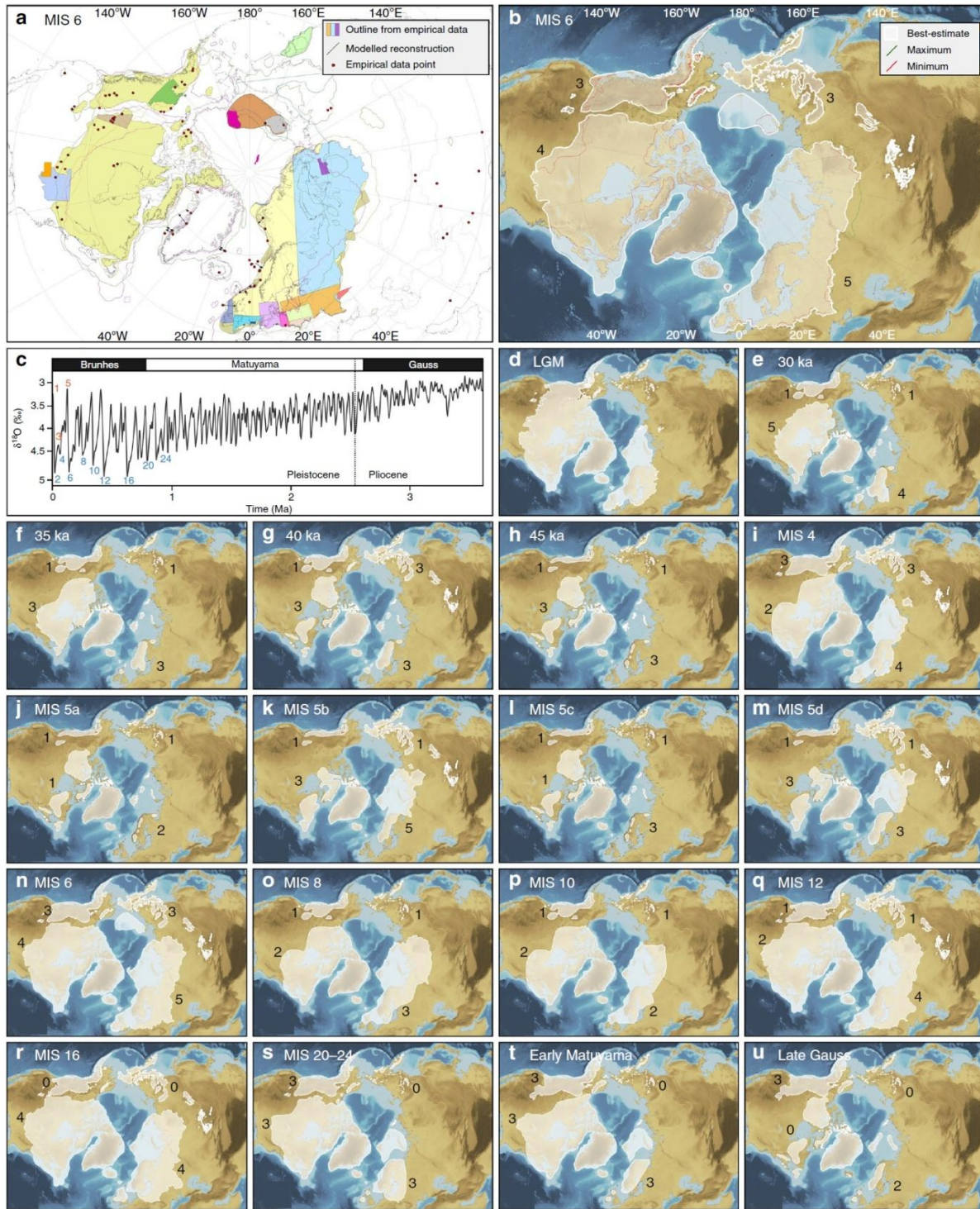
Figure 1.20: Estimated (modelled) reconstructions of Northern Hemisphere (NH) ice-sheet during the Quaternary for various glacial stages (Marine Isotopic Stages 24-2). Time slices Fig. **d-u** are the best-estimate reconstructions of NH ice-sheet extent during the Late Quaternary period. The robustness score (0-5) of this estimation is shown, 0 indicating no empirical/modelled data and higher values, i.e. 5 indicate more/or all the empirical and modeled data in agreement with the reconstructed ice-sheet margin. (cf. Batchelor et al., 2019 and references therein). (Source: Batchelor et al., 2019)

glacial cycle (Fig. 1.20). A comparison of the older glacial period (MIS 4) with the LGM, shows that the south-western margins of the LIS and EIS attained more extensive ice growth during the LGM, in comparison to the eastern margin of EIS, however, during the MIS 4, glaciations in North America and NE Asia were more extensive in contrast to the LGM (Batchelor et al., 2019; Gowan et al., 2021). The EIS showed the greatest change during the LGM compared to relatively warmer intervals of MIS 3, 5a and 5c (Fig. 1.20), which can be explained partially by the marine-based nature (more susceptible to change; Oppenheimer, 1998) of this ice sheet, which covered the Barents Sea, Kara Sea and the North Sea during full glacial periods (Ehlers, 2011; Patton et al., 2017; Svendsen et al., 2004).

1.5.2   LGM-deglacial-Holocene transition

During the most recent glacial cycle (MIS2), the glaciers and ice sheets developed in continental interiors of Eastern Europe and NE Asia (Fig. 1.20d). Whilst large ice sheets such as LIS and western EIS attained its maximum extent towards the end of the glacial cycle (LGM) and probably also influenced ice-sheet configuration elsewhere in the Northern Hemisphere. Sea level fell to about 120 m lower than the present, when large ice sheets advanced to the broad continental shelves of the Arctic and subarctic seas (Fairbanks, 1989). During the deglacial period, the disintegration of ice sheets followed and the Arctic hinterland was accompanied by increased iceberg activity and huge input of fresh water discharge in the Arctic shelves as well as increased sea level inundation. The deglaciation period from 16 ka BP to 9 ka BP could be characterized by increasingly more open-water conditions with some regional variability (Cronin et al., 2010). This period might be associated with the increased seasonal opening of sea ice cover, i.e. around the Greenland, Norwegian, and Iceland Seas (Koc et al., 1993). During the warm Bølling/Allerød (BA) period between about 14.5 and 13 ka BP, a rapid decrease in sea ice cover followed as shown by sediment cores recovered from the Lomonosov Ridge (Fahl and Stein, 2012). Afterwards, a dramatic fresh water event and enhanced fresh water flux into the North Atlantic caused enhanced sea ice formation resulting in a abrupt cold event termed as the "Younger Dryas (YD)" which caused slow-down in the AMOC and was linked to the partial drainage of Lake Agassiz into the North Atlantic (Not and Hillaire–Marcel, 2013; Hillaire-Marcel et al., 2013). During the deglacial transition, other cooling events in the Northern Hemisphere were also reported, such as the Preboreal Oscillation at about 11.7-11.2 ka BP, and the "8.2 ka event" at about 8.2 ka BP (Fig. 1.21) (Barber et al., 1999; Broecker et al., 1989). The

"8.2 ka – event" is a globally well-documented cold event, most probably caused by the influx of large volume of fresh water from the glacial lakes Agassiz and Ojibwa drained into the North Atlantic. This led to a drop in temperature of about 5-7°C (Alley et al., 1997) and has been linked to the glacial advances in central and southern Greenland (Schweinsberg et al., 2017; Balascio et a., 2015). The huge inflow of fresh water into the North Atlantic may have significantly reduced deep-water formation and weakened the thermohaline circulation, which would lead to abrupt climate change in these cold periods (Schmittner and Clement, 2002; Stocker and Wright, 1991).
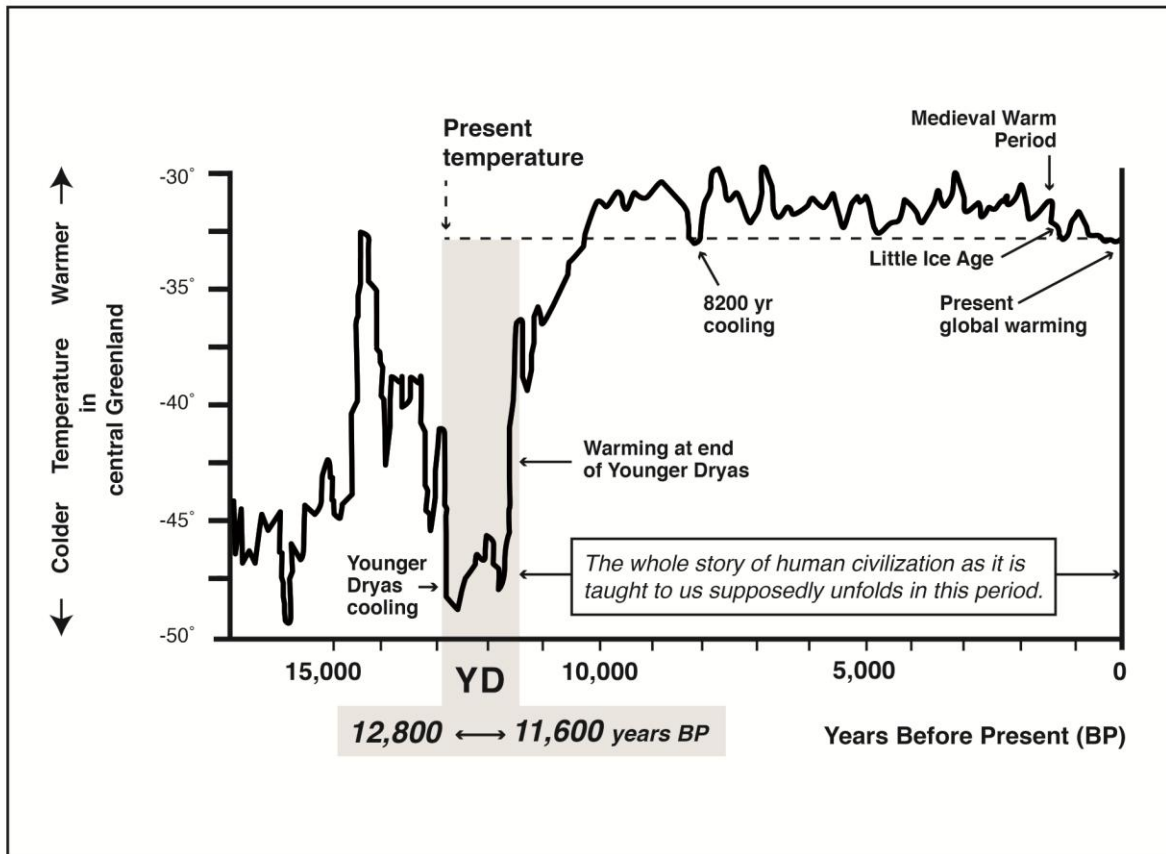
Figure 1.21: Generalized Late Glacial to Holocene temperature variations in central Greenland (Source: http://www.endeavourswake.co.uk/439202548).

1.5.3 The Holocene period

The current warmer interglacial period when humans thrived, i.e. the Holocene, began ca. 11.7 ka BP with the termination of colder and drier YD (Rasmussen et al., 2006) (Fig. 1.21).

Generally, reduced sea ice cover and high thermal maximum conditions characterized the onset of Holocene throughout most of the Arctic marginal seas (Cronin et al., 2010). Albeit, the Holocene climate fluctuations were relatively weaker than the LGM-deglacial period, it may be of great significance to test and improve our climate models (Kaufman et al., 2016; Mayewski et al., 2004). Several studies from the high northern latitudes along the West Greenland Shelf describe the Holocene into three main intervals; 1) the early Holocene (~11.5-7.8 ka BP), 2) mid Holocene (~7.8-3 ka BP) and 3) the late Holocene (last 3 ka BP).
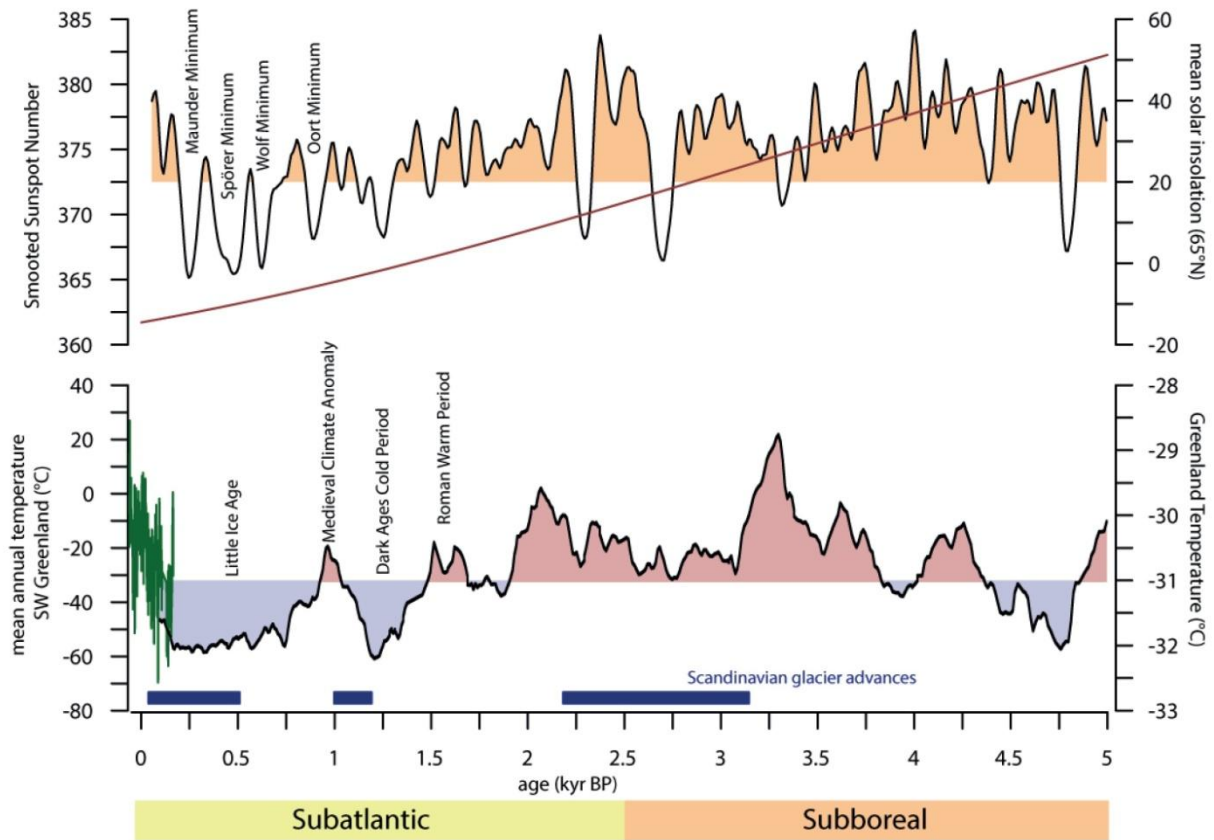
Figure 1.22: Overview of the major paleoclimatic events during the last 5 ka BP. Greenland atmospheric temperatures is based on δ^{18}O from GISP2 ice core (Alley et al., 2010) and observed atmospheric temperatures from SW Greenland during the 1880-2010 time period (Cappelen and Vinther, 2014). The trend in mean solar insolation is shown together with the sunspot number as well as specific sunspot minima (Bond et al., 2001; Solanki et al., 2004; Stuiver, 1961). (Modified from Kolling, 2017a)

The early-to-mid Holocene is generally characterized by high atmospheric temperatures, termed as the Holocene Thermal Maximum (HTM), however, its character and timing may differ between regions and especially between high and low latitudes (Kaufman et al., 2004; Renssen et al., 2012). In the early Holocene, paleoceanographic reconstructions from the North Atlantic and

circum-Greenland areas show conditions warmer than today (Briner et al., 2016; Kaufman et al., 2016). This warming could be associated with high summer insolation and/or the increased advection of Atlantic Water masses and enhanced north-westward retreat of sea ice in the Arctic (Koc et al., 1993; Svendsen et al., 2004). In particular, the melting of the GIS during the early-to-mid Holocene and its negative feedback to atmospheric warming might be linked to the distinct differences in the spatial and temporal extent of the HTM, i.e. in the Nordic Seas (Risebrobakken et al., 2011). The late Holocene, however, is widely characterized by decreased solar insolation and an increase in sea ice and glacier re-advances generally referred to as Neoglacial cooling (Fig. 1.22) (Isaksson et al., 2005; Levy et al., 2017; Nesje et al., 2001; Wanner et al., 2008). This cooling was associated with an enhanced influence of Arctic Waters into the Baffin Bay and the Fram Strait areas (Perner et al., 2012). However, the characteristics and timing of the Neoglacial cooling vary between different regions, some notice a stepwise (Werner et al., 2013) and other a gradual cooling (Müller et al., 2012). Superimposed on this general cooling trend, several short-time climate fluctuations i.e. Roman Warm Period (RWP), Medieval Climate Anomaly (MCA), and Little Ice Age (LIA) were recorded in the North Atlantic regions (Jones and Mann, 2004; Ljungqvist, 2010) which were reported to be influenced by the retreat and/or advance of Atlantic Water towards the Arctic (Fig. 1.22).

1.6   **Paleoenvironmental proxy-based reconstructions**

Since direct observation of environmental conditions is only limited to past few decades to a few hundred years, deep-time past climate reconstructions rely mainly on proxy measurements. These proxies are usually related to certain environmental parameters such as sea ice, primary productivity, oceanic currents, terrigenous input and glacier retreats/advances.

1.6.1   **Micropaleontological and sedimentological proxies**

Paleo sea ice reconstructions rely heavily on proxies preserved in marine sediments. In this context, a combination of sedimentological and micropaleontological inferred proxies such as ice-rafted debris (IRD), assemblages of dinocysts, diatoms and ostracods and δ^{18}O in foraminiferal tests may provide important information about past sea ice conditions (e.g., Cronin et al., 2014; de Vernal et al., 2005, 2013a; Gersonde et al., 2005; Hillaire-Marcel and de Vernal, 2008; Jennings et al., 2002; Limoges et a., 2018; Matthiessen et al., 2005; Pieńkowski et al., 2017; Warren, 1992). Despite the wide application of these sedimentological and

micropaleontological proxies, most of them can only be considered as indirect sea ice proxies, as sea ice being only one of several other environmental parameters affecting them. Also, microfossil records such as, for example, diatom assemblages must be interpreted with caution as they may also be influenced by dissolution and selective preservation (Bidle and Azam, 1999; Leventer, 1998; Shemesh et al., 1989). Errors of transfer functions applied to microfossils data may also increase within the application in paleorecords (de Vernal et al., 2005a). Moreover, the reconstructions from IRD cannot differentiate between sea ice and icebergs transport.

1.6.2 Biomarkers and organic-geochemical bulk parameters

The main approach of this thesis was to use specific biomarker proxies to investigate the sea ice, primary productivity and terrigenous input conditions off the eastern coast of Baffin Bay-Labrador Sea transect along the West Greenland margin. The determination of such biomarkers provides useful information for past oceanographic conditions. A detailed description and interpretation of investigated lipid biomarkers, including HBIs and specific sterols, are also presented in more detail in the following chapters 4, 5 and 6.

1.6.2.1 Sea ice

The first identification of a source-specific highly branched isoprenoid alkene (HBI) in sea ice samples from the Canadian Arctic in a pioneer study by Belt et al. (2007) has started a new field of sea ice reconstructions in the polar environments. In general, HBIs are produced by diatoms and widely found in marine and fresh water ecosystem and their sediments (Belt et al., 2000; Volkman et al., 1994). Among them, however, a specific monounsaturated HBI alkene with 25 carbon atoms (Fig. 1.23) is proposed to be directly synthesized by diatoms (mostly *Haslea* spp.) living in sea ice. This biomarker termed as "sea ice proxy IP_{25}" has been preferentially used for reconstructing sea ice variability (Belt et al., 2007, 2008; Brown et al., 2014).

A comprehensive and comparative study of IP_{25} extraction protocol, identification and quantification involving several international laboratories has revealed its source-specificity and stability and its potential for pan-Arctic sea ice proxy (Belt et al., 2014; Belt et al., 2012). The absence of IP_{25} in open-water phytoplankton samples and its isotopic ^{13}C signature in sea ice, sediment trap and marine sediments showed its specific ice-origin (Belt et al., 2008; Brown et al., 2014). In previous sediment traps studies from Canadian Arctic (Belt et al., 2007), Fram Strait (Lalande et al. 2016; Soltwedel et al., 2016), the authors found the highest sedimentary

Highly branched isoprenoids
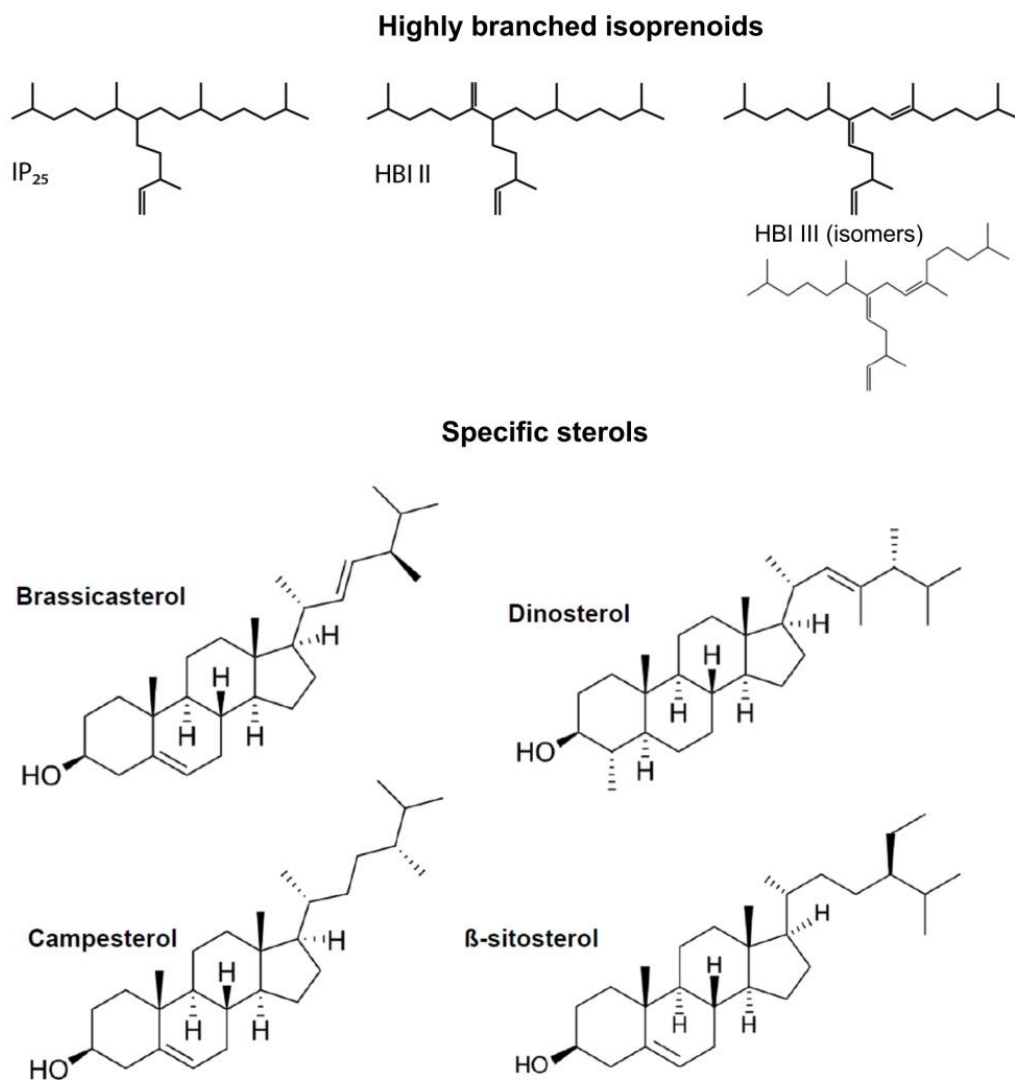
Specific sterols

Figure 1.23: Chemical structure of common highly-branched isoprenoid HBIs and of specific sterols.

IP_{25} concentrations related to spring bloom, however, in the central Arctic, the highest sedimentary IP_{25} concentrations were reported during summer months (Fahl and Stein, 2012; Nöthig et al., 2020) (Fig. 1.24). This showed the regional differences of IP_{25} producing diatoms, which depend on seasonal differences in light and sea ice conditions. The light-driven ice algae bloom is important in supporting the higher tropic food web and thus the deposition of sea ice derived organic matter into the marine sediments (Fig. 1.24).

Furthermore, IP_{25} is stable over millions of years (Stein et al., 2016) and therefore; it has emerged as a successful approach for paleo sea ice reconstructions in the Arctic regions. As

proposed first by Belt et al. (2007), the absence of IP$_{25}$ may be caused by both the permanent sea ice cover and the ice-free conditions (Fig. 1.24). To distinguish between these two extremes, Müller et al. (2011) and Smik et al. (2016) combined IP$_{25}$ with open water phytoplankton markers (i.e., brassicasterol, dinosterol and tri-unsaturated HBI) in the so-called PIP$_{25}$ index using the following equation:

$$P_pIP_{25} = IP_{25} / (IP_{25} + (p*c)),$$

Where p is the phytoplankton marker concentration (p = B(brassicasterol) or D(dinosterol) or III(HBI III), and c is a balance factor to compensate for a significant concentration difference
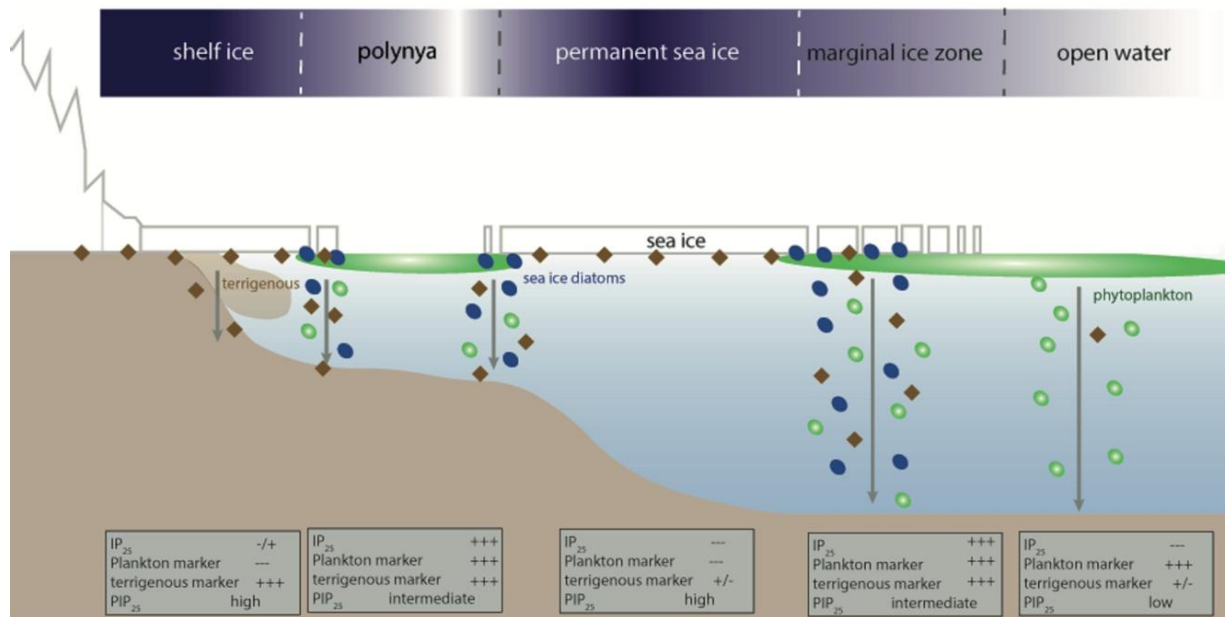
Figure 1.24: Generalized overview sketch of the Greenlandic shelf cross-section showing deposition of different biomarkers related to ice algae (in blue), phytoplankton (in green) and terrigenous supply (in brown). PIP$_{25}$ index varies from 0 to 1 from open waters towards extended sea ice conditions (Source: Kolling, 2017; modified from Müller et al., 2011; Stein et al., 2016).

between IP$_{25}$ and phytoplankton marker concentration (c = mean IP$_{25}$ concentration/mean p concentration). When using HBI III as phytoplankton biomarker and IP$_{25}$ and HBI III concentrations are similar in magnitude, a balance factor may not be needed (i.e., c = 1). Based on this equation, Müller et al. (2011) described high IP$_{25}$ and concurrently low phytoplankton biomarker yielding high PIP$_{25}$ values (>0.75) as indicative of extensive sea ice cover. However, low IP$_{25}$ and concurrently high phytoplankton biomarker yield low PIP$_{25}$ values (<0.5) as

indicative of reduced to minimal sea ice cover (Fig. 1.24). An intermediate PIP_{25} value (0.5-0.75) corresponds to marginal sea ice conditions (Müller et al., 2011). The P_BIP_{25} and P_DIP_{25} indices are most commonly used in the Arctic region and when compared from surface sediments yield a positive correlation with modern satellite-based observations and therefore were successfully applied in numerous paleo-sea ice reconstructions (see reviews by Stein et al., 2012; Belt and Müller, 2013; Belt, 2018 and references therein). The PIP_{25} approach still has its limitations, such as the inaccuracy and nonunique c factor depending on the type of phytoplankton markers used for PIP_{25} calculations. These may lead to spatially different magnitudes of sea ice cover. The review paper by Belt (2018) described the limitations and advantages of these proxies in more detail.

Z-HBI III (commonly referred as 'HBI III') has been combined with IP_{25} ($P_{III}IP_{25}$) index that provided an additional proxy for sea ice reconstructions. Based on the distribution pattern of HBI III in surface sediments from the western Barents Sea and the correlation with seasonal sea ice concentration maps, for example, Belt et al. (2015) proposed that HBI III maxima reflect winter MIZ conditions. In contrast, based on a study of East Greenland fiords surface sediments, Ribeiro et al. (2017) proposed that HBI III maxima correlate with the July MIZ situation. Based on surface sediments from Baffin Bay area, Kolling et al. (2020) proposed that the sea ice indices P_DIP_{25} and P_BIP_{25} may show late spring and/or autumn conditions, while $P_{III}IP_{25}$ may record more the early spring and/or late winter (ice-edge) conditions. However, low to zero concentrations of HBI III in Baffin Bay sediments may cause an overestimation of the sea ice cover by the $P_{III}IP_{25}$ index and therefore should be interpreted with caution (Kolling et al., 2020).

In addition to IP_{25}, another diunsaturated molecule (HBI II) (Fig. 1.23) has been identified in both the Arctic and Antarctic sediments (Belt et al., 2007; Belt, 2018) and proposed as an additional sea ice proxy in the Southern Ocean and Antarctic realm (so-called, "$IPSO_{25}$"; Belt et al., 2016). However, HBI II has also been found in ice-free and temperate fresh water systems such as Everglades in Florida, hence questioning its source-specificity and therefore, further research is needed to investigate its use and reliability as an Arctic sea ice proxy (Belt, 2018; Collins et al., 2013a; He et al., 2016; Masse et al., 2011; Summons et al., 1993; Yruela et al., 1990).

1.6.2.2 Productivity

Specific sterols such as brassicasterol and dinosterol (Fig. 1.23), usually produced by marine diatoms and dinoflagellates, have been preferentially used as biomarkers for marine phytoplankton productivity (Meyers, 1997; Robinson et al., 1984; Volkman, 1986; Volkman et al., 1993). However, brassicasterol may also be produced by fresh water diatoms. Therefore in regions that are strongly influenced by riverine discharge, the application of brassicasterol as a proxy for marine phytoplankton productivity is limited (Belt et al., 2013; Fahl and Stein, 1999; Yunker et al., 1995). Interestingly, HBIs with triple unsaturated bonds such as Z-HBI III and E-HBI III (Fig. 1.23, with Z- and E-isomers) are closely associated with open-water and marginal ice-zones conditions and can be used as another phytoplankton biomarker proxy (Belt, 2018; Belt et al., 2015; Masse et al., 2011; Smik et al., 2016a). Additionally, based on the correlation of Z-HBI III and E-HBI III to spring cholorophyll a concentrations (chl a), Belt et al. (2019) have proposed that the proportions of HBIs Z and E-isomers (TR$_{25}$) may indicate spring phytoplankton blooms, at least for the Barents Sea and surrounding regions. This approach, however, needs to be further evaluated by using additional data from surface sediments and sediment cores from other Arctic regions.

1.6.2.3 Terrigenous input and organic matter sources

Long-chain odd-numbered n-alkanes (i.e. C27+C29+C31), derived from the leaf waxes of terrestrial vascular plant material have been widely used as a proxy for terrigenous input in marine sediments (Eglinton and Eglinton, 2008; Schubert and Stein, 1996; Fahl et al., 2003; Fahl and Stein 2004a, b). Specific biomarker sterols such as ß-sitosterol (24-ethylcholest-5-en-3ß-ol) and campesterol (24-methylcholest-5-en-3ß-ol) (Fig. 1.23) are also predominantly produced by land vascular plants (Stein and Macdonald, 2004) and often and successfully applied as a proxy for land-derived terrigenous input (Fahl and Stein, 1997; Hörner et al., 2016; Kolling et al., 2017; Syring et al., 2020). Furthermore, long-chain even-carbon numbered fatty acids and n-alcohols may also provide an estimate of terrigeous input (Meyers, 1997). Even more accurate proxy for vascular plant organic carbon input can be obtained from specific lignin phenols (Kattner et al., 1999), albeit lignin data is rare in the Arctic Ocean sediments (Goñi et al., 2000; Lobbes et al., 2000; Schubert and Stein, 1996). The branched vs. isoprenoid tetraether index, the so-called "*Branched and Isoprenoid Tetraether (BIT)*" represents the relative proportion of branched GDGTs in marine sediments to an isoprenoid crenarcheol found in ubiquitous pelagic

Thaumarchaeota (Sinninghe Damsté et al., 2016) and can be used as a proxy for terrigenous organic carbon as discussed in some Arctic studies (Weijers et al., 2014; Ji et al., 2019; Sparkes et al., 2015; Yamamoto et al., 2008).

These biomarker proxies may be supported by organic bulk parameters such as carbon to nitrogen ratio (TOC/N) and stable carbon isotopes ($\delta^{13}C_{org}$) which may help distinguishing terrigenous (higher plant) and marine (algal) organic matter in marine sediments (Hedges et al., 1986; Schefuß et al., 2003; Stein and Macdonald, 2004). Based on the high TOC/N ratio (>10) lighter $\delta^{13}C_{org}$ values <-23‰, a terrigenous origin of organic matter can be inferred.

1.7 **Rationale and Outline**

The Arctic Region reacts sensibly to climate changes and at times acts as an amplifier, hence a crucial topic for paleoclimate research. Arctic sea ice plays a crucial role in Earth's climate and is very sensitive to climate change and internal feedback mechanism on short as well as longtime scales. Despite the growing wealth of research in Baffin Bay and the Labrador Sea, there are still unanswered questions regarding sea ice variability in the past, especially during the Holocene. So far, a relatively new, sea ice biomarker approach (IP_{25} and PIP_{25} index) has mainly concentrated on specific areas such as Fram Strait, central Arctic Ocean, including the Barents Sea and Russian Arctic shelf area. Sedimentary sections with high sedimentation rates recovered from Baffin Bay and NE Labrador Seas allow for the first time a high-resolution mainly biomarker-based paleoceanographic reconstruction to address the following research questions:

➢ Manuscript I: How did sea ice conditions and primary productivity varied in the Baffin Bay area during the Holocene and how melt water and oceanic currents influenced the sea ice conditions?

In chapter 4, our specific interests were to reconstruct the Holocene sea ice variability using a more direct ice-proxy (IP_{25}) and to assess the mechanisms controlling the sea ice extent/retreat in the northeastern Baffin Bay. Here, we investigated the effects of sea ice and melt water discharge on primary productivity and their relation to global climate change. The sea ice record presented here seems to be mainly influenced by a combination of processes in the adjacent fjord including solar and oceanic forcings (i.e., WGC, BC) and show close interaction with the melt water discharge from the adjacent ice sheets.

➢ Manuscript II: How did sea ice and primary productivity conditions in Baffin Bay evolved in comparison to the Labrador Sea? How did melt water and oceanic currents affected the sea ice variability along this N-S transect?

In Chapter 5, high-resolution Holocene (last 11.5 ka BP) reconstructions of sea ice cover and primary productivity conditions were investigated along a N-S transect of eastern Baffin Bay-Labrador Sea margin with intention to provide deeper insight into sea ice variability using a more direct ice-proxy (IP_{25}) on the West Greenland Shelf and compare it to previously published records. The sea ice conditions in this transect show strong variability; from a (spring-autumn) ice-free NE Labrador Sea to increased seasonal/marginal sea ice cover towards northern Baffin Bay areas throughout the Holocene. A deeper insight into sea ice evolution and primary productivity were achieved when compared with previously published proxy records in this area.

➢ Manuscript III: How did terrigenous organic carbon input varied in the Baffin Bay-Labrador Sea transect during the Holocene?

In Chapter 6, three sediment cores along the N-S transect of Baffin Bay-Labrador Sea were investigated for assessing the main factors controlling the terrigenous organic carbon input as well as to decipher the main source of organic carbon, primarily by using organic geochemical (TOC, TOC/N), stable carbon isotope ($\delta^{13}C_{org}$) and biomarker approaches. We record a general trend of decreasing terrigenous sediment supply from the early to the mid-to-late Holocene (11.5-3 ka BP) which seems to be linked to the reduction/retreat in ice-sheets and oceanic current strengths (i.e. the WGC). However, during the late Holocene, the NE Labrador Sea core may indicate increased input of terrigenous organic matter supply possibly related to the Neoglacial regrowth of local ice sheets, albeit, we cannot rule out preservation and diagenetic alterations in the upper centimetres.

2 Material and methods

This chapter describes investigations carried out on three sediment cores (GeoB19948-3, GeoB19927-3 and GeoB19905-1) collected from the eastern Baffin Bay and NE Labrador Sea areas. These cores were recovered during R/V Maria S. Merian cruise MSM44 in June/July 2015 (Dorschel et al., 2015). The location, core lengths, and other information are described in Table 1. The working half of these cores were sampled and divided into four sets of samples. One set was freeze-dried for biomarker analysis (5-10cm resolution) and the second set was used for dating (foraminifera and ^{210}Pd). The other two sets were stored at +4 ˚C for other multi-proxy analyses (i.e. dinoflagellates, foraminifera, and provenance studies).

Table 1: Investigated cores.

Core ID	Region	Lattitude [˚N]	Longitude [˚W]	Water depth [m]	Core length [cm]
GeoB19948-3	Northern Baffin Bay	75° 46.10′	64° 08.57′	778	1018
GeoB19927-3	Northeastern Baffin Bay	73° 35.26′	58° 05.66′	932	1147
GeoB19905-1	Eastern Labrador Sea	64° 21.68′	52° 57.70′	485	1045

2.1 Material

The lithology of cores GeoB19948-3, GeoB19927-3 and GeoB19905-1 summarized below are based on the core scan, density, grain size and visual description of the cores and described in detail in the cruise report (Dorschel et al., 2015).

2.1.1 Sediment core GeoB19948-3 from Northern Baffin Bay

Only one major lithological unit (LU1) was observed for the upper 280cm (Fig. 2.1). LU1 (280 to 0 cm) is composed of olive-grey silty-clay homogeneous sediments.

2.1.2 Sediment core GeoB19927-3 from NE Baffin Bay

Core GeoB19927-3 provides a continuous sedimentary record that can be divided into four lithological units (Fig. 2.1). The lowermost unit (LU1; 1147-1059cm) is primarily characterized by non-homogenous silt and fine sand sediments embedded with dropstones. Unit 2 (LU2; 1059-759cm) is composed of olive-grey to beige silty-clay sediments with sharp color boundaries with some organic remains. Inclined sand layers are prominent features. Unit 3 (LU3; 759-557cm) is

composed of laminated dark grey silty-clay sediments with embedded dropstones and shell fragments. The upper unit (LU4; 557-0cm) is characterized as homogenous olive-grey silty-clay sediments with some faint dark grey laminations and embedded shell fragments at 251 and 199 cm.
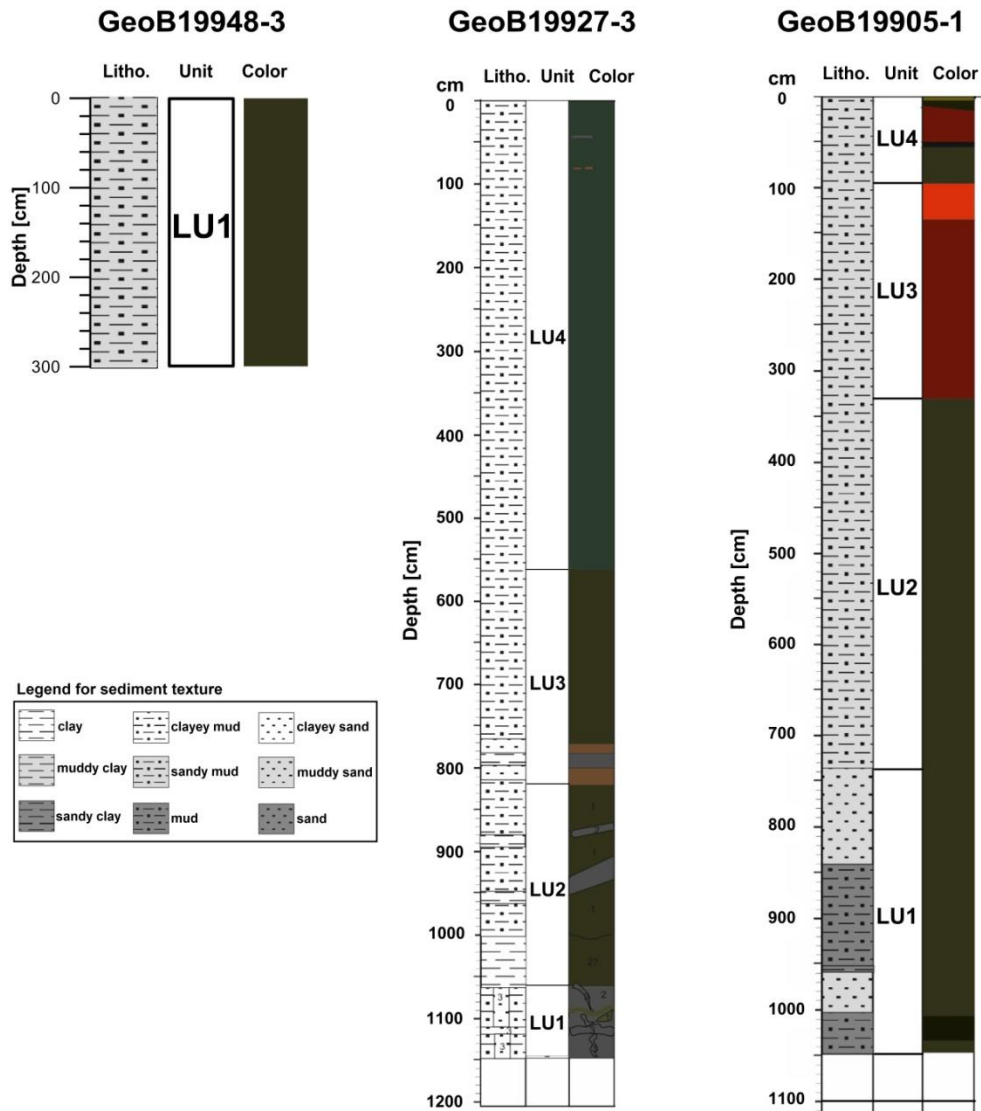
Figure 2.1: A scheme of the lithological composition of the studied sediment cores, adapted after Dorschel et al., 2015.

2.1.3 Sediment core GeoB19905-1 from the NE Labrador Sea

Significant changes in the physical parameters reveal a variable lithology throughout the core GeoB19905-1, which can be described in four units (Fig. 2.1) (Dorschel et al., 2015). Unit 1 (LU1; 1036-737cm) is composed of olive-grey muddy to sandy layers with sharp transitions and presence of some shell fragments towards the upper part of this unit. Unit 2 (LU2; 737-329cm) is composed of mainly olive-grey muddy sediments, and the presence of many shell fragments is a prominent feature of this unit. A sharp drop in dry bulk density at ~640cm is apparent (Dorschel et al., 2015; Weiser et al., 2021) . Unit 3 (LU3; 329-83cm) is composed of homogenous brown-grey muddy sediments with few organic and shell remains and a faint H_2S smell. The upper unit (LU4; 83-0cm) is characterized by brown to olive-grey homogenous, muddy sediments with distinct separating layers and a strong H_2S smell towards the top of the unit.

2.2 Methods

2.2.1 Chronostratigraphy

Constraining the correct age of Arctic Ocean sediments is imperative for the correct paleoceanographic reconstructions, as well as for the study of abrupt climate changes throughout the last deglaciation and beyond. Baffin Bay and the Labrador Sea is a challenging place to work compared to other world oceans due to low sedimentation rates and low biological production. The variability of the atmospheric radiocarbon (^{14}C) poses a critical complexity in ^{14}C dating, especially samples prior to the Holocene which is mainly based on marine and lacustrine sediments. Pre-Holocene ^{14}C in marine sediments contain higher uncertainties in comparison to Holocene ^{14}C which is relatively well constrained using much accurate tree-ring records (Reimer et al., 2013). Marine ^{14}C reservoir ages are typically depleted with respect to the atmosphere, expressed in terms of Marine Reservoir Age (MRA). MRAs may range from about 400 years in the subtropical ocean to over 1000 years in Polar Oceans (Key et al., 2004). Furthermore, regionally elevated MRAs have also been reported (Sarnthein et al., 2015; Sikes and Guilderson, 2016; Skinner et al., 2017). Thus, many studies left aside the MRA variability in their reconstructions (Jennings et al., 2014; Lloyd et al., 2011; Perner at al., 2012) for a constant reservoir correction. Overall, the global MRAs prior to Holocene are much poorly constrained in comparison to the Holocene (Butzin et al., 2017).

The chronology of sediment cores (GeoB19948-3, GeoB19927-3, and GeoB19905-1) used in this thesis is based on the Accelerator Mass Spectrometry (AMS) ^{14}C-dating performed on mollusc shell fragments and foraminifera specimens at Poznan Radiocarbon Laboratory (Poland) and MICADAS-facility at AWI (Germany), respectively. Radionuclide analyses (^{210}Pb, [40]K, ^{137}Cs) were performed on core top sediments of cores GeoB19948-3 and GeoB19927-3 at the Bremen State Radioactivity Measurements Laboratory. The final age model used in studies two and three (chapter 5, 6) was constructed using a combination of the PaleoDataView-program (PDV) (Langner and Mulitza, 2019) and the open-source software package BACON (Blaauw and Christen, 2011) . The PDV uses variable modelled reservoir ages (Butzin et al., 2017) to calibrate radiocarbon ages against IntCal13 (Reimer et al., 2013). The appropriate reservoir ages are chosen automatically based on the sample's radiocarbon age and location of the core.

Note, however, the final age model used in study one (Core GeoB19927-3; Saini et al., 2020, see chapter 4) was constructed using the *Marine13*-calibration (Reimer et al., 2013), which uses a constant reservoir age correction of 140±35yrs, widely applied for Disko Bugt and the NE Labrador Sea (Jennings et al., 2014; Lloyd et al., 2011; Perner at al., 2011, 2012; Allan et al., 2021). These reservoir ages were subsequently used to construct the final age model with BACON-software (Blaauw and Christen, 2011). For details on the methodological approach, the reader is referred to the original (individual) publication (manuscripts).

2.2.2 Organic-geochemical bulk parameters

Total organic carbon (TOC) and total nitrogen (TN) were measured using *Carbon-Sulfur Analyser CS-800, ELTRA* for TOC and Carbon-Nitrogen-Sulfur Analyzer *Elementar-III, Vario* for TN measurements after carbonate removal by hydrochloric acid (37%, 500 µl). The analytical error of the TOC measurements was within 0.02%. Assuming the contained carbonate is predominantly calcite as inferred from high occurrence of foraminifera specimens and/or inorganic data (i.e. $^{87}Sr/^{86}Sr$) in cores GeoB19905-1/GeoB19927-3 (Weiser et al., unpublished data; Madaj et al., unpublished data), carbonate contents were calculated by using the equation $CaCO_3 = (TC-TOC)*8.333$ (here, 8.333 is the stoichiometric calculation factor).

2.2.3 Stable isotopes ($\delta^{13}C_{org}$)

Organic carbon isotope compositions ($\delta^{13}C_{org}$) of cores GeoB19948-3 and GeoB19927-3 were determined at GEOTOP, UQAM, Canada using homogenized and weighed samples into (8x5

mm) silver capsules and left for carbonate removal by conc. Hydrochloric acid for 24 hours. Thereafter, the acidified samples were weighed into a tin foil and wrapped tightly. The determination of $\delta^{13}C_{org}$ was then performed using a continuous flow isotope ratio mass spectrometer (Isoprime-100 MS) using Urea/Air Isotopic laboratory method. Isotope ratios were expressed in delta notation (δ), in per mil (‰), relative to an international reference material (VPDB for $\delta^{13}C$) calculated according to Brand et al. (2014) and Coplen (2011). The error of our $\delta^{13}C$ measurements was at ±0.1‰.
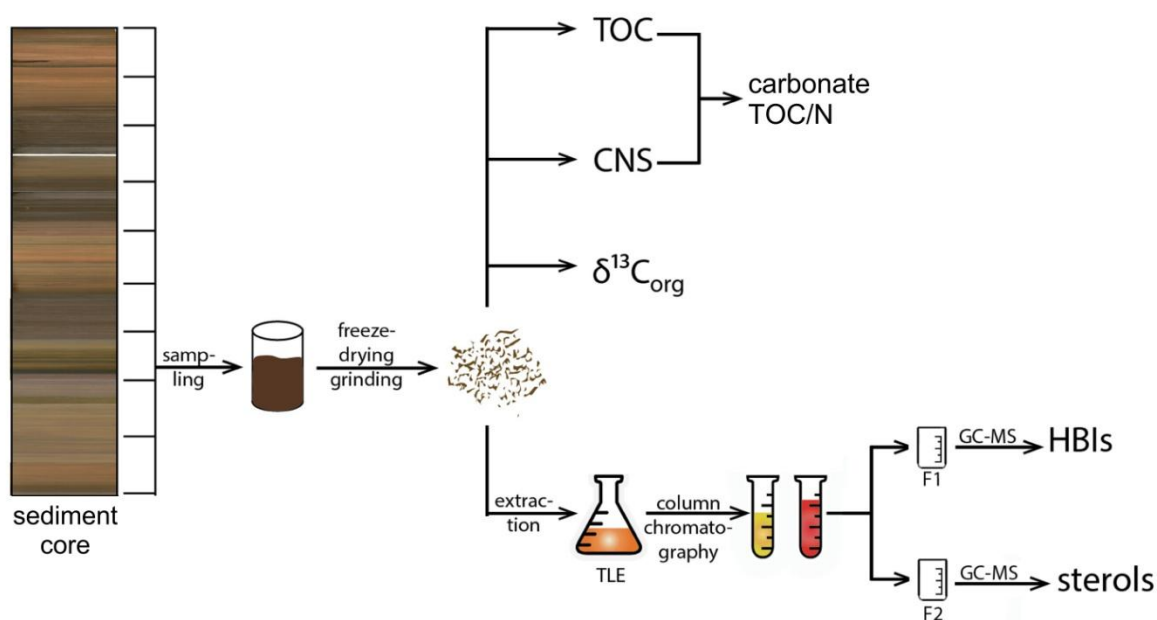
Figure 2.2: Schematic sketch of the laboratory procedures, including all steps from sampling to the GC-MS measurements. TLE = Total Lipid Extract, GC-MS = Gas Chromatograph-Mass Spectrometry (modified from Kremer, 2018).

2.2.4   Biomarker identification and quantification

For each sediment sample, the contents of specific biomarker (Fig. 2.2) HBIs (i.e. IP$_{25}$, tri-unsaturated HBIs) were quantified. Prior to extraction, 9-octylheptadec-8-ene (9-OHD; 0.1 µg/sample), 7-hexylnonadecane (7-HND; 0.076 µg/sample), 5α-Androstan-3β-ol (Androstanol;

10.7 µg/sample) and 2,6,10,15,19,23-Hexamethyltetracosane (Squalane; 3.2 µg/sample) were added as internal standard for the quantification of biomarkers. For each sample, about 4-5 g of freeze-dried and homogenized sediment was used for extraction. Dichloromethane: methanol (2:1 v/v) was used as a solvent for ultrasonication (3x15min). After that, the extracts were separated in two fractions by open silica (SiO_2) column chromatography with *n*-hexane (5 ml) and ethyl-acetate: *n*-hexane (9 ml, 2:8 v/v) as eluent into hydrocarbon and sterol fraction, respectively. The sterol fraction was silylated using 200 µl BSTFA (bis-trimethylsilyl-trifluoroacet-amide) (60˚C, 2 h) to convert it to respective trimethylsilyl ethers.

In the following step, two separate gas chromatography-mass spectrometers (GC-MS) (Fig. 2.3) with same basic configuration were used to qualify and quantify the hydrocarbon and sterol fractions. For hydrocarbon fraction (HBIs) identification and quantification, a gas chromatograph (Agilent Technologies GC6850, 30 m DB-1MS column, 0.25 mm id, 0.25 µm film) coupled to an Agilent Technologies 5977C VL MSD mass selective detector (Triple-Axis Detector, 70eV constant ionization potential, Scan 50-550 m/z, 1 scan/s, ion source temperature 230°C) was used. The sterols (quantified as trimethylsilyl ethers) fraction was analyzed using a GC Agilent 6850 (30 m DB-1MS column, 0.25 mm id, 0.25 µm film) coupled to an Agilent 5975C VL MSD mass selective detector. GC measurements were carried out with the following temperature program for the hydrocarbons: 60 ˚C (3 min), 150 ˚C (15 ˚C/min), 320 ˚C (10 ˚C/min), 320 ˚C (15 min isothermal) for the hydrocarbons and 60 ˚C (2 min), 150 ˚C (15 ˚C/min), 320 ˚C (3 ˚C/min), 320 ˚C (20 min isothermal) for the sterols. Helium gas served as carrier with a constant flow of 1 ml/min. Specific compound identification was based on the comparison of gas chromatography retention times with those of reference compounds and published mass spectra (Belt et al., 2007; Boon et al., 1979; Brown and Belt, 2016; Volkman, 1986). The hydrocarbon fractions were measured additionally in selected ion monitoring (SIM) mode for the identification. For the quantification of IP_{25} and HBI III (Z & E isomer) their molecular ion (m/z 350 for IP_{25} and m/z 346 for HBI III (Z & E isomer) in relation to the abundant fragment ion m/z 266 of internal standard (7-HND) was used. The different responses of these ions and a detailed quantification method is given by Fahl and Stein (2012). For the quantification of the sterols, the molecular ions m/z 470 for brassicasterol (as 24-methylcholesta-5,22E-dien-3β-o-Si(CH3)3), m/z 472 for campesterol (as 24-methylcholesta-5-en-3β-ol), m/z 486 for ß-sitosterol (as 24-ethylcholest-5-en-3β-ol) and m/z 500 for dinosterol (4α,23,24R-trimethyl-5α-cholest-22E-en-3β-

o-Si(CH3)3) were used in relation to the molecular ion m/z 348 for the internal standard androstanol. The instrument stability was controlled using external standards measurements of individual samples. For further details on the methodology, we refer to Fahl and Stein (2012).
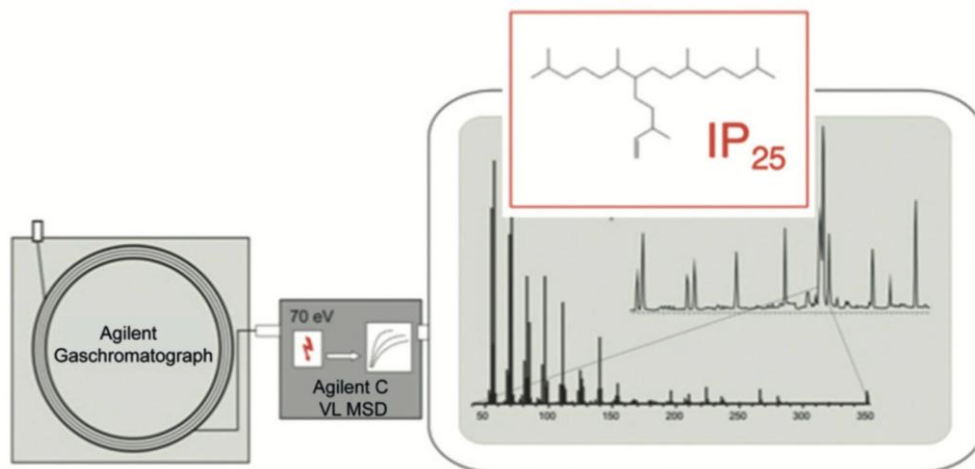
Figure 2.3: Identification and quantification of biomarkers using GC-MS (Source: Stein et al., 2012).

Changes in the percentage of organic carbon may result from changes in the supply of both mineralogical and organic carbon fraction; hence it might be ambiguous to interpret %TOC record. Therefore, converting them to their mass accumulation rates, using the equation developed by Van Andel et al. (1975); Weber et al. (1997), which could exclude dilution effects caused by inorganic components, the carbon data can be interpreted in terms of changes in supply and/or preservation of organic matter (ten Haven et al., 1990). Subsequently, all biomarker concentrations (or percentages) were normalized to either gram sediment or to TOC. The absolute biomarker concentration per gram sediment was normalized to TOC in order to compensate for different depositional and burial effects ("dilution effects") and provide useful information about relative changes in sediment composition. However, for extremely low TOC concentrations, the absolute amount should also be considered for the absolute changes. Furthermore, for information about absolute changes in biomarkers input/fluxes, the accumulation rates of respective biomarkers were calculated by using the following equations which may indicate absolute productivity (e.g., Stein and MacDonald, 2004a).

$$Bulk\ accumulation\ rate = LSR * DBD$$

$$TOC\ accumulation\ rate = Bulk\ accumulation\ rate * TOC/100$$

$$CaCO_3\ accumulation\ rate = Bulk\ AR * CaCO_3/100$$

$$Terrigenous\ accumulation\ rate = (Bulk - TOC - CaCO_3)\ \text{accumulation rate}$$

$$BM\ accumulation\ rate = Bulk\ accumulation\ rate * BM$$

Where, LSR = sedimentation rate (cm ka^{-1}); DBD = dry bulk density (g cm^{-3}); TOC = total organic carbon (%); BM = biomarker concentration (µg g^{-1}); Bulk accumulation rate = total sediments accumulation rate (g cm^{-2} ka^{-1}); TOC accumulation rate = total organic carbon accumulation rate (g cm^{-2} ka^{-1}); CaCO$_3$ accumulation rate = carbonate accumulation rate (g cm^{-2} ka^{-1}); Terrigenous accumulation rate = Terrigenous accumulation rate (non-biogenic and non-organic); BM accumulation rate = biomarker accumulation rate (µg cm^{-2} ka^{-1})

For semi-quantitative sea ice reconstruction, ratio of IP$_{25}$ and phytoplankton biomarkers can be used in order to calculate the so-called "PIP$_{25}$ index", which can be used to infer sea ice conditions using the following equation (Müller et al., 2011).

P$_p$IP$_{25}$=IP$_{25}$/ (IP$_{25}$ + (p*c)),

Where p is the phytoplankton marker concentration (p = B(brassicasterol) or D(dinosterol) or III(HBI III), and c is a balance factor to compensate for a significant concentration difference between IP$_{25}$ and phytoplankton marker concentration (c = mean IP$_{25}$ concentration/mean p concentration). When using HBI III as phytoplankton biomarker and IP$_{25}$ and HBI III concentrations are similar in magnitude, a balance factor may not be needed (i.e., c = 1) (Smik et al., 2016a).

The tri-unsaturated HBI ratio "TR$_{25}$" was calculated according to Belt et al. (2019) and can be used as indicator for (early) spring bloom conditions (i.e. in Barents Sea) using the following equation as proposed by Belt et al. (2019):

[TR$_{25}$=Z-HBI III / (Z-HBI III + E-HBI III)].

3   Paleoenvironmental studies

3.1   Declaration of author's contribution

This cumulative thesis is part of a PhD project that is embedded in the International Research Training Group Program "ArcTrain" and proposed by R. Stein. It comprises of three joint-authorship manuscripts that are or will be published as peer-reviewed articles within appropriate scientific journals. These studies were compiled in close collaboration of all co-authors as clarified below.

(1) Holocene variability in sea ice and primary productivity in the NE Baffin Bay

<u>Authors</u>: Saini, J., Stein, R., Fahl, K., Weiser, J., Hebbeln, D., Hillaire-Marcel, C., de Vernal, A.

<u>Publication state</u>: This manuscript is published (February 2020) in the Journal *Springer-arktos*.

J. Saini, R. Stein and K. Fahl conceived and designed the experiment. J. Saini performed the sampling of the sediment core, the preparation of samples (freeze-drying, grinding), the bulk organic-geochemical analyses (TOC, CNS) and the biomarker analyses (HBIs, sterols). J. Weiser performed the AMS^{14}C-datings on core GeoB19927-3. K. Fahl performed quality control of the biomarkers. J. Saini performed the interpretation of the results and wrote the preliminary versions of the manuscript with strong support and input by R. Stein. R. Stein, K. Fahl, J. Weiser, D. Hebbeln, C. Hillaire-Marcel and A. de Vernal further supported the interpretation of results and improvements on the manuscript. All authors reviewed the results and approved the final version of the manuscript.

(2) Holocene variability in sea ice and primary productivity in the Baffin Bay-Labrador Sea- A North-South transect study

<u>Authors</u>: Saini, J., Stein, R., Fahl, K., Weiser, J., Hebbeln, D., Madaj, L.

<u>Publication state</u>: This manuscript is submitted (26th March 2021) to the Journal *Boreas-International Journal of Quaternary Research*.

J. Saini, R. Stein and K. Fahl conceived and designed the experiment. J. Saini performed the sampling of the sediment cores, the preparation of samples (freeze-drying, grinding), the bulk organic-geochemical analyses (TOC, CNS) and the biomarker analyses (HBIs, sterols). L. Madaj performed the TOC, CNS analyses of core GeoB19948-3. J. Weiser performed the AMS[14]C-datings on cores GeoB19948-3, GeoB19927-3 and GeoB19905-1. K. Fahl performed quality control of the biomarkers. J. Saini performed the interpretation of the results and wrote the first versions of the manuscript with strong support and input of R. Stein. R. Stein, K. Fahl, J. Weiser and D. Hebbeln supported the interpretation of results and improvements on the manuscript. All authors reviewed the results and approved the final version of the manuscript.

(3) Holocene variability in terrigenous organic carbon input in eastern Baffin Bay-Labrador Sea margin

Authors: Saini, J., Stein, R., Fahl, K.

Publication state: This manuscript will be submitted to an appropriate scientific journal as soon as finalized.

J. Saini, R. Stein, A. de Vernal and K. Fahl conceived and designed the experiment. J. Saini performed the sampling of the sediment core, the preparation of samples (freeze-drying, grinding), the bulk organic-geochemical analyses (TOC, CNS), stable isotopes ($\delta^{13}C_{org}$) and the biomarker analyses (sterols). K. Fahl and A. de Vernal performed quality control of the biomarkers and stable isotopes data. J. Saini performed the interpretation of the results and wrote the first version of the manuscript. R. Stein supported the interpretation of results and improvements on the manuscript. All authors reviewed the results and approved the final version of the manuscript.

4   Holocene variability in sea ice and primary productivity in the NE Baffin Bay

Jeetendra Saini[1], Ruediger Stein[1,2], Kirsten Fahl[1], Jens Weiser[2], Dierk Hebbeln[2], Claude Hillaire-Marcel[3], Anne de Vernal[3]

[1]Alfred Wegener Institute Helmholtz Centre for Polar and Marine Research, Bremerhaven, Germany

[2]Marum-Center for Marine Environmental Sciences, University of Bremen, Bremen, Germany

[3]Université du Québec à Montréal, Montreal, Canada

Abstract

Arctic sea ice is a critical component of the climate system, known to influence ocean circulation, earth's albedo, and ocean-atmosphere heat and gas exchange. Current developments in the use of IP_{25} (a sea ice proxy with 25 carbon atoms only synthesized by Arctic sea ice diatoms) have proven it to be a suitable proxy for paleo-sea ice reconstructions over hundreds of thousands to even millions of years. In the NE-Baffin Bay, off NW-Greenland, Melville Bugt is a climate-sensitive region characterized by strong seasonal sea ice variability and strong melt-water discharge from the Greenland Ice Sheet (GIS). Here, we present a centennial-scale resolution Holocene sea ice record, based on IP_{25} and open-water phytoplankton biomarkers (brassicasterol, dinosterol and HBI III) using core GeoB19927-3 (73°35.26' N, 58°05.66' W). Seasonal to ice-edge conditions near the core site is documented for most of the Holocene period with some significant variability. In the lower-most part, a cold interval characterized by extensive sea ice cover and very low local productivity is succeeded by an interval (~9.4-8.5 ka BP) with reduced sea ice cover, enhanced GIS spring melting, and strong influence of the West Greenland Current (WGC). From ~8.5 until ~7.8 ka BP, a cooling event is recorded by ice algae and phytoplankton biomarkers. They indicate an extended sea ice cover, possibly related to the opening of Nares Strait, which may have led to an increased influx of Polar Water into NE-Baffin Bay. The interval between ~7.8 and ~3.0 ka BP is characterized by generally reduced sea ice cover with millennial-scale variability of the (late winter/early spring) ice-edge limit,

increased open-water conditions (polynya-type), and a dominant WGC carrying warm waters at least as far as the Melville Bugt area. During the last ~3.0 ka BP, our biomarker records do not reflect the late Holocene 'Neoglacial cooling' observed elsewhere in the Northern Hemisphere, possibly due to the persistent influence of the WGC and interactions with the adjacent fjords. Peaks in HBI III at about ~2.1 and ~1.3 ka BP, interpreted as persistent ice-edge situations might, correlate with the Roman Warm Period (RWP) and Medieval Climate Anomaly (MCA), respectively, in-phase with the North Atlantic Oscillation (NAO) mode. When integrated with marine and terrestrial records from other circum-Baffin Bay areas (Disko Bay, the Canadian Arctic, the Labrador Sea), the Melville Bugt biomarker records point to close ties with high Arctic and Northern Hemispheric climate conditions, driven by solar and oceanic circulation forcings.

4.1 **Introduction**

Polar regions in the Northern Hemisphere, especially the Arctic and Greenland areas, are undergoing dramatic changes due to an accelerating reduction in sea ice cover and ice sheet extent for the past three to four decades. Since the late 70s, the Arctic sea ice cover has decreased rapidly (Kinnard et al., 2011; NSIDC, 2018). The summer sea ice extent and thickness of multi-year ice are decreasing at the fastest rate ever observed during recent times (-8.6 % per decade), and model simulations suggest that Arctic summer sea ice may disappear within the next fifty or even thirty years (Holland et al., 2006; Stroeve and Notz, 2018; Stroeve et al., 2012; Wang et al., 2012). Given the magnitude of the ongoing reduction in the sea ice cover, information on its impact on water mass circulation and related natural climate conditions over longer time scales is important, notably for the testing of predictive climate models. However, historical and satellite records only span a few centuries or decades, respectively (Walsh and Chapman (2001); NSIDC, 2018), thus limiting the understanding of natural variability of sea ice, emphasizing the need for high-resolution multi-proxy records of its past variations (Jones et al., 2001; Massé et al., 2010). Reliable long-term, at least semi-quantitative sea ice reconstructions are thus needed for the validation of Arctic climate scenarios (Collins et al., 2013; de Vernal et al., 2013a). Furthermore, the ongoing enhanced melting of the Greenland Ice Sheet (GIS), and its significant contribution (~ 0.34 mm/yr) (Rignot and Kanagaratnam, 2006) to global annual sea-level rise (~ 3.3 mm/yr) (Cazenave and Remy, 2011), also need to be appraised in relation to natural processes that occurred at millenial to centennial time scales during the present interglacial.
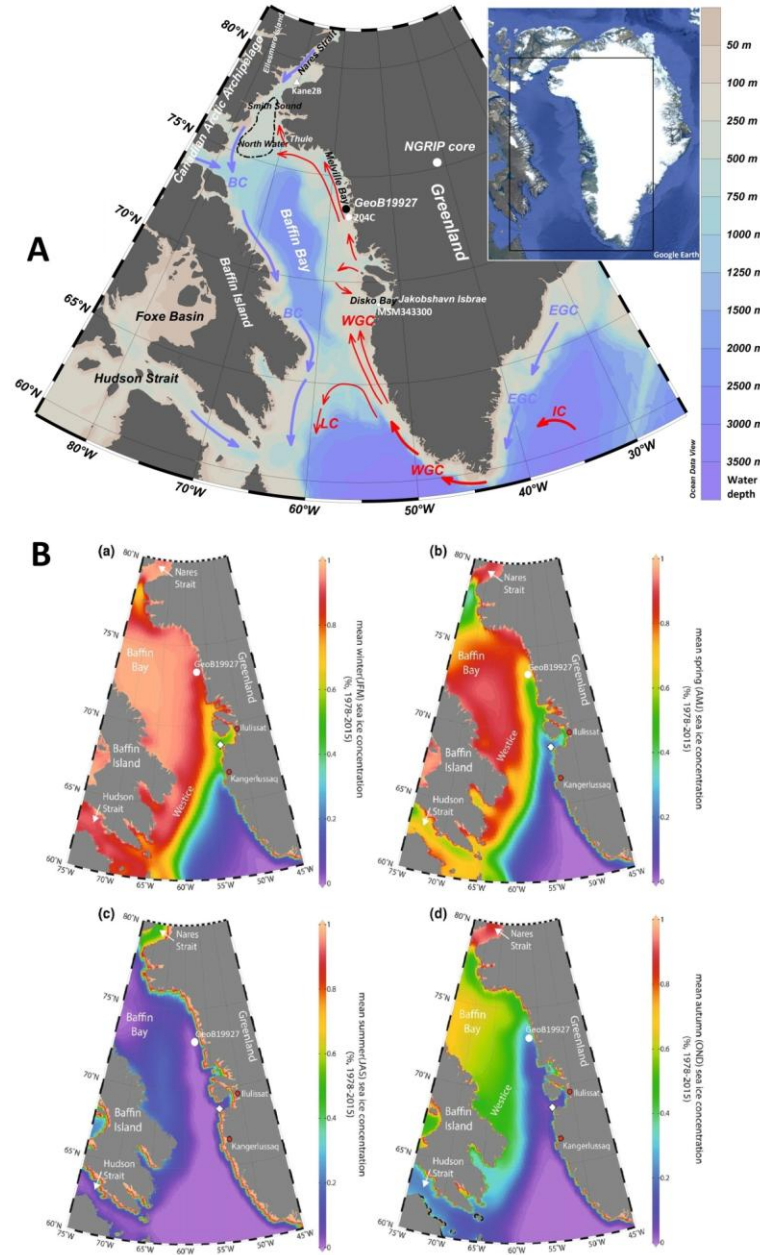
Figure 4.1: (A) Bathymetric map of the Baffin Bay and the location of sediment core GeoB19927 from southern Melville Bugt. A schematic modern surface circulation system in Baffin Bay and around Greenland is also shown, i.e., WGC-West Greenland Current, BC-Baffin Current, IC-Irminger Current, LC- Labrador Current and EGC-East Greenland Current. The area marked with the dotted black line indicates the approximate extent of the North Water Polynya, and the solid white triangle, hexagon, and diamond indicate the location of Cores AMD14-Kane2B (Kane Basin), AMD14-204C (Upernavik), and MSM343300 (Disko Bay), respectively. (B) Satellite-based modern, monthly sea ice concentrations in (%, 1978-2015 (Cavalieri et al., 1996); updated 2015) in Baffin Bay for (a) winter (Jan-Mar), (b) spring (Apr-Jun), (c) summer (Jul-Sept), and (d) autumn (Oct-Dec), adapted from Kolling et al. (2018). The white dot indicates the position of Core GeoB19927, and the white diamond indicates the location of core MSM343300 in Disko Bay.

Northern Baffin Bay (Fig. 4.1A) is of particular interest due to the interaction of the relatively warm high-salinity West Greenland Current (WGC) water with the cold polar water of the Baffin Current (BC) originating from the Arctic Ocean, resulting in the presence of the high productivity North Water Polynya (NWP) kept open by winds, tides and ice bridges (Barber et al., 2001). Eastward of the polynya, Melville Bugt borders the heavily glaciated NW Greenland region, only separated by narrow fringes of ice-free islands, nunataks, and peninsulas. Fast-flowing (>1000 m a^{-1}) glaciers such as Ussing Braeer and Cornell glaciers, are in close proximity to Melville Bugt (Rignot and Kanagaratnam, 2006; Joughin et al., 2010; Wood et al., 2018). Marine sedimentary archives from this area may thus provide records of sea ice and past ice sheet dynamics in this highly climate-sensitive area. So far, the sea ice variability and long-term changes in water masses of the NE-Baffin Bay, especially the WGC, as well as the impact of melt-water discharge from the GIS that occurred since deglaciation, all remain barely documented (Briner et al., 2013; Caron et al., 2019; Hansen et al., 2020).

The present study aims at filling this gap. It is based on a detailed analysis of a ~11.5 m long gravity core from the southern Melville Bugt (core GeoB19927-3; Fig. 4.1A) spanning a time interval of the last approximately 10 ka BP. Special attention is paid to the high-resolution reconstruction of sea ice conditions, mainly documented from the abundance and flux of IP$_{25}$ and open-water phytoplankton biomarkers (brassicasterol, dinosterol and HBI III) and sand content (grain size). These data are complemented by information about the core lithology and dry bulk density, as well as additional published paleoclimate records from circum-Baffin Bay areas.

4.1.1 Biomarker proxies for paleo-environmental reconstruction

Paleo sea ice reconstructions rely heavily on proxy-based methods. In this context, combination of proxies (i.e., sedimentological, biogeochemical and micropaleontological) preserved in marine sediments such as ice-rafted debris, assemblages of diatoms, dinocysts and ostracods as well as δ^{18}O in foraminiferal tests may provide indirect information about past sea ice conditions (e.g., Cronin et al., 2014; de Vernal et al., 2005, 2013a; Gersonde et al., 2005; Hillaire-Marcel and de Vernal, 2008; Jennings et al., 2002; Limoges et a., 2018; Matthiessen et al., 2005; Pieńkowski et al., 2017; Warren, 1992). However, microfossil records such as, for example, diatom

assemblages must be interpreted with caution as they may also be influenced by dissolution and selective preservation (Bidle and Azam, 1999; Leventer, 1998; Shemesh et al., 1989).

As a more direct approach, the "sea ice proxy IP$_{25}$", after its first introduction in a pioneer study by Belt et al. (2007), has been preferentially used for reconstructing the variability of sea ice in the Arctic region (see Belt, 2018 for a recent review). IP$_{25}$ is a highly-branched isoprenoid (HBI) alkene with 25 carbon atoms, derived from specific sea ice diatoms (mostly *Haslea* spp.) living in/under first-year ice and in brine channels (Belt et al., 2007, 2008; Brown et al., 2014). As IP$_{25}$ preserves well in the sediments and is resistant to degradation, it was possible to reconstruct sea ice variability dating back to hundreds of thousands to even millions of years ago (Knies et al., 2014; Kremer et al., 2018; Stein and Fahl, 2013; Stein et al., 2016).

Further, an even more reliable and detailed picture is achieved when combining IP$_{25}$ with open-water phytoplankton biomarkers such as brassicasterol, dinosterol and/or a tri-unsaturated HBI (Z-isomer; hereinafter referred to as "HBI III") and its E-isomer (Belt et al., 2015, 2019; Müller et al., 2009, 2011; Navarro-Rodriguez et al., 2013; Smik et al., 2016; Volkman et al., 1998; Xiao et al., 2015). In this way, the problem of distinguishing perennial ice cover from ice-free water can be solved. The absence or low values of both IP$_{25}$ and phytoplankton biomarkers indicate a more permanent ice cover, whereas a minimal (to zero) IP$_{25}$ and high phytoplankton biomarkers are indicative of ice-free conditions, and a variable amount of these biomarkers may reflect changing seasonal sea ice cover. This approach has been successfully applied to sediments from the Fram Strait, the central Arctic Ocean, and Arctic marginal seas in order to reconstruct sea ice conditions during late Quaternary times (e.g., Belt and Müller, 2013; Belt et al., 2015; Fahl and Stein, 2012; Müller et al., 2009; Müller and Stein, 2014; for the most recent review with pros and cons of this approach see Belt, 2018).

The use of different phytoplankton biomarkers (in combination with IP$_{25}$) may even allow distinguishing between different seasonal sea ice conditions including marginal ice zone (MIZ) situations (e.g., Belt et al., 2015, 2019; Ribeiro et al., 2017). Based on the distribution pattern of HBI III in surface sediments from the western Barents Sea and the correlation with seasonal sea ice concentration maps, for example, Belt et al. (2015) proposed that HBI III maxima reflect winter MIZ conditions. Based on a study of East Greenland fiords surface sediments, on the other hand, Ribeiro et al. (2017) proposed that HBI III maxima correlate with the July MIZ

situation. Based on biomarker investigations of surface sediments across Baffin Bay and the correlation with modern satellite observations, Kolling (2017) suggested that the sea ice indices P_DIP_{25} and P_BIP_{25} may record the late spring and/or autumn conditions, whereas $P_{III}IP_{25}$ index may reflect more the late winter/early spring (ice-edge) conditions in the Baffin Bay. Furthermore, Belt et al. (2019) recently suggested that the proportions of tri-unsaturated HBIs; Z and E-isomer (TR_{25}), may indicate spring phytoplankton blooms, at least for the Barents Sea region. This approach, however, needs to be further evaluated by using additional data from surface sediments and sediment cores from other Arctic regions.

4.2 Environmental setting

Melville Bugt is part of the broad shelf area in NE-Baffin Bay (Fig. 4.1A) covering ca. 120,000 km^2 in the 200 km wide continental shelf offshore NW-Greenland. Baffin Bay acts as a pathway for sea ice and fresh-water exchange between the Arctic and North Atlantic Oceans. The oceanographic circulation in Baffin Bay (Fig. 4.1A) is characterized by the WGC (~150-1330 m water depth), flowing northwards along the west coast of Greenland and the cold BC (~100-300 m water depth) flowing southward and originating from the Arctic Ocean (Tang et al., 2004). The WGC is formed by a combination of :(1) Atlantic sourced, relatively warm and saline water from the Irminger Current (IC), (2) polar sourced cold, low salinity water from the East Greenland Current (EGC) and (3) local melt-water discharge along the SW-Greenland coast (Fig. 4.1A) (Tang et al., 2004). The WGC near Melville Bugt is believed to split into two branches, one turning west that joins the BC near Smith Sound and the other branch circulating towards Nares Strait (Caron et al., 2018; Sadler, 1976).

This area displays high seasonal sea ice variability, especially the Melville Bugt area off West Greenland (Fig. 4.1B). In winter, this area is almost completely ice-covered as the sea ice margin, the so-called 'Westice', expands further southwards (Tang et al., 2004; Stern and Heide-Jorgensen, 2003). In summer, however, the area becomes almost ice-free. The ecological setting of Melville Bugt is highly affected by outlet glaciers of the GIS and receives about ~27% of GIS drainage (Rignot and Kanagaratnam, 2006). Wind stresses here are highly seasonal with stronger wind stress in winter compared to summer (Tang et al., 2004).

During the Last Glacial Maximum (LGM), the extended Greenland, Laurentide, and Innuitian ice sheets (GIS, LIS and IIS, respectively) stretched across Baffin Bay coast to the shelf edge as

demonstrated by the presence of cross-shelf troughs (Funder et al., 2011; Newton et al., 2017; Slabon et al., 2016). Although no geochronological records are currently available for the onset of deglaciation in Melville Bugt, numerical modelling data suggest the onset of deglaciation occurred as early as at ~16.0 ka BP (Lecavalier et al., 2014). However, the general-present day like water mass circulations were probably established in the central-eastern Baffin Bay ~14 ka BP and by ~10.4-9 ka BP in northern Baffin Bay (Levac et al., 2001; Sheldon et al., 2016). The opening of Nares Strait ~9 ka BP allowed the connection between Baffin Bay and the Arctic Ocean, which led to the establishment of the modern ocean circulations in the Baffin Bay (Jennings et al., 2011b, 2019; Georgiadis et al., 2018). The sediments deposited at the seafloor of Baffin Bay are predominantly derived from glacial erosion of the surrounding land masses, and high sedimentation rates of 40-140 cm/ka make this area an ideal site for paleoenvironmental studies (St-Onge and St-Onge, 2014).

4.3   Material and methods

4.3.1   Field methods

The current study is based on the analysis of the 1147 cm long gravity core GeoB19927-3 (Fig. 4.1A; black circle) (Lat: 73°35.26' N; Lon: 58°05.66' W; Water depth: 932 m), recovered from southern Melville Bugt during the RV Maria S. Merian cruise MSM44 (BAFFEAST) in June/July 2015 (Dorschel et al., 2015). The working half of the core was sampled and divided into four sets of samples. One set was freeze-dried for biomarker analysis (5 to 10 cm resolution in this study) and the second set was used for dating (foraminifera and ^{210}Pb). The other two sets were stored at +4°C for other multi-proxy analyses (i.e., dinoflagellates, foraminifera, and provenance studies).

4.3.2   Chronology/age model

Age control is provided through a combination of radiocarbon and ^{210}Pb-dating, followed by Bayesian age modelling. Accelerator Mass Spectrometry (AMS) [14]C- dating was performed on 12 samples, partially on mollusc shell fragments, partially on mixed benthic foraminifera (in one case mixed with specimens of the planktic foraminifera *Neogloboquadrina pachyderma* sin.) (see Table 4.1 for details). Mollusc fragments were measured at the Poznan Radiocarbon Laboratory, Poland, whereas the foraminifera were dated at the MICADAS-facility at the Alfred-Wegener-Institute in Bremerhaven, Germany. The larger mollusc fragments were measured as

graphite, whereas a novel technology for very small sample sizes was used for the foraminifera picked from the >100 µm fraction. Here, the CO_2 released from the foraminiferal carbonate upon acid treatment is directly analysed with a compact AMS facility equipped with a hybrid ion source (for a detailed explanation, see Wacker et al., 2013). Radionuclide analyses (^{210}Pb, ^{40}K, ^{137}Cs) were performed at the Bremen State Radioactivity Measurements Laboratory on a total of seven one-cm-slices of sediment.

Table 4.1: Results of the radiocarbon dating on core GeoB19927-3. Minimum and maximum ages denote the 95% (2σ) uncertainty of the BACON age model.

Sample ID	Lab ID	Depth [cm]	14C-age [yrs]	14C-error [yrs]	Weight [mg]	Material	Min Age [yrs BP]	Max Age [yrs BP]	Mean Age [yrs BP]
GeoB19927-3_33cm	AWI-1468.1.1	33	1821	176	0.69	mixed benthic forams	557	1348	970
GeoB19927-3_62cm	AWI-1469.1.1	62	2072	177	0.62	mixed benthic forams	1027	1764	1408
GeoB19927-3_199cm	Poz-85919	199	3360	30	15	mollusk shells	2818	3190	3009
GeoB19927-3_410cm	AWI-1259.1.1	410	4692	197	0.8	mixed benthic forams	4478	5122	4799
GeoB19927-3_411cm	AWI-1261.1.1	411	4836	192	1	mixed benthic forams	4489	5127	4807
GeoB19927-3_538cm	Poz-85920	538	5495	35	10	mollusk shells	5618	5901	5764
GeoB19927-3_561cm	Poz-85921	561	5720	35	12	mollusk shells	5803	6062	5994
GeoB19927-3_607cm	Poz-85924	607	5885	35	10	mollusk shells	6094	6369	6222
GeoB19927-3_689cm	Poz-85925	689	6670	50	10	mollusk shells	6821	7219	7028
GeoB19927-3_767cm	Poz-85926	767	7410	10	10	mollusk shells	7584	7893	7740
GeoB19927-3_790cm	Poz-85927	790	7640	50	10	mollusk shells	7801	8071	7938
GeoB19927-3_1000cm	AWI-1260.1.1	1000	8831	205	0.8	planktonic (*N. pachyderma* sin.) and mixed benthic	8956	9876	9371

The final age model was constructed using the software package *BACON* (Blaauw and Andres Christen, 2011), written as open-source code for the statistical computation program 'R'. *BACON* uses a Bayesian approach to determine the most likely age-depth relation, resulting in greater flexibility regarding, e.g., the accumulation rates between two dating points. Prior to the actual age modelling, all radiocarbon dates were converted to calendar ages using the *Marine13*-calibration curve as proposed by Reimer et al. (2013) with the built-in calibration function of the program.

Using historical, pre-bomb samples, Lloyd et al. (2011) estimated a local reservoir correction of 140±35 years for the Disko Bay area. This value has been discussed in more detail in Jackson et al. (2017) and widely accepted in previous studies (Jennings et al., 2014; Lloyd et al., 2011; Ouellet-Bernier et al., 2014; Perner et al., 2012) and was, therefore, applied here in the same manner during the calibration.
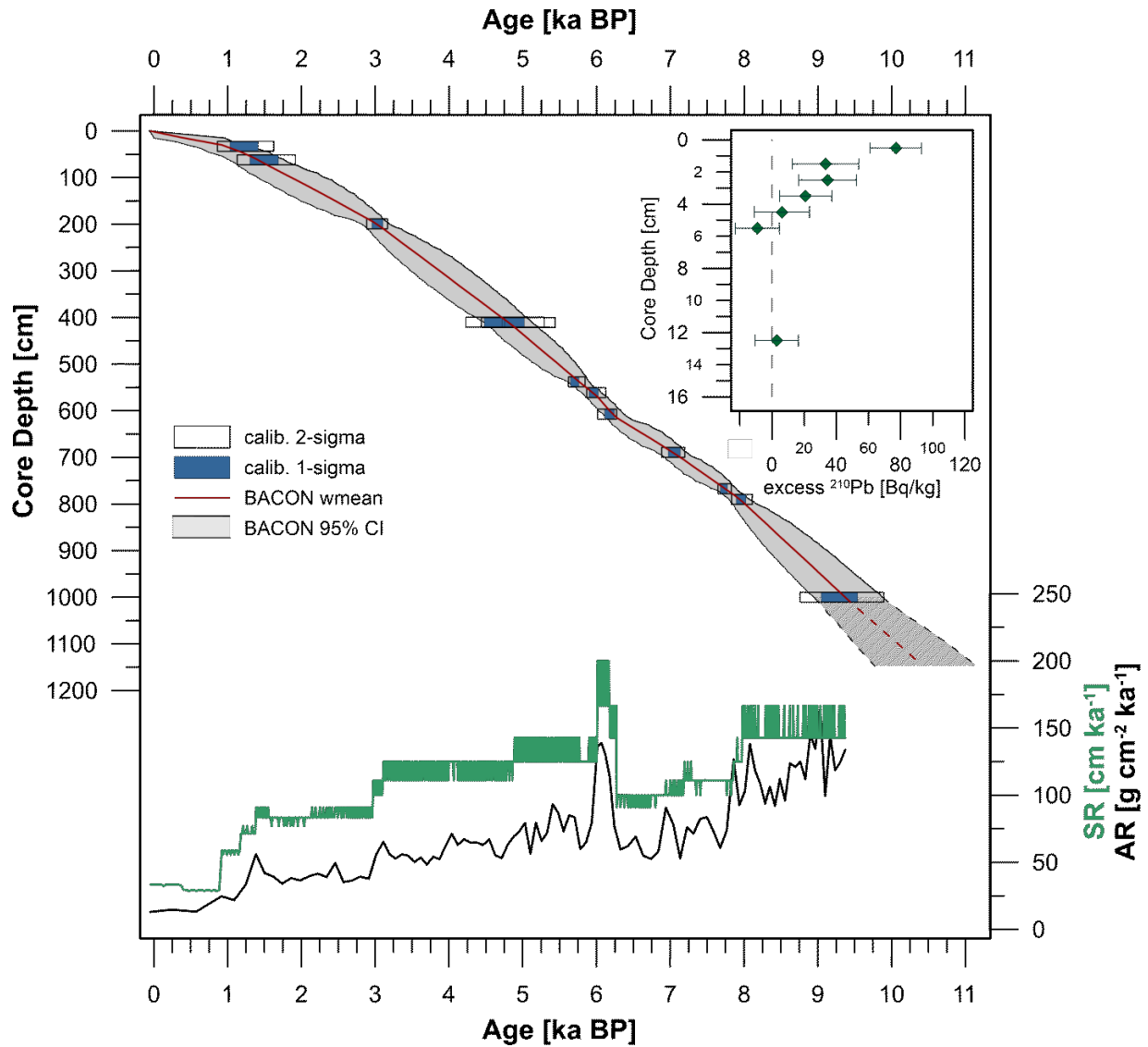
Figure 4.2: Age model for gravity core GeoB19927-3, with rectangles denoting the results of the radiocarbon dating and calibration for one and two σ-ranges (blue and unfilled boxes, respectively), the red line marking the most likely age and the grey shading indicating the extend of the 95% confidence interval as determined by BACON (Blaauw and Andres Christen, 2011). Stippled lines indicate the solely extrapolated age model at the core base. The Inset shows the results of the radionuclide analysis. The sedimentation rate (SR) and accumulation rate (AR) of core GeoB19927-3 are shown versus the age in kilo years before present [ka BP].

4.3.3 Bulk parameters (TOC and sand content)

Freeze-dried and homogenized sediments were taken (5 cm intervals) for Total Organic Carbon (TOC) measurement using a Carbon-Sulfur ELTRA Analyser (CS-800, ELTRA) after removal of carbonates by adding hydrochloric acid (37%, 500 µl). The machine was calibrated with a

standard before measurements, and the accuracy of these measurements was controlled by additional standard measurements after every 10 samples, the error of our TOC measurements is at ±0.02%.

Sand content (grain size) measurements were performed at 10 to 30 cm resolution at the Particle-Size Laboratory at MARUM, University of Bremen with a Beckman Coulter Laser Diffraction Particle Size Analyzer LS 13320. The obtained results provide the particle-size distribution of a sample from 0.04 to 2000 µm, and the sand content class used was between 63-2000 µm. The average standard deviation integrated over all size classes (63-2000 µm) is better than ±4 vol%. (cf., Bartels et al. (2017) for a detailed explanation).

4.3.4   Sea ice biomarkers (IP$_{25}$, HBI III and sterols)

For biomarker analysis ~4 g of freeze-dried and homogenized sediment (10 cm intervals) was extracted using dichloromethane:methanol (2:1 v/v) as solvent for ultrasonication (3x15min). Beforehand, 9-octylheptadec-8-ene (9-OHD; 0.1 µg/sample), 7-hexylnonadecane (7-HND; 0.076 µg/sample), 5α-Androstan-3β-ol (Androstanol; 10.7 µg/sample) and 2,6,10,15,19,23-Hexamethyltetracosane (Squalane; 3.2 µg/sample) were added for biomarker quantification. Sterols and hydrocarbons were separated by open silica (SiO$_2$) column chromatography with *n*-hexane (5 ml) and ethyl-acetate: *n*-hexane (9 ml, 2:8 v/v) as eluent. The latter fraction was silylated with 200 µl BSTFA (bis-trimethylsilyl-trifluoroacet-amide) (60 ˚C, 2 h).

The identification of the compounds was carried out with a gas chromatograph (Agilent Technologies GC6850, 30 m DB-1MS column, 0.25 mm id, 0.25 µm film) coupled to an Agilent Technologies 5977 C VL MSD mass selective detector (triple-axis Detector, 70eV constant ionization potential, Scan 50-550 m/z, 1 scan/s, ion source temperature 230°C) for HBI and sterol. GC measurements were carried out with the following temperature program for the hydrocarbons: 60 ˚C (3 min), 150 ˚C (15 ˚C/min), 320 ˚C (10 ˚C/min), 320 ˚C (15 min isothermal) for the hydrocarbons and 60 ˚C (2 min), 150 ˚C (15 ˚C/min), 320 ˚C (3 ˚C/min), 320 ˚C (20 min isothermal) for the sterols. Helium served as carrier gas (1 ml/min constant flow). Specific compound identification was based on the comparison of gas chromatography retention times with those of reference compounds and published mass spectra (Belt et al., 2007; Boon et al., 1979; Brown and Belt, 2016; Volkman, 1986). For the quantification of IP$_{25}$ and HBI III and IV their molecular ion (m/z 350 for IP$_{25}$ and m/z 346 for HBIs III and IV in relation to the

abundant fragment ion m/z 266 of internal standard (7-HND) was used (in selected ion monitoring mode, SIM). The different responses of these ions were balanced by an external calibration curve (Fahl and Stein, 2012). For the quantification of the sterols (quantified as trimethylsilyl ethers), the molecular ions m/z 470 for brassicasterol (as 24-methylcholesta-5,22E-dien-3β-ol) and m/z 500 for dinosterol (4α,23,24R-trimethyl-5α-cholest-22E-en-3β-ol) were used in relation to the molecular ion m/z 348 for the internal standard Androstanol. All biomarker concentrations were either normalized to the organic carbon (TOC) content or converted to respective accumulation rates (or flux rates) (See data sets available at https://doi.pangaea.de/10.1594/PANGAEA.911365).

The PIP_{25} indices were calculated by combining IP_{25} with different phytoplankton markers for semi-quantitative sea ice reconstruction, according to Müller et al., 2011:

$$P_pIP_{25}=IP_{25}/ (IP_{25} + (p*c)),$$

where p is the phytoplankton marker concentration (p = B(brassicasterol) or D(dinosterol) or III(HBI III), and c is a balance factor to compensate for a significant concentration difference between IP_{25} and phytoplankton marker concentration (c = mean IP_{25} concentration/mean p concentration). When using HBI III as phytoplankton biomarker and IP_{25} and HBI III concentrations are similar in magnitude, a balance factor is not needed (i.e., c = 1). The tri-unsaturated HBI ratio "TR_{25}" was calculated according to Belt et al., 2019:

$$[TR_{25}=Z/(Z+E)].$$

4.4 Results

4.4.1 Core chronology and sedimentation rates

The resulting depth-age model ranges between about 10 ka BP and the present (Fig. 4.2). The sedimentation rates vary between 32 and 172 cm/ka. However, mostly high sedimentation rates of 100 - 150 cm/ka occur throughout the majority of the recovered intervals. A step-wise decrease in sedimentation rates to about ~80 cm/ka (Fig. 4.2) is observed at about 8 to 6 ka BP and to about ~30 cm/ka at about 3 to 1 ka BP, respectively. Excess lead is present down to 4.5 cm core depth, indicating that the core top is of recent age and only experienced minor disturbance during coring (see inset in Fig. 4.2). Cesium (^{137}Cs) was discovered in the topmost

sample at 0-1 cm core depth. Accordingly, we assume that the core top is of near-recent age and used an additional tie point of -50 years (i.e., 0 a BP) for the core top. The basal age of the core was determined by extrapolation of the age model beyond the lowermost radiocarbon dating to the core base within *BACON*. Consequently, the age model for the lowermost section (1000 – 1147cm / > 9.4 ka) should be regarded with caution, and thus accumulation rates were not calculated. Further details of the age modelling are given in Table 4.1 and Fig. 4.2. Mass accumulation rates (g cm^{-2}ka^{-1}) were calculated based on sedimentation rates and dry bulk density data and were finally used to convert biomarker concentrations into flux rates.

4.4.2   Bulk parameters (sand content and TOC)

The sand content (63-2000 µm) displays high-amplitude changes between 0.5 and 63% (vol) in the lowermost part of the core (early Holocene), followed by low and stable values of <2% in the upper part of the core (7.8 ka to present) (Fig. 4.3a). The TOC contents range from 0 to 1.5% (Fig. 4.3b) with minimum but increasing values in the early Holocene (10.4 to 7.8 ka BP), high values of >1% in the mid to late Holocene (7.8 ka to present).

The accumulation rates (or fluxes) of TOC range from 0 to 1.3 g cm^{-2} ka^{-1} and show distinctly variable but higher values in the early Holocene (9.3 to 7.8 ka BP), followed by slightly enhanced values of 0.4 to 1.3 g cm^{-2} ka^{-1} in the mid Holocene (7.8 to 3.0 ka BP) with a distinct maximum (~1.3 g cm^{-2} ka^{-1}) at ~6 ka BP (Fig. 4.4b). Between 3.0 and 0 ka BP, the TOC flux decreases, reaching a minimum value of 0.16 g cm^{-2} ka^{-1} at the top of the core.
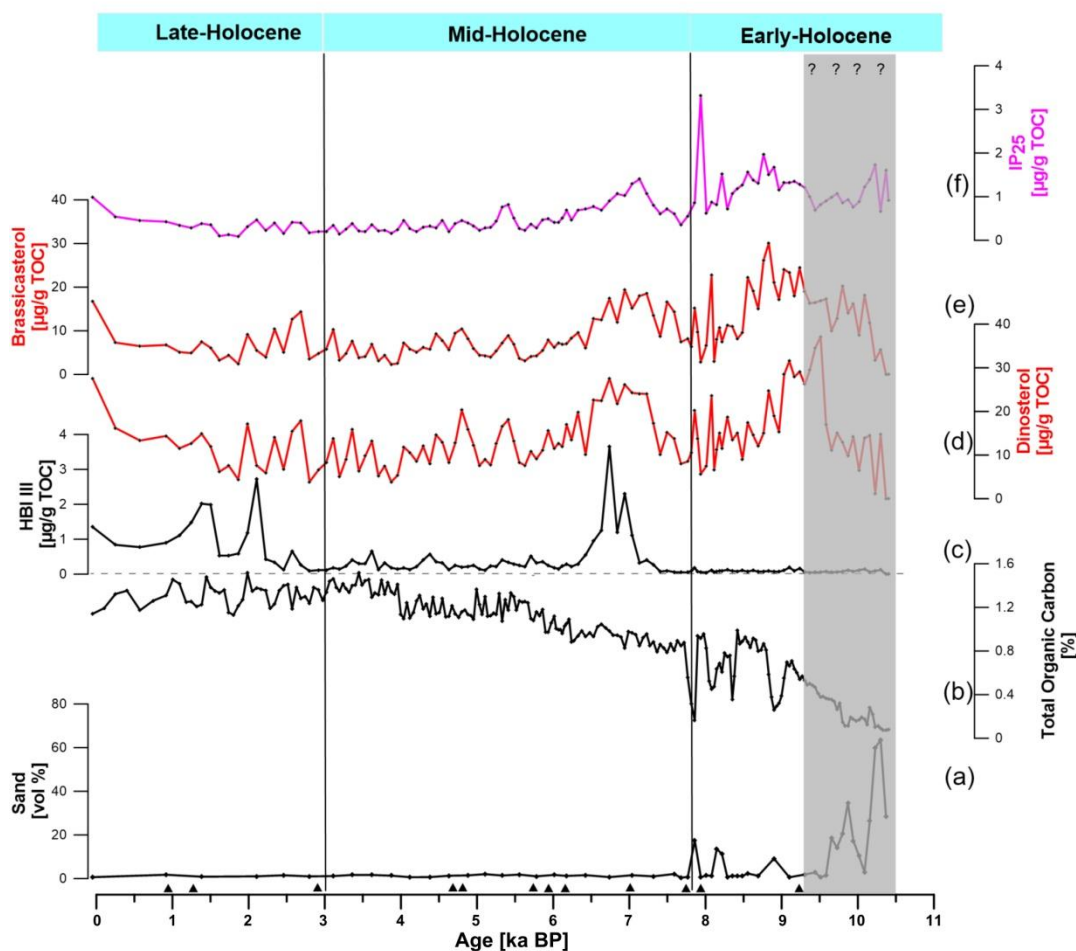
Figure 4.3: Combined record of bulk parameters and biomarkers of core GeoB19927-3 (a) Sand content [vol %], (b) Total organic carbon (TOC) content (Levy et al.), (c) HBI III [µg/g TOC], (d) dinosterol [µg/g TOC], (e) brassicasterol [µg/g TOC] and (f) IP_{25} [µg/g TOC]. Gray box marks the lower-most section of core, where the age model is extrapolated, and data have to be interpreted with caution. All plots are shown versus age in years before present [a BP]. Black solid triangles mark the AMS ^{14}C-datings.

4.4.3 IP_{25} and other biomarkers

IP_{25} concentrations vary between about 0.5 and 1.5 µg/gTOC in the early Holocene (10.4-7.8 ka BP) with a single distinct maximum of ~3.3 µg/gTOC at 7.9 ka BP, followed by a gradual decrease in the mid Holocene (Fig. 4.3f). Relatively constant and minimum concentrations of IP_{25} (~0.34 µg/gTOC) are observed in the late Holocene period (3.0-0 ka BP). The phytoplankton biomarkers brassicasterol and dinosterol show a very similar trend in their concentration record

57

with (sub-) millennial-scale fluctuations ranging from 0 to 30 µg/gTOC and 0 to 37 µg/gTOC, respectively (Fig. 4.3e, d). Intervals of enhanced brassicasterol and dinosterol concentrations are observed from about 9.4 to 8.5 ka BP of ~30 and 37 µg/gTOC and from about 7.4 to 6.3 ka BP of ~19 and 27 µg/gTOC, respectively. In the late Holocene (3.0 to 0 ka BP), the sterols concentrations are still variable but remain generally low. HBI III concentrations are almost zero before 7.4 ka BP (Fig. 4.3c), and remain generally low throughout the mid-Holocene (mean ~0.4 µg/gTOC), except for a prominent peak of 3.6 µg/gTOC at about 7-6.3 ka BP. In the late-Holocene, however, HBI III concentrations increase to ca. 0.8 µg/gTOC, except for two prominent peaks of 2.7 and 2.0 µg/gTOC at about 2.1 and 1.3 ka BP, respectively.

IP_{25} fluxes range from 0 to 1.65 µg cm^{-2} ka^{-1} and are - except for the lowermost part - relatively high in the early Holocene, reaching maximum values at 8.6-8.4 ka BP. In the mid Holocene, the IP_{25} fluxes decrease until 3 ka BP, with some peaks of 1.0, 0.8, 0.9, and 0.4 µg cm^{-2} ka^{-1} at about 7, 6.1, 5.4, and 4.5 ka BP, respectively (Fig. 4.4f). Minimum IP_{25} flux rates of about 0.14 µg cm^{-2} ka^{-1} are observed in the late Holocene. Flux rates of brassicasterol (Fig. 4.4e) vary between 0 and 23 µg cm^{-2} ka^{-1} with the absolute maximum at ~9.3 to 8.6 ka. While flux rates of dinosterol vary between 0 and 19 µg cm^{-2} ka^{-1} and attain a maximum of about 19 µg cm^{-2} ka^{-1} at ~ 6.1 ka BP (Fig. 4.4d). During the mid Holocene, brassicasterol and dinosterol fluxes show a cyclic variability with a decrease in maximum values towards the top.

During the last 3 ka BP, minimum fluxes of brassicasterol and dinosterol between 1.1 and 6.8 and 1.9 and 4.9 µg cm^{-2} ka^{-1}, respectively, are typical. In general, the HBI III fluxes display a similar pattern to its concentration record throughout the core (Fig. 4.4c). Low HBI III fluxes of <0.1 and between 0.1 and 0.4 µg cm^{-2} ka^{-1} occur in the oldest part > 7.5 and between 6.4 and 2.4 ka BP, respectively. Prominent maxima of 1.96, 1.54 and 1.21 µg cm^{-2} ka^{-1} are recorded at 7.0-6.3, ~2.0, and 1.4 ka BP, respectively. Both P_BIP_{25} and P_DIP_{25} indices are intermediate to high, varying in the range between 0.3 and 1, whereas $P_{III}IP_{25}$ index remained high (~0.9) in the early Holocene (Fig. 4.5a). In the mid to late Holocene P_BIP_{25}, P_DIP_{25} and $P_{III}IP_{25}$ indices display cyclic variability with minima at 7.0-6.3, 5.8-5.5, 4.5-4.2, 3.7-3.2 and 2.1-1.3 ka BP (Fig. 5.5a; green dots). HBI TR_{25} ratio (Fig. 4.5b) is highly variable and ranges from ~0.5 to 0.8. The ratio is generally low (~0.6) in the early Holocene, except for peaks of about 0.7 at ~9.1 and ~8.7 ka
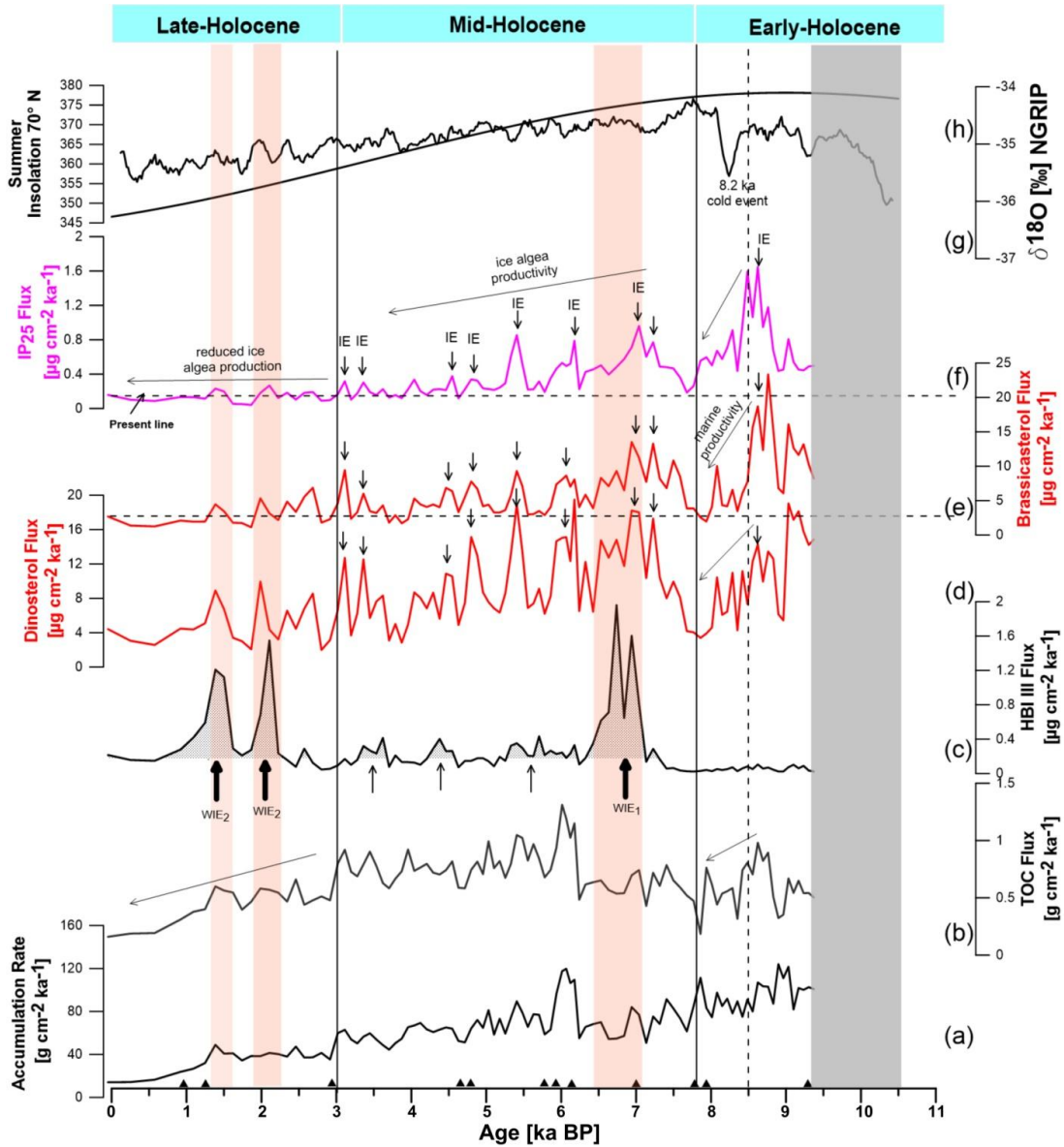
Figure 4.4: (a) Bulk accumulation rate and accumulation (flux) rates of (b) total organic carbon (TOC) [g cm-2 ka-1], (c) HBI III [µg cm-2 ka-1], (d) dinosterol [µg cm-2 ka-1], (e) brassicasterol [µg cm-2 ka-1], (f) sea ice proxy IP$_{25}$ [µg cm-2 ka-1], (g) δ18O record of the NGRIP ice core from Greenland (Vinther et al., 2006), (h) Summer insolation at 70˚N (Laskar et al., 2004). All plots are shown versus age in years before present [a BP]. WIE1 and WIE2 shown as orange bars, are interpreted as (late) winter-ice-edge (WIE) situations. (cf., Belt et al. (2015) and discussion for further explanation). Simultaneous peaks in IP$_{25}$ and phytoplankton; brassicasterol and dinosterol, shown as black downward arrows, are interpreted as (polynya-type) reoccurring ice-edge (IE) situations. Gray box marks the core base where the age model is extrapolated and interpreted with caution. Thus, accumulation rates were not calculated. Black solid triangles mark the AMS ^{14}C-datings.

59
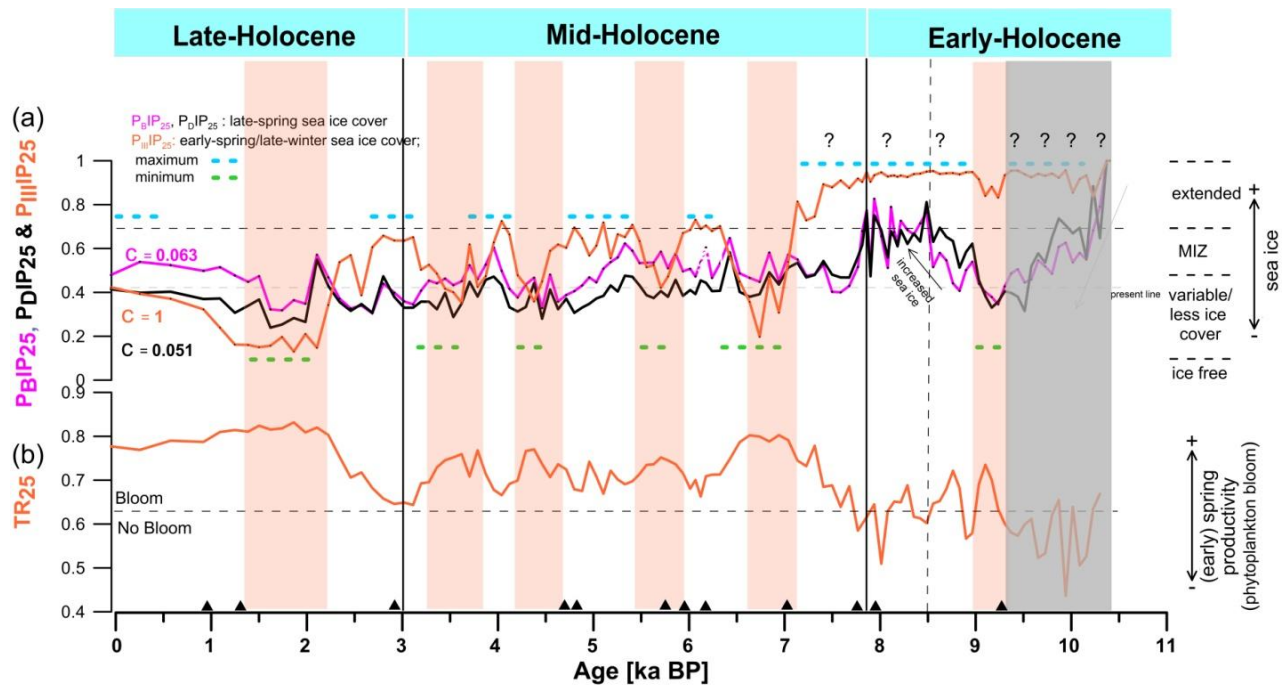
Figure 4.5: (a) PIP$_{25}$ indices using brassicasterol (P$_B$IP$_{25}$), dinosterol (P$_D$IP$_{25}$), and HBI III (P$_{III}$IP$_{25}$). P$_{III}$IP$_{25}$ cyclicity with minimum values marked as orange bars, probably represents different marginal ice zone (MIZ) situations. Classification of different sea ice scenarios based on Müller et al. (2011). (b) HBI TR$_{25}$ as a potential proxy for (early) spring productivity and/or phytoplankton bloom (cf., Belt et al., 2019). The dotted line ~0.62 distinguishing between bloom/no bloom is based on the binary threshold model proposed by Belt et al., 2019. Gray box marks the core base where the age model is extrapolated, and data have to be interpreted with caution. Black solid triangles mark the AMS ^{14}C-datings.

BP. In the mid to late Holocene, it displays cyclic variability and maxima (>0.7) at 7.1-6.6, 5.9-5.4, 4.6-4.2, 3.8-3.2, and 2.2-1.3 ka BP, coinciding with minima in P$_{III}$IP$_{25}$ index (Fig 4.5b; orange bars). In the last 2.3 ka BP, however, TR$_{25}$ displays the highest concentrations with values of ~0.8.

4.5 Discussion

The biomarker approach presented here allows a comprehensive investigation of paleoceanographic changes in NE Baffin Bay, including variations in sea ice cover, primary production and in combination with other proxies- the variability in strengths of oceanic currents (i.e., WGC, BC, etc.) with a ca 100 years time resolution during the Holocene. The Holocene is

characterized by significant changes in oceanic forcing as well as Northern Hemisphere solar insolation (Laskar et al., 2004) and, as a result, affecting the advance and retreat of sea ice cover and ice sheets in the region. Furthermore, the combined use of the different PIP_{25} approaches allowed to distinguish between different seasonal ice-edge situations (cf., Müller et al., 2011; Belt et al., 2015; see chapter 4.3). Notably, the phytoplankton biomarkers brassicasterol and dinosterol from our records show a high correlation ($R^2=0.8$) suggesting co-production of these sterols in a similar open marine environment. This is also reflected in similar trends in their P_BIP_{25} and P_DIP_{25} indices (Fig. 4.5a). Our combined proxy record based on sea ice (IP_{25}), phytoplankton biomarkers (brassicasterol, dinosterol, and HBI III) and bulk parameters indicate a consistent presence of seasonal sea ice (Fig. 4.3 and 4.6) during the Holocene, although the extent and duration of ice cover situation have changed throughout the Holocene.
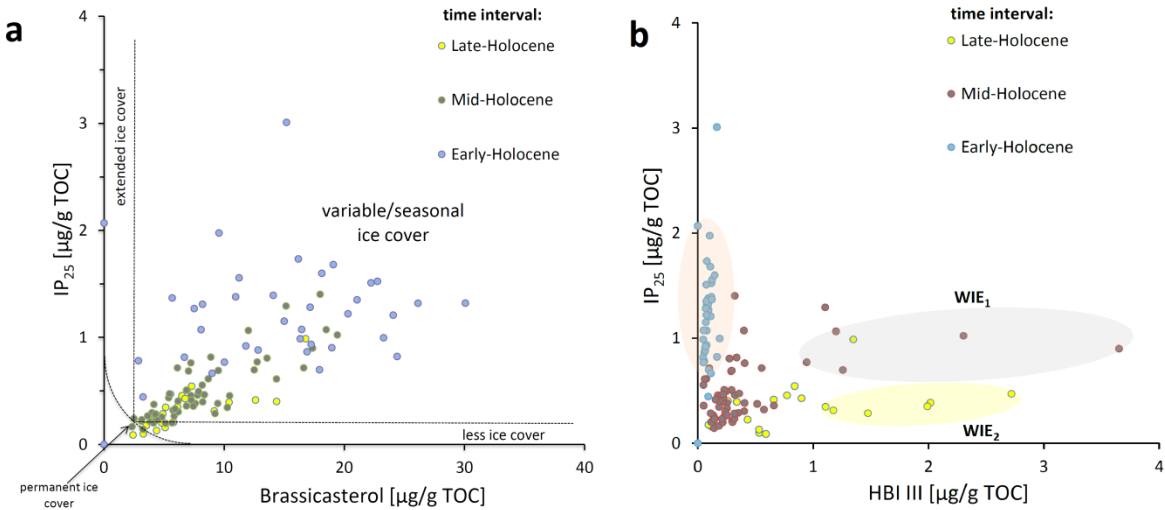
Figure 4.6: (a) X-Y plot of IP_{25} vs. brassicasterol, indicating variable seasonal to ice-edge conditions, according to Müller et al. (2011). Time intervals and different symbols are explained in the legend. (b) X-Y plot of IP_{25} vs. HBI III. There is no clear correlation of IP_{25} to HBI III, however, unusually elevated values of HBI III compared to (low) IP_{25} and vice versa are shown in colored ellipses marked as WIE1 & WIE2, interpreted as (late) winter-ice-edge (WIE) situations and longer (spring) sea ice seasons, respectively (cf., Belt et al. 2015 and discussion for further explanation).

4.5.1 Sea ice variations in the NE Baffin Bay during the Holocene

4.5.1.1 Early Holocene

From final deglacial cold phase to early Holocene warming between ~10.4 (?) to ~8.5 ka BP

In the lower-most period (1147 – 1070cm / > 9.4 ka; see Supplementary Fig. S4.1), minimum values to absence of ice algae biomarkers, phytoplankton biomarkers, TOC and TR_{25} but high $P_{III}IP_{25}$ (~0.9) index (Fig. 4.3 and 4.5) indicate colder conditions with extensive sea ice cover during most part of the year except very short seasonal break up periods during late spring and/or autumn (P_BIP_{25}~0.6), coinciding with high ice-rafted debris (IRD) values (indicated by high sand content; Fig. 4.3a). The high amount of terrigenous material (indicated by high IRD) entrapped during sea ice formation in winter and released nutrients in late spring may have facilitated some primary production (Fig. 4.3d, e) (Sakshaug, 2004). The colder conditions in Baffin Bay could also be due to the presence of active ice-streams (Aksu and Piper, 1979; Dyke, 2008) and strongly stratified conditions, possibly related to glacial outwash events and melt-water influx from the retreating ice, and a limited strength of the WGC (Jennings et al., 2019; Ledu et al., 2010; Ren et al., 2009).

Following this initial period, the interval ~9.4-8.5 ka BP (1070-890cm) is marked by pronounced peaks in the fluxes of $IP_{25,}$ phytoplankton biomarkers brassicasterol and dinosterol and TOC as well as TR_{25} (Fig. 4.4 and 4.5), pointing all towards rapid changes in the area characterized by variable/less sea ice to ice-edge (MIZ) conditions and high in-situ productivity (Fig. 4.5a). This reduction in sea ice and increased marine productivity might point towards warmer surface conditions in the early Holocene, marked by strong atmospheric forcing (Fig. 4.7i). Low values of P_BIP_{25} and P_DIP_{25} indices, coinciding with low IRD (Fig. 4.3a and 4.5a), may reflect a retreat in sea ice cover (and glaciers) and indicate a phase of more open water conditions in late spring and/or autumn. Based on the $P_{III}IP_{25}$ values, high sea ice cover might have persisted until early-springs seasons (Fig. 4.5a). These numbers, however, have to be interpreted very cautiously due to the extremely low HBI III values.

We think this is linked to the northward penetration of the WGC, transporting warm Atlantic Water along the West Greenland coast since at least ~10.4-9 ka BP (Hansen et al., 2020;

Jennings et al., 2019) and, thus, causing higher sea surface temperatures in northern Baffin Bay. Knudsen et al. (2008) reported an increase in calcareous benthic foraminiferal flux and heavier
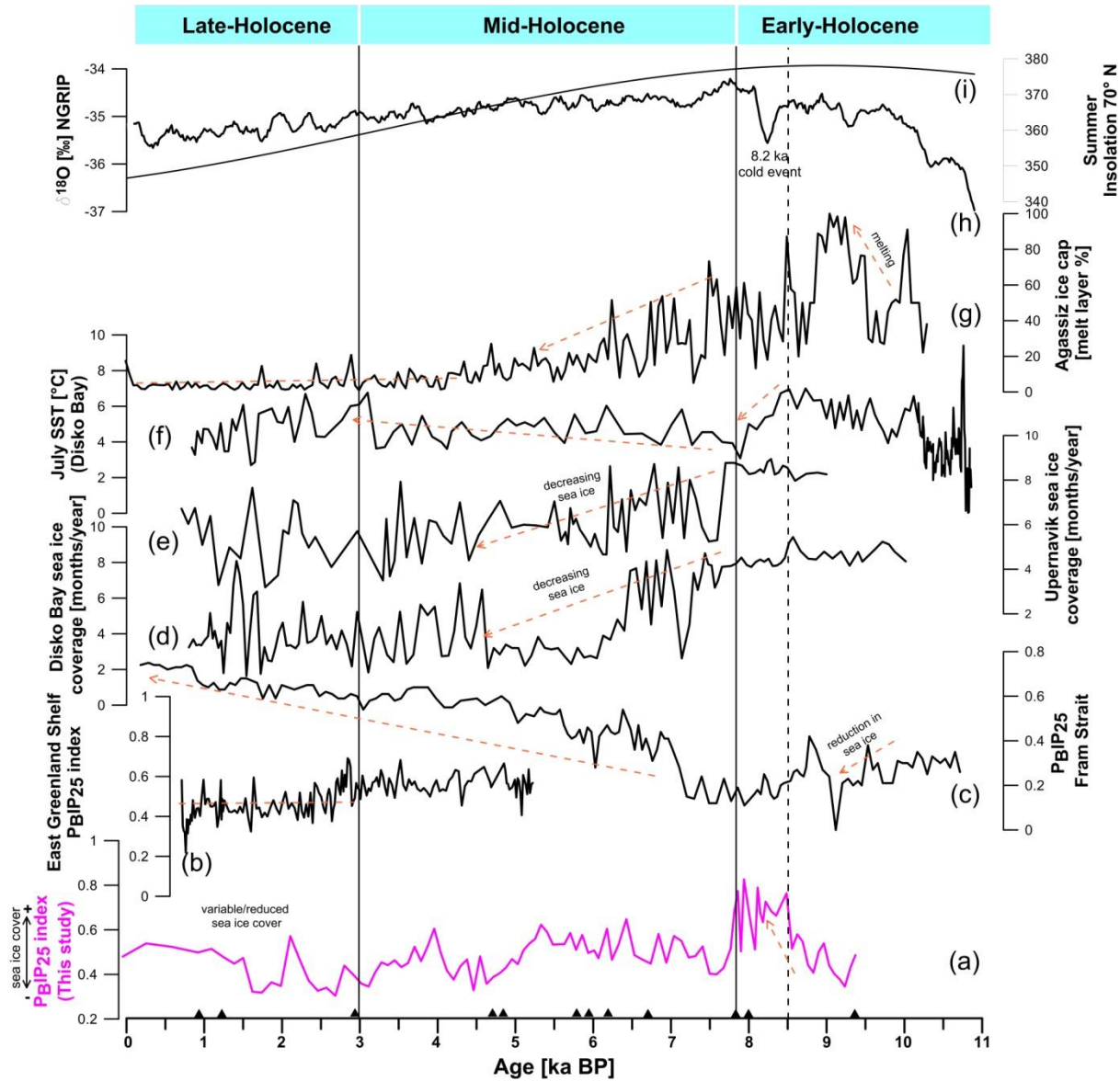
Figure 4.7: Comparison of different environmental proxy records around and from Greenland. (a) PBIP$_{25}$ record from the Melville Bugt (Core GeoB19927-3, this study), (b) PBIP$_{25}$ record from East Greenland Shelf (Core PS2641; Kolling et al., 2017), (c) Fram Strait (Core MSM5/5-712-2; Müller and Stein, 2014), (d) dinocyst based sea ice cover reconstruction (months of sea ice/year) from Disko Bay (Core MSM343300; Ouellet-Bernier et al., 2014), (e) dinocyst based sea ice cover reconstruction (months of sea ice/year) from Upernavik (Core AMD14-204C; Caron et al., 2019), (f) diatom based SST reconstruction from West Greenland (Core MSM343300; Krawczyk et al., 2017), (g) the Agassiz Melt Layer Record (Fisher and Koerner, 2003), (h) the δ18O record of the NGRIP ice core from Greenland (Vinther et al., 2006) and (i) the summer insolation at 70˚N (Laskar et al., 2004). Black solid triangles mark the AMS ^{14}C-datings.

$\delta^{18}O_{benthic}$ values through this interval supporting the influence of WGC up to the northern Baffin Bay and subsequently more open surface waters and reduced sea ice coverage. Based on bowhead bone remains (Dyke et al. (1996)), IP_{25} record from the Canadian Arctic Archipelago (Vare et al. (2009)), and ice-edge indicator foraminifera species (*S. feylingi*) from Upernavik area (Hansen et al. (2020)), the authors reported reduced to ice-edge sea ice cover, similar to our findings in this study. Based on foraminifera, Ostermann and Nelson (1989) reported a similar influx of relatively warm, high saline water into the north of Baffin Bay between ~9.8 and 8.5 ka BP. Furthermore, Levac et al. (2001) reported an increase in dinoflagellate abundances from a sediment core in the northern Baffin Bay, suggesting similar warming of surface waters.

The interpretation of continued strong melting with warmer summer waters in Baffin Bay corresponds to the significant climate warming in the early Holocene, widely recognized in the Northern Hemisphere (Kaufman et al., 2004; Vinther et al., 2009). These warm conditions might have led to high sedimentation rates as a result of increased marine productivity, ice melting, and glacially-derived material from adjacent ice-sheets in NE Baffin Bay (Caron et al., 2018; Hansen et al., 2020). This is in agreement with high accumulation rates and relatively high terrigenous detritus (Fig. 4.2 and 4.3a) recorded in the sediments in this interval, which may indicate a strong melt-water input associated with melting of sea ice, GIS and nearby glaciers such as Ussing Braeer and Cornell glacier located near Melville Bugt (Joughin et al., 2010; Kaufmann et al., 2004). Notably, the period with maximum dinosterol flux (Fig. 4.4d) and spring ice melting in Baffin Bay coincides with maximum Agassiz Ice Cap melt percent (~9.4-8.5 ka BP) (Fisher and Koerner, 2003) and maximum summer insolation at 70˚N or higher latitudes (Laskar et al., 2004) (Fig. 4.7g, i), which suggests significant warm conditions and increased marine productivity in the area. Ice retreat velocity data (~4.8 km/a) from Jakobshavns Isbrae also indicate similar rapid deglacial melting following increased atmospheric temperatures at about 9.4 to 8.5 ka BP (Long and Roberts, 2003; Vinther et al., 2006). Additionally, the increase in the amount of pollen grains from Ellesmere Island could also indicate the maximum summer melting between ~9.8 and 8.5 ka BP (Bourgeois et al., 2000; Kutzbach et al., 1993). This characteristic warming, reduction of spring/summer sea ice and deglacial melting of the GIS has been widely reported in the areas

such as Fram Strait and Disko Bay based on PIP_{25} (Fig. 4.7c) and SST record (Fig. 4.7e) (Müller and Stein, 2014; Krawczyk et al., 2017; Weidick and Bennike, 2007).

Extended sea ice cover and opening of connection to the Arctic between ~8.5 and ~7.8 ka BP

Despite the high solar insolation and deglacial melting having culminated, environmental conditions in northern Baffin Bay remained cold and unstable between ~8.5 to ~7.8 ka BP (England et al., 2006) likely due to counter-effect of the Laurentide, Greenland and Innuitian ice sheets and a connection to the Arctic Ocean (Knudsen et al., 2008). A distinct decrease in ice algae and phytoplankton productivity (Fig. 4.4d, e, and f), coinciding with peaks in IRD (Fig. 4.3a) during this interval, indicate a period of major environmental change in the area. Cold surface water conditions and increased, partly almost closed sea ice cover in this period are indicated by the P_BIP_{25}, P_DIP_{25}, and $P_{III}IP_{25}$ indices, increasing to a maximum of 0.8 to 0.9 (Fig. 4.5a). Our biomarker records point to an interval of extended sea ice and major changes in Baffin Bay that might be related to the opening towards the Arctic Ocean via Nares Strait as proposed in several studies: based on sedimentological and geological data, Jennings et al. (2011b, 2019) and Georgiadis et al. (2018) suggested that Nares Strait opened at ~9-8.3 ka BP. Although, given the uncertainties in ΔR values, the timing of the exact opening of the strait is still subject to debate (Jennings et al., 2019).

In the period between 8.5 and 7.8 ka BP, our interpretation of extended ice cover throughout the year, except during a short summer season and colder conditions and declined marine productivity, is in accordance to previously reported increase in assemblages of cold water foraminifera and diatoms in Baffin Bay (Jennings et al., 2014; Moros et al., 2016; Lochte et al., 2019). Similarly, Knudsen et al. (2008) and Ouellet-Bernier et al. (2014) reported an increase in the abundance of large-sized diatoms after ~8.2 ka BP, related to Polar Water influx from the Arctic Ocean, and the opening of Nares Strait (Jennings, 1993). Furthermore, based on higher abundances of the Arctic water foraminifera (*I. norcrossi*) (Moros et al. (2016); Hansen et al. (2020)) and a distinct maximum of dinocyst assemblages (Fig. 4.7d, e) at ~8.3 ka BP (Ouellet-Bernier et al., 2014; Caron et al., 2019), the authors describe an interval of dense sea ice cover (>9 months/yr) and cold sub-surface water inflow (core MSM343300, AMD14-204C; Fig 4.1A, B) in Baffin Bay, whereas GIS was probably retreating. The cold event coincided with the final phase of deglaciation of the IISs and LISs (Dyke et al., 2002; Jennings et al., 2015) and might

also be concurrent to the widely reported ~8.2 ka cold event in the Northern Hemisphere (Alley and Agustsdottir, 2005; Jennings et al., 2011a; Matero et al., 2017; Nesje and Dahl, 2001). A decrease in the number of melt-layers from the Agassiz Ice Cap shows a temperature decrease between 8.5 and 7.8 ka BP and thus colder conditions (Vinther et al., 2006; Fig. 4.7g). Similarly, Jennings et al. (2011a) also observed episodic cooling of the Irminger Current (that feeds the WGC) resulting from the last phases of the waning LIS. Either or a combination of these scenarios could be responsible for cold fresh-water input into Baffin Bay, resulting in increased sea ice cover and colder conditions in the area.

4.5.1.2 Mid-Holocene

A cyclic change of minima and maxima in sea ice cover is evident after 7.8 ka BP, as shown by PIP_{25} index cyclicity (Fig. 4.5a). Furthermore, contemporaneous peaks in accumulation rates of IP_{25} and the phytoplankton biomarkers brassicasterol and dinosterol (Fig. 4.4d, e, f) display reoccurring spring ice-edge conditions. This may be related to oscillations in the strengths of the WGC and the melting of sea ice (Caron et al., 2019; Ouellet-Bernier et al., 2014; Knudsen et al., 2008). Interestingly, the HBI III record shows a pronounced maximum between 6.3 to 7.0 ka BP, followed by three smaller peaks of elevated HBI III values at 5.7-5.2, 4.5-4.3, and 3.6-3.3 ka BP (Fig. 4.4c). According to Belt et al. (2015), such HBI III maxima may indicate increased phytoplankton productivity and winter ice-edge limit (Fig. 4.6b). Baffin Bay is strongly influenced by seasonal melt-water inflow from the GIS, wind favored deep upwelling and light availability, which may, in turn, also influence the production of HBI III (Humlum, 1985; Belt et al., 2017). The strong seasonality in this area may explain such an elevated occurrence of HBI III in ice-edge scenarios. Peaks in HBI III, associated with enhanced growth of phytoplanktons near MIZ may also indicate an up-welling situation (i.e., sites near polynya settings; NWP) caused by wind favored mixing in the late-winter months, when northwesterly wind stress is stronger (Cormier et al., 2016; Knudsen et al., 2008; Levac et al., 2001; Melling et al., 2001; Mudie et al., 2004; Tang et al., 2004). The $P_{III}IP_{25}$ indices display minima at 7.0-6.3, 5.8-5.5, 4.5-4.2, and 3.7-3.2 ka BP, coinciding with maxima in the TR_{25} record, may be interpreted as ice-edge (polynya-type) situation with reduced sea ice cover and elevated primary production during late winter/early spring (Fig. 4.5b). The intervals in between are characterized by more extended late-winter/early-spring sea ice conditions.

A number of paleoclimatic records from the Canadian Arctic islands, the Baffin Bay, and offshore Greenland, supports the reconstruction of sea-surface conditions presented herein. The northward retreat of ice sheets, further from the coastline, may have led to reduced melt-water supply (Caron et al., 2019; Hansen et al., 2020) and further establishment of rather stable oceanographic conditions. Widespread presence of mollusks and Atlantic water indicator species, i.e., *P. bipolaris*, as well as increased organic carbon accumulation beginning at ~7.9-7.5 ka BP offshore NW Greenland, supports the dominant influence of the WGC in the region (Hansen et al., 2020; Ren et al., 2009; Seidenkrantz, 2013). Several records from circum-Greenland, the Canadian Arctic Archipelago, the Barents Sea, Iceland, and Svalbard shelves reported the similar strengthening of WGC and Irminger Current since ~7.8 ka BP (Anderson and Leng, 2004; Dyke, 1996; Jennings et al., 2011a, 2014; Justwan et al., 2008; Lloyd et al., 2005; Ouellet-Bernier et al., 2014). Furthermore, between ~7.3 and ~6.2 ka BP, a reduced sea ice cover and relatively warm WGC were recorded at several sites, including northern Baffin Bay and the eastern Labrador Sea (de Vernal et al., 2013b; Perner et al., 2012). Thomas et al. (2016) have shown a major increase in winter snowfall during mid Holocene caused by reduced sea ice and open surface water conditions in Baffin Bay and the Labrador Sea, consistent with the occurrence of polynya-type (winter) ice-edge variability. Slightly less pronounced, but warming trend is also observed from the Disko Bay area, based on diatoms based SST data (Fig. 4.7f) (Krawczyk et al., 2017). Many marine and terrestrial records have also reported the GIS retreat from Disko Bay during this time interval (Lloyd et al., 2005; Long and Roberts, 2002; St-Onge and St-Onge, 2014), in agreement with our reconstructions in NE Baffin Bay.

4.5.1.3 Late Holocene

During the last 3 ka BP, the concentrations and accumulation rates of IP_{25}, marine sterols (Fig. 4.3, 4.4;d, e and f), and related PIP_{25} index values remain relatively low and do not reflect the Late Holocene 'Neoglacial' cooling trend that follows the decreasing insolation pattern (Laskar et al., 2004) (Fig. 4.7a and i), widely observed in Northern Hemisphere, such as in eastern Baffin Bay, the Fram Strait and the Canadian Arctic Archipelago area (Fig. 4.7d and f) (Hansen et al., 2020; Krawczyk et al., 2017; Ouellet-Bernier et al., 2014; Müller et al., 2011; Wanner et al., 2011). This difference might be due to the dominance of the WGC along the West Greenland coast and sea ice interactions with the adjacent fjord, which may further mitigate sea ice growth. Furthermore, our PIP_{25} indices show relatively moderate values (0.2-0.6), suggesting a reduced

sea ice cover, especially between about 2.4 and 1.0 ka BP (Fig. 4.5a). Sea ice might have only occurred during the late winter/early spring of this time span, as shown by minimum $P_{III}IP_{25}$ values and the HBI III maxima (Fig. 4.4c and 4.5a). Notably, the pronounced peaks in HBI III flux and TR_{25} (Fig. 4.5b) at about 2.1 and 1.3 ka BP that might coincide with the Roman Warm Period (RWP) and Medieval Climate Anomaly (MCA), respectively, can be associated with stronger WGC pulses. As our core site is not too distant from NWP, a polynya-type, marginal ice zone situation, driven by northerly winds and occasional upwelling during the warm periods is another option to explain increased productivity and related elevated HBI III values. Similarly, Knudsen et al. (2008) reported an increase in large diatoms between 2-0.6 ka BP, interpreted as warmer conditions and high productivity in Disko Bay. Based on foraminiferal and sedimentological proxies from West Greenland, Lloyd et al. (2007) and Norgaard-Pedersen and Mikkelsen (2009) also observed relatively warm oceanic conditions at ~2-1.4 ka BP. Furthermore, based on benthic foraminifera analysis, Perner et al. (2012) described a period of warming from ~1.4 to 0.9 ka BP and a relatively warm phase at ~1.8 ka BP and suggested an increased IC contribution to the WGC during the RWP and MCA. Perner et al. (2012), Kolling et al. (2017) and Allan et al. (2018) suggested an enhanced Atlantic Water inflow to the WGC and reduced (winter-only) sea ice between ~1.4-0.9 ka BP and ~1.8 ka BP, with beneficial conditions for phytoplankton blooms, in agreement with our findings.

Several studies have recognized a complex feedback system between Arctic sea ice and the North Atlantic Oscillation (NAO) and reported an anti-phase correlation to the NAO mode associated with the RWP and MCA (Krawczyk et al., 2013; Lasher and Axford, 2019; Porter and Mosley-Thompson, 2011; Siedenkrantz et al., 2008). However, our records point towards an in-phase response of sea ice cover with changes in NAO modes (i.e., warming during the positive NAO mode associated with the RWP and MCA (Ljungqvist, 2010; Trouet et al., 2009). However, it should be noted that NAO reconstructions are still subject to debate and far from being fully understood (cf., Kolling et al. (2018) and Seidenkrantz et al. (2008) for a detailed discussion).

Based on an IP_{25} record from the East Greenland shelf (Fig. 4.7b), Kolling et al. (2017) reported that the PIP_{25} index therein also does not reflect the 'Neoglacial' cooling trend, similar to the records of our study. Based on diatom and foraminifera assemblages, Moros et al. (2016) and

Caron et al. (2019) (Fig. 4.7e) suggested warm, stratified and highly productive waters in Baffin Bay area (Matthiessen et al., 2005; Rochon et al., 1999), in agreement with the our interpretation. Glaciers, land-fast ice, and local fjords may also have a more direct and unfavourable influence on the growth of sea ice cover (Ribeiro et al., 2017).

4.6   Summary and conclusions

Holocene sea ice conditions and marine phytoplankton productivity were reconstructed to gain direct insights into the sea ice variability and its driving mechanisms using a multi-proxy biomarker approach. Organic geochemical and biomarker analyses of a well ^{14}C-AMS and ^{210}Pb dated sediment core from NE Baffin Bay show that major environmental and paleoceanographic changes occurred in this area.

In the lower-most part, a cold interval characterized by extensive sea ice cover and very low local productivity is succeeded by an interval (~9.4-8.5 ka BP) of persistent, albeit strongly variable (reduced) sea ice cover, enhanced GIS spring melting, and strong influence of the WGC in the earliest part of the record. A short-term cooling event is recorded by the ice algae and phytoplankton biomarkers between 8.5 and 7.8 ka BP, pointing towards an increased seasonal sea ice cover as a result of the opening of Nares Strait which led to an increased influx of Polar Water into the Baffin Bay, albeit insolation remained generally high.

The interval between 7.8 and 3.0 ka BP is characterized by reduced sea ice with millennial-scale variability of (late winter) ice-edge limit and WGC strength, and increased open-water (polynya-type) conditions correspond to 'warmer' conditions.

Our IP$_{25}$ based sea ice reconstructions and related PIP$_{25}$ index do not reflect the late Holocene Neoglacial cooling trend during the last 3 ka BP, probably due to the strong influence of the WGC and interactions with the adjacent fjords. Peaks in HBI III at about 2.1 and 1.3 ka BP might coincide with the RWP and MCA, respectively, and are associated with an enhanced WGC and in phase correlation with NAO mode.

The result of this multi-proxy approach presented here seems to display the rapid transitions between different climate events and indicate a close connection of sea ice variations in the Northern Hemisphere driven by the interplay between melt-water discharge and solar and oceanic forcings (i.e., WGC, BC). These findings may help to understand the recent reduction in

sea ice cover and further improve our climate models and climate predictions. More high-resolution studies are needed to understand the complex interaction of sea ice, its driving mechanisms, and fjord interactions in Baffin Bay.

Acknowledgements

5 Holocene variability in sea ice and primary productivity in the Baffin Bay-Labrador Sea- A N-S transect study

Jeetendra Saini[1], Ruediger Stein[1,2], Kirsten Fahl[1], Jens Weiser[2], Dierk Hebbeln[2]

[1]Alfred Wegener Institute Helmholtz Centre for Polar and Marine Research, Bremerhaven, Germany

[2]Marum-Center for Marine Environmental Sciences, University of Bremen, Bremen, Germany

Abstract

Reconstructions of sea-surface conditions during the Holocene were achieved using three sediment cores from northeastern Baffin Bay (GeoB19948-3 and GeoB19927-3) and the Labrador Sea (GeoB19905-1) along a north-south transect based on sea ice IP_{25} and open-water phytoplankton biomarkers (brassicasterol, dinosterol and HBI III). In Baffin Bay, sea-surface conditions in the early Holocene were characterized by extended (early) spring sea ice cover (SIC) and low primary productivity conditions prior to 9.4 ka BP, followed by a variable to marginal SIC and increased primary productivity during ~9.4-8.8 ka BP possibly associated with increasing but limited presence of Atlantic Water as West Greenland Current (WGC) as well as high summer insolation. Thereafter, a short period of increased SIC and reduced productivity was recorded between ~8.8-7.6 ka BP, probably related to the opening of the Nares Strait and subsequently increased Arctic Water influx and decreased WGC strengths. The conditions in the NE Labrador Sea, however, remained predominantly ice-free in spring/autumn due to the enhanced influx of Atlantic Water (WGC) from 11.5 until ~9.1 ka BP, succeeded by a period of high biological production and continued (spring-autumn) ice-free conditions between 9.1 and 7.6 ka BP corresponding to the onset of Holocene Thermal Maximum (HTM)-like conditions. A transition towards reoccurring ice-edge and significantly reduced SIC and primary productivity conditions in Baffin Bay is evident in the mid Holocene (~7.6-3 ka BP) probably caused by the variations in the WGC influence associated with the ice melting, probably representing HTM-like conditions. These HTM-like conditions are predominantly recorded in the NE Labrador Sea area shown by (spring-autumn) ice-free conditions and increased primary production from 5.9-3

ka BP. In the late Holocene (last ~3 ka), our combined proxy records from eastern Baffin Bay do not correlate with the Neoglacial cooling trend and surface conditions can be characterized by a decrease in SIC and primary productivity. The conditions in the NE Labrador Sea during the last 3 ka, however, continued to remain (spring-autumn) ice-free with decreased biological carbonate production probably linked to decreased WGC strength and/or increased Arctic Water influx, coinciding with the Neoglacial cooling. The results from this transect study provide further insight into the understanding of the influence of melt water discharges and oceanic current variability on sea ice and marine productivity conditions in this highly sensitive area.

5.1 Introduction

Sea ice with its strong seasonal and inter-annual variability plays a fundamental role in the earth's climate system as it influences the heat, moisture, albedo and gas exchange between the ocean and the atmosphere as well as deep-water formation (Dieckmann and Hellmer, 2003; McPhee et al., 2009; Morison et al., 2012; Thomas and Dieckmann, 2010). Over the last few decades, the Arctic sea ice has undergone a considerable reduction in its extent and thickness due to modern climate warming (Kinnard et al., 2011; NSIDC, 2020; Serreze and Stroeve, 2015) and indeed this has raised considerable concerns (Bhatt et al., 2014). It is expected that this ongoing reduction of Arctic sea ice will continue and amplify, further decreasing the Arctic Ocean albedo thus increasing sea-surface temperatures (SST) (Manabe et al., 1992; Screen and Simmonds, 2010). To understand these rapid changes in sea ice cover in a long-term perspective, there is a need for better understanding of the sea ice variability as well as its dynamics and interaction with climate throughout the geological past (Jakobsson et al., 2010).

Various proxies preserved in marine sediments may indicate indirect changes in sea ice occurrence and variability, as inferred from micropaleontology (e.g. dinoflagellate cysts, diatoms, and foraminifera assemblages) (de Vernal et al., 2013a; de Vernal et al., 2013c; Gersonde et al., 2005; Jennings et al., 2002), geochemistry (Hillaire-Marcel and de Vernal, 2008) and sedimentology (e.g. ice-rafted debris) (Polyak et al., 2010). The biomarker proxy "IP_{25}" exclusively synthesized by sea ice algae and well preserved in the sediments, however, seems to be a direct indicator for the presence of Arctic sea ice as shown in the pioneer study by Belt et al. (2007) (see (Belt, 2018) for a recent review). Even more detailed and semi-quantitative reconstructions of sea ice cover can be obtained when combining IP_{25} with open-water

phytoplankton biomarkers such as brassicasterol, dinosterol and/or a highly branched unsaturated triene (HBI III) ("PIP$_{25}$ index" Belt et al., 2015, 2019; Müller et al., 2011; Smik et al., 2016) .

Arctic outflow through Baffin Bay, via the Labrador Sea, acts as a substantial contributor of fresh water to the North Atlantic, as suggested by modelling and observational studies (Aksenov et al., 2010; Bunker, 1976; Serreze et al., 2006; Tang et al., 2004). Baffin Bay is characterized by a sea ice cover during most time of the year, however further to the south, the eastern Labrador Sea is predominantly ice-free (Tang et al., 2004). Thus the Baffin Bay-Labrador Sea region is a key location to study the interactions of sea ice, ice margin, and changes in sea-surface conditions (Fig. 5.1). Furthermore, it is of particular interest to investigate how climatic and oceanographic changes have affected sea ice and primary productivity conditions along this north-south transect along the eastern Baffin Bay and Labrador Sea margin, from where long-term Holocene records are sparse (Briner et al., 2013; Caron et al., 2019; Gibb et al., 2015; Hansen et al., 2020; Saini et al., 2020).

In this study, we aim for a continuous Holocene climate record along a north-south transect through the eastern Baffin Bay-Labrador Sea from three sediment cores recovered from northern Baffin Bay (GeoB19948-3), NE Baffin Bay (GeoB19927-3; see also Saini et al. (2020)) and the NE Labrador Sea (GeoB19905-1) (Fig. 5.1), approximately representing the last 11.5 ka. Special attention is given to high-resolution reconstructions of sea ice conditions and primary productivity documented by the abundance and accumulation rates of IP$_{25}$ and open-water phytoplankton biomarkers (brassicasterol, dinosterol and HBI III).

5.2   Environmental setting

The surface and subsurface waters in Baffin Bay and the Labrador Sea form a counter-clockwise gyre due to interaction of northward-flowing warm high salinity water transported by the West Greenland Current (WGC) with southward flowing cold polar sourced Arctic Water transported via the Baffin Current (BC) (Fig. 5.1A) (Ribergaard et al., 2008; Tang et al., 2004). The WGC carries water from the warmer more saline western branch of the Irminger Current (IC), modified by the less saline Arctic Water from the East Greenland Current (EGC) and local melt water discharge along the SW Greenland coast. The WGC flows northwards along the west Greenland

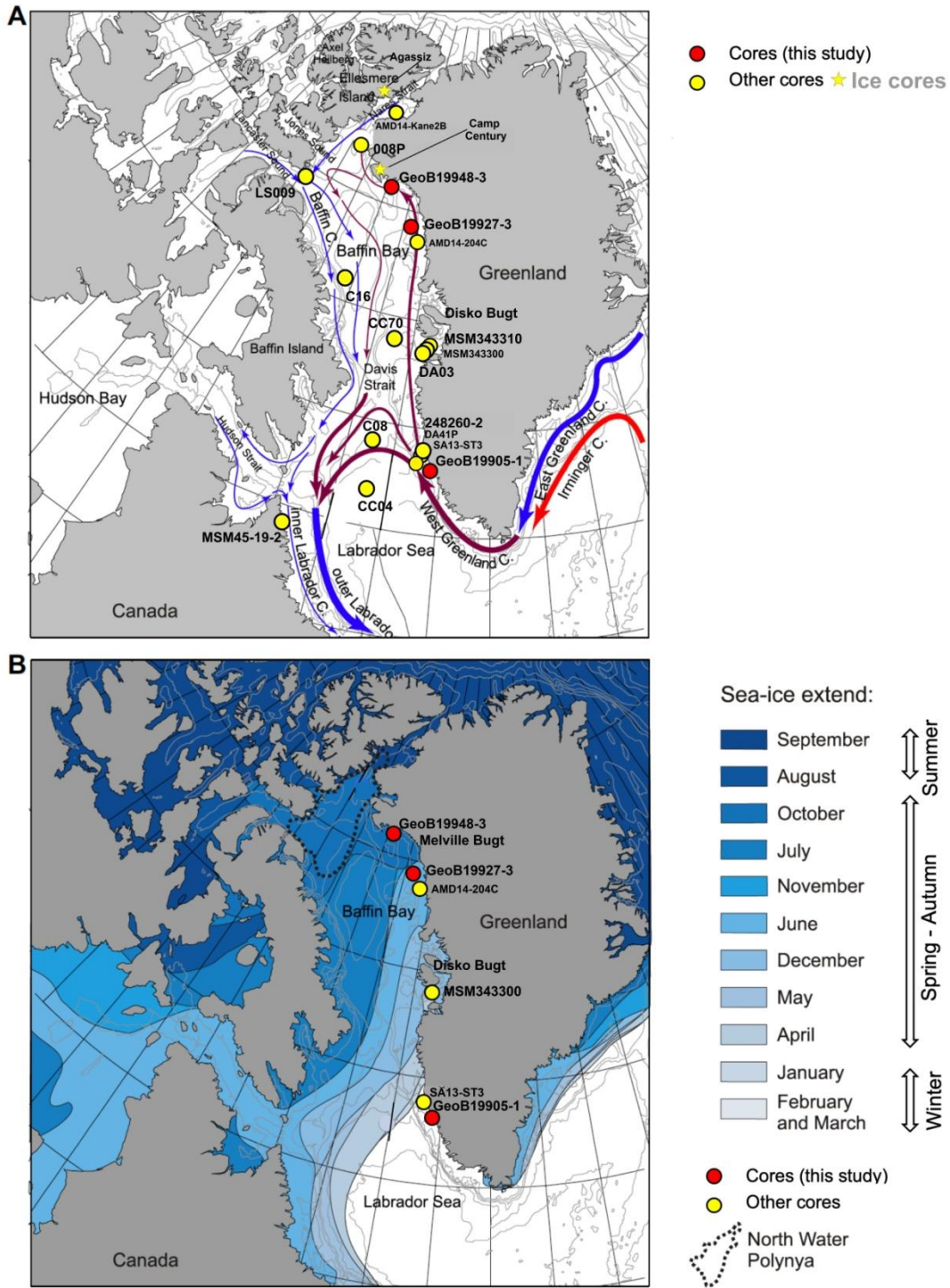Figure 5.1: A. Map of Baffin Bay and Labrador Sea areas with general surface circulation (warm surface current in red and cold polar sourced currents in blue) and locations of three sediment cores studied (GeoB19948-3, GeoB19927-3 and GeoB19905-1) herein, shown as red dots. B. The average maximum extent of the sea ice edge for each month of the year (as per data from NSIDC, 2012), adapted from Seidenkrantz (2013a).

coast and turns west in the Melville Bugt before merging with the BC in northeastern Baffin Bay. The BC flows south along Baffin Island through Davis Strait before joining into the Labrador Current (LC). In the western Labrador Sea, the LC overlies the WGC that partly turns west and south again near Davis Strait.

Sea ice cover in Baffin Bay is variable and may range from 0 to ~10 months/year, with much of Baffin Bay covered by near-continuous sea ice during winter (Fig. 5.1B) (Tang et al., 2004). Ice growth first starts in northwestern Baffin Bay at the end of September and expands southwestwards, with a maximum extent in March, sometimes even reaching the NW Labrador Sea. After melting during the summer months it attains a minimal extent in September (Tang et al., 2004; Wang et al., 1994). The warm WGC negatively affects sea ice formation and prevents its further growth along eastern Baffin Bay. The large inter-annual variability in sea ice has a major impact not only on ice extent but on phytoplankton blooms and therefore marine productivity as well, which is coupled with the strong seasonality in surface air temperatures and wind patterns (Sakshaug, 2004; Tang et al., 2004).

5.3 Material and methods

The three cores used in this study were collected during R/V *Maria S. Merian* cruise MSM44 (Dorschel et al., 2015). Site information, core lengths, and sampling intervals are described in Table 5.1. Cores GeoB19948-3 and GeoB19927-3 were taken from northeastern Baffin Bay, whereas core GeoB19905-1 was taken from the northeastern Labrador Sea (Fig. 5.1; Table 5.1).

Table 5.1: Coordinates of the three cores used in this study.

Core ID	Region	Lattitude [°N]	Longitude [°W]	Water depth [m]	Core length [cm]
GeoB19948-3	Northern Baffin Bay	75° 46.10′	64° 08.57′	778	1018
GeoB19927-3	Northeastern Baffin Bay	73° 35.26′	58° 05.66′	932	1147
GeoB19905-1	Eastern Labrador Sea	64° 21.68′	52° 57.70′	485	1045

Based on visual description and color measurements of core GeoB19948-3 the upper 280 cm are mainly composed of olive-grey to silty clay homogeneous sediments (Dorschel et al., 2015). In core GeoB19927-3 the lowermost part is characterized by non-homogenous silt and fine sand sediments embedded with dropstones and sharp color boundaries. The upper part of this core can be mainly represented as homogenous olive-grey silty-clay sediments (Dorschel et al., 2015). In core GeoB19905-1, sediments are mainly composed of olive-grey muds with some sandy layers at the lower part of the core and sharp color transitions displayed by distinct lithological units (LU), for a more detailed description, however, see Dorschel et al. (2015).

5.3.1 Chronostratigraphy

Core GeoB19948-3

The chronostratigraphic framework of the upper 280 cm of core GeoB19948-3 (Fig. 5.2) is based on four AMS ^{14}C-dates measured on 0.57-1.12 mg of foraminifera from the >100µm fraction (table 2), performed directly on the CO_2 gas with the MICADAS (Mini Carbon Dating System) at the Alfred Wegener Institute in Bremerhaven, Germany (for methodological details see (Wacker et al., 2013)). Radionuclide analyses (^{210}Pb, ^{40}K, ^{137}Cs) were performed on core top sediments (depths; 2, 6 and 10 cm) at the Bremen State Radioactivity Measurements Laboratory. Subsequently, the AMS dates were calibrated to calendar years using PaleoDataView (Langner and Mulitza, 2019), which uses modelled reservoir ages (Butzin et al., 2017, see Table 5.1) to calibrate radiocarbon ages against IntCal13 (Reimer et al., 2013). The appropriate reservoir ages are chosen automatically based on the sample's radiocarbon age and location of the core. The calibrated ages were subsequently used to construct the final age model by linear interpolation between the calibrated ages and linear extrapolation between the topmost age and the core top.

Table 5.2: Results of the AMS-dating and subsequent calibration from core GeoB19948-3. Reservoir ages are in respect to IntCal13, min. and max. ages correspond to the 5% & 95% confidence interval defined by PDV. The last column denotes the final ages used for the stratigraphic framework.

AMS-dating, MICADAS, AWI Bremerhaven					Reservoir Correction and Calibration, PaleoDataView			
Lab ID AWI-	Depth [cm]	^{14}C-age [yrs]	^{14}C-error [yrs]	material	Reservoir age [yrs]	Min. age [cal. yrs. BP]	Max. age [cal. yrs. BP]	**Weighted mean age [cal. yrs. BP]**
1252.1.1	14	2,443	108	mixed foraminifera	734 ± 64	1.354	1.890	**1.625**
1253.2.1	150	5,431	198	mixed benthic foraminifera	818 ± 58	4.824	5.874	**5.281**
1253.1.1	150	5,427	114	*N. pachyderma* sin	818 ± 58	4.892	5.591	**5.285**
1475.1.1	274	7,789	184	mixed foraminifera	660 ± 61	7.623	8.336	**7.965**
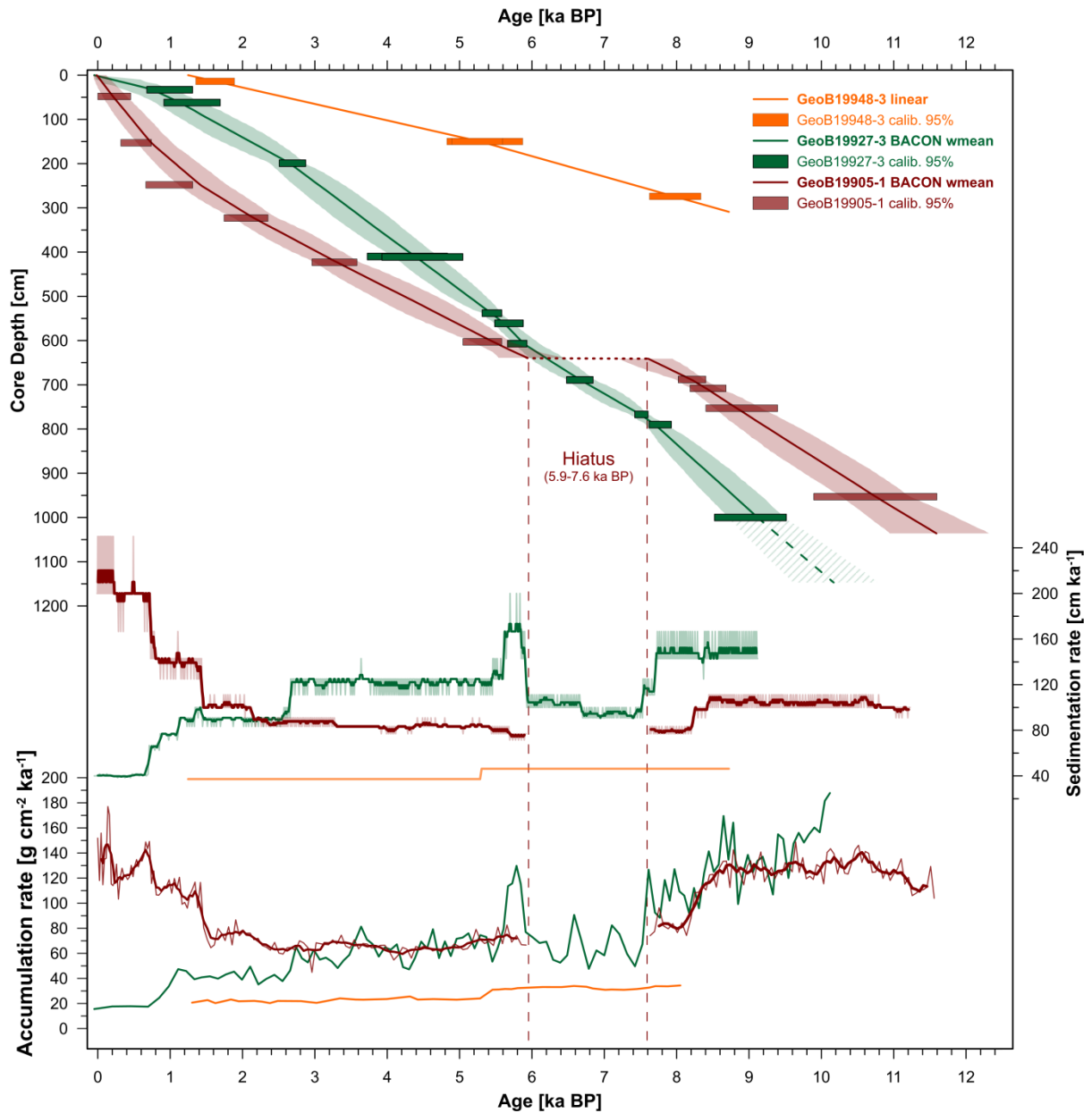
Figure 5.2: Age models of GeoB19948-3 (orange), GeoB19927-3 (green) and GeoB19905-1 (red). For GeoB19927-3 and GeoB19905-1 the bold lines show weighted mean age after modelling in BACON, while the lighter shades indicate 95% confidence intervals (CIs). For GeoB19948-3 the age-depth relation is given by linear interpolation between the AMS dates, shown as bold line. Stippled lines (GeoB19905-1) indicate areas of less robust age control. Rectangles denote 95% CIs of the AMS-dates after calibration with PDV. In the centre and bottom panels the derived sedimentation and accumulation rates are shown, including 5-point running averages where applicable.

Core GeoB19927-3

The chronostratigraphy of core GeoB19927-3, previously published by Saini et al. (2020) (Supplementary Fig. S5.1) is based on 12 AMS 14C-dates and radionuclide analyses (210Pb, 40K, 137Cs) and was developed using "BACON" software (Blaauw and Christen, 2011) assuming a constant reservoir age of 140±35yrs. However, to ensure consistency between the age models, we recalibrated the AMS dates (Fig. 5.2) using PaleoDataView (Butzin et al., 2017) that uses modelled reservoir ages to calibrate radiocarbon ages against IntCal13 (Reimer et al., 2013) (see, Supplementary Fig. S5.1 for comparison). According to the new age model, core GeoB19927-3 covers a time interval from ca. 0 to 10.1 ka BP, which is almost similar, i.e., only about 0.2 ka younger than the original age model (Supplementary Fig. S5.1).

Core GeoB19905-1

The chronostratigraphy of core GeoB19905-1 (Fig. 5.2) is based on 12 Accelerator Mass Spectrometry (AMS) ^{14}C-dates, previously published by Weiser at al. (2021) (See data sets available at https://doi.org/10.1016/j.quascirev.2021.106833). The age model was constructed using a combination of the PaleoDataView-program (Langner and Mulitza, 2019) and the open source software package BACON (Blaauw and Christen, 2011)   . For details on the methodological approach, the reader is referred to the original publication.

5.3.2   Bulk parameters (TOC and CaCO$_3$)

For organic-geochemical analyses, freeze-dried and homogenized subsamples were taken (n=60, at 4 cm intervals for core GeoB19948-3 and n=207, at 5 cm intervals for core GeoB19905-1) and stored in glass vials at -20 ˚C. TOC contents were measured using a Carbon-Sulfur Eltra Analyser (CS-800, ELTRA) after carbonate removal with hydrochloric acid (37%, 500 µl). The error of our TOC measurements is at ±0.02%. The amount of total carbon (TC) was measured on untreated samples using a Carbon-Nitrogen-Sulfur Analyser (Elementar-III, Vario). Assuming the predominant carbonate phase is calcite, carbonate contents were calculated as CaCO$_3$ = (TC-TOC)*8.333, where 8.333 is the stoichiometric calculation factor.

5.3.3   Sea ice biomarkers (IP$_{25}$, HBI III and sterols)

For biomarker analyses, we extracted ~4 g of freeze-dried and homogenized sediment using dichloromethane: methanol (2:1 v/v) as a solvent for ultrasonication (3x15min). Prior to

extraction, 9-octylheptadec-8-ene (9-OHD; 0.1 µg/sample), 7-hexylnonadecane (7-HND; 0.076 µg/sample), 5α-Androstan-3β-ol (Androstanol; 10.7 µg/sample) and 2,6,10,15,19,23-Hexamethyltetracosane (Squalane; 3.2 µg/sample) were added for quantification of biomarkers. The extracts were separated by open silica (SiO_2) column chromatography with *n*-hexane (5 ml) and ethyl-acetate: *n*-hexane (9 ml, 2:8 v/v) as eluent into hydrocarbon and sterol fraction, respectively. The sterol fraction was silylated using 200 µl BSTFA (bis-trimethylsilyl-trifluoroacet-amide) (60˚C, 2 h).

Two different gas chromatography-mass spectrometers (GC-MS) with similar basic configuration were used to qualify and quantify the hydrocarbon and sterol fractions. The quantification of HBI fraction was carried out with a gas chromatograph (Agilent Technologies GC6850, 30 m DB-1MS column, 0.25 mm id, 0.25 µm film) coupled to an Agilent Technologies 5977C VL MSD mass selective detector (Triple-Axis Detector, 70eV constant ionization potential, Scan 50-550 m/z, 1 scan/s, ion source temperature 230°C). The quantification of the sterols (quantified as trimethylsilyl ethers) was carried out with a GC Agilent 6850 (30 m DB-1MS column, 0.25 mm id, 0.25 µm film) coupled to an Agilent 5975C VL MSD mass selective detector. GC measurements were carried out with the following temperature program: 60 ˚C (3 min), 150 ˚C (15 ˚C/min), 320 ˚C (10 ˚C/min), 320 ˚C (15 min isothermal) for the hydrocarbons and 60 ˚C (2 min), 150 ˚C (15 ˚C/min), 320 ˚C (3 ˚C/min), 320 ˚C (20 min isothermal) for the sterols. Helium served as carrier gas (1 ml/min constant flow). Specific compound identification was based on the comparison of gas chromatography retention times with those of reference compounds and published mass spectra (Belt et al., 2007; Boon et al., 1979; Brown and Belt, 2016; Volkman, 1986). For the quantification of IP_{25} and HBI III (Z-isomer, generally referred to as "HBI III") their molecular ion ratio (m/z 350 for IP_{25} and m/z 346 for HBI III in relation to the abundant fragment ion m/z 266 of internal standard (7-HND) was used (in selected ion monitoring mode, SIM). The different responses of these ions and a detailed quantification method is given by Fahl and Stein (2012). For the quantification of the sterols, the molecular ions m/z 470 for brassicasterol (as 24-methylcholesta-5,22E-dien-3β-o-Si(CH$_3$)$_3$) and m/z 500 for dinosterol (4α,23,24R-trimethyl-5α-cholest-22E-en-3β-o-Si(CH$_3$)$_3$) were used in relation to the molecular ion m/z 348 for the internal standard Androstanol.

The PIP_{25} indices were calculated by combining IP_{25} with different phytoplankton markers for semi-quantitative sea ice reconstruction according to Müller et al., 2011:

$$PIP_{25} = \frac{[IP_{25}]}{([IP_{25}] + c*p)} \qquad \text{with } c = mean\ [IP_{25}]/mean\ [IP_{25}]$$

and p is the phytoplankton biomarker concentration (p = B (brassicasterol) or D (dinosterol) or III (HBI III)). Recently, based on surface sediments from Baffin Bay, Kolling et al. (2020) suggested that sea ice indices P_DIP_{25} and P_BIP_{25} may indicate late spring and/or autumn conditions, while $P_{III}IP_{25}$ may record more the early spring and/or late winter (ice-edge) conditions. However, low concentrations approaching absence of HBI III in Baffin Bay sediments may result in an overestimation of the sea ice cover by the $P_{III}IP_{25}$ index and therefore should be interpreted with caution (Kolling et al., 2020).

5.3.4 Calculation of accumulation rates

Biomarker contents were converted into accumulation rates by using the following equations (e.g., Stein & Macdonald, 2004a)

$$(1)\ Bulk\ accumulation\ rate = LSR * DBD$$

$$(2) TOC\ accumulation\ rate = Bulk\ accumulation\ rate * TOC/100$$

$$(3)\ CaCO_3\ accumulation\ rate = Bulk\ accumulation\ rate * CaCO_3/100$$

$$(4)\ BM\ AR = Bulk\ accumulation\ rate * BM$$

LSR = sedimentation rate (cm ka^{-1}); DBD = dry bulk density (g cm^{-3}); TOC = total organic carbon content (%); CaCO$_3$ = carbonate content (%); BM = biomarker content (µg g^{-1}); Bulk accumulation rate = total sediments accumulation rate (g cm^{-2} ka^{-1}); TOC accumulation rate = total organic carbon accumulation rate (g cm^{-2} ka^{-1}); CaCO$_3$ accumulation rate = carbonate accumulation rate (g cm^{-2} ka^{-1}); BM accumulation rate = biomarker accumulation rate (µg cm^{-2} ka^{-1}).

5.4 Results

5.4.1 Core chronology and sedimentation rates

Core GeoB19948-3

Given the scarcity of calcareous material in the sediment resulting in only 3 AMS ^{14}C-dates for core GeoB19948-3, a preliminary chronological framework could be constructed. Still, this framework suggests continuous sedimentation since ~8 ka BP (Fig. 5.2), with sedimentation rates in the order of 40–50 cm ka^{-1}. No excess ^{210}Pb and/or ^{137}Cs were found in the top sediments and thus the age of the topmost date (1.6 ka BP, 14cm core depth) suggests that the core top is not of recent age, but instead ~1.2 ka old.

Core GeoB19927-3

The updated age model of core GeoB19927-3 suggests continuous sedimentation since ~ 10.1 ka BP (Fig. 5.2). Sedimentation rates vary between 40 and 200 cm ka^{-1}, although high sedimentation rates of about 100—200 cm ka^{-1} prevail in the majority of the record, except a prominent decrease at 2.6 ka BP leading to low values of <50 cm ka^{-1} after 0.7 ka to present.

Core GeoB19905-1

The age model of core GeoB19905-1 (Weiser et al., 2021) suggests a continuous sedimentation from 11.5 ka BP to 7.6 ka BP and since 5.9 ka BP (Fig. 5.2). A hiatus spanning about 1.7 ka in between these intervals was identified at 640 cm core depth. Sedimentation rates range from 71 to 250 cm ka^{-1} with high values of ~100 cm ka^{-1} between 11.5-8.2 ka BP and decreasing to about 80 cm ka^{-1} from 8.2-7.6 and 5.9-2.4 ka BP. A strong increase in sedimentation rates to 80—100 cm ka^{-1} is recorded after 2.4 ka BP, that rises even further up to 150 cm ka^{-1}, 200 cm ka^{-1} and 250 cm ka^{-1} after 1.4 ka BP, 0.7 ka BP and 0.3 ka BP, respectively.

5.4.2 Organic geochemical bulk parameters and biomarkers

The organic-geochemical and biomarker records of core GeoB19927-3, excluding CaCO$_3$, have already been described and published by Saini et al. (2020). Thus, here only the new data of cores GeoB19948-3 and GeoB19905-1 are presented. In the discussion, however, data from all three cores are included. The results of all biomarkers contents are plotted in µg/gTOC and as accumulation rates in µg cm^{-2} ka^{-1} (Fig. 5.3-5.6). They are also presented in µg/g sediment in the

supplementary material (see, Supplementary Fig. S5.2-5.4). The distribution of contents and accumulation rates of biomarkers and bulk parameters reveals significant down-core variations.

Core GeoB19948-3

The GeoB19948-3 record presented here extends to ~8 ka BP. The $CaCO_3$ contents vary between 3.6 to 1% over the last ~8 ka (Fig. 5.3a). Higher values of about 2.4% (mean) occur from ca. 8 to 5.3 ka BP (278-154cm) followed by lower contents of 1.9% (mean) towards the top of the core. TOC contents vary between about 0.8 to 0.4% over the last ~8 ka (Fig. 5.3b), and display higher values of about 0.7% (mean) from ca. 8 to 5.3 ka BP (278-154cm), followed by lower contents of 0.6% (mean) towards the top of the core. HBI III contents were typically near zero over the last ~8 ka, except for two prominent peaks of 0.6 and 0.4 µg/gTOC at about 6.5 ka BP (210cm) and 1.6 ka BP (14cm), respectively (Fig. 5.3c). The phytoplankton sterols dinosterol and brassicasterol display higher contents from 8 to 5.3 ka BP (278-154cm), followed by a gradual decrease towards the top of the core (Fig. 5.3d, e). The IP_{25} contents vary between 0.2 to 2.0 µg/gTOC and display higher values from 8 to 5.3 ka BP (278-154cm), followed by lower values towards the core top (Fig. 5.3f).

The accumulation rates of TOC range from 0.10 to 0.26 g cm^{-2} ka^{-1} and are marked by a gradual decrease from ca. 8 to 1.2 ka BP (Fig. 5.5b). The $CaCO_3$ accumulation rates show a similar generally decreasing trend from 8 to 1.2 ka BP and vary between about 0.2 to 1 g cm^{-2} ka^{-1} (Fig. 5.5c). HBI III accumulation rates are typically low (near zero) throughout the mid-to-late Holocene (mean ~0.02 µg cm^{-2} ka^{-1}) (Fig. 5.5d), except for a prominent peak around 6.7-6.3 ka BP. The accumulation rates of phytoplankton biomarkers dinosterol and brassicasterol vary between 0.7 to 5.7 µg cm^{-2} ka^{-1} and show a gradual decrease from ca. 8-1.2 ka BP (Fig. 5.5e, f). IP_{25} accumulations rates range between 0.03 and 0.5µg cm^{-2} ka^{-1} and are relatively high in the early part of mid Holocene between 8-5.3 ka BP, followed by constantly low values between ca. 5.3-1.2 ka BP (Fig. 5.5g). The P_DIP_{25} index varies in the range from 0.3 to 0.6; whereas the $P_{III}IP_{25}$ index varies between 0.1 and 0.8 and they display variable but higher values at the onset of the mid Holocene from ca. 8 to 4 ka BP, followed by generally decreasing $P_{III}IP_{25}$ values in the late Holocene (Fig. 5.7f). Although, P_DIP_{25} index show reduced values from ca. 4-1.2 ka BP but they exhibit a slight increase towards the end of this period. Moreover, $P_{III}IP_{25}$ attains two

minimum values of ~0.29 and ~0.15 at about 6.7-6.3 (mid Holocene) and ~1.8-1.3 ka BP (late Holocene), respectively.

Figure 5.3: Combined record of core GeoB19948-3 including bulk parameters and biomarkers; (a) CaCO$_3$ content, (b) total organic carbon (TOC), (c) HBI III [µg/g TOC], (d) dinosterol [µg/g TOC], (e) brassicasterol [µg/g TOC] and (f) IP$_{25}$ [µg/g TOC]. Black solid triangles mark the AMS ^{14}C datings. All plots are shown versus depth in [cm].
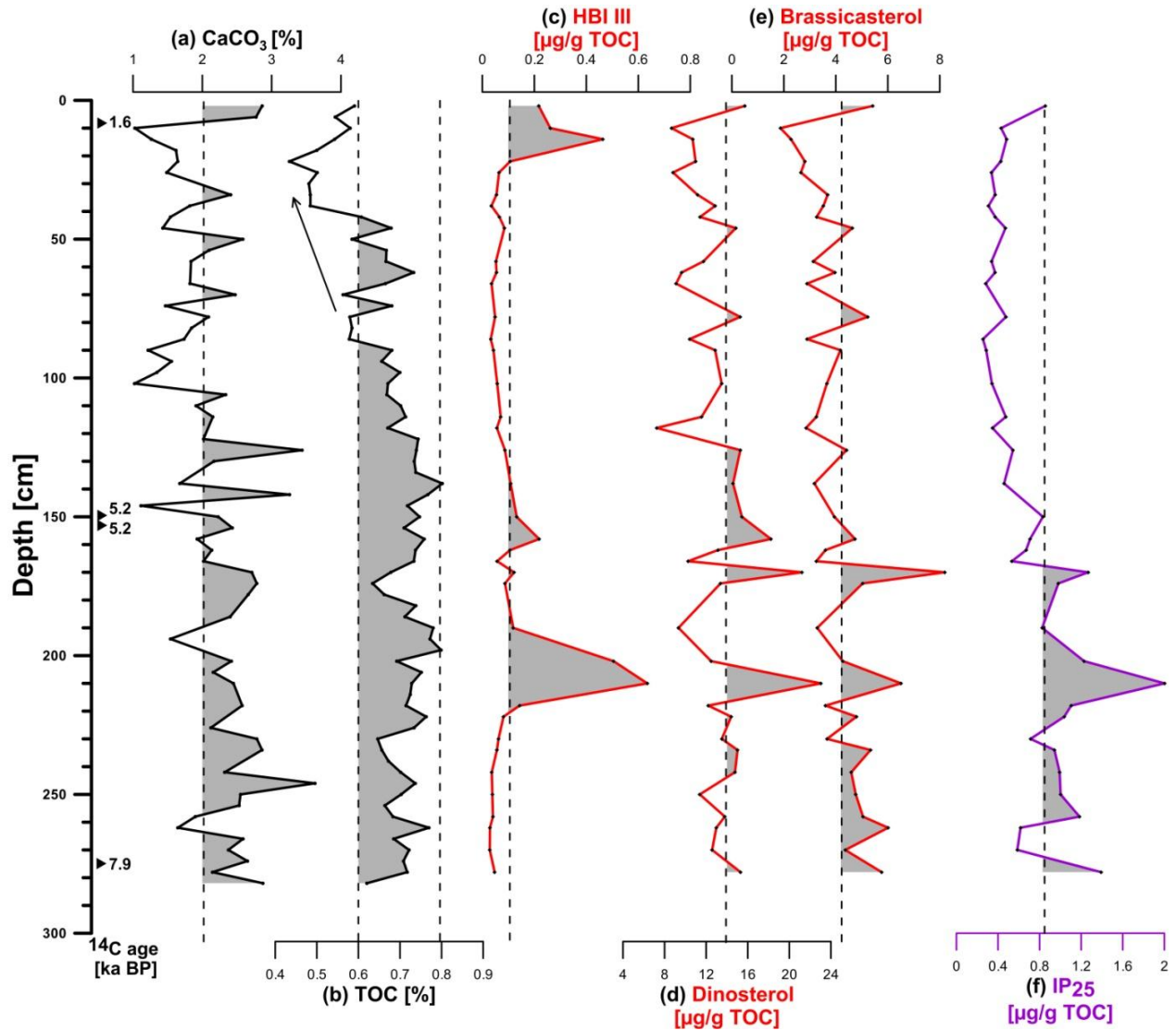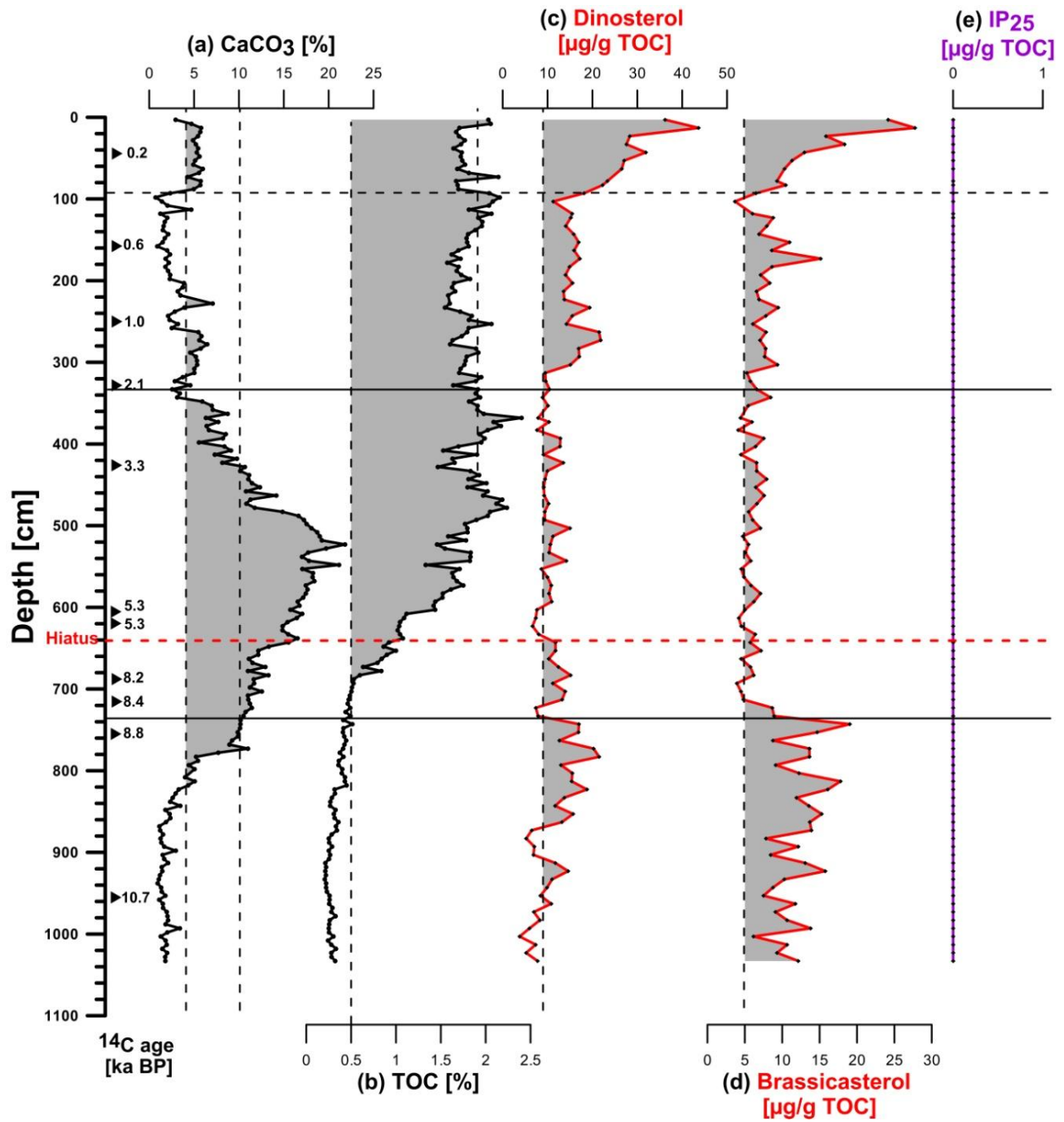
Figure 5.4: Combined record of core GeoB19905-1 including bulk parameters and biomarkers; (a) CaCO$_3$ content, (b) total organic carbon (TOC), (c) dinosterol [µg/g TOC], (d) brassicasterol [µg/g TOC] and (e) IP$_{25}$ [µg/g TOC]. Black solid triangles mark the AMS ^{14}C datings (Weiser et al., 2021). All plots are shown versus depth in [cm].

Figure 5.5: Downcore variations of core GeoB19948-3 showing (a) bulk accumulation rate, and accumulation rates of (b) total organic carbon, (c) CaCO₃, (d) HBI III, (e) dinosterol, (f) brassicasterol, and (g) sea ice proxy. The orange bar might indicate an ice-edge (IE) situation. Arrows indicate decreasing/increasing trend in proxy records. All plots are shown versus age in 1000 years before present (ka BP).

Core GeoB19905-1

The CaCO₃ contents range from 0.7 to 21.8% throughout the record and display continuously low values of about 3.3% (mean) between ~11.5 to 8.6 ka BP (1036-737cm) (Fig. 5.4a). It increases to maximum values of 21%, attaining the maximum at about 4.4 ka BP (523cm) and drops to generally lower values (mean 3.3) between 2.1 to 0.4 ka BP (329-83cm), followed by a minor rise to about 5% (mean) in the upper part of the core in the last ca.0.4 ka BP (83-0cm). TOC contents vary between 0.2 and 2.4%, show the lowest values between ~11.5 to 8.2 ka BP (1036-680cm) followed by a sharp rise afterwards, and acquire highest (mean 1.8%) values

during the last ca. 5 ka (600-0cm) (Fig. 5.4b). The phytoplankton biomarkers dinosterol and brassicasterol co-vary between 3 and 43 µg/gTOC throughout the Holocene (Fig. 5.4c, d). Phases with variable but high values (mean 11.4 µg/gTOC) of dinosterol were observed between ~11.5 to 8.6 ka BP (1036-737cm), however, they show no increase in µg/g sediment in this period (Supplementary Fig. S5.4). A slight decrease in dinosterol contents (mean 10.4 µg/gTOC) occurs between 8.6-7.6 and 5.9-2.1 ka BP. Afterwards, a strong increase in dinosterol content is recorded from 2.1-0.4 ka BP (329-83cm) followed by an even stronger rise even to about 40 µg/gTOC during the last ca. 0.4 ka BP (83-0cm). IP$_{25}$ and HBI III are absent throughout the record of the last 11.5 ka BP (Fig. 5.4e).
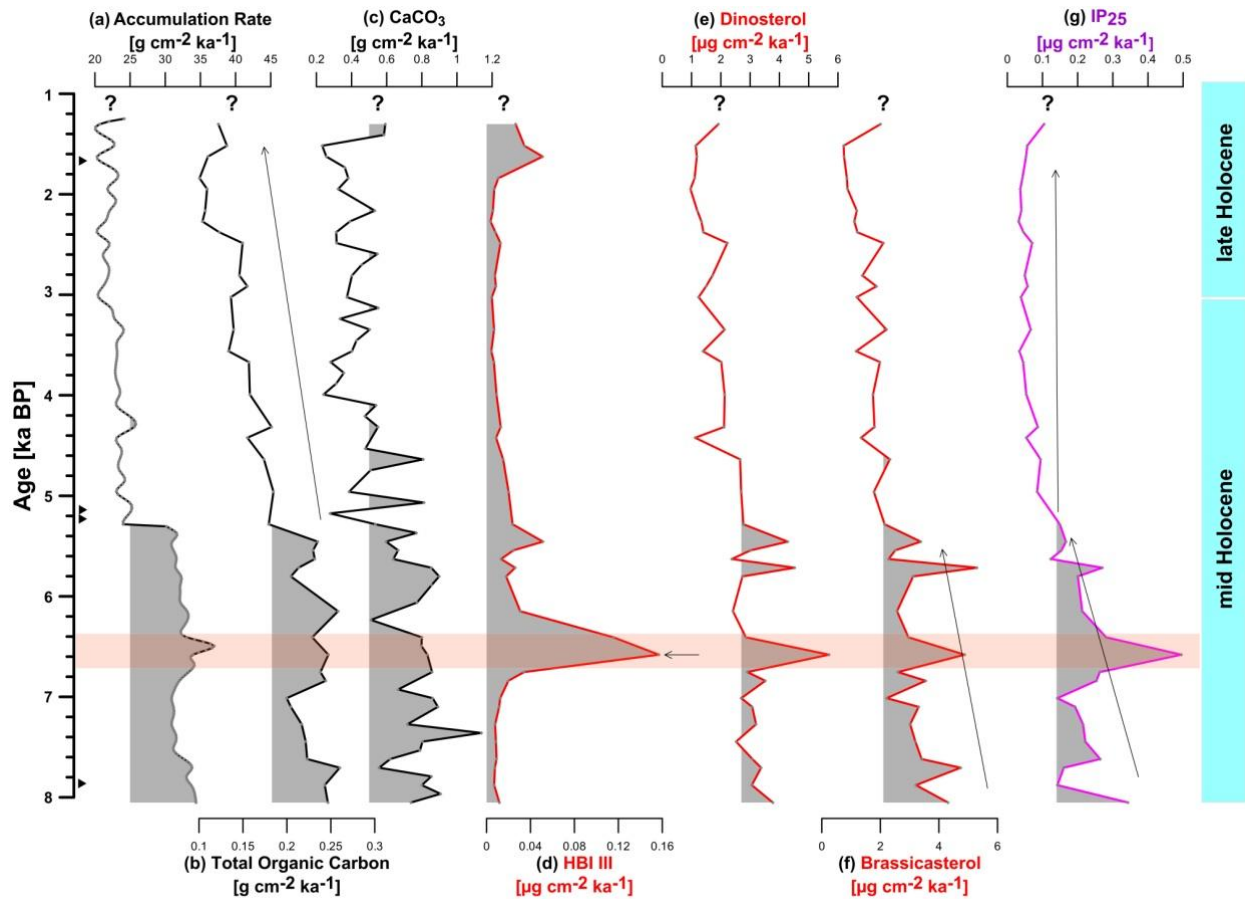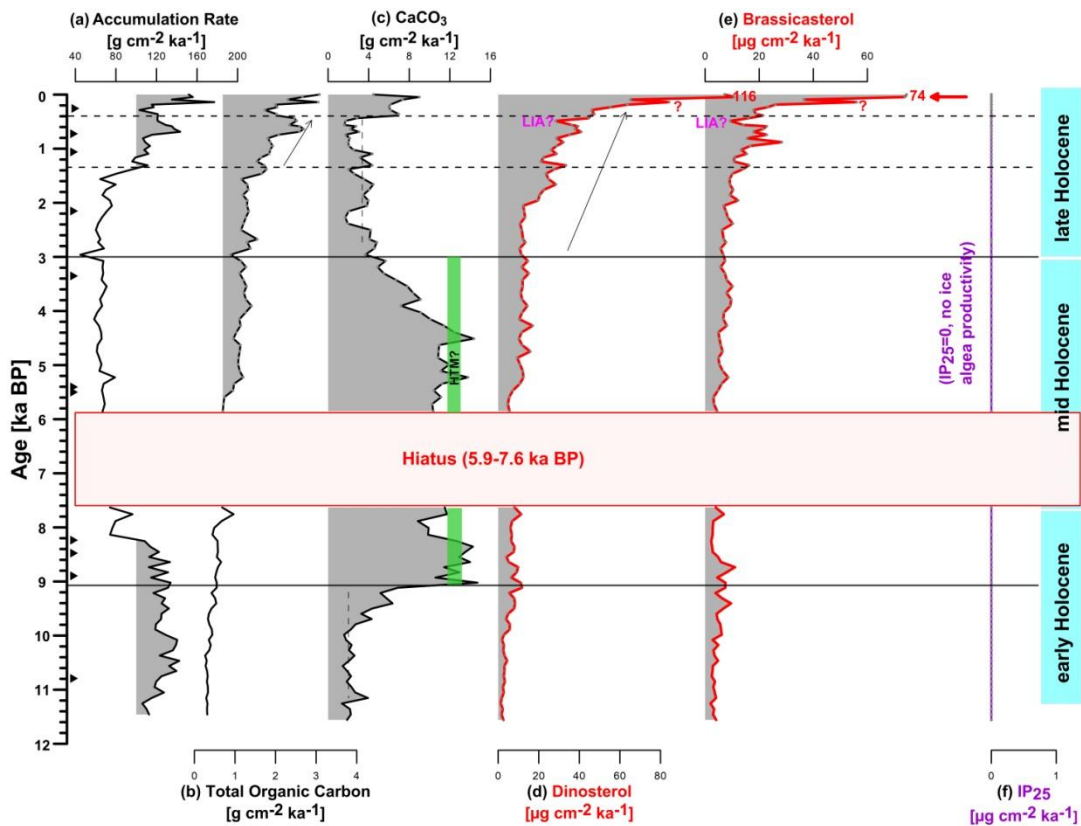

Figure 5.6: Downcore variations of core GeoB19905-1 showing (a) bulk accumulation rate, and accumulation rates of (b) total organic carbon, (c) CaCO$_3$, (d) dinosterol, (e) brassicasterol, and (f) sea ice proxy IP$_{25}$. A green bar indicates the maximum occurrence of foraminifera in this core (Weiser et al., unpublished data). Thick red arrow at the top may indicate enhanced primary production/preservation but the possibility of diagenetic alteration in the upper ~100cm cannot be excluded (cf. discussion for further explanation). Arrows indicate decreasing/increasing trend in proxy records. All plots are shown versus age in 1000 years before present (ka BP).
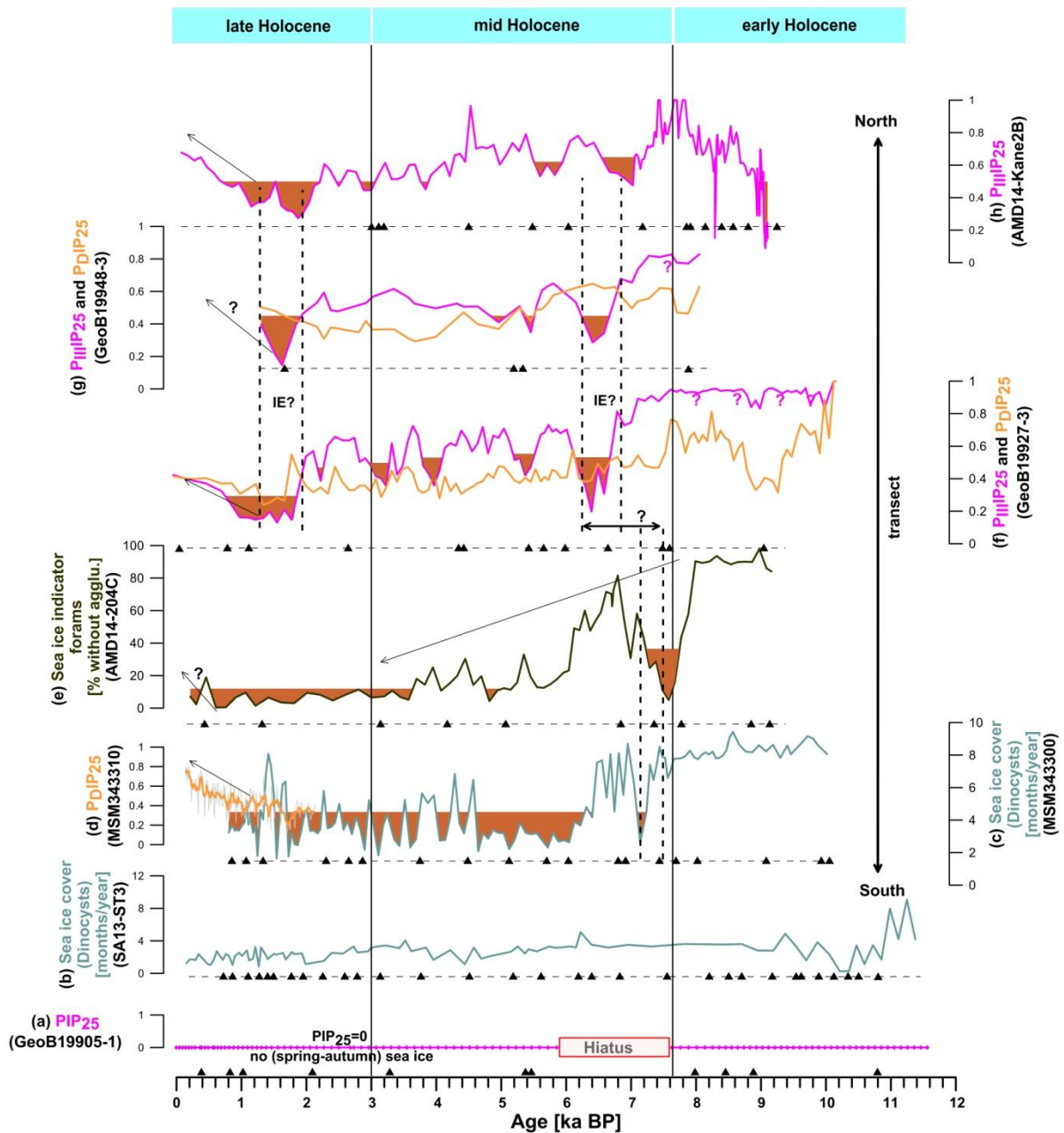
Figure 5.7: Comparison of different sea ice records based on P_DIP_{25}, $P_{III}IP_{25}$ indices, foraminifera and dinocysts records along the eastern Baffin Bay-Labrador Sea (N-S) transect (a) Core GeoB19905-1 (this study), (b) Core SA13-ST3 (Allan et al., 2021), (c) Core MSM343300 (Ouellet-Bernier et al., 2014), (d) Core MSM343300 (Kolling et al., 2018), (e) Core AMD14-204C (Hansen et al., 2020), (f) Core GeoB19927-3 (Saini et al., 2020), (g) GeoB19948-3 (this study), (h) Core AMD14-Kane2B (Georgiadis et al., 2020). Orange shading in PIP_{25} records might be interpreted as ice-edge (IE?) situations. (cf. Saini et al. (2020)). Arrows indicate decreasing/increasing trend in proxy records. The positions of these cores are indicated in Fig. 1. Calibrated AMS ^{14}C ages of cores with varying age-resolution are shown as solid triangles for correct correlation of data.
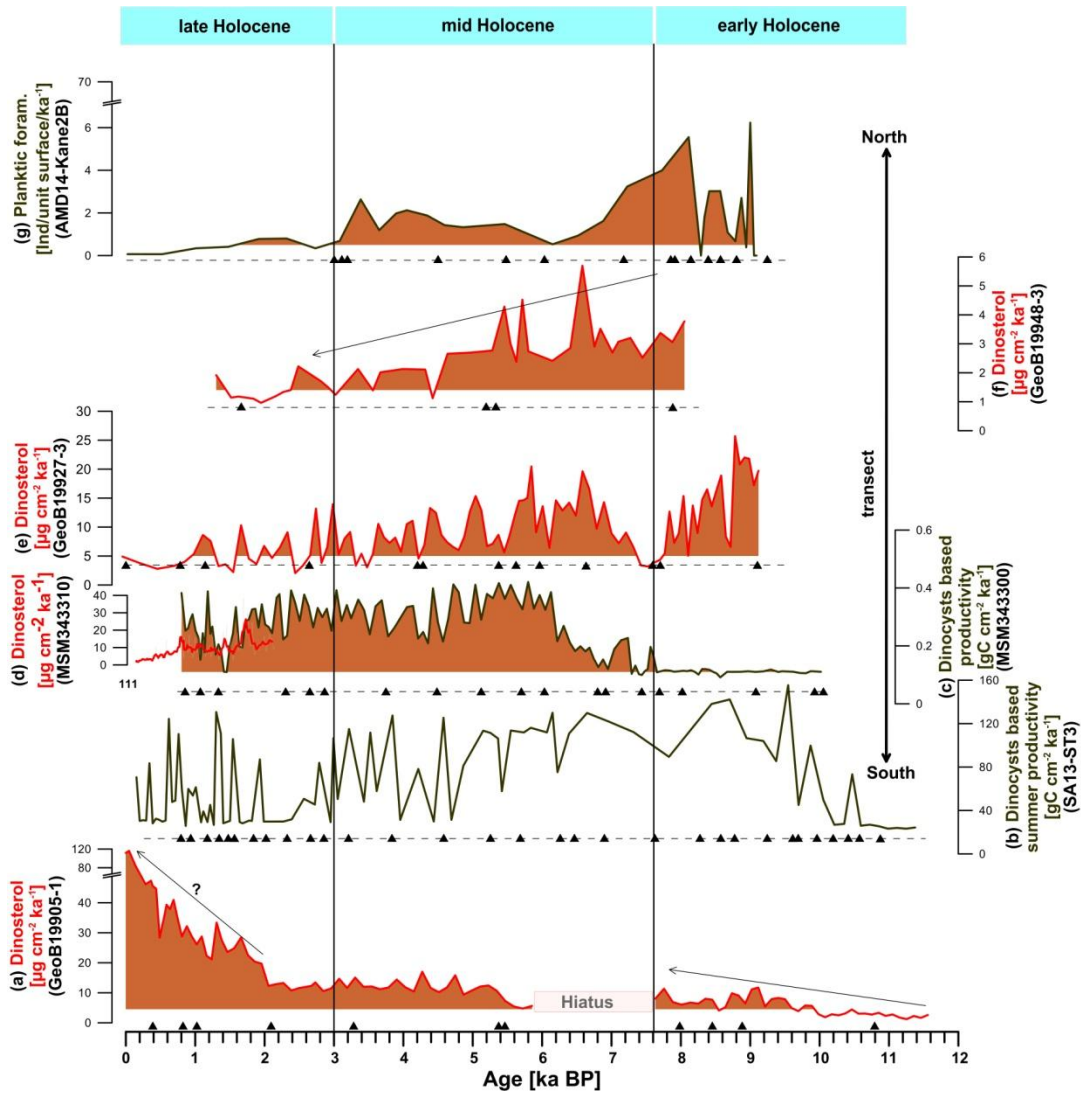
Figure 5.8: Comparison of selected proxies for primary productivity along the eastern Baffin Bay-Labrador Sea (N-S) transect (a) Core GeoB19905-1 (this study), (b) Core SA13-ST3 (Allan et al., 2021), (c) Core MSM343300 (Ouellet-Bernier et al., 2014), (d) Core MSM343300 (Kolling et al., 2018), (e) Core GeoB19927-3 (Saini et al., 2020), (f) Core GeoB19948-3 (this study), (g) Core AMD14-Kane2B (Georgiadis et al., 2020). Note different scales of dinocysts based accumulation rates and a strong increase in primary productivity from north to south of transect, in agreement with the general decrease in sea ice cover from high to lower latitudes. Arrows indicate decreasing/increasing trend in proxy records. The positions of these cores are indicated in Fig. 1. Calibrated AMS ^{14}C ages of cores with varying age-resolution are shown as solid triangles for correct correlation of data.

The accumulation rates of TOC, $CaCO_3$ and phytoplankton biomarkers dinosterol and brassicasterol vary between about 0.2-3 g cm^{-2} ka^{-1}, 1-14 g cm^{-2} ka^{-1}, 1-116 µg cm^{-2} ka^{-1}, and 2-74 µg cm^{-2} ka^{-1}, respectively (Fig. 6b, c, d, e). IP_{25} accumulation rates are zero (as $IP_{25}=0$)

throughout the record (Fig. 6f). Overall, the accumulation rates of TOC and phytoplankton biomarkers dinosterol and brassicasterol remain relatively low and constant until about 7.6 ka BP and show slightly increased values from 5.9 to about 2 ka BP. A period of a strong increase in the accumulation rates of dinosterol and brassicasterol followed during the last ~2 ka BP. However, TOC accumulation rates remain relatively low until about 1.5 ka BP and show a strong increase during the last 1.5 ka BP. During the last ca. 0.4 ka BP, the highest accumulation rates of TOC, dinosterol and brassicasterol were recorded. $CaCO_3$ accumulation rates are low until 9.1 ka BP, followed by increased and maximum values from 9.1-7.6 ka BP and 5.9-3.0 ka BP and thereafter decrease during the last 3 ka, except for a minor rise during the last 0.4 ka BP.
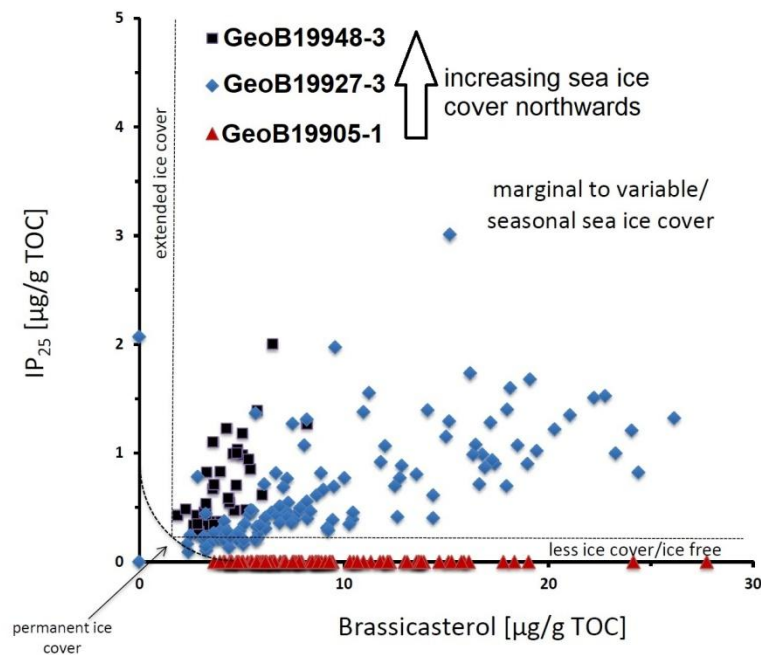
Figure 5.9: Correlation of IP_{25} vs. phytoplankton brassicasterol based on GeoB19948-3, GeoB19927-3 and GeoB19905-1, indicating variable seasonal to marginal ice-edge to ice-free conditions along the eastern Baffin Bay-Labrador Sea (north-south) transect. See Müller et al. (2011) for the classification of different sea ice scenarios. (cf. discussion for further explanation).

5.5 Discussion

In order to investigate the paleoceanographic changes along a N-S transect through eastern Baffin Bay to the Labrador Sea margin on the West Greenland Shelf, we have used a combination of sea ice, open-water phytoplankton productivity biomarkers and organic

geochemical bulk parameters that are discussed together with relevant literature data. The records from this study show variability in sea ice formation and primary productivity along this north-south transect (Fig. 5.7, 5.8, 5.9) throughout the Holocene.
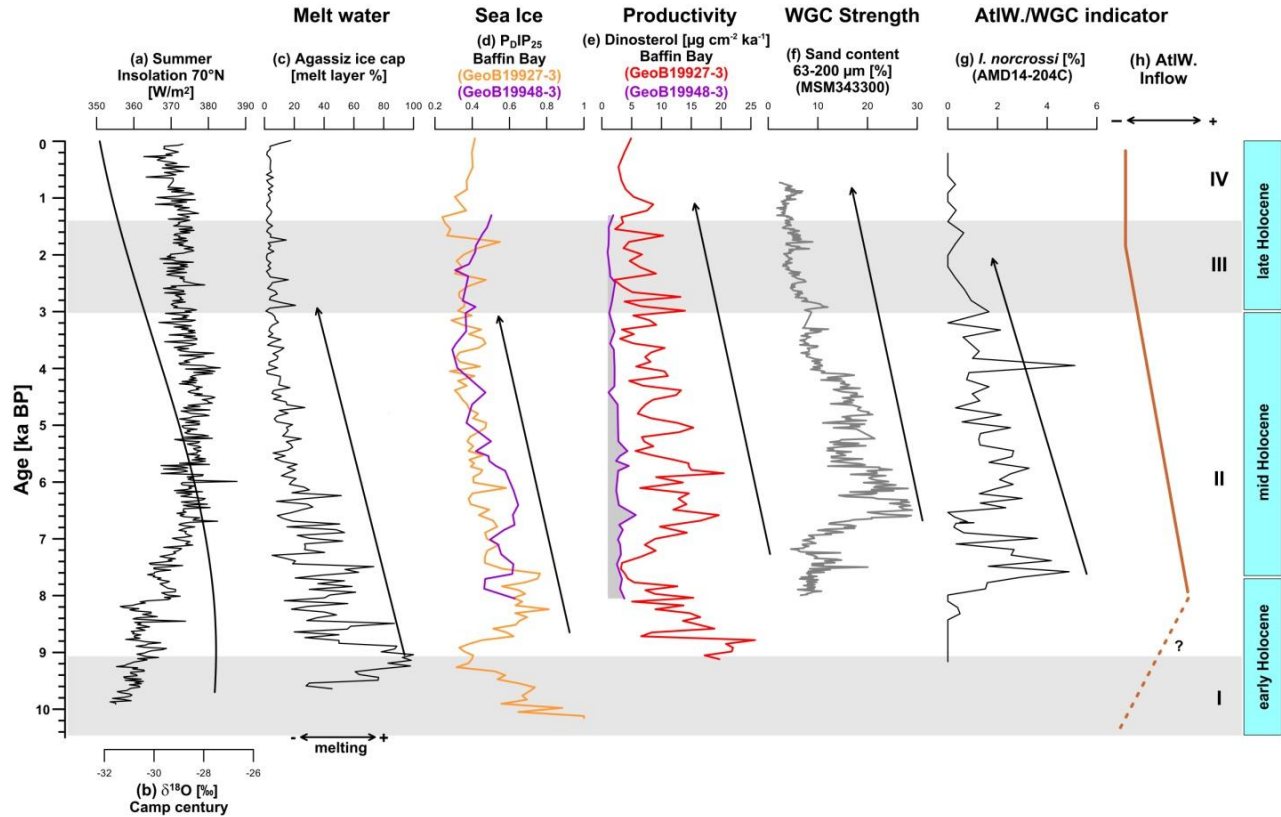
Figure 5.10: Comparison of selected proxies for sea ice and productivity from Baffin Bay with proxies for the inflow of warm Atlantic Water (AtlW.), WGC strengths and/or melt water from circum Baffin Bay areas (a) summer insolation at 70°N (Laskar et al., 2004), (b) Camp Century δ^{18}O record (Vinther et al., 2009), (c) Agassiz melt layer record (Fisher, 2003), (d) sea ice and (e) productivity (dinosterol accumulation rate) data from cores GeoB19927-3 (Saini et al., 2020) and GeoB19948-3 (this study) in Baffin Bay, (f) Core MSM343300 (Perner et al., 2012), (g) Core AMD14-204C (Hansen et al., 2020), and (h) qualitative reconstruction of AtlW. inflow into northeastern Baffin Bay. I to IV represent different environmental periods shown in the maps of Fig. 5.13, based on our proxy records. Arrows indicate decreasing/increasing trend in proxy records.

5.5.1 Deglacial to early Holocene (11.5-7.6 ka BP)

Minimum occurrence or even absence of ice algae and phytoplankton biomarkers (cf. Saini et al., 2020) and related variably high P_DIP_{25} and $P_{III}IP_{25}$ indices (Fig. 5.7) at core GeoB19927-3 in Baffin Bay suggests conditions with extensive (spring) SIC with very low primary productivity

prior to ~9.4 ka BP. Previous studies based on marine sediment cores from Baffin Bay have suggested that this region was controlled by cold deglacial conditions prior to ca. 7.6 ka BP, especially during the initial part of the early Holocene (Caron et al., 2019; Georgiadis et al., 2020; Hansen et al., 2020). These generally harsh conditions were further supported by high IRD counts and extensive SIC (>10 months/year) reconstructions from eastern Baffin Bay (core CC70) for the period of ca. 11.5-9.4 ka BP (Gibb et al., 2015; Jennings et al., 2014). Afterwards, a short warm interval marked by a reduction in marginal SIC between ca. 9.4-8.8 ka BP followed, based on biomarkers (core GeoB19927-3) and foraminifera data (core 008P) (Knudsen et al., 2008; Saini et al., 2020). Based on dinocysts assemblages (core LS009), Ledu et al. (2008) also reported the breakup of semi-perennial ice to more seasonal-type SIC at ~9.4 ka BP. This might imply a weaker surface to sub-surface WGC influence, albeit higher WGC inflow from ca. 9.4-8.8 ka BP along the SW Greenland margin (cf. Weiser et al., 2021), linked to the high melt water influx from the adjacent ice sheets over-capping the Atlantic Water (WGC) (Fig. 5.10c, 5.11) (Harff et al., 2016; Jennings et al., 2019; Ledu et al., 2010a). A strong decrease in summer SIC is also reported in the north Iceland shelf and the Fram Strait area (Fig. 5.12c, d) in this period which might be related to intensified inflow of warm Atlantic Water (Justwan and Koc, 2008; Müller and Stein, 2014; Syring et al., 2020). Thereafter, surface ocean conditions marked by increased SIC and decreased marine productivity between ~8.8-7.6 ka BP in Baffin Bay (core GeoB19927-3) followed, probably caused by the opening of Nares Strait and the inflow of cold Polar Water into Baffin Bay (Fig. 5.13b) (Georgiadis et al., 2018; Jennings, 1993; Jennings et al., 2019; Saini et al., 2020).

However, prior to ~9.1 ka BP, the surface and subsurface conditions in the NE Labrador Sea (core GeoB19905-1) are characterized by the absence of ice algae biomarkers (Fig. 5.6f) as well as by extremely low accumulation rates of $CaCO_3$ and phytoplankton biomarkers (Fig. 5.11f, g). Note, however, some peaks in dinosterol values in µg/gTOC (Fig. 5.11e) are primarily due to the extremely low TOC content and may not represent the absolute content in the sediments (see, Supplementary Fig. S5.4c), therefore, we interpreted their accumulation rates (Fig. 5.11f) for absolute productivity. These (spring, summer and autumn) ice-free, albeit low primary productivity conditions might be related to the limited presence of warm Atlantic Water in the surface waters together with relatively high deglacial melt water discharge (Fig. 5.11c, h; Weiser et al., 2021) from the adjacent ice sheets (Fig. 5.13a). Such conditions might be attributed to the

rapid deglaciation of the Greenland ice sheet (GIS) (Andrews et al., 1999; Briner et al., 2016). Based on dinocysts reconstructions in the vicinity (core SA13-ST3), Allan et al. (2021) have reported generally low sea ice cover (<6 months/year) (Fig. 5.7b), mainly in winter months only. The occurrence of dinocyst P. dalei. at core CC70 off Disko Bugt, generally associated with large seasonal gradients from cold winters to mild summers and related to salinity fluctuations induced by melt water discharge from the retreating ice sheets (GIS), also indicates colder conditions and a weaker influence of the Atlantic Water (WGC) in central Baffin Bay region (Gibb et al., 2015), in agreement with our reconstructions in the Labrador Seas (Fig. 5.11i, 5.13a, 14b).

In the interval after ~9.1 ka BP, the NE Labrador Sea (core GeoB19905-1) is marked by an increase in the accumulation rates of $CaCO_3$ and phytoplankton biomarker dinosterol as well as the absence of ice algae biomarkers, all pointing towards increased marine productivity and ice-free conditions, which might correlate with the onset of the Holocene Thermal Maximum (HTM) conditions (Kaufman et al., 2004) (Fig. 5.6, 5.11). Maximum occurrence of foraminifera from the same core (GoeB19905-1; Fig. 5.6) in this interval also points towards the increased surface to subsurface productivity. This might be also related to the disappearance of winter sea ice, which may have released an additional input of sympagic carbon to the water column further driving high marine productivity (Yunda-Guarin et al., 2020). This increased productivity conditions were most likely associated with a strong inflow of Atlantic Water and a decreased melt water input (Fig. 5.11c, h; Weiser et al., 2021) and therefore, strengthened WGC influence from ~9.1 ka BP onwards (Fig. 5.13b) penetrating up to northern Baffin Bay (Lloyd et al., 2005; Saini et al., 2020). Based on an increase in salinity and reduction in SIC from the outer shelf of Disko Bugt (core CC70), Jennings et al. (2014) and Gibb et al. (2015) suggested diminution of GIS melt water input into the West Greenland areas. This rapid retreat of the GIS ice margin, thinning of ice sheets and spring-autumn ice-free conditions related to the strong oceanic forcing and high summer insolation in the early Holocene correspond well to the significant climate warming (Lloyd et al., 2005; Renssen et al., 2012; Vinther et al., 2009), widely recognized in the North Atlantic and western Arctic (Kaufman et al., 2004). Syring et al. (2020) and Müller and Stein (2014) also implied reduced SIC and increased productivity conditions (Fig. 5.12), as a result of strong inflow of warmer Atlantic Water in the Fram Strait area (Werner et al., 2016), in agreement with our reconstructions from the eastern margin of the Labrador Sea and Baffin Bay.
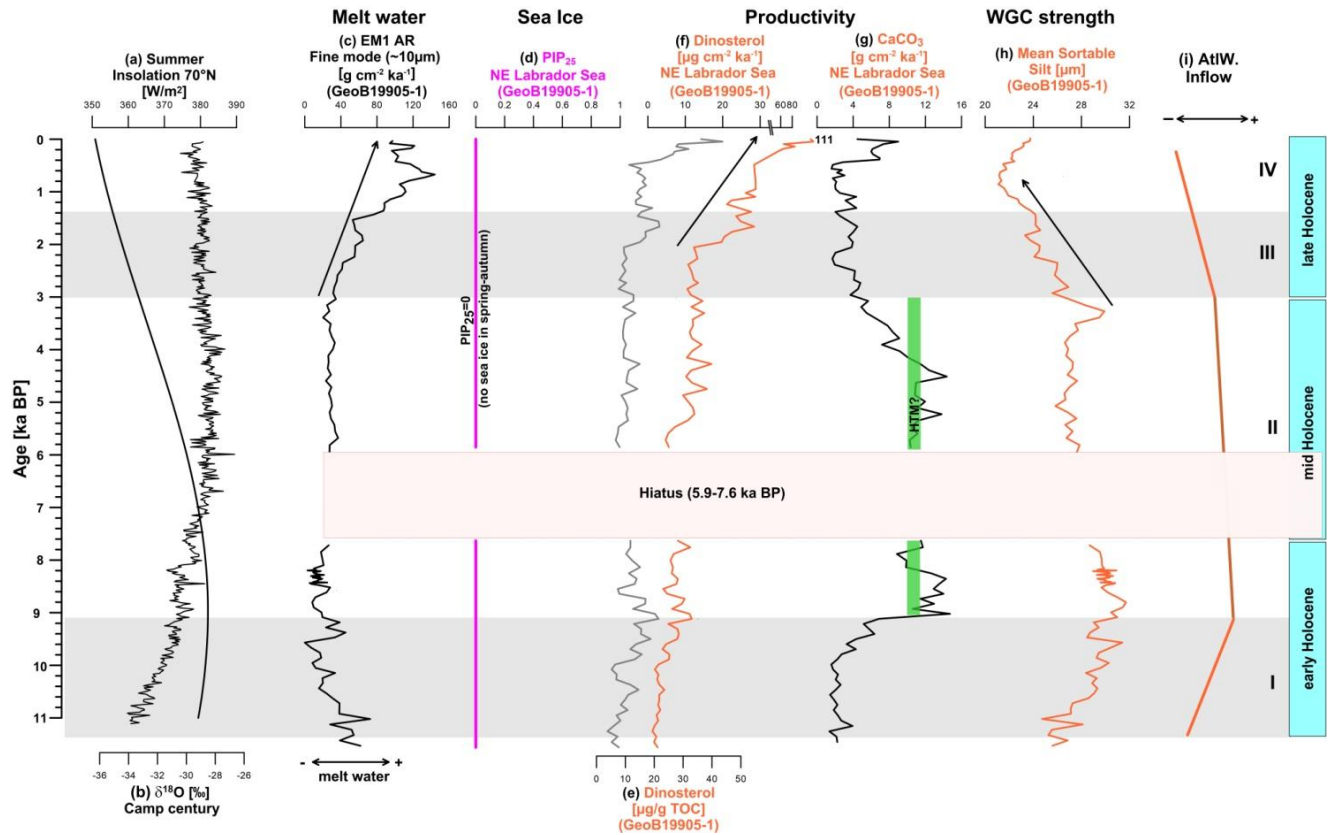
Figure 5.11: Comparison of selected proxies for sea ice, productivity and current strengths from the NE Labrador Sea with proxies for the inflow of warm Atlantic Water (AtlW.), WGC strengths and/or cold melt water (a) summer insolation at 70˚N (Laskar et al., 2004), (b) Camp Century $\delta^{18}O$ record (Vinther et al., 2009), (c) Core GeoB19905-1 fine grain size mode AR (EM1) accumulation rate (Weiser et al., 2021), (d) Core GeoB19905-1 sea ice (PIP_{25}=0), (e) Core GeoB19905-1 dinosterol [µg/g TOC], (f, g) Core GeoB19905 productivity (dinosterol and $CaCO_3$; accumulation rates), (h) Core GeoB19905-1, $\overline{SS}$ (mean sortable silt) (Weiser et al., 2021), and (i) qualitative assessment of the AtlW. inflow into the NE Labrador Sea. A green bar indicates the maximum occurrence of foraminifera in core GeoB19905-1 (Weiser et al., unpublished data) that might correlate with the HTM-like conditions in the mid Holocene (cf. discussion for more explanation). I to IV represent different environmental periods shown in the maps of Fig. 5.13, based on our proxy records. Arrows indicate decreasing/increasing trend in proxy records.
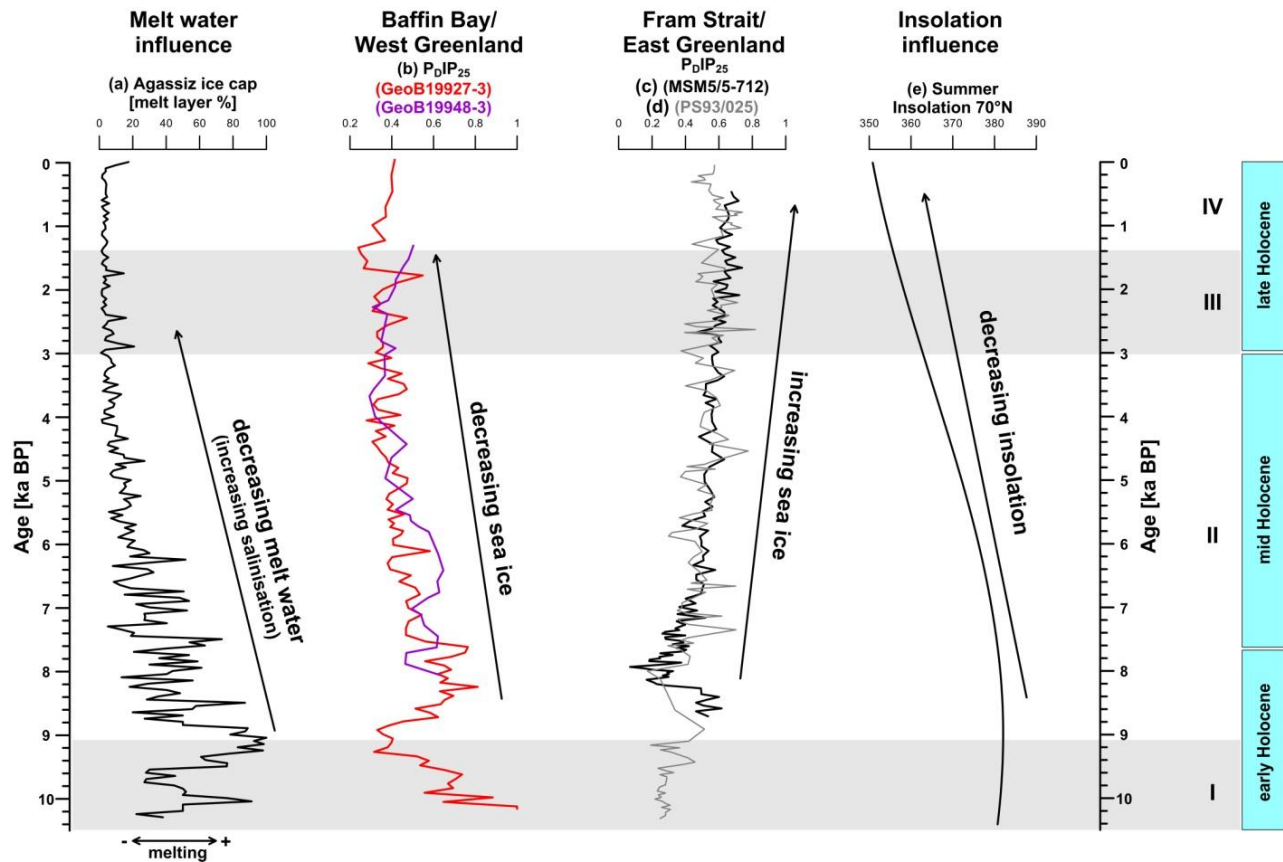
Figure 5.12: Comparison and downcore variations of sea ice conditions in Baffin Bay and Fram Strait area (a) Agassiz melt layer record (Fisher, 2003), (b) Core GeoB19927-3 (Saini et al., 2020), (c) Core MSM5/5-712 (Müller et al., 2012), (d) PS93/025 (Syring et al., 2020) and (e) summer insolation at 70˚N (Laskar et al., 2004).
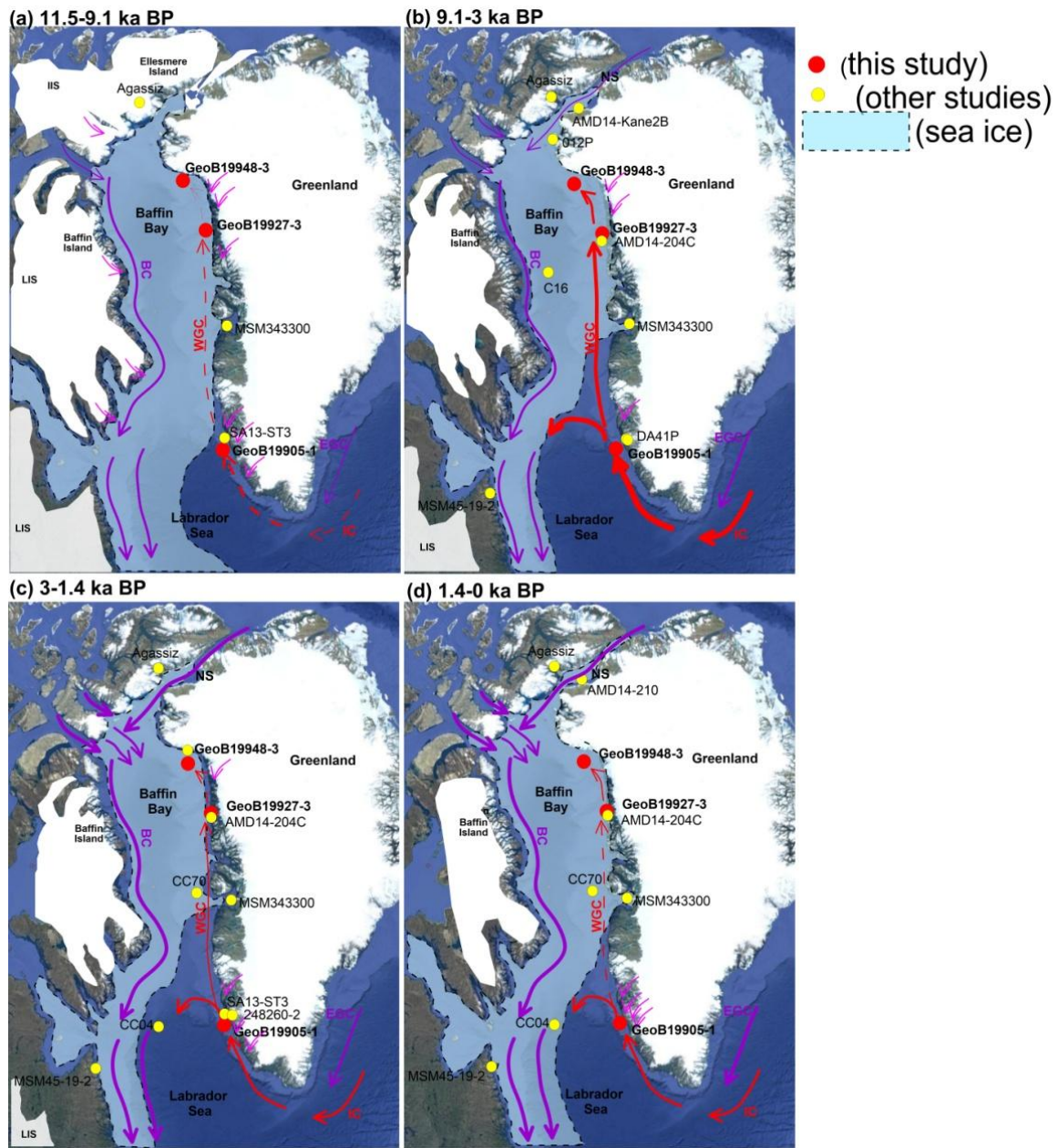
Figure 5.13: Schematic oceanographic conditions in Baffin Bay and the Labrador Sea for four time intervals (a-d) during Holocene from 11.5 ka to present based on this and previous studies from the area: core MSM343300 (Moros et al., 2016; Perner et al., 2012), core 012P (Knudsen et al., 2008; Levac et al., 2001), core AMD14-204C, AMD14-210 and GeoB19927-3 from Melville Bugt (Caron et al., 2019; Hansen et al., 2020; Saini et al., 2020), core AMD14-Kane2B (Georgiadis et al., 2020), core DA41P, SA13-ST3 and 248260-2 from NE Labrador Sea (Seidenkrantz et al., 2013a, b; Allan et al., 2021), core CC04 and CC70 (Gibb et al., 2015), and core MSM45-19-2 (Lochte et al., 2019). Red and blue arrows indicate warmer and colder ocean currents whereas solid (or thick) and dashed (or thin) arrows indicate stronger or weaker current strengths. The magenta arrows indicate melt water inflow to the core-site.
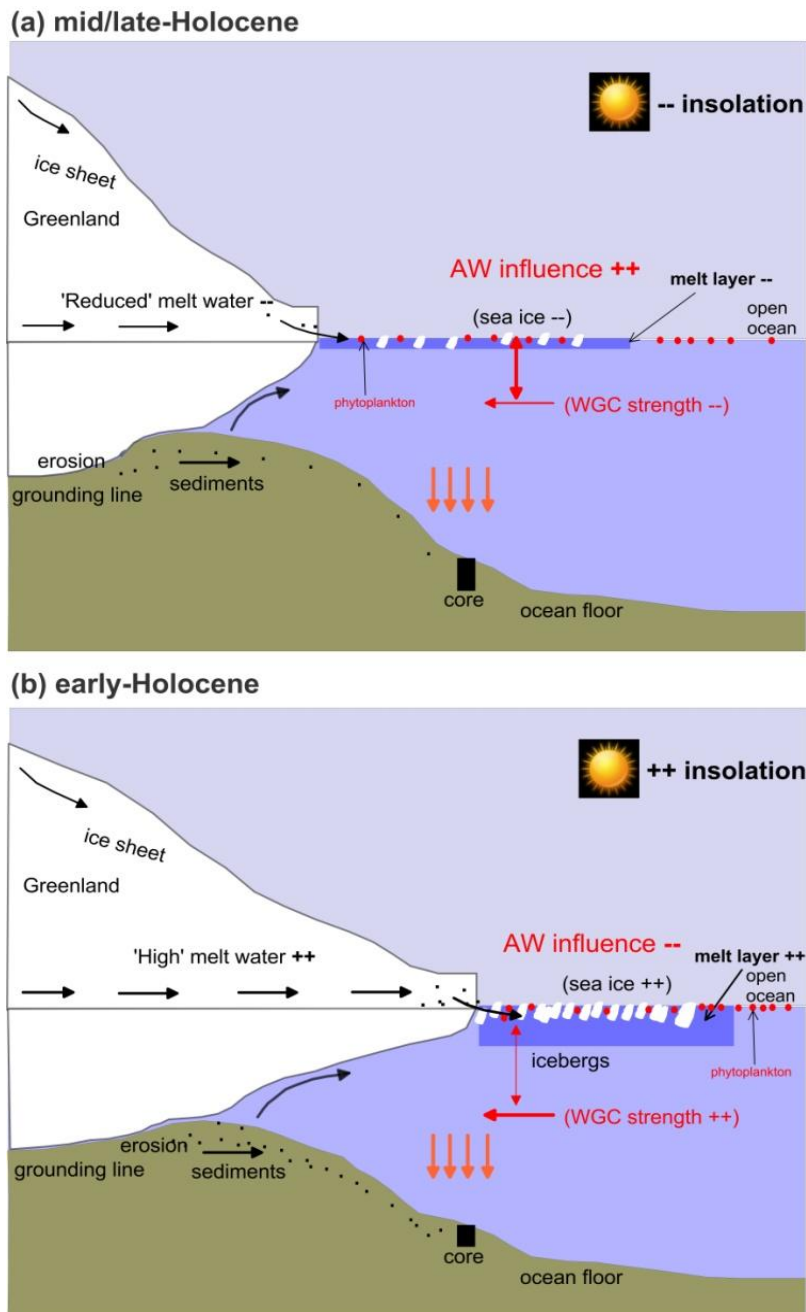
Figure 5.14: Generalized sketch of the large scale hydrographic variations in Baffin Bay area, reflected by changes in the Atlantic Water inflow, sea ice cover, insolation and melt water discharge. Note the relative changes in Atlantic Water (AW) influence as a result of changing melt water layer thickness during (a) mid-to-late Holocene and (b) early Holocene. A thick melt water layer causes decreased influence of warm Atlantic Water (AW) to the surface, thereby increased sea ice and decreased primary productivity in the early Holocene, even though WGC strengths are stronger, and vice versa. (cf. Weiser et al. (2021) for detailed explanation).

5.5.2 Mid Holocene- transition to full interglacial conditions (7.6-3.0 ka BP)

During the mid Holocene near 7.6 ka, SIC and primary productivity started to decrease in Baffin Bay (cores GeoB19927-3 and GeoB19948-3) (Fig. 5.10). This reduction in SIC was likely accompanied by strongly reduced melt water input, causing increased salinity (Fig. 5.12), despite a decrease in Atlantic Water inflow (Fig. 5.11h; Weiser et al. 2021). In sum, this can be explained, when assuming an increased influence of Atlantic Water (Fig. 5.14a) on the surface waters. Short-term (cyclic) changes of minima and maxima in SIC are evident after ~7.6 ka BP in Baffin Bay, displayed by PIP_{25} indices (Fig. 5.7f, g) at core GeoB19927-3. These reoccurring spring ice-edge conditions based on simultaneous peaks in accumulation rates of IP_{25} and the phytoplankton biomarkers brassicasterol and dinosterol (see, Supplementary Fig. S5.2) are possibly related to oscillations in the ice melt influx and the influence of the WGC in the surface waters (Caron et al., 2019; Hansen et al., 2020). Additionally, the P_DIP_{25} and $P_{III}IP_{25}$ indices along this north-south transect in eastern Baffin Bay (core GeoB19927-3, GeoB19948-3, AMD14-Kane2B) (Fig. 5.7) indicate a sharp decline in SIC starting from ~7.6-6.3 ka BP. Based on dinoflagellate cyst data at core CC70, Gibb et al. (2015) reported an increased winter SST at ~7.6 ka BP associated with the strengthening of the warmer Atlantic Water influence that might support our reconstruction. Interestingly, dinocysts based sea ice reconstructions from Disko Bugt (core MSM343310) in eastern Baffin Bay exhibit a similar reduction in SIC from 7.5-7.1 ka BP (cores GeoB19927-3, GeoB19948-3, AMD14-Kane2B). However, different reservoir ages (few hundreds to sometimes thousand years) may limit the exact age correlation (Fig. 5.7) (Caron et al., 2019; Georgiadis et al., 2020; Hansen et al., 2020; Saini et al., 2020). On the other hand, the reduced SIC may have occurred earlier in the southern areas of Baffin Bay transect (7.5-7.1 ka BP) before penetrating northwards up to the Kane Basin. The decreased SIC after ~7.6 ka BP (Fig. 5.7) together with high Atlantic Water influence, associated with a decreased inflow of melt water (Fig. 5.10c, 5.13b, 5.14a) might suggest significant warming of the subsurface conditions corresponding to the HTM-like conditions observed in NE Baffin Bay throughout the mid Holocene (Fig. 5.10b) (Gibb et al., 2015; Lloyd et al., 2005). Several records from circum Greenland, the Canadian Arctic Archipelago, and Svalbard areas also suggested a similar increased influence of Atlantic Water (WGC, IC) in the mid Holocene since ~7.6 ka BP (Dyke et al., 1996b; Jennings et al., 2011a; Justwan et al., 2008; Ouellet-Bernier et al., 2014). Note, in contrast to sea ice records from the Fram Strait area (cores MSM5/5-712 and PS93/025)

which seem to follow predominantly the summer insolation trend (Müller et al., 2012; Syring et al., 2020), our records from eastern Baffin Bay indicate a dominant influence of melt water influx on sea ice formation throughout the Holocene (Fig. 5.12).

Furthermore, a general northwards increase in SIC is shown by the IP_{25} vs. biomarker brassicasterol plot as well as PIP_{25} indices (Fig. 5.7, 5.9). A contemporaneous decrease in primary productivity is indicated by the biomarker dinosterol accumulation rates as well as dinocyst based reconstructions along the studied N-S transect (Fig. 5.8 and references therein). These trends in SIC and primary productivity situations might be linked to the fading Atlantic Water inflow (WGC) northwards and/or due to interaction with southwards flowing polar currents (BC) along the Canadian Arctic. These trends may also be related to the seasonal differences in light and sea ice conditions as a function of latitude as the timing and extent of the ice and phytoplankton productivity vary from April to late summers from the south towards higher latitudes (cf. Wassmann et al., 2020 for a detailed explanation).

For the mid Holocene between 5.9-3.0 ka BP i.e., after the hiatus, our records from core GeoB19905-1 off NE Labrador Sea show ice-free conditions in spring-autumn as displayed by the continued absence of ice algae biomarkers (IP_{25}=0) (Fig. 5.6f). Dinosterol accumulation rates show a slight increase in this interval, however, $CaCO_3$ accumulation rates remained rather high until about 4 ka BP (Fig. 5.11f, g), suggesting subsurface conditions characterized by high biological (carbonate) productivity. This interpretation is supported by the continuously maximum occurrence of foraminifera in the same core GeoB19905 (Fig. 5.11; Weiser et al., unpublished data). Based on dinocyst data in the vicinity core SA13-ST3 (Fig. 5.7b, 5.8b), Allan et al. (2021) have reported subsurface conditions characterized by a slight decrease in (winter) SIC (<4 months/year) and a variably high summer primary productivity. Overall, this may indicate persistent warm subsurface conditions in this area corresponding to the final stage of the HTM. Moros et al. (2016) (core MSM343300) and Seidenkrantz et al. (2013b) (core 248260-2) also suggested warm surface water conditions, in combination with low melt water influx from the GIS in eastern Baffin Bay area. Based on terrestrial evidences from SW Greenland and NE Canada, a rather late HTM lasting until about 4.0 ka BP has been suggested (Fredskild, 1985 a, b; Kaplan et al., 2002; Moros et al., 2006; Willemse and Tornqvist, 1999). Based on the foraminifera records from offshore East Greenland, Jennings et al. (2002) described a strong

influence of Atlantic Intermediate Water during the mid Holocene lasting until about ~4 ka BP. In the Ameralik Fjord (cores DA41P, 248260-2), close to our core site (GeoB19905-1), relatively warm subsurface conditions linked to strong WGC influence have also been reported, in agreement with our study (Moller et al., 2006; Seidenkrantz et al., 2007). Additionally, based on mean sortable silt (grain-size) data on the same core (GeoB19905-1; Fig. 5.11h), Weiser et al. (2021b) showed a slight decrease in the WGC strength during the mid-Holocene. However, a distinct decrease in the melt water discharge along the SW Greenland margin in this interval (Gibb et al., 2015; Holland et al., 2008; Ren et al., 2009) may have substantially increased subsurface salinity (Allan et al., 2021), thus maintaining a strong influence of warm Atlantic Water (WGC) to the ocean surface. Furthermore, biomarker proxies, including sediment composition (grain-size) data, have been also previously successfully applied for subsurface and bottom water conditions in the northern High latitude areas, i.e. Denmark Strait (Andrews et al., 2020).

Towards the final stage of the mid Holocene (~4-3 ka BP) at core GeoB19905-1 off the Labrador Sea, the accumulation rates of $CaCO_3$ display a sharp decrease whereas dinosterol accumulation rates remain unchanged (Fig. 5.11f, g). This suggests changes in subsurface conditions characterized by a decrease in biological (carbonate) productivity possibly linked to a decline in the WGC strengths (Fig. 5.11h; core GeoB19905-1). This change may coincide with the onset of Neoglacial cooling, widely reported around Greenland areas (Briner et al., 2010; Krawczyk et al., 2017; Levac et al., 2001; Long and Roberts, 2003; Müller et al., 2012; Perner et al., 2012; Schweinsberg et al., 2017). Dinocyst based reconstructions in the vicinity core SA13-ST3 also indicate a decrease in summer primary productivity in this interval (Allan et al., 2021) (Fig. 5.8b), in agreement with the results of our study. Moros et al. (2004) also argued for a period (4-3 ka BP) of climate instability and significant fluctuation in EGC and IC strengths in the east Greenland margin leading to cooling. Several lake sediment records in the vicinity of southwest Greenland also showed renewed ice growth and enhanced glacier activity starting ca. 4 ka BP (Larsen et al., 2017), supporting the onset of Neoglacial cooling in this time interval.

5.5.3 Late Holocene changes in sea-surface conditions (3-0 ka BP)
Surface water cooling along the West Greenland coast during the late Holocene Neoglacial period is attributed to the variability in the strength of the Atlantic (IC) versus Arctic (EGC, BC)

currents (Andresen et al., 2011; Moros et al., 2006; Ouellet-Bernier et al., 2014; Seidenkrantz et al., 2007). Interestingly, our sea ice (IP_{25}) and phytoplankton biomarkers (dinosterol, HBI III), and related P_DIP_{25} and $P_{III}IP_{25}$ indices from Baffin Bay show a decreased SIC (Fig. 5.7, Supplementary Fig. S5.2) and apparently do not show a clear Neoglacial cooling trend as observed in other records. Low accumulation rates of all biomarkers during the late Holocene recorded at cores GeoB19948-3 and GeoB19927-3 (Fig. 5.5, Supplementary Fig. S5.2) from eastern Baffin Bay sites may be caused by stratified conditions associated with an enhanced input of fresh water (Fig. 5.13c, d) hampering productivity. Based on the increased abundance of agglutinated foraminifera species at core AMD14-204C and MSM343300, Hansen et al. (2020) and Perner et al. (2012) suggested enhanced Arctic Water influx into Baffin Bay and strongly stratified conditions during the late Holocene. The reduction in SIC might be also attributed to strong sea ice interactions with the local fjords which can also hamper ice growth (Ribeiro et al., 2017). Additionally, moderate PIP_{25} values (0.2-0.6) between 1.8 and 1.2 ka BP at cores GeoB19927-3 and GeoB19948-3 (Fig. 5.7) indicate a reduced sea ice cover, which might be also associated with a positive NAO mode and related warmer subsurface conditions in eastern Baffin Bay area (Andresen et al., 2011; Gibb et al., 2015; Moros et al., 2006; Trouet et al., 2009). Increased SSTs were also suggested near the east Greenland shelves at ca. 1.8-1.2 ka BP (Knudsen et al., 2004; Roncaglia and Kuijpers, 2004). The short-term warming in the North Atlantic and the in-phase relationship between sea ice and NAO mode has been previously reported (Ljungqvist, 2010; Saini et al., 2020; Trouet et al., 2009). However, after ~1.4 ka BP a slight increase in SIC (PIP_{25}) and a decline in productivity (dinosterol) (Fig. 5.10d, e) may indicate Neoglacial cooling observed elsewhere (Fig. 5.13d and references therein). Based on the increase in Arctic Water indicator dinocysts (*I. minitum*) (core AMD14-204C) during the last ~1.4 ka, Caron et al. (2019) have described an increase in SIC and colder conditions in eastern Baffin Bay related to Neoglacial cooling. This is further supported by enhanced driftwood findings in the Canadian Arctic Archipelago, possibly carried along by the strengthened Polar Water (i.e. BC) masses (Dyke et al., 1997). This increase in SIC during the Neoglacial period is in agreement with the reconstructions from the northern Baffin Bay (Levac et al., 2001) and the eastern Fram Strait area (Fig. 5.12) (Müller and Stein, 2014; Syring et al., 2020).

However, in the NE Labrador Sea, after 3 ka BP, HTM-like conditions were followed by surface and subsurface conditions characterized by the absence of ice algae biomarkers and significantly

decreased $CaCO_3$ accumulation rates, albeit very high accumulation of phytoplankton biomarker dinosterol (Fig. 5.6, 5.11) (core GeoB19905-1). Based on the end-member grain-size analysis at the same core (GeoB19905-1), Weiser et al. (2021) documented a strong increase in the accumulation of poorly-sorted fine-grained sediments (Fig. 5.11c) presumably originating from the Neoglacial ice margin advances. In such finer-grained sediments organic matter may become enriched (cf., Knies and Stein, 1998; Fahl and Stein, 2007; Iversen and Robert, 2015) as documented in elevated TOC values (Fig. 5.4) and high accumulation rates of organic carbon (Fig. 5.6b). This may have resulted in more labile organic matter preservation in the sediments. Another explanation for the increased accumulation rates of the phytoplankton biomarker (Fig. 5.11f) in the late Holocene might be the increased nutrient supply (e.g. Fe, silica) associated with the enhanced local melt water discharge (Arrigo et al., 2017; Bhatia et al., 2013; Cape et al., 2019; Hawkings et al., 2015). Based on exploration studies from nearby Sinarsuk deposit, Grammatikopoulos et al. (2002) and Secher (1980) found a significant amount of magnetite in the host rock which might be a potential source of high Fe contents recorded in the late Holocene section of the core GeoB19905-1 (Weiser et al., 2021).

The last 0.4 ka (upper ~100cm, core GeoB19905-1, Fig. 5.6) are characterized by very high phytoplankton biomarker accumulation rates that might be explained on one hand by increased phytoplankton productivity/ increased preservation. On the other hand, the topmost maximum value and its downcore decrease may represent diagenetic alterations in the uppermost centimetres (cf. Fahl and Stein, 2012; Belt & Müller, 2013). The drop in productivity biomarkers (Fig. 5.6d, e) evident at about 0.3 ka BP (ca. 1700 AD) may be correlated with the Little Ice Age (LIA), widely reported in the Western Europe and North Atlantic regions (Jones and Mann, 2004; Ljungqvist, 2010; Spielhagen et al., 2011). However, more high-resolution reconstructions are needed to resolve the decadal to centennial-scale climate events.

5.6 Conclusions

Organic geochemical and biomarker investigation of ^{14}C-AMS-dated sediment cores (GeoB19948-3, GeoB19927-3, GeoB19905-1) from a N-S transect of the eastern Baffin Bay-Labrador Sea margin was used for environmental and paleoceanographic reconstruction covering the Holocene period (last ~11.5 ka). Our data based on cores GeoB19948-3 and GeoB19927-3 suggest that Baffin Bay was seasonally covered by sea ice during the last ~10.1 ka (Fig. 5.7). In

contrast, predominantly ice-free (spring and/or autumn) conditions were observed during the last 11.5 ka in the NE Labrador Sea (core GeoB19905-1). We note a general increase in primary productivity from north to south in the studied transect, which could be linked to the general decrease in sea ice cover observed along the N-S transect throughout the Holocene (Fig. 5.7, 5.8).

Extended SIC and very low primary productivity conditions prior to ~9.4 ka BP in the early Holocene were succeeded by a short interval of persistent and variable to marginal sea ice condition and associated increased primary productivity between 9.4 to 8.8 ka BP in eastern Baffin Bay, possibly linked to the limited subsurface presence of Atlantic Water as WGC. Thereafter, a short period of enhanced SIC and decreased primary productivity was recorded between 8.8 and 7.6 ka BP, which might be related to the opening of the Nares Strait and subsequently increased influence of Arctic Water masses and decreased WGC strengths. However, in the NE Labrador Sea, conditions remained mostly ice-free in spring-autumn, albeit with low primary productivity in the early Holocene due to the increasing but limited influence of Atlantic Water (WGC), in combination with the high deglacial melt influx.

A transition towards decreased SIC and reduced productivity, as well as reoccurring ice-edge conditions, is evident in the mid Holocene (~7.6-3 ka BP), possibly caused by the short-term (cyclic) changes in the WGC influence associated with ice melting, probably representing HTM-like conditions. This decrease in SIC is synchronous to the decrease in the melt water inflow leading to the salinisation of surface waters in Baffin Bay area. The HTM-like conditions in the mid Holocene accompanied by the final retreat of the GIS, are also recorded in the NE Labrador Sea, displayed by spring-autumn ice-free ($PIP_{25}=0$) conditions together with an increased accumulation of open-water phytoplankton biomarker proxies.

Our combined sea ice records from Baffin Bay do not exactly correlate with the Neoglacial cooling trend observed elsewhere during the late Holocene. Instead, the surface conditions can be characterized by a decrease in SIC and primary productivity, linked to stratification caused by an enhanced influx of Polar Water masses. However, in the NE Labrador Sea, surface conditions were characterized by (spring-autumn) ice-free conditions with a strong decrease in carbonate productivity during the last ca. 4 ka, in line with decreased WGC strengths and/or enhanced

advection of cold Arctic Water masses and increased melt water inflow linked to the Neoglacial cooling.

Acknowledgements

6   Holocene variability in terrigenous organic carbon input along the eastern Baffin Bay-Labrador Sea margin

Jeetendra Saini[1], Ruediger Stein[1,2], Kirsten Fahl[1]

[1]Alfred Wegener Institute Helmholtz Centre for Polar and Marine Research, Bremerhaven, Germany

[2]Marum-Center for Marine Environmental Sciences, University of Bremen, Bremen, Germany

Abstract

A better understanding of the past variability in terrigenous organic carbon input and climate change was achieved by investigating organic bulk parameters (TOC, TOC/N and $\delta^{13}C_{org}$), specific biomarkers (ß-sitosterol and campesterol), and their accumulation rates using three sediment cores (GeoB19948-3, GeoB19927-3, GeoB19905-1) from the eastern Baffin Bay-Labrador Sea margin. The biomarker data in all these cores shows a high amount of terrigenous organic carbon deposition during the early Holocene period between 11.5-8 ka BP. In the mid Holocene period between 8-3 ka BP, our combined data show decreasing accumulation rates of terrigenous organic carbon in Baffin Bay-Labrador Sea, a part of warm Holocene Thermal Maximum (HTM)-like conditions characterized by a decrease in ice cover, melt water discharge and reduction in sediment supply due to decreased strength of the WGC. During the last ca. 3 ka, reduced accumulation rates of terrigenous (and marine) biomarkers in Baffin Bay are related to the Neoglacial cooling. However, the NE Labrador Sea (core GeoB19905-1) is characterized by increased preservation/accumulation of terrigenous organic matter during the last 3 ka and related to high fine-grained siliciclastic material deposition caused by decreased current strengths, however, increased terrigenous organic carbon related to regrowth of Glaciers linked to Neoglacial cooling cannot be ruled out.

6.1 Introduction

Arctic regions have shown dramatic changes over the recent decades, including increased annual river discharge, open-water areas over the Arctic shelves and a decrease in summer and winter sea ice cover (SIC) (Fichot et al., 2013; Peterson et al., 2002; Serreze et al., 2007a; Stroeve et al., 2012). These changes will probably lead to significant changes in the sedimentary environment and processes controlling terrigenous matter cycling (Wegner et al., 2015). The increased export of terrigenous sediments may also alter the delivery of nutrients and promote marine primary productivity (Retamal et al., 2008). Since the Last Glacial Maxima (LGM), the increased inundation of the Arctic shelves following low sea-level stand, climatically driven changes in fresh water delivery by major rivers, ice sheets and variable SIC led to significant changes in terrigenous sediment supply (Wegner et al., 2015).

The variability in terrigenous organic carbon input into the Arctic Ocean has been the subject of debate for a long time (Schubert and Stein, 1996; Stein and MacDonald, 2004a). The large seasonal input of terrigenous organic carbon ($\sim 12 \times 10^6$ t/a POC) driven by ice, riverine, coastal erosion, aeolian transport is mostly deposited in the near continental shelves and less in the deep seas (Stein, 2008; Stein and MacDonald, 2004a). Sea ice and oceanic currents are assumed to play a dominant role in sediment transport over large distances (Darby et al., 2009; Polyak et al., 2010). The variability in terrigenous organic carbon input allows for simultaneous reconstructions of marine and terrestrial climate conditions, including the possible transport pathways and the fate of organic matter. Thus, understanding the variability in past terrigenous organic matter input is important for assessing modern and future changes, as it can serve as boundary conditions in models for the changing Arctic.

Specific sterols such as ß-sitosterol (24-ethylcholest-5-en-3ß-ol) and campesterol (24-methylcholest-5-en-3ß-ol) are predominantly produced by land vascular plants (Stein and Macdonald, 2004) and often and successfully applied as a proxy for land-derived terrigenous input (Fahl and Stein, 1997; Horner et al., 2016; Kolling et al., 2017; Syring et al., 2020). Long chain n-alkanes, long chain fatty acids and alcohols have been also previously successfully applied to estimate terrigenous organic carbon input in the lake and marine sediments, including Arctic Ocean sediments (Eglinton and Hamilton, 1963; Eglinton and Eglinton, 2008; Fahl and Stein, 1999; Meyers, 1997; Yunker et al., 1995). Furthermore, specific lignin and recently

developed "*Branched and Isoprenoid Tetraether (BIT)*" index may be used as an additional proxy for terrigenous organic carbon input; however, their application might be limited to certain areas only (Hopmans et al., 2004; Stein, 2008). In addition, bulk geochemical proxies such as organic C/N ratio and $\delta^{13}C_{org}$ may also provide useful information to distinguish between terrigenous (higher plant) and marine (algal) organic matter in marine sediments (Hedges et al., 1986; Meyers, 1994; Stein and Macdonald, 2004). A predominant terrigenous source of organic carbon may be inferred in sediments with organic C/N ratio of value higher than 10 and light $\delta^{13}C_{org}$ values of about -23‰ to -27‰ (Fahl et al., 2003; Krishnamurthy et al., 2001; Stein and Macdonald, 2004).
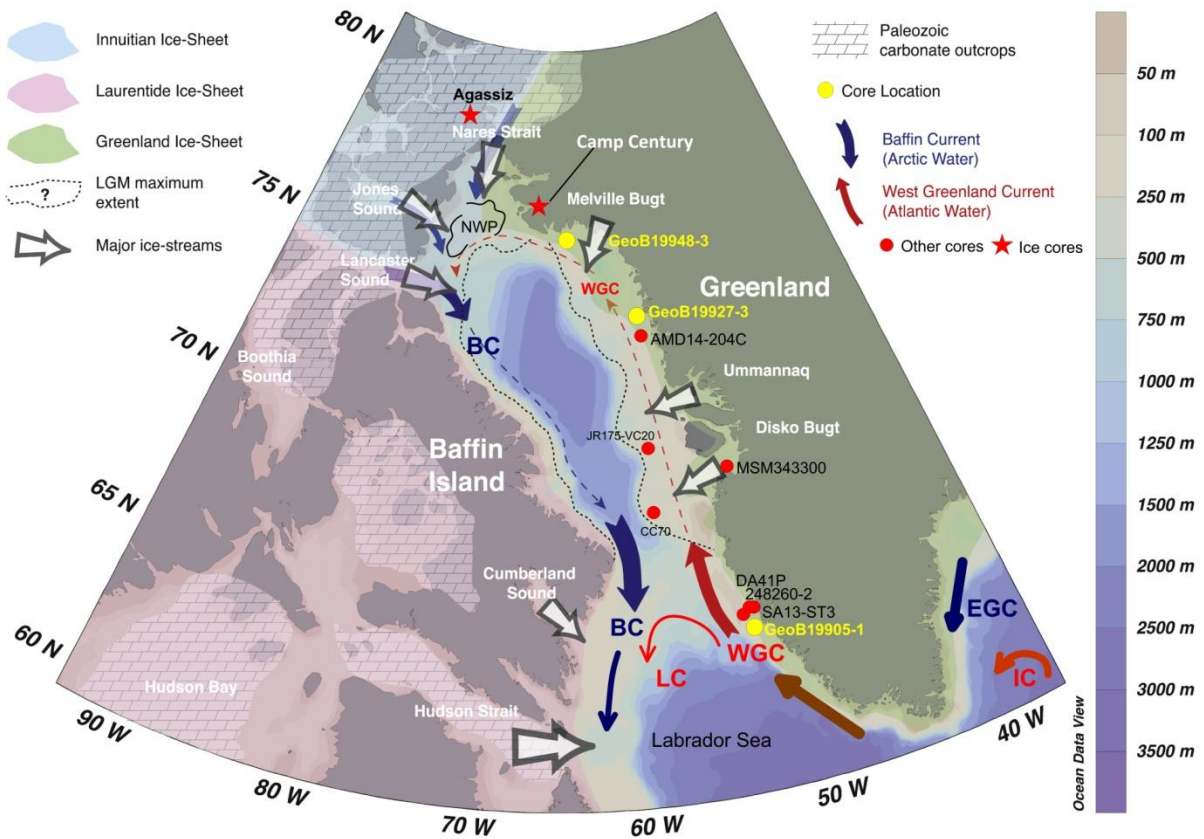

Figure 6.1: Map of Baffin Bay and the Labrador Sea areas with general surface circulation (warm surface current in red and cold polar sourced currents in blue) and locations of sediment cores studied herein, shown as yellow dots, adapted after Simon et al., 2016.

This study concentrates on marine sediment cores collected from a north-south transect of the eastern Baffin Bay and Labrador Sea margin to reconstruct the paleoenvironmental evolution during the Holocene using organic geochemical and biomarker data. Measurements of specific biomarkers (campesterol, ß-sitosterol) and organic geochemical bulk parameters (TOC, TOC/N) and stable carbon isotopes ($\delta^{13}C_{org}$) were carried out on three cores; GeoB19948-3, GeoB19927-3 and GeoB19905-1 (Fig. 6.1) along the western Greenland continental margin and compared with other regional data from around the Labrador Sea and Baffin Bay. Special attention is paid to the high-resolution reconstruction of terrigenous organic matter, mainly documented from the accumulation rates of terrigenous-sourced biomarker sterols.

6.2 Modern environmental setting

The study area lies on the eastern margin of Baffin Bay and the Labrador Sea under the West Greenland Current (WGC) (Fig. 6.1), which flows northwards along the western continental margin of Greenland. The WGC is characterized by advection of both warm, Atlantic-sourced Water (Irminger Current) and cold, polar-sourced water from the Arctic Ocean (EGC) as well as freshwater and icebergs from the Greenland Ice Sheet (GIS). A part of the WGC is deflected westwards towards the Canadian margin just before entering the Davis Strait while the remaining water continues northwards, reaching the northernmost regions of Baffin Bay (Tang et al., 2004). Arctic-sourced cold water along Baffin Island (BC) flows southwards and mixes with Arctic water exiting Hudson Strait forming the Labrador Currents (LC) and finally mixing with the northern branch of the WGC and Irminger Current (IC) (Drinkwater, 1996). Sea ice cover in Baffin Bay and the northwestern Labrador Sea is at its maximum in March and minimum in September, however, the northeastern Labrador Sea remains generally ice-free year-round due to the strong influence of the WGC (NSIDC, 2020; Tang et al., 2004).

6.3 Material and methods

The three cores used in this study were recovered during the Maria S. Merian MSM44 cruise. The cores GeoB19948-3 (75°46.10' N, 64°08.57' W) and GeoB19927-3 (73°35.26' N, 58°05.66' W) were retrieved from northeast Baffin Bay, whereas core GeoB19905-1 (64°21.68' N, 52°57.70' W) from the northeastern Labrador Sea (Fig. 6.1). The lithological visual description and color measurements of core GeoB19948-3 indicates that the upper 280cm mainly consists of olive-grey silty clay homogeneous sediments (Dorschel et al., 2015). Whereas in core

GeoB19927-3, the lowermost part can be described as non-homogenous silt and fine sand sediments embedded with few dropstones. The upper part of core GeoB19927-3, however, can be characterized by homogenous olive-grey silty-clay sediments (Dorschel et al., 2015). In core GeoB19905-1, sediments are mainly composed of olive-grey muds with some sandy layers at the lower part of the core and sharp color transitions displayed by distinct lithological units (LU), for a more detailed description, however, see chapter 2.1.

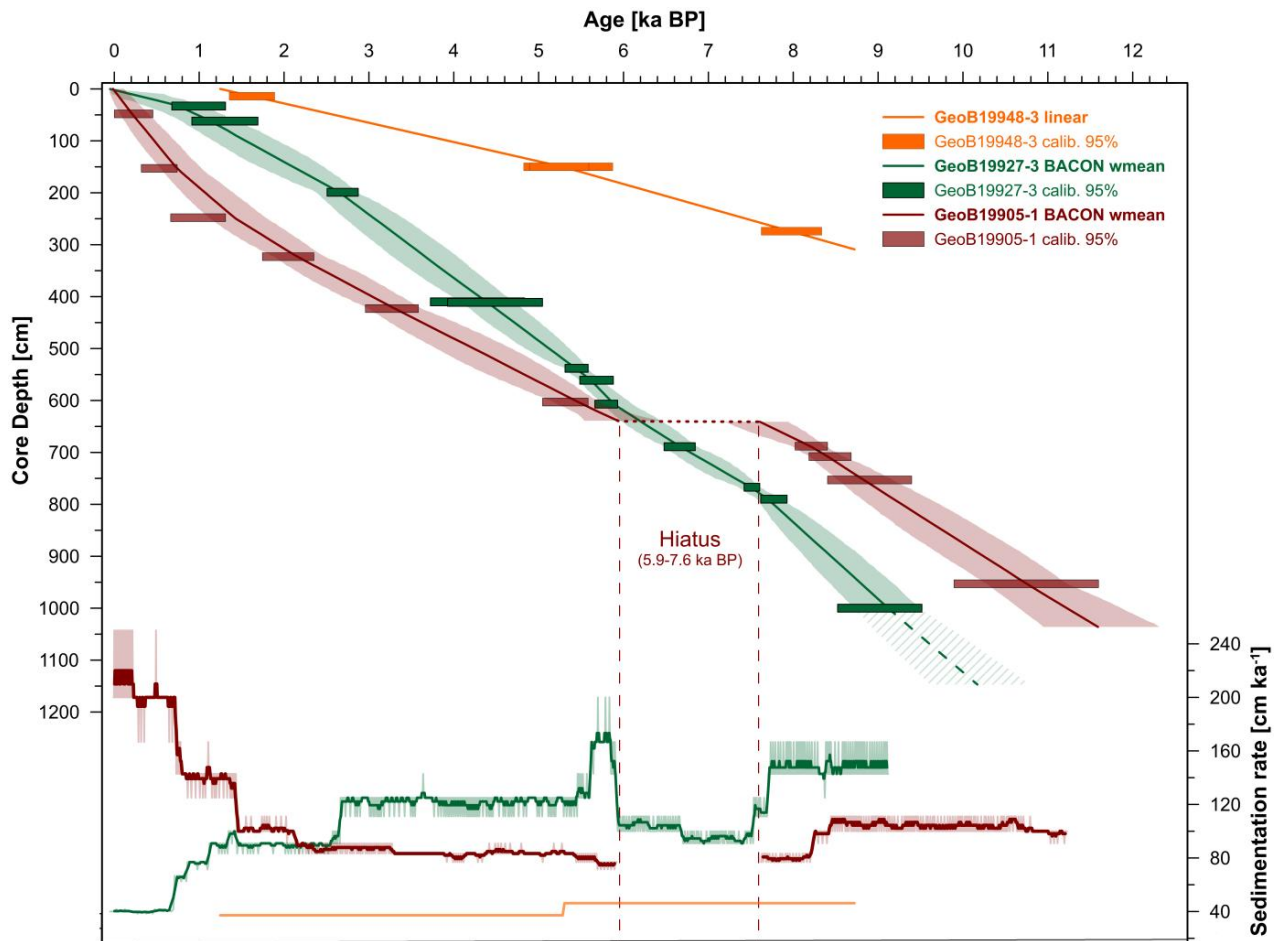Figure 6.2: Age-depth plot of the studied cores; GeoB19948-3, GeoB19927-3 and GeoB19905-1 together with sedimentation rates (cf. Saini et al., submitted; Weiser et al., 2021 for a detailed description).

The chronostratigraphic framework of cores GeoB19948-3, GeoB19927-3 and GeoB19905-1 is based on ^{14}C-radiocarbon dating and has already been described by Saini et al. (2020) and Weiser et al., (2021) (Fig. 6.2).

6.3.1 Organic geochemical bulk parameters (TOC, TOC/N and TOC/N$_{corr}$)

For organic-geochemical analyses, freeze-dried and homogenized subsamples were taken and stored in glass vials at -20 ˚C. Total organic carbon (TOC) and total nitrogen (TN) were analysed by means of *Carbon-Sulfur Analyser CS-800, ELTRA* for TOC and Carbon-Nitrogen-Sulfur Analyzer *Elementar-III, Vario* for TN measurements after carbonate removal by hydrochloric acid (37%, 500 µl). The analytical error of our TOC measurements was within 0.02%.
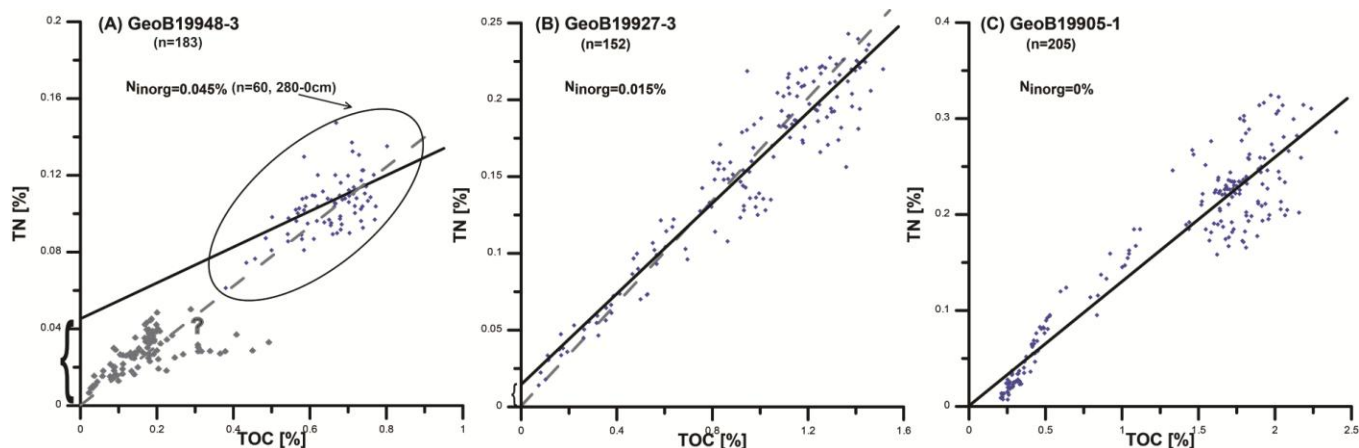
Figure 6.3: Estimation of inorganic nitrogen content by correlating Total organic carbon (TOC) with Total nitrogen (TN). The positive intercept at TOC = 0% (Schubert and Calvert, 2001) provides the inorganic nitrogen fraction (Ninorg).

The TOC/N ratio may be used to distinguish between marine (algae) and terrigenous (vascular land plants); marine algae typically range between 4 and 10 while land vascular plants show values above 20 (Meyers, 1994; Stein and Macdonald, 2004). However, values in a range of 10-20 reflect a mixed signal of terrigenous and marine organic matter sources. Still, the TOC/N ratio should be considered with caution as it may be altered through selective degradation during early diagenesis (Meyers, 1994) and thus should be used in combination with the other environmental proxies such as the stable carbon isotope ratio $\delta^{13}C_{org}$. With low TOC concentration, inorganic nitrogen fraction becomes more significant, and it becomes imperative to determine the inorganic nitrogen (N$_{inorg}$). N$_{inorg}$ can be roughly estimated by correlating TOC vs. TN and calculating the positive TN intercept at TOC = 0% (Schubert and Calvert, 2001). N$_{inorg}$ were subtracted from the TN in order to calculate the organic nitrogen fraction (N$_{corr}$) which was then used for TOC/N$_{corr}$ ratios (for cores GeoB19948-3 and GeoB19927-3) (cf. Schubert and Calvert

2001) (Fig. 6.3A, B). For core GeoB19948-3, only the upper 280cm (n=60) were considered for calculating inorganic nitrogen (N_{inorg}=0.045%; Fig. 6.3A, 'black line'). However, for core GeoB19905-1, the TOC/N ratio (without correction) is used due to negligible inorganic nitrogen (see, Fig. 6.3C).

6.3.2 Stable isotopes ($\delta^{13}C_{org}$)

Organic carbon isotope ($\delta^{13}C_{org}$) analysis of cores GeoB19948-3 and GeoB19927-3 were performed at GEOTOP, University of Quebec at Montreal, Canada using homogenized and weighed samples into (8x5 mm) silver capsules and left for carbonate removal by conc. Hydrochloric acid for 24 hrs. Thereafter, the acidified samples were weighed into a tin foil and wrapped tightly. The determination of $\delta^{13}C_{org}$ was then performed by means of a continuous flow isotope ratio mass spectrometer (Isoprime-100 MS) using the Urea/Air Isotopic laboratory method. Isotope ratios were expressed in delta notation (δ), in per mil (‰), relative to an international reference material (VPDB for $\delta^{13}C$) calculated according to Brand et al. (2014) and Coplen (2011). The error of our $\delta^{13}C$ measurements was at ±0.1‰.

6.3.3 Biomarker sterols (ß-sitosterol and campesterol)

Biomarker analyses were achieved by extracting ~4 g of freeze-dried and homogenized sediment using dichloromethane: methanol (2:1 v/v) as a solvent for ultrasonication (3x15min). Prior to extraction, 9-octylheptadec-8-ene (9-OHD; 0.1 µg/sample), 7-hexylnonadecane (7-HND; 0.076 µg/sample), 5α-Androstan-3β-ol (Androstanol; 10.7 µg/sample) and 2,6,10,15,19,23-Hexamethyltetracosane (Squalane; 3.2 µg/sample) were added for the quantification of biomarkers. The extracts were separated by open silica (SiO$_2$) column chromatography with *n*-hexane (5 ml) and ethyl-acetate: *n*-hexane (9 ml, 2:8 v/v) as eluent into hydrocarbon and sterol fraction, respectively. The sterol fraction was silylated using 200 µl BSTFA (bis-trimethylsilyl-trifluoroacet-amide) (60˚C, 2 h).

Gas chromatography-mass spectrometer (GC-MS) was used to qualify and quantify the sterol fractions. The quantification of the sterols (quantified as trimethylsilyl ethers) was carried out with a GC Agilent 6850 (30 m DB-1MS column, 0.25 mm id, 0.25 µm film) coupled to an Agilent 5975C VL MSD mass selective detector. GC measurements were carried out with the following temperature program: 60 ˚C (2 min), 150 ˚C (15 ˚C/min), 320 ˚C (3 ˚C/min), 320 ˚C (20 min isothermal). Helium served as carrier gas (1 ml/min constant flow). Specific compound

identification was based on the comparison of gas chromatography retention times with those of reference compounds and published mass spectra (Belt et al., 2007; Boon et al., 1979; Brown and Belt, 2016; Volkman, 1986). The different responses of these ions and a detailed quantification method are given by Fahl and Stein (2012). For the quantification of the sterols, the molecular ions m/z 472 for campesterol (as 24-methylcholesta-5-en-3β-ol) and m/z 486 for ß-sitosterol (as 24-ethylcholest-5-en-3β-ol) were used in relation to the molecular ion m/z 348 for the internal standard Androstanol. The precision and stability of the instrument were controlled by reruns of external standards several times during one analytical sequence and by replicate analysis of random samples.

All biomarker concentrations were normalized to the TOC in order to compensate for dilution effects caused by variations in sedimentation rates. Additionally, non-biogenic and non-organic terrigenous accumulation rates (referred to as 'Terrigenous accumulation rate') were calculated by subtracting organic and biogenic (TOC + CaCO3) accumulation rates from the bulk accumulation rate (see, section 6.3.4). All biomarker concentrations were converted into their accumulation rates to provide information about absolute changes in sediment fluxes/input by using the following five equations (e.g., Stein & Macdonald, 2004).

(1) Bulk accumulation rate = LSR*DBD, (2) TOC accumulation rate = Bulk accumulation rate*TOC/100, (3) $CaCO_3$ accumulation rate = Bulk accumulation rate*$CaCO_3$/100, (4) Terrigenous accumulation rate = Bulk accumulation rate – TOC accumulation rate – $CaCO_3$ accumulation rate, and (5) BM accumulation rate = Bulk accumulation rate*BM

Where, LSR = sedimentation rate (cm ka^{-1}); DBD = dry bulk density (g cm^{-3}); TOC = total organic carbon (%); BM = biomarker concentration (µg g^{-1}); Bulk accumulation rate = total sediments accumulation rate (g cm^{-2} ka^{-1}); TOC accumulation rate = total organic carbon accumulation rate (g cm^{-2} ka^{-1}); $CaCO_3$ accumulation rate = carbonate accumulation rate (g cm^{-2} ka^{-1}); Terrigenous accumulation rate = Terrigenous accumulation rate (non-biogenic and non-organic); BM accumulation rate = biomarker accumulation rate (µg cm^{-2} ka^{-1}).

6.4   Results

All biomarkers concentrations are mainly described as µg/gTOC and as accumulation rates in µg cm^{-2} ka^{-1} (Fig. 6.4-6.9). The distribution of biomarkers, bulk geochemical parameters and stable

carbon isotope ($\delta^{13}C_{org}$) showed significant downcore variations that correlate partly with lithological units (LU).

Core GeoB19948-3

Figure 6.4: Combined record of core GeoB19948-3 (a) lithology (Dorschel et al., 2015) and bulk parameters and biomarkers (b) total organic carbon (TOC), (c) ß-sitosterol+campesterol (µg/g Sed), (d) ß-sitosterol+campesterol [µg/g TOC], (e) TOC/N ratio, (f) TOC/N$_{corr}$ and (g) $\delta^{13}C_{org}$ [‰]. Black solid triangles mark the AMS ^{14}C datings. All plots are shown versus depth in [cm].

TOC concentrations of core GeoB19948-3 show generally higher values of about 0.7% (mean) from 278-150cm (ca. 8 to 5 ka BP), followed by decreasing values of 0.6% (mean) towards the top of the core (Fig. 6.4b). The concentrations of terrigenous biomarkers (ß-sitosterol+campesterol) range from 15 to 53 µg/gTOC throughout the record (Fig. 6.4c) and

show a trend of continuously decreasing values towards the core top (over the last about 8 ka). TOC/N_{corr} ratio varies between about 6 to 15 (Fig. 6.4f), and display high variability throughout the core from 278-0cm (ca. 8 to 1.2 ka BP). $\delta^{13}C_{org}$ values range from -23.4 ‰ to -22.2 ‰ and show a general trend of increasingly heavier values towards the top of the core (Fig. 6.4g).

The bulk accumulation rates were dominated by terrigenous accumulation rates and vary between 19 to 35 g cm^{-2} ka^{-1}, and displays generally decreasing values from the mid-to-late Holocene (~8-1.2 ka BP) (Fig. 6.7b, c). TOC accumulation rate range from 0.10 to 0.26 g cm^{-2} ka^{-1} and is marked by a gradual decrease from the mid-to-late Holocene (Fig. 6.7d). The accumulation rates of terrigenous biomarkers (ß-sitosterol+campesterol) vary in the range from 2 to 13 µg cm^{-2} ka^{-1} and display a trend of decreasing values from ca. 8 to 1.2 ka BP (Fig. 6.7e).

Core GeoB19927-3

TOC concentrations, described previously by Saini et al. (2020) vary between 0.1 and 1.5% and show extremely low values in the early Holocene from 1147-1059cm (ca. 10.1 to 9.5 ka BP), followed by slightly increasing values from 1059-815cm (~9.5 to 7.6 ka BP), and acquire highest (mean 1.1%) values from 815-0cm (7.6 ka to present) (Fig. 6.5b). The terrigenous biomarkers (ß-sitosterol+campesterol) concentrations range from 0 to 114 µg/gTOC (Fig. 6.5d). They are the lowest at the bottom of the core at ~10 ka BP and show variable but generally high values (mean 74 µg/gTOC) from 1059-557cm (9.5-6.1 ka BP), except a slight decrease at 760cm (~7.6 ka BP), followed by decreasing values (mean 34 µg/gTOC) towards the core top (557-20cm). Additionally, they show a slight increase in the uppermost centimetres over the upper 40cm (last ca. 0.4 ka BP). TOC/N_{corr} ratio range from 4 to 26 (Fig. 6.5f), and exhibits low values (<10) throughout the core, except a distinct maximum of ~26 at 1120cm (ca. 10 ka BP). The $\delta^{13}C_{org}$ values vary between -24.8 to -21.8 ‰ and are generally lighter (<-23‰) at the core bottom between 1147-815cm (10-8 ka BP), followed by increasingly heavier values towards the core top (last 8 ka) (Fig. 6.5g).
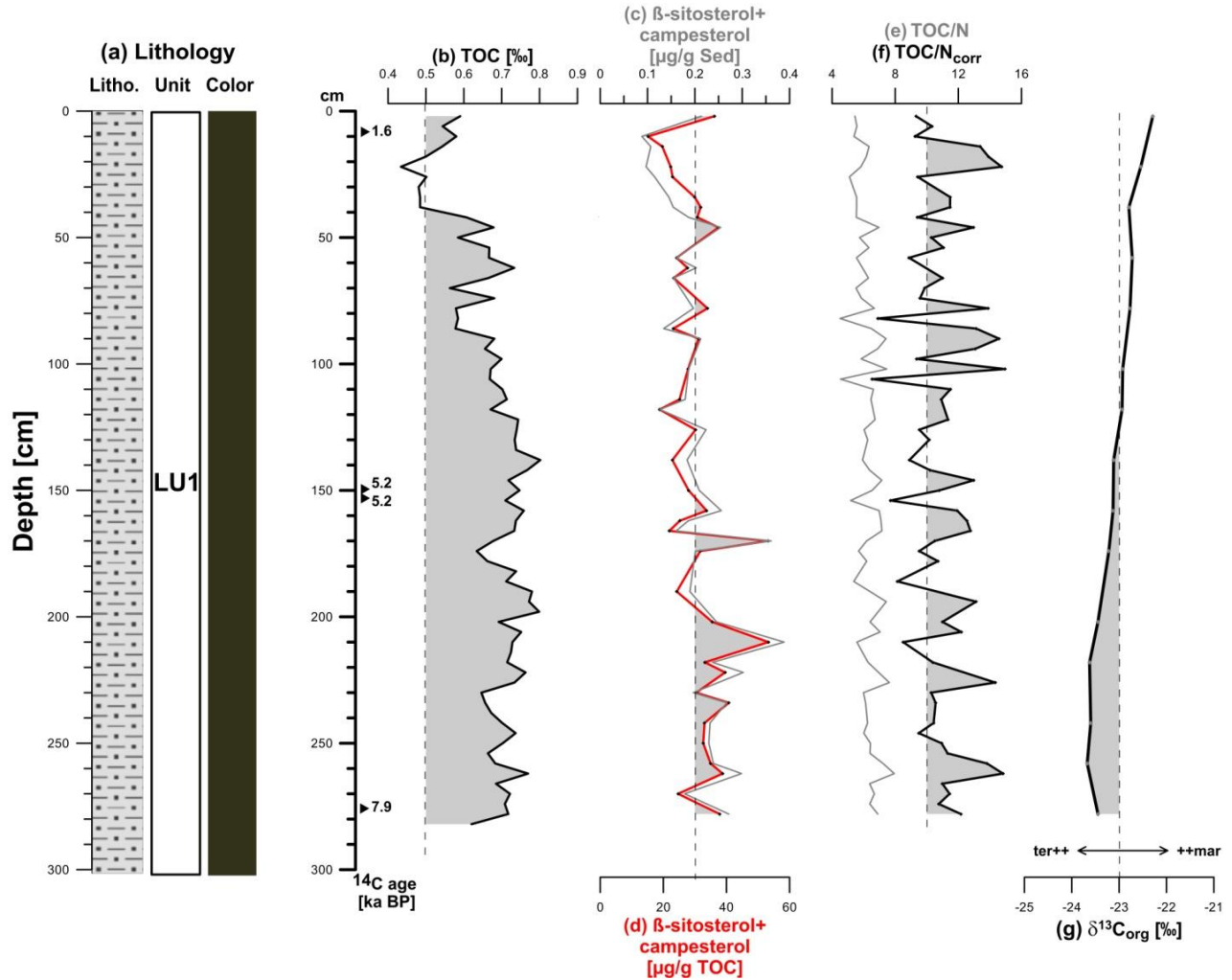
Figure 6.5: Combined record of core GeoB19927-3 (a) lithology (Dorschel et al., 2015) and bulk parameters and biomarkers (b) total organic carbon (TOC), (c) ß-sitosterol+campesterol (µg/g Sed), (d) ß-sitosterol+campesterol [µg/g TOC], (e) TOC/N ratio, (f) TOC/Ncorr and (g) $\delta^{13}C_{org}$ [‰]. Black solid triangles mark the AMS ^{14}C datings. All plots are shown versus depth in [cm].

The bulk accumulation rates were dominated by terrigenous accumulation rates and range from 15 to 187 g cm^{-2} ka^{-1}, and displays generally higher values in the early Holocene prior to 8 ka BP, followed by decreasing values in the mid-to-late Holocene (Fig. 6.8b, c). TOC accumulation rates exhibit strong fluctuations ranging from 0.1 to 1.2 g cm^{-2} ka^{-1} and display generally decreasing values towards the core top during the Holocene. The accumulation rates of terrigenous biomarkers (ß-sitosterol+campesterol) (Fig. 6.8e) range from 0 to 88 µg cm^{-2} ka^{-1} and

114

exhibit generally high values in the early Holocene, followed by decreasing values in the mid-to-late Holocene.
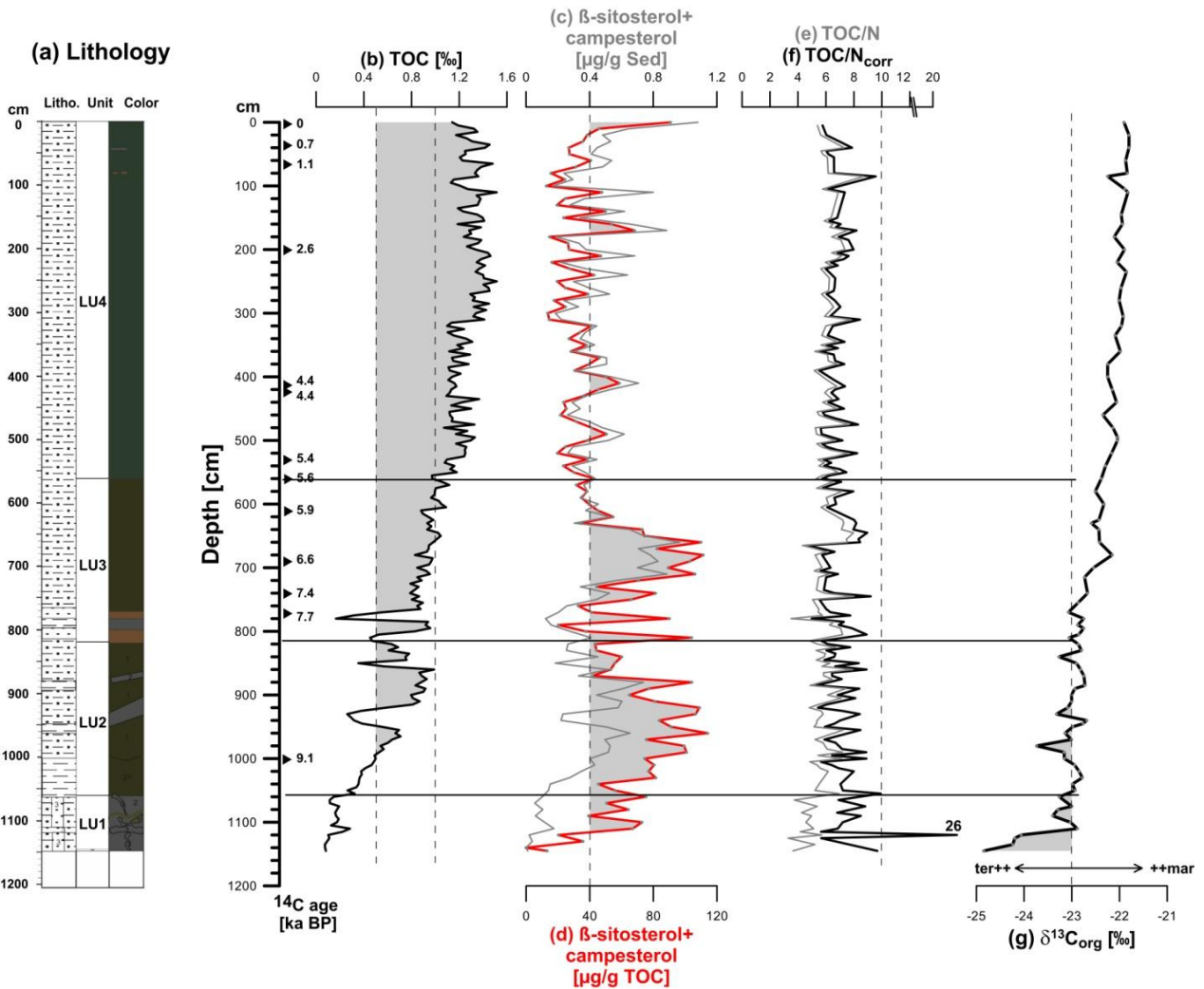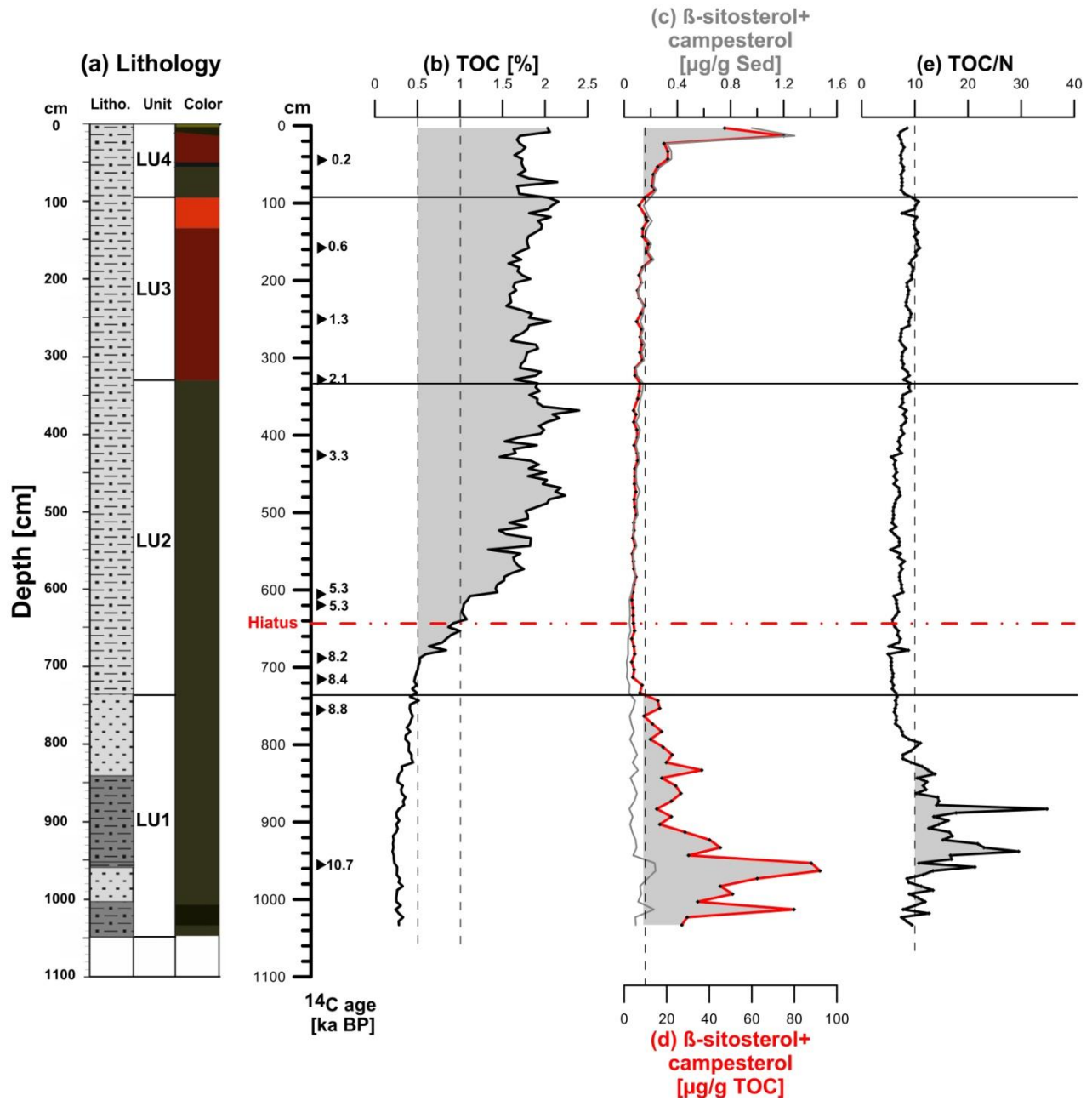

Figure 6.6: Combined record of core GeoB19905-1 (a) lithology (Dorschel et al., 2015) and bulk parameters and biomarkers (b) total organic carbon (TOC), (c) ß-sitosterol+campesterol (µg/g Sed), (d) ß-sitosterol+campesterol [µg/g TOC] and (e) TOC/ N ratio. Black solid triangles mark the AMS ^{14}C datings. All plots are shown versus depth in [cm].
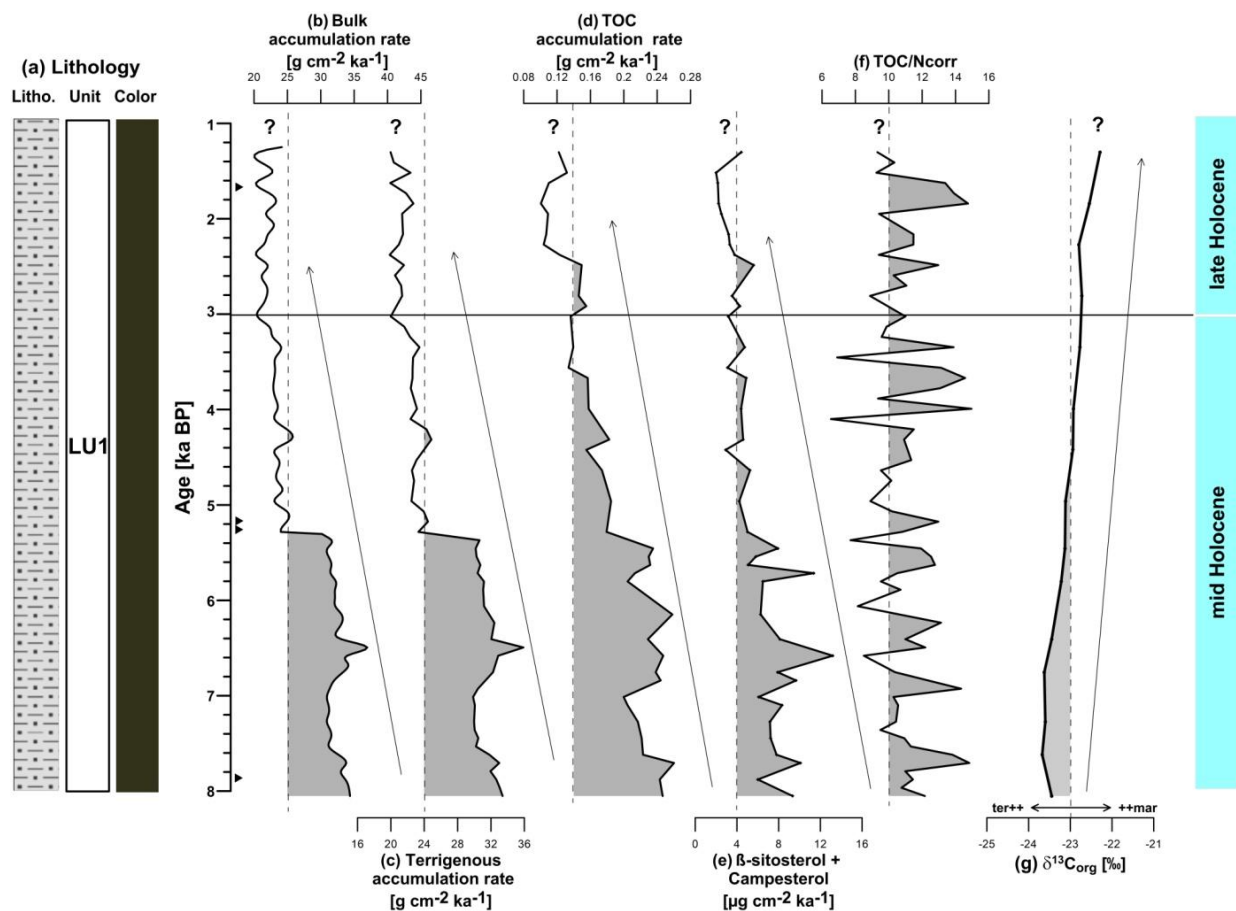
Figure 6.7: Downcore profile of core GeoB19948-3 showing (a) lithological column (units), (b) bulk accumulation rate, (c) terrigenous accumulation rate, (d) TOC accumulation rate, (e) accumulation rate of terrigenous biomarkers; ß-sitosterol+campesterol, (f) TOC/Ncorr and (g) $\delta^{13}C_{org}$. All plots are shown versus age in thousand years before present [ka BP]. Black solid triangles mark the AMS ^{14}C datings. Arrows indicate decreasing/increasing trend in proxy records.

Core GeoB19905-1

TOC concentrations of core GeoB19905-1 display extremely low values of about 0.3% (mean) from 1036-737cm (ca. 11.5 to 8.6 ka BP), followed by an increase from 737-329cm and attaining the maximum values (mean 1.8%) in the upper part of the core between 329-0cm (last ca. 2 ka BP) (Fig. 6.6b). The terrigenous biomarkers (ß-sitosterol+campesterol) concentrations vary between 3 and 92 µg/gTOC throughout the core (Fig. 6.6d) and display the highest values (mean 32 µg/gTOC) in the lowest unit LU1 (1036-737cm) (~11.5 to 8.6 ka BP). Note, however, they show no significant increase in µg/g sediment record in this period (Fig. 6.6c). Afterwards, they

116

(Fig. 6.6d) show reduced values from 737-83cm (ca. 8.6 to 0.4 ka BP), succeeded by a strong increase in the uppermost 83cm (last 0.4 ka BP). TOC/N ratio varies between 4 and 34 (Fig. 6.6e), and display the highest values (>10) in the early Holocene from 1036-737cm (~11.5 to 9 ka BP), followed by generally reduced values (<10) in between 800-0cm (last 9 ka BP).
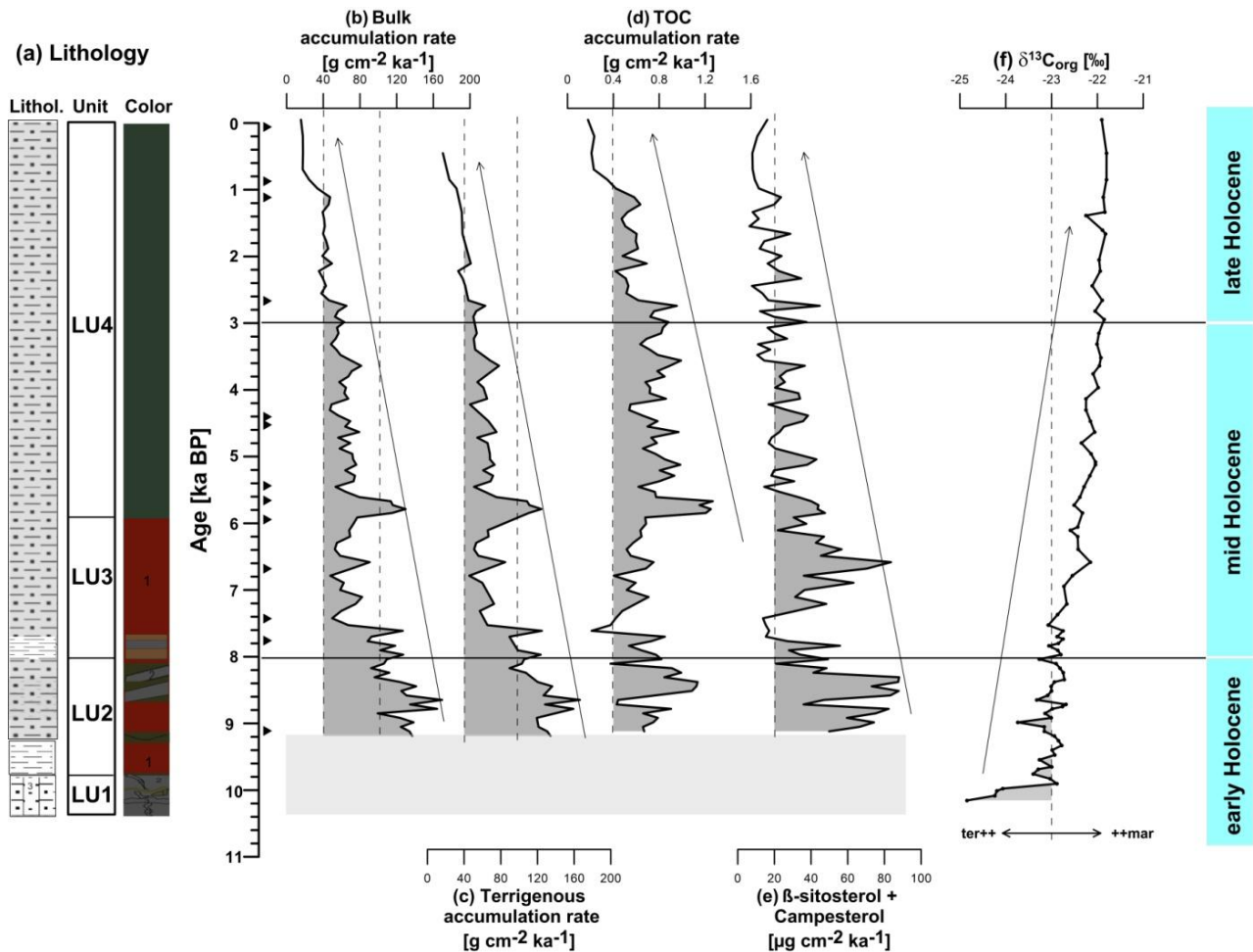
Figure 6.8: Downcore profile of core GeoB19927-3 showing (a) lithological column (units), (b) bulk accumulation rate, (c) terrigenous accumulation rate, (d) TOC accumulation rate, (e) accumulation rate of terrigenous biomarkers; ß-sitosterol+campesterol and (f) $\delta^{13}C_{org}$. The increasing/decreasing trends in proxy records are depicted as arrows. All plots are shown versus age in thousand years before present [ka BP]. The Gray box shows the core base where the age model is extrapolated, and thus the accumulation rates were not calculated for this time interval. Black solid triangles mark the AMS ^{14}C datings.

The bulk accumulation rates in this core as well is dominated by terrigenous accumulation rates and range from 44 to 177 g cm^{-2} ka^{-1}, and show generally higher values in the early Holocene (11.5-8.1 ka BP) and late Holocene (1.4 ka to present), in between (8.1-1.4 ka BP) they exhibit

reduced values (Fig. 6.9b, c). The TOC accumulation rates, however, display increasing values towards the top of the core and range from 0.2 to 3 g cm^{-2} ka^{-1} (Fig. 6.9d). The accumulation rates of terrigenous biomarkers (ß-sitosterol+campesterol) (Fig. 6.9e) range from 2 to 199 µg cm^{-2} ka^{-1} and exhibit generally high values in the early Holocene during 11.5 to about 8 ka BP. They show decreased values in the mid Holocene, succeeded by a strong increase in the late Holocene, especially in the uppermost centimetres of the last 0.4 ka.
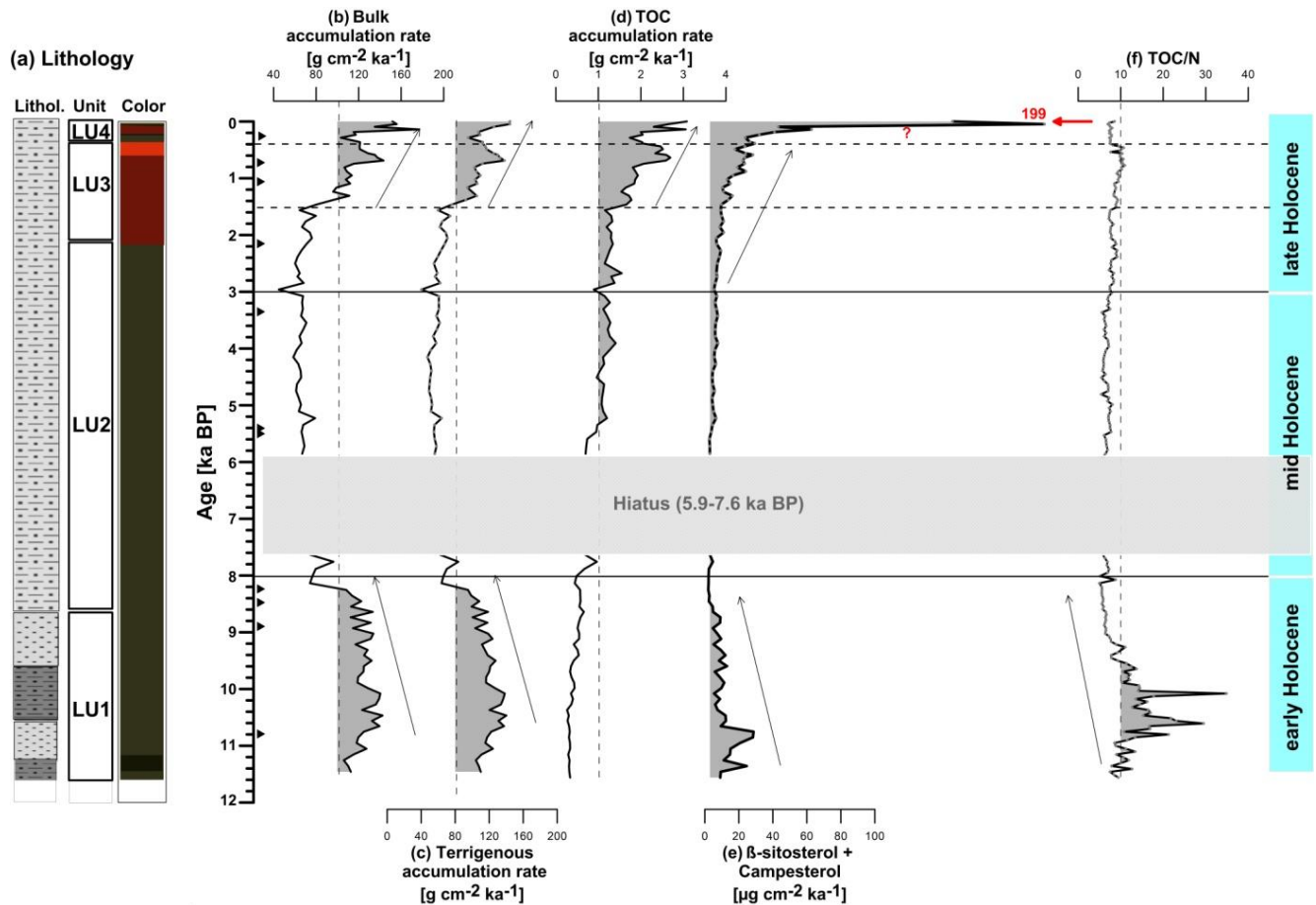
Figure 6.9: Downcore profile of core GeoB19905-1 showing (a) lithological column (units), (b) bulk accumulation rate, (c) terrigenous accumulation rate, (d) TOC accumulation rate, (e) accumulation rate of terrigenous biomarkers; ß-sitosterol+campesterol and (f) TOC/N ratio. All plots are shown versus age in thousand years before present [a BP]. Black solid triangles mark the AMS ^{14}C datings. Arrows indicate decreasing/increasing trend in proxy records.

6.5 Discussion

6.5.1 Deglacial to early Holocene transition (11.5-8 ka BP)

In the lower-most period between about 10.1-9.4 ka BP at core GeoB19927-3 from NE Baffin Bay, minimum to near-zero values of TOC as well as terrigenous biomarkers (ß-sitosterol and campesterol) (Fig. 6.4d, 6.7e), and lighter $\delta^{13}C_{org}$ values (<-23‰), indicate deglacial conditions and organic matter of predominantly terrigenous origin.

The TOC/N_{corr} ratio, however, varies between 8 and 26 showing mixed to a predominantly terrigenous source of organic matter. Based on very high sand content values at GeoB19927-3, Saini et al. (2020) argued for high IRD in this interval. This suggests the possibility of an ice-proximal environment and cold deglacial conditions in the Baffin Bay area (Fig. 6.11a). Briner et al. (2013) argued for the existence of a marine-based ice sheet along most of NE Baffin Bay, especially during the earliest part of the Holocene. Several studies from the eastern Baffin Bay area also suggested cold deglacial conditions in this area prior to 9.4 ka BP (Caron et al., 2019; Georgiadis et al., 2020; Hansen et al., 2020; Jennings et al., 2014). These conditions could have been also felicitated by the presence of active ice-streams and high melt water discharge in the area and possibly strongly stratified conditions (Aksu and Piper, 1979; Dyke, 2008). Extended sea ice cover, as well as the limited presence of WGC influence in the Baffin Bay area, may have also contributed to colder conditions resulting in extremely low terrestrial organic matter production in this time interval (Jennings et al., 2019; Ledu et al., 2010a; Saini et al., 2020).

In the following time interval between 9.4 and 8 ka BP (1059-815cm; GeoB19927-3) the conditions in NE Baffin Bay can be characterized by very high accumulation rates of terrigenous sediments (>100 g cm^{-2} ka^{-1}) (Fig. 6.8c), with a distinct maximum of ~160 g cm^{-2} ka^{-1} at around 8.7 ka BP. These are accompanied by maximum accumulation rates of terrigenous biomarkers (ß-sitosterol and campesterol) (~80 µg cm^{-2} ka^{-1}) (Fig. 6.10f). The lighter $\delta^{13}C_{org}$ values (<-23‰) but low (<10) TOC/N_{corr} ratio shows a more mixed source of organic matter in this interval. Note, however, $\delta^{13}C_{org}$ signature in the Arctic regions may be altered by the mixing of isotopically enriched phytoplankton (-20‰) and ice algae (-15 to -8‰), thus should be regarded with caution (Kremer, 2018a). In this interval at core GeoB19927-3, Saini et al. (2020) reported
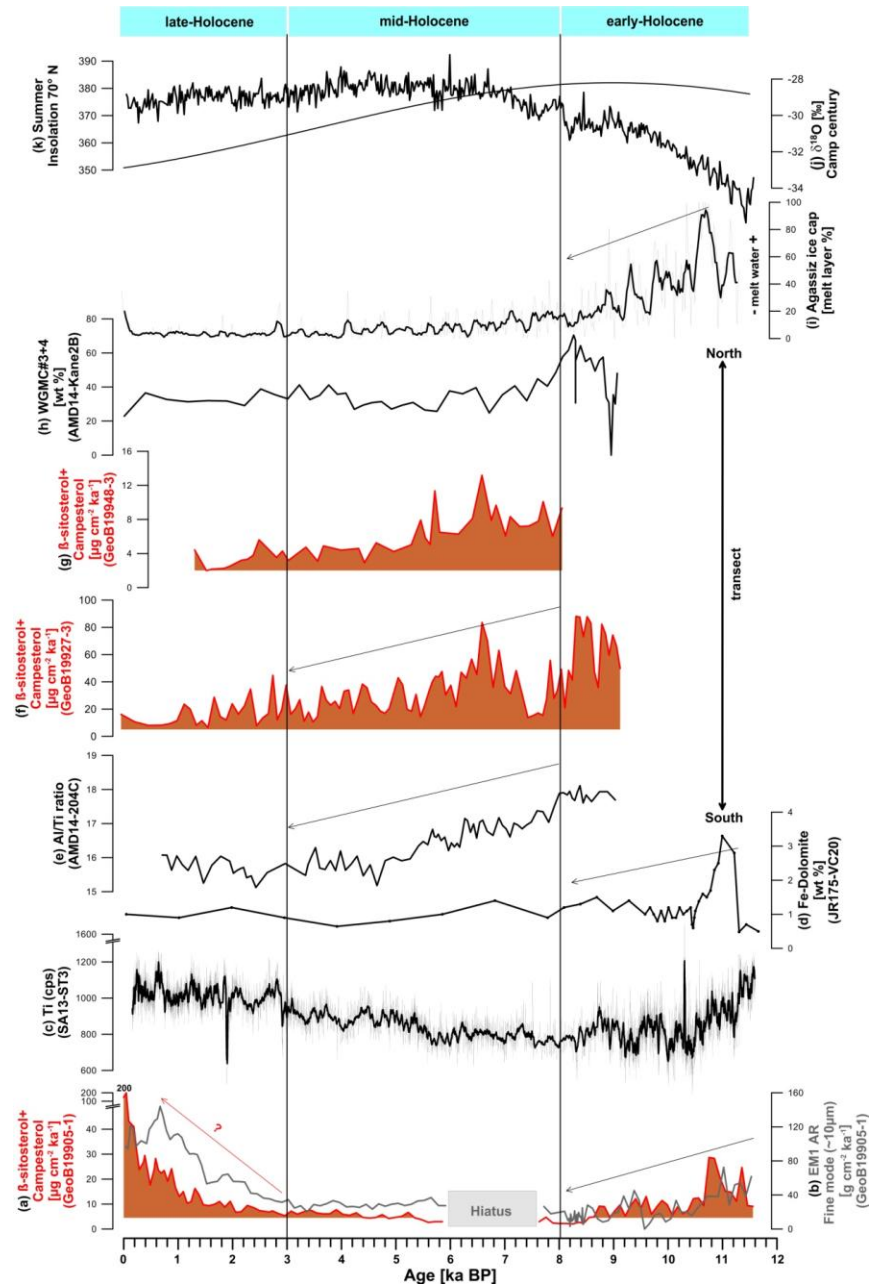
Figure 6.10: Comparison of selected proxies for terrigenous input along the eastern Baffin Bay-Labrador Sea (N-S) transect (a) accumulation rates of terrigenous biomarkers; ß-sitosterol+campesterol (GeoB19905-1) (b) fine sediments (EM1) accumulation rate (GeoB19905-1) (Weiser at al. 2021), (c) XRF intensity of titanium (Ti) (in counts per second 'cps') (SA13-ST3) (Allan et al., 2021), (d) Fe-Dolomite (JR175-VC20) (Jennings et al., 2014), (e) Al/Ti ratio, based on geochemical (XRF) data (AMD14-204C) (Caron et al., 2020), (f) terrigenous biomarkers; ß-sitosterol+campesterol accumulation rates (GeoB19927-3), (g) terrigenous biomarkers; ß-sitosterol+campesterol accumulation rates (GeoB19948-3) and (h) West Greenland Mineral Cluster#3+4 (eroded sediments from NW Greenland sources) (AMD14-Kane2B) (cf. Caron et al., 2020) with (i) Agassiz melt layer record (Fisher, 2003), (j) Camp Century δ^{18}O record (Vinther et al., 2009) and (k) summer insolation at 70˚N (Laskar et al., 2004). Arrows indicate decreasing/increasing trend in proxy records. The positions of these cores are indicated in Fig. 1.
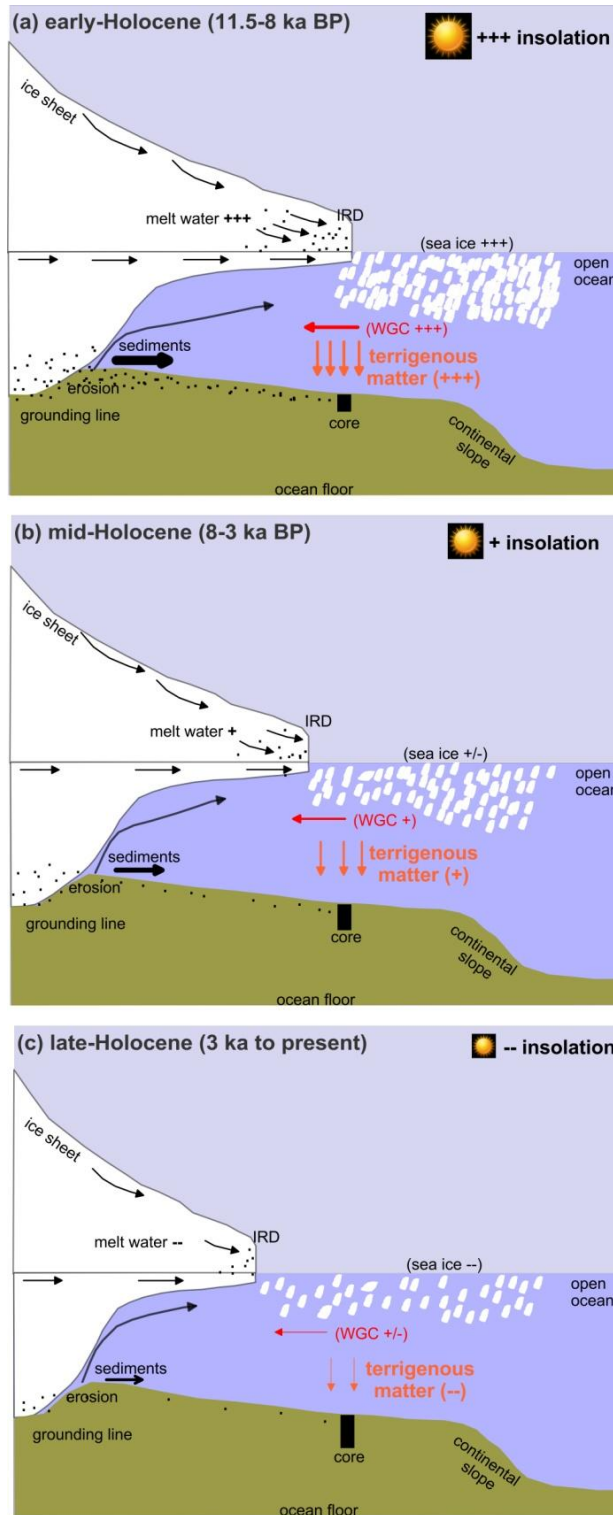
Figure 6.11: Sketch of the large scale hydrographic variations, reflected by changes in the Atlantic Water (WGC) inflow and ice conditions during the (a) early Holocene, (b) mid Holocene and (c) late Holocene. A thick ice-sheet and related high melt water and erosional input may have led to high terrigenous input in the early Holocene, which is decreasing from the mid-to-late Holocene (cf., discussion).

synchronous peaks in accumulation rates of sea ice proxy IP_{25} and phytoplankton biomarkers brassicasterol and dinosterol, interpreted as marginal ice-edge conditions. Moderate summer conditions with strong winter storms may have contributed to enhanced sea ice cover near the coastlines, increasing further the eroded material picked up sea ice freezing processes (COHMAP, 1988). High deposition of terrigenous and marine organic matter is typical of ice-edge situation. Rapid retreat/thinning of adjacent ice-sheets due to high summer melting during the early Holocene may have increased supply of terrigenous material to the core site (Fig. 6.10i, k). This is in accordance with the interpretation that most GIS land-based deglaciation occurred after the Younger Dryas (YD) and peaked in the early Holocene between about 10 and 8 ka BP in West Greenland (Lecavalier et al., 2017; Sinclair et al., 2016). This relatively rapid ice retreat combined with sea-level transgression and glacio-isostatic rebound could have triggered enhanced sediment input through glacial erosion (Fleming and Lambeck, 2004; Long et al., 2011). Based on the high component of Charnockite mineral assemblage (WGMC#3+4), high Al/Ti ratio and high Fe-dolomite supply (Fig. 6.10d, h) at cores AMD14-Kane2B and JR175-VC20, Caron et al. (2020) and Jennings et al. (2014) also suggested high detrital (IRD) supply from northern Baffin Bay and the NW Greenland areas into eastern Baffin Bay. Additionally, terrigenous material entrapped during new sea ice formation in other Arctic regions can also be transported via the ocean currents and released at the marginal ice zones, i.e. in Baffin Bay due to ablative processes (Reimnitz et al., 1994; Stein et al., 1994). Increased strength of the WGC was also reported in this interval (Giraudeau et al., 2020, Weiser et al., 2021). Overall, this may also suggest relatively dense vegetation cover and fluvial sediment supply from Baffin Island and/or Greenland caused by warmer climate in the early Holocene and plants and animal migration northwards (Axford et al., 2021; Kaufman et al., 2004; Weiser et al., 2021). Other studies also support high terrigenous matter supply linked to high melt water discharge from the disintegrating GIS, in combination with high surface melting (Fig. 6.10i) until about 8 ka BP (Giraudeau et al., 2020, Weiser et al., 2021).

Further south, the conditions in the NE Labrador Sea between 11.5 to 8 ka BP are characterized by the maximum accumulation rates of terrigenous material (Fig. 6.9c), accompanied with generally high accumulation rates of terrigenous biomarkers (ß-sitosterol and campesterol) (Fig. 6.10a). High TOC/N ratios (10-40) in this interval (Fig. 6.9f), especially during 11.5-9.1 suggest a predominantly terrigenous origin of organic matter and is supported by the extremely low value

of TOC accumulation rates (Fig. 6.9d). This might be related to the final stage of deglaciation and related erosive dynamics and linked to the huge amounts of terrigenous material supply from the retreating GIS. An increased shelf erosion due to increased sea level could have intensified the detrital (IRD) material supply up to the southwestern Greenland areas, as shown by the Fe-dolomite peak in central Baffin Bay (core JR175-VC20) (Jennings et al., 2014; Keigwin et al., 1992). An enhanced oceanic circulation off SE Greenland and the Labrador Sea area ca. 9 ka BP (Weiser et al., 2021; McCave and Andrews, 2019) may have also promoted long-distance transport of terrigenous matter supply into the region. Based on the absence of sea ice biomarker IP_{25} (GeoB19905-1), Saini et al. (submitted) have suggested no presence of (spring-autumn) sea ice cover, thus indicating no significant sea ice related transport. Based on paleolimnological records and high magnetic susceptibility values from the Canadian Arctic, Finkelstein and Gaiewski (2007) suggested high energy glacial outwash during the early Holocene. Based on the geochemical data and high values of iron (Fe), potassium (K) and titanium (Ti) at cores DA41P, 248260-2 and SA13-ST3 (Fig. 6.10c) in the vicinity (Allan et al., 2021; Ren et al., 2009; Seidenkrantz et al., 2013b), the authors also reported high terrestrial influx, linked to rapid sediment accumulation in an ice-proximal environment. This is in accordance with the final stage of deglaciation of Laurentide, Innutian and Greenland ice sheets during the early Holocene in the Canadian Arctic and West Greenland areas (England et al., 2006; Sinclair et al., 2016; Vinther et al., 2009; Zreda et al., 1999), in agreement with our records from the NE Labrador Sea.

6.5.2 Mid Holocene conditions (8-3 ka BP)

In the mid Holocene, a major change in sediment delivery took place after about 8 ka BP, as shown by a significant decrease in the mean accumulation rates of terrigenous (and bulk) sediments, from around 100 g cm^{-2} ka^{-1} to less than 40 g cm^{-2} ka^{-1} as shown by cores GeoB19927-3 (Fig. 6.8) and GeoB19948-3 (Fig. 6.7) from eastern Baffin Bay. This synchronous decrease in the accumulation rates of terrigenous biomarkers (ß-sitosterol and campesterol) in this period is part of the so-called Holocene Thermal Maximum (HTM) in Greenland (8-3 ka BP) when surface temperatures showed consistently higher values than today and oceanographic conditions were favorable for marine productivity (Caron et al., 2019; Dahl-Jensen et al., 1998; Jennings et al., 2011a; Ledu et al., 2010b). Increasingly heavier $\delta^{13}C_{org}$ values (>-23‰) and low (<10) TOC/N_{corr} ratio at Baffin Bay cores support the increased marine origin of organic matter, however, overall the accumulation rates of terrigenous sediments remain dominant. These

records demonstrate the decreased (increased) terrigenous (marine) influence in Baffin Bay. Less terrigenous material reached the core sites, possibly due to the increasing distance between the core site and sediment sources (Caron et al., 2019; Hansen et al., 2020; Saini et al., 2020). This decrease in terrigenous sediment supply may reflect the landward shift of the main depocenter, as reported in the nearby core AMD14-204C at Upernavik Trough (Giraudeau et al., 2020). Significantly decreased sand input at the core site GeoB19927-3, also support the idea of a significant ice retreat towards the land and thus reduced IRD input in this area (Giraudeau et al., 2020; Saini et al., 2020) (Fig. 6.11b).

Other studies in the vicinity of NE Baffin Bay have shown that the retreat in GIS was related to major changes in climate and oceanic conditions. Based on decreased Charnockite mineral assemblage (WGMC#3+4) and Al/Ti ratio (Fig. 6.10) at core AMD14-204C from eastern Baffin Bay, Caron et al. (2020) point towards decreased terrigenous/detrital supply in this interval. Jennings et al. (2014) also support the idea of decreased detrital (IRD) supply from northern Baffin Bay based on decreased Fe-dolomite peaks (Fig. 6.10d) at core JR175-VC20 from central Baffin Bay. Furthermore, based on sedimentological and micropaleontological proxies from Disko Bugt, Perner et al. (2013) and Jennings et al. (2014) have described increased influence and warming of the WGC, as a result of decreased melt water discharge together with decreased sea ice cover in the area (Fisher, 2003; Moros et al., 2016; Saini et al., 2020). Based on sedimentological data and low counts of zircon (Zr) in the Disko Bugt area, Giraudeau et al. (2020) argued for decreasing terrestrial influence in the area, in agreement with our reconstructions.

In the interval between 8-7.6 ka BP and after hiatus between 5.9-3 ka BP, the accumulation of bulk terrigenous sediments at core GeoB19905-1 from NE Labrador Sea exhibit a sharp decrease at about 8 ka BP, and remain low throughout the mid Holocene. The accumulation rates of terrigenous biomarkers (ß-sitosterol and campesterol) show reduced values in this period (Fig. 6.9e) and coincide with the increased accumulation rates of open-water phytoplankton biomarkers derived from the same sediment core (GeoB19905-1) (Saini et al., submitted, see chapter 5). This period is marked by low TOC/N (<10) ratios and an increase in TOC accumulation rates indicating a dominant marine source of organic matter deposition which coincides well with the decrease in terrigenous sediments supply (Fig. 6.9). Based on dinocysts,

$\delta^{13}C_{org}$ and geochemical data (Ti) data (Fig. 6.10c) near the NE Labrador Sea (core SA13-ST13), Allan et al. (2021) reported an increase in marine productivity and a significant decrease in terrigenous organic matter supply. Furthermore, based on the absence of sea ice proxy IP_{25}, Saini et al. (submitted) also suggested no (spring-autumn) sea ice occurrence in this time interval. This agrees well with the idea of a less dominant sediment transport via ice stream/glacial erosion and increased influence of the WGC as well as decreased melt water influence in eastern Baffin Bay area (Lloyd et al., 2005; Moros et al., 2016; Perner et al., 2012). Based on grain-size analyses and reduction in fine-grained sediments, Weiser et al. (2021b) noted a reduction in melt water input and linked it to the shrinking extent of the northwestern GIS in the period (Young and Briner, 2015), which further decreased terrigenous sediments supply in this interval. Overall, these results indicate a decreased input of terrigenous organic matter due to reduced detrital supply and/or increased marine productivity caused primary by reduction in melt water (IRD) discharge and a decreased WGC strength in the NE Labrador Sea area.

6.5.3   Late Holocene (3 ka to present)

The late Holocene is characterized by an even further decrease in terrigenous sediment supply, as reflected by the continued decrease in terrigenous sediments accumulation rates (Fig. 6.7, 6.8) as well as reduced accumulation of terrigenous biomarkers (ß-sitosterol and campesterol) at cores GeoB19927-3 and GeoB19948-3 in the Baffin Bay area (Fig. 6.10). Heavier $\delta^{13}C_{org}$ values (>-23‰) and low (<10) TOC/N_{corr} ratio at these cores in Baffin Bay further support an increased proportion of marine organic matter in relation to terrigenous sources. Additionally, reduced accumulation rates of sea ice (IP_{25}) and phytoplankton biomarkers dinosterol and brassicasterol at cores GeoB19927-3 and GeoB19948-3 were also described and report a general decrease of sea ice cover (Saini et al., submitted). In sum, this overall decrease in accumulation rates of bulk, terrigenous and marine organic matter (Fig. 6.11c) might indicate reduced vegetation cover in the Baffin Island-Greenland areas and point towards colder conditions. This is in accordance with the Neoglacial cooling widely reported in Baffin Bay and circum Greenland areas. Accompanying proxy records from eastern Baffin Bay suggested glacier advances in this time interval linked to colder oceanic and atmospheric conditions (Gajewski, 2015; Ouellet-Bernier et al., 2014). Based on the continued decrease in Charnockite mineral assemblage (WGMC#3+4) and decrease in Al/Ti ratio in this interval (Fig. 6.10) at core AMD14-204C from eastern Baffin Bay, Caron et al. (2020) also suggested decreased terrigenous/detrital supply during the late

Holocene. Alternatively, the reduction in terrigenous sediment delivery could be related to the late Holocene decrease in WGC strengths and possibly enhanced Polar Water currents (EGC, BC) in the West Greenland areas (Hansen et al., 2020; Moros et al., 2016; Perner et al., 2012).

However, core GeoB19905-1 from the NE Labrador Sea display increased accumulation of terrigenous biomarkers (ß-sitosterol and campesterol) during the late Holocene (last ca. 3 ka) (Fig. 6.10a). This is accompanied by a strong increase in the accumulation rates of TOC and terrigenous material supply, especially during the last 1.5 ka (Fig. 6.9). Weiser et al. (2021b) reported reduced WGC strengths and increased accumulation of poorly sorted fine sediments during the last 3 ka on the same sediment core: GeoB19905-1 (Fig. 6.10b). In such finer-grained sediments, the organic matter may become more efficient and labile and thus become enriched in the sediments (cf., Kneis and Stein, 1998; Fahl and Stein, 2007; Iversen and Roberts, 2015) as showed by elevated values of TOC (6.6d) and further supported by high accumulation rates of organic carbon (Fig. 6.9d). Alternatively, this increase in terrigenous organic matter may be also related to the increased sediment delivery from Neoglacial GIS advances (Fig. 6.10c) (Weiser et al., 2021; Seidenkrantz et al., 2007; Allan et al., 2021). Based on maximum peaks in TOC/C_{inorg} ratio in the vicinity core (SA13-ST3), Allan et al. (2021) suggested major changes in the nature of biogenic fluxes and/or preservation of organic matter in this time interval, in agreement with our interpretation. Furthermore, the upper ~100cm of the last 0.4 ka are characterized by very high terrigenous biomarkers that may be caused by increased preservation, however, the topmost maximum and its downcore decrease may also relate to diagenetic alterations and thus should be interpreted with caution (cf. Fahl and Stein, 2012; Belt & Müller, 2013).

6.6 Conclusion

(1) The study of accumulation rates of biomarkers and bulk geochemical parameters carried out on three AMS ^{14}C-radiocarbon dated sediment cores from the north-south transect of eastern Baffin Bay-Labrador Sea margin gives important information on terrigenous carbon input and paleoclimatic changes through Holocene times

(2) Although, terrigenous sediment fluxes are predominant throughout the Holocene, however, during the early Holocene, terrigenous carbon input remained relatively very high, possibly related to the large-scale melt water discharge, high ice rafting (IRD) and enhanced sediment transport by the strengthened WGC prior to 8 ka BP.

(3) The mid Holocene is characterized by reduced input of terrigenous organic matter and increased marine organic matter, part of warm HTM-like conditions and related to decreased melt water discharge, ice cover as well as reduced sediment supply by decreased strength of the WGC.

(4) During the last 3 ka, Baffin Bay is characterized by a reduced accumulation of all biomarkers, including terrigenous organic carbon, and might be related to Neoglacial cooling. However, the Labrador Sea core displayed increased efficiency of the coagulation process of fine-grain siliciclastic material resulted in enhanced accumulation/preservation of terrigenous organic matter, albeit, increased terrigenous organic carbon input linked to Neoglacial regrowth of Glaciers cannot be ruled out.

7 Conclusion and Outlook

7.1 Conclusion

In this thesis, one major objective was to improve the understanding of sea ice, primary productivity and terrigenous input variability during Holocene times in a climatically challenging environment. In this regard, three sedimentary cores (GeoB19948-3, GeoB19927-2 and GeoB19905-1) were retrieved on a north-south transect from eastern Baffin Bay to the Labrador Sea margin. The data presented here encompasses important relationships between sea ice and ice-ocean-atmosphere interaction, as well as variability in primary productivity and terrigenous matter supply to the seafloor. To achieve that, organic geochemical bulk parameters (TOC, CaCO$_3$, TOC/N ratio, $\delta^{13}C_{org}$) and specific biomarker proxies such as specific sterols (brassicasterol, dinosterol, campesterol and ß-sitosterol) were used to comprehend the variability in primary productivity, terrigenous input and/or organic matter sources. A source-specific sea ice proxy IP$_{25}$ was applied for sea ice algae productivity, which in combination with phytoplankton biomarkers may indicate sea ice conditions (see, 1.6.2 for a detailed introduction). First of all, it could be shown that the northern sector of the studied transect i.e. Baffin Bay is characterized by persistent seasonal to ice-edge conditions throughout the Holocene period with some significant variability (Fig. 7.1). However, in the south i.e. in the NE Labrador Sea, the conditions remained predominantly ice-free (in spring/autumn) possibly due to continuous and enhanced influx of Atlantic Water (WGC) throughout the Holocene, in comparison to Baffin Bay.

Chapters 4 describe the past climate and sea ice evolution on northeastern Baffin Bay. Baffin Bay was covered by marginal/seasonal SIC throughout the Holocene and that the GIS melting and the variability in the oceanic current (WGC, BC) strengths had an extensive impact on sea ice formation and were linked to variable changes in primary productivity. After the high marginal/seasonal SIC during the early Holocene, the mid Holocene was characterized by reduced sea ice with millennial-scale variability of (late winter) ice-edge limit linked to the stronger WGC influence and increased open-water (polynya-type) conditions corresponding to 'warmer' conditions. Our IP$_{25}$ based sea ice reconstructions and related PIP$_{25}$ index do not reflect the late Holocene (the last 3 ka BP) Neoglacial cooling trend probably due to a strong sea ice
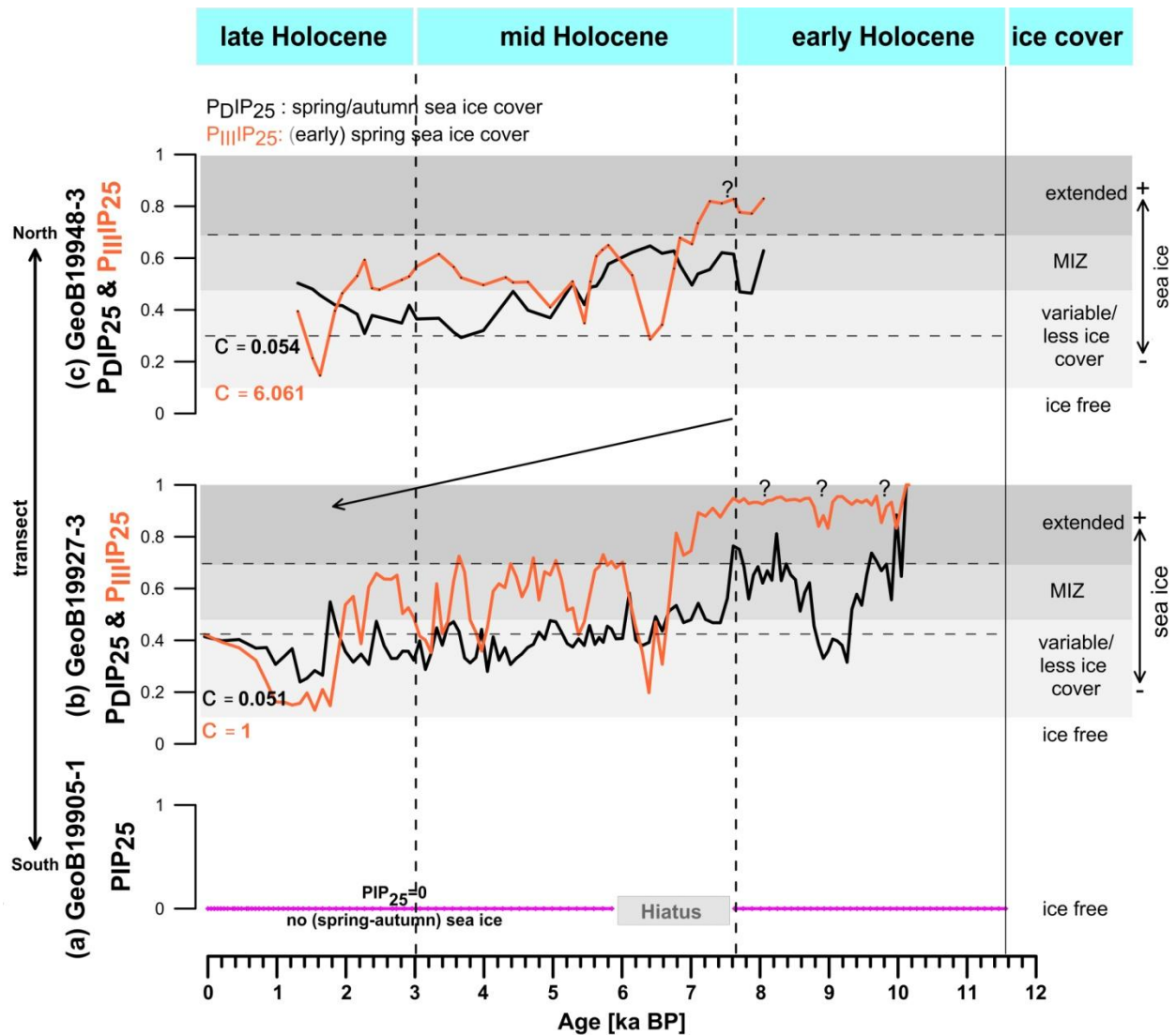
Figure 7.1: Comparison of different PIP indices (and sea ice conditions) using brassicasterol (P_BIP_{25}), dinosterol (P_DIP_{25}) and HBI III ($P_{III}IP_{25}$) as phytoplankton biomarker from the cores (a) GeoB19905-1, (b) GeoB19927-3 (Saini et al., 2020), and (c) GeoB19948-3 along the eastern Baffin Bay-Labrador Sea (north-south) transect. Classification of different sea ice scenarios is based on Müller et al. (2011) and Smik et al. (2016).

interaction with the adjacent fjords. However, peaks in HBI III at about 2.1 and 1.3 ka BP might correlate with the RWP and MCA, respectively, and may be linked to the positive NAO mode and possibly enhanced WGC influence in the Baffin Bay area.

In Chapter 5, Holocene evolution of paleoenvironmental, including sea ice and primary productivity conditions, was achieved by investigating three sediment cores along a north-south transect along the eastern Baffin Bay-Labrador Sea margin. Our IP_{25} and related PIP_{25} records based on combined cores GeoB19948-3 and GeoB19948-3 from Baffin Bay indicate variability in sea ice conditions; from extended to marginal to seasonal SIC during the last 10.1 ka BP (Fig. 7.1). However, in the NE Labrador Sea, the conditions remain mostly ice-free in spring-autumn throughout the Holocene (last 11.5 ka BP). We noticed a general increase in primary productivity from north to south in the studied transect, which could be linked to the general decrease in SIC observed along the N-S transect throughout the Holocene (Fig. 7.1). We described these changes in four distinct periods characterized mainly by the accumulation rates of sea ice; IP_{25} and phytoplankton biomarker; dinosterol.
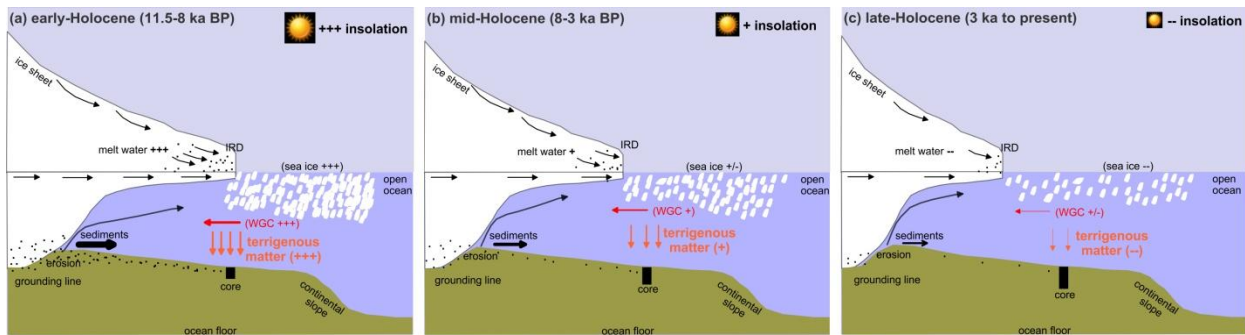
Figure 7.2: Generalized large-scale hydrographic variation, reflected by changes in sea ice and Atlantic Water (WGC) strengths during the (a) early Holocene, (b) mid Holocene, and (c) late Holocene. A proximity to thick ice-sheet and related high melt water and erosional input may contributed to high terrigenous organic carbon accumulation during the early Holocene, followed by a decrease in the mid-to-late Holocene (cf., see 6.5 for a detailed discussion)

Chapter 6 displays the variability in terrigenous organic carbon input along the eastern Baffin Bay-Labrador Sea margin throughout the Holocene. Although terrigenous sediment supply is predominant throughout the Holocene in this N-S transect, the relative accumulation of terrigenous organic carbon is very high during the early Holocene (prior to ~8 ka BP). The terrigenous organic carbon supply reduced significantly in the mid-to-late Holocene which seems to be linked with the decreased input of melt water discharge and reduced WGC strength in this interval (Fig. 7.2). Despite the cores from the Baffin Bay area displaying reduced input of terrigenous organic matter during the late Holocene, the NE Labrador Sea core recorded increased accumulation of terrigenous biomarkers. We interpreted this to be caused by the

increased preservation of organic matter associated with the high deposition of fine-grained poorly-sorted sediments linked to reduced WGC strengths, however, the idea of increased terrigenous organic matter associated with Neoglacial regrowth of Glaciers cannot be ruled out.

7.2 Outlook

These paleoceanographic reconstructions on the eastern side of Baffin Bay-Labrador Sea transect improved our understanding of the past ecological response of climate change that is quite useful for forecast models. However, in order to get an overall impression about the climate response, similar high-resolution investigations of sea ice cover, primary productivity and terrigenous sediment supply to the other (western) side of Baffin Bay and the Labrador Sea, i.e. the eastern Canadian Arctic are also essential. These parameters might have also shown significant variability with the varying influence of the WGC and the BC on the Canadian Arctic. Comparing and merging these results would be of significant importance since both would provide a much better picture of the ice-ocean-atmosphere interaction. Also, despite the contributions of this study to research in Baffin Bay and the Labrador Sea, it remains a challenging work to the construction of reliable age models. A large source of uncertainty might come from local marine reservoir correction, especially in deep time records. Furthermore, the comparison of different proxies i.e. biomarker (IP$_{25}$, HBI III, sterols), micropaleontological (dinocysts, foraminifera, diatoms) and sedimentological (IRD) in modern and paleorecords remains still a challenging area of research. Therefore, it seems worthwhile to increase and compare the knowledge of different signals provided by different proxies. Furthermore, seasonality in the production of different biomarkers such as dinosterol and HBIs also complicate the reliability of sea ice reconstructions and further research of this kind would help overcome these challenges.

8 References

Aagaard, K., Carmack, E.C., 1989. The role of sea ice and other fresh water in the Arctic circulation. Journal of Geophysical Research 94, 14485-14498.

Aksenov, Y., Bacon, S., Coward, A.C., Holliday, N.P., 2010. Polar outflow from the Arctic Ocean: A high resolution model study. Journal of Marine Systems 83, 14-37.

Aksu, A.E., Piper, D.J.W., 1979. Baffin Bay in the past 100,000 yr Geology 7, 245-248.

Allan, E., de Vernal, A., Knudsen, M.F., Hillaire-Marcel, C., Moros, M., Ribeiro, S., Ouellet-Bernier, M.M., Seidenkrantz, M.S., 2018. Late Holocene Sea Surface Instabilities in the Disko Bugt Area, West Greenland, in Phase With delta O-18 Oscillations at Camp Century. Paleoceanography and Paleoclimatology 33, 227-243.

Allan, E., de Vernal, A., Seidenkrantz, M.-S., Briner, J.P., Hillaire-Marcel, C., Pearce, C., Meire, L., Røy, H., Mathiasen, A.M., Nielsen, M.T., Plesner, J.L., Perner, K., 2021. Insolation vs. meltwater control of productivity and sea surface conditions off SW Greenland during the Holocene. Boreas n/a, DOI 10.1111/bor.12514.

Alley, R.B., Agustsdottir, A.M., 2005. The 8k event: cause and consequences of a major Holocene abrupt climate change. Quaternary Science Reviews 24, 1123-1149.

Alley, R.B., Mayewski, P.A., Sowers, T., Stuiver, M., Taylor, K.C., Clark, P.U., 1997. Holocene climatic instability: A prominent, widespread event 8200 yr ago. Geology 25, 483-486.

Alley, R.B., Andrews, J.T., Brigham-Grette, J., Clarke, G.K.C., Cuffey, K.M., Fitzpatrick, J.J., Funder, S., Marshall, S.J., Miller, G.H., Mitrovica, J.X., Muhs, D.R., Otto-Bliesner, B.L., Polyak, L., White, J.W.C., 2010. History of the Greenland Ice Sheet: paleoclimatic insights. Quaternary Science Reviews 29, 1728-1756.

Anderson, N.J., Leng, M.J., 2004. Increased aridity during the early Holocene in West Greenland inferred from stable isotopes in laminated-lake sediments. Quaternary Science Reviews 23, 841-849.

Andresen, C.S., McCarthy, D.J., Dylmer, C.V., Seidenkrantz, M.-S., Kuijpers, A., Lloyd, J.M., 2011. Interaction between subsurface ocean waters and calving of the Jakobshavn Isbrae during the late Holocene. Holocene 21, 211-224.

Andrews, J.T., Keigwin, L., Hall, F., Jennings, A.E., 1999. Abrupt deglaciation events and Holocene palaeoceanography from high-resolution cores, Cartwright Saddle, Labrador Shelf, Canada. Journal of Quaternary Science 14, 383-397.

Andrews, J.T., Smik, L., Belt, S.T., Sicre, M.A., McCave, I.N., 2020. Ocean surface and bottom water conditions, iceberg drift and sediment transport on the North Iceland margin during MIS 3 and MIS 2. Quaternary Science Reviews 252, 106722.

Ardyna, M., Babin, M., Devred, E., Forest, A., Gosselin, M., Raimbault, P., Tremblay, J.-É., 2017. Shelf-basin gradients shape ecological phytoplankton niches and community composition in the coastal Arctic Ocean (Beaufort Sea). Limnology and Oceanography 62, 2113-2132.

Arrigo, K.R., van Dijken, G.L., Castelao, R.M., Luo, H., Rennermalm, A.K., Tedesco, M., Mote, T.L., Oliver, H., Yager, P.L., 2017. Melting glaciers stimulate large summer phytoplankton blooms in southwest Greenland waters. Geophysical Research Letters 44, 6278-6285.

Axford, Y., de Vernal, A., Osterberg, E.C., 2021. Past Warmth and Its Impacts During the Holocene Thermal Maximum in Greenland. Annual Review of Earth and Planetary Sciences 49, 1, https://doi.org/10.1146/annurevearth-081420-063858.

Balascio, N.L., D'Andrea, W.J., Bradley, R.S., 2015. Glacier response to North Atlantic climate variability during the Holocene. Clim. Past 11, 1587-1598.

Bamber, J., 2016. Chapter 5 - Land Ice: Indicator and Integrator of Climate Change, in: Letcher, T.M. (Ed.), Climate Change (Second Edition). Elsevier, Boston, pp. 63-77.

Barber, D., Marsden, R., Minnett, P., Ingram, G., Fortier, L., 2001. Physical processes within the North Water (NOW) Polynya. Atmosphere-Ocean 39, 163-166.

Barber, D.C., Dyke, A., Hillaire-Marcel, C., Jennings, A.E., Andrews, J.T., Kerwin, M.W., Bilodeau, G., McNeely, R., Southon, J., Morehead, M.D., Gagnon, J.M., 1999. Forcing of the cold event of 8,200 years ago by catastrophic drainage of Laurentide lakes. Nature 400, 344-348.

Barber, D.G., Hop, H., Mundy, C.J., Else, B., Dmitrenko, I.A., Tremblay, J.-E., Ehn, J.K., Assmy, P., Daase, M., Candlish, L.M., Rysgaard, S., 2015. Selected physical, biological and biogeochemical implications of a rapidly changing Arctic Marginal Ice Zone. Progress in Oceanography 139, 122-150.

Bartels, M., Titschack, J., Fahl, K., Stein, R., Seidenkrantz, M.S., Hillaire-Marcel, C., Hebbeln, D., 2017. Atlantic Water advection vs. glacier dynamics in northern Spitsbergen since early deglaciation. Climate of the Past 13, 1717-1749.

Batchelor, C.L., Margold, M., Krapp, M., Murton, D.K., Dalton, A.S., Gibbard, P.L., Stokes, C.R., Murton, J.B., Manica, A., 2019. The configuration of Northern Hemisphere ice sheets through the Quaternary. Nature Communications 10, 3713.

Belchansky, G.I., Douglas, D.C., 2002. Seasonal comparisons of sea ice concentration estimates derived from SSM/I, OKEAN, and RADARSAT data. Remote Sensing of Environment 81, 67-81.

Belt, S.T., 2018. Source-specific biomarkers as proxies for Arctic and Antarctic sea ice. Organic Geochemistry 125, 277–298.

Belt, S.T., Allard, W.G., Masse, G., Robert, J.M., Rowland, S.J., 2000. Highly branched isoprenoids (HBIs): Identification of the most common and abundant sedimentary isomers. Geochimica Et Cosmochimica Acta 64, 3839-3851.

Belt, S.T., Brown, T.A., Ampel, L., Cabedo-Sanz, P., Fahl, K., Kocis, J.J., Masse, G., Navarro-Rodriguez, A., Ruan, J., Xu, Y., 2014. An inter-laboratory investigation of the Arctic sea ice biomarker proxy IP25 in marine sediments: key outcomes and recommendations. Climate of the Past 10, 155-166.

Belt, S.T., Brown, T.A., Ringrose, A.E., Cabedo-Sanz, P., Mundy, C.J., Gosselin, M., Poulin, M., 2013. Quantitative measurement of the sea ice diatom biomarker IP25 and sterols in Arctic sea ice and underlying sediments: Further considerations for palaeo sea ice reconstruction. Organic Geochemistry 62, 33-45.

Belt, S.T., Brown, T.A., Rodriguez, A.N., Sanz, P.C., Tonkin, A., Ingle, R., 2012. A reproducible method for the extraction, identification and quantification of the Arctic sea ice proxy IP25 from marine sediments. Analytical Methods 4, 705-713.

Belt, S.T., Brown, T.A., Smik, L., Tatarek, A., Wiktor, J., Stowasser, G., Assmy, P., Allen, C.S., Husum, K., 2017. Identification of C-25 highly branched isoprenoid (HBI) alkenes in diatoms of the genus Rhizosolenia in polar and sub-polar marine phytoplankton. Organic Geochemistry 110, 65-72.

Belt, S.T., Cabedo-Sanz, P., Smik, L., Navarro-Rodriguez, A., Berben, S.M.P., Knies, J., Husum, K., 2015. Identification of paleo Arctic winter sea ice limits and the marginal ice zone: Optimised biomarker-based reconstructions of late Quaternary Arctic sea ice. Earth and Planetary Science Letters 431, 127-139.

Belt, S.T., Masse, G., Rowland, S.J., Poulin, M., Michel, C., LeBlanc, B., 2007. A novel chemical fossil of palaeo sea ice: IP25. Organic Geochemistry 38, 16-27.

Belt, S.T., Masse, G., Vare, L.L., Rowland, S.J., Poulin, M., Sicre, M.-A., Sampei, M., Fortier, L., 2008. Distinctive C-13 isotopic signature distinguishes a novel sea ice biomarker in Arctic sediments and sediment traps. Marine Chemistry 112, 158-167.

Belt, S.T., Müller, J., 2013. The Arctic sea ice biomarker IP25: a review of current understanding, recommendations for future research and applications in palaeo sea ice reconstructions. Quaternary Science Reviews 79, 9-25.

Belt, S.T., Smik, L., Brown, T.A., Kim, J.H., Rowland, S.J., Allen, C.S., Gal, J.K., Shin, K.H., Lee, J.I., Taylor, K.W.R., 2016. Source identification and distribution reveals the potential of the geochemical Antarctic sea ice proxy IPSO25. Nature Communications 7, 12655.

Belt, S.T., Smik, L., Koseoglu, D., Knies, J., Husum, K., 2019. A novel biomarker-based proxy for the spring phytoplankton bloom in Arctic and sub-arctic settings - HBI T-25. Earth and Planetary Science Letters 523, 11.

Berger, A., Mélice, J.L., Loutre, M.F., 2005. On the origin of the 100-kyr cycles in the astronomical forcing. Paleoceanography 20, 10.1029/2005PA001173.

Bhatia, M.P., Kujawinski, E.B., Das, S.B., Breier, C.F., Henderson, P.B., Charette, M.A., 2013. Greenland meltwater as a significant and potentially bioavailable source of iron to the ocean. Nature Geoscience 6, 274-278.

Bhatt, U.S., Walker, D.A., Walsh, J.E., Carmack, E.C., Frey, K.E., Meier, W.N., Moore, S.E., Parmentier, F.-J.W., Post, E., Romanovsky, V.E., Simpson, W.R., 2014. Implications of Arctic Sea Ice Decline for the Earth System. Annual Review of Environment and Resources 39, 57-89.

Bi, H., Zhang, Z., Wang, Y., Xu, X., Liang, Y., Huang, J., Liu, Y., and Fu, M., 2019. Baffin Bay sea ice inflow and outflow: 1978–1979 to 2016–2017, The Cryosphere, 13, 1025–1042, https://doi.org/10.5194/tc-13-1025-2019.

Bidle, K.D., Azam, F., 1999. Accelerated dissolution of diatom silica by marine bacterial assemblages. Nature 397, 508-512.

Blaauw, M., Christen, J.A., 2011. Flexible Paleoclimate Age-Depth Models Using an Autoregressive Gamma Process. Bayesian Analysis 6, 457-474.

Bond, G., Kromer, B., Beer, J., Muscheler, R., Evans, M.N., Showers, W., Hoffmann, S., Lotti-Bond, R., Hajdas, I., Bonani, G., 2001. Persistent solar influence on north Atlantic climate during the Holocene. Science 294, 2130-2136.

Boon, J.J., Rijpstra, W.I.C., Delange, F., Deleeuw, J.W., Yoshioka, M., Shimizu, Y., 1979. Black Sea sterol - Molecular fossil for dinoflagellate blooms. Nature 277, 125-127.

Bourgeois, J.C., Koerner, R.M., Gajewski, K., Fisher, D.A., 2000. A holocene ice-core pollen record from Ellesmere Island, Nunavut, Canada. Quaternary Research 54, 275-283.

Brand, W.A., Coplen, T.B., Vogl, J., Rosner, M., Prohaska, T., 2014. Assessment of international reference materials for isotope-ratio analysis (IUPAC Technical Report). Pure and Applied Chemistry 86, 425-467.

Briner, J.P., Hakansson, L., Bennike, O., 2013. The deglaciation and neoglaciation of Upernavik Isstrom, Greenland. Quaternary Research 80, 459-467.

Briner, J.P., McKay, N.P., Axford, Y., Bennike, O., Bradley, R.S., de Vernal, A., Fisher, D., Francus, P., Frechette, B., Gajewski, K., Jennings, A., Kaufman, D.S., Miller, G., Rouston, C., Wagner, B., 2016. Holocene climate change in Arctic Canada and Greenland. Quaternary Science Reviews 147, 340-364.

Briner, J.P., Stewart, H.A.M., Young, N.E., Philipps, W., Losee, S., 2010. Using proglacial-threshold lakes to constrain fluctuations of the Jakobshavn Isbrae ice margin, western Greenland, during the Holocene. Quaternary Science Reviews 29, 3861-3874.

Bröder, L., Andersson, A., Tesi, T., Semiletov, I., Gustafsson, Ö., 2019. Quantifying Degradative Loss of Terrigenous Organic Carbon in Surface Sediments Across the Laptev and East Siberian Sea. Global Biogeochemical Cycles 33, 85-99.

Broecker, W.S., Kennett, J.P., Flower, B.P., Teller, J.T., Trumbore, S., Bonani, G., Wolfli, W., 1989. Routing of meltwater from the Laurentide Ice Sheet during the Younger Dryas cold episode. Nature 341, 318-321.

Brown, T.A., Belt, S.T., 2016. Novel tri- and tetra-unsaturated highly branched isoprenoid (HBI) alkenes from the marine diatom Pleurosigma intermedium. Organic Geochemistry 91, 120-122.

Brown, T.A., Belt, S.T., Tatarek, A., Mundy, C.J., 2014. Source identification of the Arctic sea ice proxy IP25. Nature Communications 5, p. 4197, 4110.1038/ncomms5197.

Bunker, A.F., 1976. Computations of Surface Energy Flux and Annual Air–Sea Interaction Cycles of the North Atlantic Ocean. Mon. Weather Rev. 104(9), 1122–1140. 1110.1175/1520-0493(1976)1104<1122:cosefa>1122.1120.co;1122, 1976.

Butzin, M., Köhler, P., Lohmann, G., 2017. Marine radiocarbon reservoir age simulations for the past 50,000 years. Geophysical Research Letters 44, 8473-8480.

Cape, M.R., Straneo, F., Beaird, N., Bundy, R.M., Charette, M.A., 2019. Nutrient release to oceans from buoyancy-driven upwelling at Greenland tidewater glaciers. Nature Geoscience 12, 34-39.

Cappelen, J., Vinther, B.M., 2014. SW Greenland temperature data 1784-2013. Technical Report 14–6.

Carmack, E.C., 2000. The Arctic Ocean's Freshwater Budget: Sources, Storage and Export, in: Lewis, E.L., Jones, E.P., Lemke, P., Prowse, T.D., Wadhams, P. (Eds.), The Freshwater Budget of the Arctic Ocean. Springer Netherlands, Dordrecht, pp. 91-126.

Caron, M., Montero-Serrano, J.-C., St-Onge, G., Rochon, A., 2020. Quantifying Provenance and Transport Pathways of Holocene Sediments From the Northwestern Greenland Margin. Paleoceanography and Paleoclimatology 35, e2019PA003809.

Caron, M., Rochon, A., Montero-Serrano, J.C., St-Onge, G., 2019. Evolution of sea-surface conditions on the northwestern Greenland margin during the Holocene. Journal of Quaternary Science 34, 569-580.

Caron, M., St-Onge, G., Masse', G., 2018. Holocene chronostratigraphy of northeastern Baffin Bay based on radiocarbon and high-resolution paleomagnetic data. Boreas 48, 147-165.

Cazenave, A., Remy, F., 2011. Sea level and climate: measurements and causes of changes. Wiley Interdisciplinary Reviews-Climate Change 2, 647-662.

Coachman, L.K., Aagaard, K., 1974. Physical Oceanography of Arctic and Subarctic Seas. Springer Berlin Heidelberg, Berlin, Heidelberg, pp. 1-72.

COHMAP, 1988. Climatic Changes of the Last 18,000 Years: Observations and Model Simulations. Science 241, 1043.

Collins, L.G., Allen, C.S., Pike, J., Hodgson, D.A., Weckstrom, K., Masse, G., 2013a. Evaluating highly branched isoprenoid (HBI) biomarkers as a novel Antarctic sea-ice proxy in deep ocean glacial age sediments. Quaternary Science Reviews 79, 87-98.

Collins, M., Knutti, R., Arblaster, J., 2013b. Long-term climate change: Projections, commitments and irreversibility. In: Stocker TF, Qin D, Plattner G-K et al. (eds) Climate Change 2013:

The Physical Science Basis: Contribution of Working Group I to the Fifth Assessment Report of the Intergovernmental Panel on Climate Change. Cambridge University Press, 1029–1136.

Comiso, J.C., 2012. Large Decadal Decline of the Arctic Multiyear Ice Cover. Journal of Climate 25, 1176-1193.

Coplen, T.B., 2011. Guidelines and recommended terms for expression of stable-isotope-ratio and gas-ratio measurement results. Rapid Communications in Mass Spectrometry 25, 2538-2560.

Cormier, M.A., Rochon, A., de Vernal, A., Gelinas, Y., 2016. Multi-proxy study of primary production and paleoceanographical conditions in northern Baffin Bay during the last centuries. Marine Micropaleontology 127, 1-10.

Cremer, H., 1999. Distribution patterns of diatom surface sediment assemblages in the Laptev Sea (Arctic Ocean). Marine Micropaleontology 38, 39-67.

Cronin, T.M., DeNinno, L.H., Polyak, L., Caverly, E.K., Poore, R.Z., Brenner, A., Rodriguez-Lazaro, J., Marzen, R.E., 2014. Quaternary ostracode and foraminiferal biostratigraphy and paleoceanography in the western Arctic Ocean. Marine Micropaleontology 111, 118-133.

Cronin, T.M., Gemery, L., Briggs, W.M., Jakobsson, M., Polyak, L., Brouwers, E.M., 2010. Quaternary Sea-ice history in the Arctic Ocean based on a new Ostracode sea-ice proxy. Quaternary Science Reviews 29, 3415-3429.

Dahl-Jensen, D., Mosegaard, K., Gundestrup, N., Clow, G.D., Johnsen, S.J., Hansen, A.W., Balling, N., 1998. Past temperatures directly from the Greenland Ice Sheet. Science 282, 268-271.

Darby, D.A., Ortiz, J., Polyak, L., Lund, S., Jakobsson, M., Woodgate, R.A., 2009. The role of currents and sea ice in both slowly deposited central Arctic and rapidly deposited Chukchi–Alaskan margin sediments. Global and Planetary Change 68, 58-72.

Darby, D.A., Ortiz, J.D., Grosch, C.E., Lund, S.P., 2012. 1,500-year cycle in the Arctic Oscillation identified in Holocene Arctic sea-ice drift. Nature Geoscience 5, 897-900.

de Vernal, A., Eynaud, F., Henry, M., Hillaire-Marcel, C., Londeix, L., Mangin, S., Matthiessen, J., Marret, F., Radi, T., Rochon, A., Solignac, S., Turon, J.L., 2005a. Reconstruction of sea-surface conditions at middle to high latitudes of the Northern Hemisphere during the Last Glacial Maximum (LGM) based on dinoflagellate cyst assemblages. Quaternary Science Reviews 24, 897-924.

de Vernal, A., Gersonde, R., Goosse, H., Seidenkrantz, M.S., Wolff, E.W., 2013a. Sea ice in the paleoclimate system: the challenge of reconstructing sea ice from proxies - an introduction. Quaternary Science Reviews 79, 1-8.

de Vernal, A., Hillaire-Marcel, C., Darby, D.A., 2005b. Variability of sea ice cover in the Chukchi Sea (western Arctic Ocean) during the Holocene. Paleoceanography 20, p. PA4018.

de Vernal, A., Hillaire-Marcel, C., Rochon, A., Frechette, B., Henry, M., Solignac, S., Bonnet, S., 2013b. Dinocyst-based reconstructions of sea ice cover concentration during the Holocene in the Arctic Ocean, the northern North Atlantic Ocean and its adjacent seas. Quaternary Science Reviews 79, 111-121.

de Vernal, A., Rochon, A., Frechette, B., Henry, M., Radi, T., Solignac, S., 2013c. Reconstructing past sea ice cover of the Northern Hemisphere from dinocyst assemblages: status of the approach. Quaternary Science Reviews 79, 122-134.

Dickson, R., Lazier, J., Meincke, J., Rhines, P., Swift, J., 1996. Long-term coordinated changes in the convective activity of the North Atlantic. Progress in Oceanography 38, 241-295.

Dieckmann, G.S., Hellmer, H.H., 2003. The importance of sea ice: an overview. In: Thomas, D.N., Dieckmann, G.S. (Eds.), Sea Ice: An Introduction to Its Physics, Chemistry, Biology and Geology. Blackwell Science Ltd, Oxford, UK. http://dx.doi.org/10.1002/9780470757161.ch1.

Dorschel, B., Afanasyeva, V., Bender, M., Dreutter, S., Eisermann, H., Gebhardt, A.C., Hansen, K., Hebbeln, D., Jackson, R., Jeltsch-Thömmes, A., Jensen, L., Kolling, H., Le Duc, C., Lenz, K.-F., Lübben, B., Madaj, L., Martínez-Méndez, G., Meyer-Schack, B., Schade, T., Siccha, M., Slabon, P., Wangner, D.J., 2015. Past Greenland Ice Sheet dynamics, Palaeoceanography and Plankton Ecology in the Northeast Baffin Bay - Cruise No. MSM44 'BAFFEAST' - June 30-July 30, 2015 - Nuuk (Greenland), MARIA S. MERIAN-Berichte. https://doi.org/10.2312/cr_msm2344.

Drinkwater, K.F., 1996. Atmospheric and Oceanic Variability in the Northwest Atlantic During the 1980s and Early 1990s. Journal of Northwest Atlantic Fishery Science, 18, 77-97.

Dunbar, M. and Dunbar, M. J., 1972. The history of the NorthWater, Proceedings of the Royal Society of Edinburgh, Section B Biological Sciences, 72, 231–241.

Dyke, A.S., 2008. The Steensby Inlet Ice Stream in the context of the deglaciation of Northern Baffin Island, Eastern Arctic Canada. 33, 573-592.

Dyke, A.S., Andrews, J.T., Clark, P.U., England, J.H., Miller, G.H., Shaw, J., Veillette, J.J., 2002. The Laurentide and Innuitian ice sheets during the Last Glacial Maximum. Quaternary Science Reviews 21, 9-31.

Dyke, A.S., Dale, J.E., McNeely, R.N., 1996a. Marine molluscs as indicators of environmental change in glaciated North America and Greenland during the last 18,000 years. Geographie Physique Et Quaternaire 50, 125-184.

Dyke, A.S., England, J., Reimnitz, E., Jette, H., 1997. Changes in driftwood delivery to the Canadian arctic archipelago: The hypothesis of postglacial oscillations of the transpolar drift. Arctic 50, 1-16.

Dyke, A.S., Hooper, J., Savelle, J.M., 1996b. A history of sea ice in the Canadian Arctic Archipelago based on postglacial remains of the bowhead whale (Balaena mysticetus). Arctic 49, 235-255.

Eglinton, G., Hamilton, R.J., 1963. The distribution of alkanes. In: T Swan (Ed.). Chemical Plant Taxonomy. Academy Press: London, 187-208.

Eglinton, T.I., Eglinton, G., 2008. Molecular proxies for paleoclimatology. Earth and Planetary Science Letters 275, 1-16.

Eglinton, T.I., Repeta, D.J., 2003. Organic Matter in the Contemporary Ocean. Treatise on Geochemistry 6, 625.

Ehlers, J., Gibbard, P. L. & Hughes, P. D. (eds), 2011. Quaternary Glaciation Extent and Chronology: a Closer Look. Developments in Quaternary Science 15 (Elsevier, Amsterdam, 2011).

England, J., Atkinson, N., Bednarski, J., Dyke, A.S., Hodgson, D.A., Cofaigh, C.O., 2006. The Innuitian Ice Sheet: configuration, dynamics and chronology. Quaternary Science Reviews 25, 689-703.

Fahl, K., Stein, R., 1997. Modern organic carbon deposition in the Laptev sea and the adjacent continental slope: Surface water productivity vs. terrigenous input. Organic Geochemistry 26, 379-390.

Fahl, K., Stein, R., 1999. Biomarkers as organic-carbon-source and environmental indicators in the Late Quaternary Arctic Ocean: problems and perspectives. Marine Chemistry 63, 293-309.

Fahl, K., Stein, R., 2007. Biomarker records, organic carbon accumulation, and river discharge in the Holocene southern Kara Sea (Arctic Ocean). Geo-Marine Letters 27, 13-25.

Fahl, K., Stein, R., 2012. Modern seasonal variability and deglacial/Holocene change of central Arctic Ocean sea-ice cover: New insights from biomarker proxy records. Earth and Planetary Science Letters 351, 123-133.

Fahl, K., Stein, R., Gaye-Haake, B., Gebhardt, C., Kodina, L.A., Unger, D., Ittekkot, V., 2003. Biomarkers in surface sediments from the Ob and Yenisei estuaries and the southern Kara Sea: evidence for particulate organic carbon sources, pathways, and degradation. In: Stein R, Fahl K, Fütterer DK, Galimov EM, Stepanets OV (eds), Siberian River Run-off in the Kara Sea: Characterization, Quantification, Variablity, and Environmental Significance. Proceedings in Marine Sciences Vol 6, Elsevier, Amsterdam, pp 329-348.

Fahrbach, E., Meincke, J., Østerhus, S., Rohardt, G., Schauer, U., Tverberg, V., Verduin, J., 2001. Direct measurements of volume transports through Fram Strait. Polar Research 20, 217-224.

Fairbanks, R.G., 1989. A 17,000-year glacio-eustatic sea level record: influence of glacial melting rates on the Younger Dryas event and deep-ocean circulation. Nature 342, 637-642.

Fichot, C.G., Kaiser, K., Hooker, S.B., Amon, R.M.W., Babin, M., Bélanger, S., Walker, S.A., Benner, R., 2013. Pan-Arctic distributions of continental runoff in the Arctic Ocean. Scientific Reports 3, 1053.

Finkelstein, S.A., Gaiewski, K., 2007. A palaeolimnological record of diatomcommunity dynamics and late-Holocene climatic changes from Prescott Island, Nunavut, central Canadian Arctic. Holocene 17, 803-812.

Fisher, D.A.K., R. M., 2003. Holocene ice-core climate history – a multi-variable approach. Global Change in the Holocene In Mackay, A., Battarbee, R., Birks, J. & Oldfield, F. (eds.):, 281–292.

Fleming, K., Lambeck, K., 2004. Constraints on the Greenland Ice Sheet since the Last Glacial Maximum from sea-level observations and glacial-rebound models. Quaternary Science Reviews 23, 1053-1077.

Fredskild, B., 1985a. Holocene pollen records from West Greenland. In Quaternary Environments, Eastern Canadian Arctic, Baffin Bay and Western Greenland. Andrews JT (ed.). Allen and Unwin: London. , 643–681.

Fredskild, B., 1985b. The Holocene vegetational development of Tugtuligssuaq and Qeqertat, Northwest Greenland. Meddelelser om Grønland, Geoscience 14, 1–20.

Funder, S., Goosse, H., Jepsen, H., Kaas, E., Kjaer, K.H., Korsgaard, N.J., Larsen, N.K., Linderson, H., Lysa, A., Moller, P., Olsen, J., Willerslev, E., 2011. A 10,000-Year Record of Arctic Ocean Sea-Ice Variability-View from the Beach. Science 333, 747-750.

Gajewski, K., 2015. Quantitative reconstruction of Holocene temperatures across the Canadian Arctic and Greenland. Global and Planetary Change 128, 14-23.

Georgiadis, E., Giraudeau, J., Jennings, A., Limoges, A., Jackson, R., Ribeiro, S., Massé, G., 2020. Local and regional controls on Holocene sea ice dynamics and oceanography in Nares Strait, Northwest Greenland. Marine Geology 422, 106115.

Georgiadis, E., Giraudeau, J., Martinez, P., Lajeunesse, P., St-Onge, G., Schmidt, S., Masse, G., 2018. Deglacial to postglacial history of Nares Strait, Northwest Greenland: a marine perspective from Kane Basin. Climate of the Past 14, 1991-2010.

Gersonde, R., Crosta, X., Abelmann, A., Armand, L., 2005. Sea-surface temperature and sea ice distribution of the Southern Ocean at the EPILOG Last Glacial Maximum - A circum-

Antarctic view based on siliceous microfossil records. Quaternary Science Reviews 24, 869-896.

Gibb, O.T., Steinhauer, S., Fréchette, B., de Vernal, A., Hillaire-Marcel, C., 2015. Diachronous evolution of sea surface conditions in the Labrador Sea and Baffin Bay since the last deglaciation. The Holocene 25, 1882-1897.

Giraudeau, J., Georgiadis, E., Caron, M., Martinez, P., St-Onge, G., Billy, I., Lebleu, P., Ther, O., Massé, G., 2020. A high-resolution elemental record of post-glacial lithic sedimentation in Upernavik Trough, western Greenland: History of ice-sheet dynamics and ocean circulation changes over the last 9100 years. Global and Planetary Change 191, 103217.

Goñi, M.A., Yunker, M.B., Macdonald, R.W., Eglinton, T.I., 2000. Distribution and sources of organic biomarkers in arctic sediments from the Mackenzie River and Beaufort Shelf. Marine Chemistry 71, 23-51.

Gosselin, M., Levasseur, M., Wheeler, P.A., Horner, R.A., Booth, B.C., 1997. New measurements of phytoplankton and ice algal production in the Arctic Ocean. Deep Sea Research Part II: Topical Studies in Oceanography 44, 1623-1644.

Gow, A.J., Tucker, W.B., 1987. Physical Properties of Sea Ice Discharged from Fram Strait. 236, 436-439.

Gowan, E.J., Zhang, X., Khosravi, S., Rovere, A., Stocchi, P., Hughes, A.L.C., Gyllencreutz, R., Mangerud, J., Svendsen, J.-I., Lohmann, G., 2021. A new global ice sheet reconstruction for the past 80 000 years. Nature Communications 12, 1199.

Gradinger, R., 2009. Sea-ice algae: Major contributors to primary production and algal biomass in the Chukchi and Beaufort Seas during May/June 2002. Deep Sea Research Part II: Topical Studies in Oceanography 56, 1201-1212.

Grammatikopoulos, T., McKen, A., Hamilton, C., Christiansen, O., 2002. Vanadium-bearing magnetite and ilmenite mineralization and beneficiation from the Sinarsuk V-Ti project, West Greenland. Cim Bulletin 95, 87-95.

Gualtieri, L., Vartanyan, S., Brigham-Grette, J., Anderson, P.M., 2003. Pleistocene raised marine deposits on Wrangel Island, northeast Siberia and implications for the presence of an East Siberian ice sheet. Quaternary Research 59, 399-410.

Hansen, K.E., Giraudeau, J., Wacker, L., Pearce, C., Seidenkrantz, M.S., 2020. Reconstruction of Holocene oceanographic conditions in the Northeastern Baffin Bay. Climate of the Past. 16, 1075–1095.

Harff, J., Perner, K., Moros, M.E., 2016. Deglaciation history, coastal development, and environmental change in West Greenland during the Holocene: Results of the R/V "Maria S. Merian" expedition MSM05/03 15th June to 4th July 2007. Meereswissenschaftliche Berichte, Warnemünde 99, doi:10.12754/msr-12016-10099.

Hawkings, J.R., Wadham, J.L., Tranter, M., Lawson, E., Sole, A., Cowton, T., Tedstone, A.J., Bartholomew, I., Nienow, P., Chandler, D., Telling, J., 2015. The effect of warming climate on nutrient and solute export from the Greenland Ice Sheet. Geochemical Perspectives Letters 1, 94-104.

He, D., Simoneit, B.R.T., Xu, Y., Jaffé, R., 2016. Occurrence of unsaturated C25 highly branched isoprenoids (HBIs) in a freshwater wetland. Organic Geochemistry 93, 59-67.

Hebbeln, D., Wefer, G., 1991. Effects of ice coverage and ice-rafted material on sedimentation in the Fram Strait. Nature 350, 409-411.

Hedges, J.I., Clark, W.A., Quay, P.D., Richey, J.E., Devol, A.H., Santos, M., 1986. Compositions and fluxes of particulate organic material in the Amazon River1. Limnology and Oceanography 31, 717-738.

Hill, V., Ardyna, M., Lee, S.H., Varela, D.E., 2018. Decadal trends in phytoplankton production in the Pacific Arctic Region from 1950 to 2012. Deep Sea Research Part II: Topical Studies in Oceanography 152, 82-94.

Hillaire-Marcel, C., de Vernal, A., 2008. Stable isotope clue to episodic sea ice formation in the glacial North Atlantic. Earth and Planetary Science Letters 268, 143-150.

Hillaire-Marcel, C., Maccali, J., Not, C., Poirier, A., 2013. Geochemical and isotopic tracers of Arctic sea ice sources and export with special attention to the Younger Dryas interval. Quaternary Science Reviews 79, 184-190.

Holland, M.M., Bitz, C.M., Tremblay, B., 2006. Future abrupt reductions in the summer Arctic sea ice. Geophysical Research Letters 33, 10.1029/2006GL028024.

Hopmans, E.C., Weijers, J.W.H., Schefuß, E., Herfort, L., Sinninghe Damsté, J.S., Schouten, S., 2004. A novel proxy for terrestrial organic matter in sediments based on branched and isoprenoid tetraether lipids. Earth and Planetary Science Letters 224, 107-116.

Hörner, T., Stein, R., Fahl, K., Birgel, D., 2016. Post-glacial variability of sea ice cover, river run-off and biological production in the western Laptev Sea (Arctic Ocean) - A high-resolution biomarker study. Quaternary Science Reviews 143, 133-149.

Humlum, O., 1985. The Glaciation level in West Greenland. Arctic and Alpine Research 17, 311-319.

Hurrell, J.W., Kushnir, Y., Visbeck, M., 2001. Climate - The North Atlantic oscillation. Science 291, 603-605.

Isaksson, E., Kohler, J., Pohjola, V., Moore, J., Igarashi, M., Karlöf, L., Martma, T., Meijer, H., Motoyama, H., Vaikmäe, R., van de Wal, R.S.W., 2005. Two ice-core δ18O records from Svalbard illustrating climate and sea-ice variability over the last 400 years. 15, 501-509.

Ittekkot, V., Haake, B., M., B., Nair, R., V., R., 1992. Organic carbon removal in the sea: the continental connection. In: Summerhayes CP, Prell WL, Emeis KC (eds Upwelling systems: evolution since the early Miocene. Geological Society Special, London, pp 167–176.

Iversen, M.H., Robert, M.L., 2015. Ballasting effects of smectite on aggregate formation and export from a natural plankton community. Marine Chemistry 175, 18-27.

Jackson, R., Carlson, A.E., Hillaire-Marcel, C., Wacker, L., Vogt, C., Kucera, M., 2017. Asynchronous instability of the North American-Arctic and Greenland ice sheets during the last deglaciation. Quaternary Science Reviews 164, 140-153.

Jakobsson, M., 2002. Hypsometry and volume of the Arctic Ocean and its constituent seas. Geochemistry Geophysics Geosystems 3, 1-18.

Jakobsson, M., Grantz, A., Kristoffersen, Y., Macnab, R., MacDonald, R.W., Sakshaug, E., Stein, R., Jokat, W., 2004. The Arctic Ocean: Boundary Conditions and Background Information, in: Stein, R., MacDonald, R.W. (Eds.), The Organic Carbon Cycle in the Arctic Ocean. Springer Berlin Heidelberg, Berlin, Heidelberg, pp. 1-32.

Jakobsson, M., Long, A., Ingolfsson, O., Kjaer, K.H., Spielhagen, R.F., 2010. New insights on Arctic Quaternary climate variability from palaeo-records and numerical modelling. Quaternary Science Reviews 29, 3349-3358.

Jennings, A., Andrews, J., Pearce, C., Wilson, L., Ólfasdótttir, S., 2015. Detrital carbonate peaks on the Labrador shelf, a 13–7ka template for freshwater forcing from the Hudson Strait outlet of the Laurentide Ice Sheet into the subpolar gyre. Quaternary Science Reviews 107, 62-80.

Jennings, A., Andrews, J., Wilson, L., 2011a. Holocene environmental evolution of the SE Greenland Shelf North and South of the Denmark Strait: Irminger and East Greenland current interactions. Quaternary Science Reviews 30, 980-998.

Jennings, A.E., 1993. The Quaternary history of Cumberland Sound, southeastern Baffin-Island - The marine evidence. Geographie Physique Et Quaternaire 47, 21-42.

Jennings, A.E., Andrews, J.T., Oliver, B., Walczak, M., Mix, A., 2019. Retreat of the Smith Sound Ice Stream in the Early Holocene. Boreas 48, 825-840.

Jennings, A.E., Knudsen, K.L., Hald, M., Hansen, C.V., Andrews, J.T., 2002. A mid-Holocene shift in Arctic sea-ice variability on the East Greenland Shelf. Holocene 12, 49-58.

Jennings, A.E., Sheldon, C., Cronin, T.M., Francus, P., Stoner, J., Andrews, J., 2011b. The Holocene hostory of Nares Strait: Transition from Glacial Bay to Arctic-Atlantic throughflow. Oceanography 24, 26-41.

Jennings, A.E., Walton, M.E., Cofaigh, C.O., Kilfeather, A., Andrews, J.T., Ortiz, J.D., De Vernal, A., Dowdeswell, J.A., 2014. Paleoenvironments during Younger Dryas-Early Holocene retreat of the Greenland Ice Sheet from outer Disko Trough, central west Greenland. Journal of Quaternary Science 29, 27-40.

Ji, Z., Jin, H., Stein, R., Li, Z., Bai, Y., Li, H., Zhang, Y., Chen, J., 2019. Distribution and Sources of Organic Matter in Surface Sediments of the Northern Bering and Chukchi Seas by Using Bulk and Tetraether Proxies. Journal of Ocean University of China 18, 563-572.

Jones, E.P., Swift, J.H., Anderson, L.G., Lipizer, M., Civitarese, G., Falkner, K.K., Kattner, G., McLaughlin, F., 2003. Tracing Pacific water in the North Atlantic Ocean. Journal of Geophysical Research-Oceans 108, 3116, 3110.1029/2001JC001141.

Jones, P.D., Jonsson, T., Wheeler, D., 1997. Extension to the North Atlantic oscillation using early instrumental pressure observations from Gibraltar and south-west Iceland. 17, 1433-1450.

Jones, P.D., Mann, M.E., 2004. Climate over past millennia. Reviews of Geophysics 42, 1-42.

Jones, P.D., Osborn, T.J., Briffa, K.R., 2001. The evolution of climate over the last millennium. Science 292, 662-667.

Joughin, I., Smith, B.E., Howat, I.M., Scambos, T., Moon, T., 2010. Greenland flow variability from ice-sheet-wide velocity mapping. Journal of Glaciology 56, 415-430.

Justwan, A., Koc, N., 2008. A diatom based transfer function for reconstructing sea ice concentrations in the North Atlantic. Marine Micropaleontology 66, 264-278.

Justwan, A., Koç, N., Jennings, A.E., 2008. Evolution of the Irminger and East Icelandic Current systems through the Holocene, revealed by diatom-based sea surface temperature reconstructions. Quaternary Science Reviews 27, 1571-1582.

Kaplan, M.R., Wolfe, A.P., Miller, G.H., 2002. Holocene environmental variability in southern Greenland inferred from lake sediments. Quaternary Research 58, 149-159.

Kattner, G., Lobbes, J.M., Fitznar, H.P., Engbrodt, R., Nothig, E.M., Lara, R.J., 1999. Tracing dissolved organic substances and nutrients from the Lena River through Laptev Sea (Arctic). Marine Chemistry 65, 25-39.

Kaufman, D.S., Ager, T.A., Anderson, N.J., Anderson, P.M., Andrews, J.T., Bartlein, P.J., Brubaker, L.B., Coats, L.L., Cwynar, L.C., Duvall, M.L., Dyke, A.S., Edwards, M.E., Eisner, W.R., Gajewski, K., Geirsdottir, A., Hu, F.S., Jennings, A.E., Kaplan, M.R., Kerwin, M.N., Lozhkin, A.V., MacDonald, G.M., Miller, G.H., Mock, C.J., Oswald, W.W., Otto-Bliesner, B.L., Porinchu, D.F., Ruhland, K., Smol, J.P., Steig, E.J., Wolfe, B.B., 2004. Holocene thermal maximum in the western Arctic (0-180 degrees W). Quaternary Science Reviews 23, 529-560.

Kaufman, D.S., Axford, Y.L., Henderson, A.C.G., McKay, N.P., Oswald, W.W., Saenger, C., Anderson, R.S., Bailey, H.L., Clegg, B., Gajewski, K., Hu, F.S., Jones, M.C., Massa, C., Routson, C.C., Werner, A., Wooller, M.J., Yu, Z., 2016. Holocene climate changes in eastern Beringia (NW North America) - A systematic review of multi-proxy evidence. Quaternary Science Reviews 147, 312-339.

Keigwin, L.D., Jones, G.A., Froelich, P.N., 1992. A 15,000 year paleoenvironmental record from Meiji Seamount, far northwestern Pacific. Earth and Planetary Science Letters 111, 425-440.

Key, R.M., Kozyr, A., Sabine, C.L., Lee, K., Wanninkhof, R., Bullister, J.L., Feely, R.A., Millero, F.J., Mordy, C., Peng, T.-H., 2004. A global ocean carbon climatology: Results from Global Data Analysis Project (GLODAP). Global Biogeochemical Cycles 18, GB4031, 10.1029/2004GB002247.

Kinnard, C., Zdanowicz, C.M., Fisher, D.A., Isaksson, E., de Vernal, A., Thompson, L.G., 2011. Reconstructed changes in Arctic sea ice over the past 1,450 years. Nature 479, 509-U231.

Knies, J., Cabedo-Sanz, P., Belt, S.T., Baranwal, S., Fietz, S., Rosell-Mele, A., 2014. The emergence of modern sea ice cover in the Arctic Ocean. Nature Communications 5, 5608, https://doi.org/5610.1038/ncomms6608.

Knies, J., Stein, R., 1998. New aspects of organic carbon deposition and its paleoceanographic implications along the northern Barents Sea margin during the last 30,000 years. Paleoceanography 13, 384-394.

Knudsen, K.L., Jiang, H., Jansen, E., Eiriksson, J., Heinemeier, J., Seidenkrantz, M.S., 2004. Environmental changes off North Iceland during the deglaciation and the Holocene: foraminifera, diatoms and stable isotopes. Marine Micropaleontology 50, 273-305.

Knudsen, K.L., Stabell, B., Seidenkrantz, M.S., Eiriksson, J., Blake, W., 2008. Deglacial and Holocene conditions in northernmost Baffin Bay: sediments, foraminifera, diatoms and stable isotopes. Boreas 37, 346-376.

Koc, N., Jansen, E., Haflidason, H., 1993. Paleoceanographic reconstruction of surface ocean conditions in the Greenland, Iceland and Norwegian Seas through the last 14 ka based on diatoms. Quaternary Science Reviews 12, 115-140.

Kolling, H.M., 2017a. Decadal to centennial variability of (sub-) Arctic sea ice distribution and its paleoenvironmental significance. University of Bremen. PhD dissertation.

Kolling, H.M., Stein, R., Fahl, K., Perner, K., Moros, M., 2017. Short-term variability in late Holocene sea ice cover on the East Greenland Shelf and its driving mechanisms. Palaeogeography Palaeoclimatology Palaeoecology 485, 336-350.

Kolling, H.M., Stein, R., Fahl, K., Perner, K., Moros, M., 2018. New insights into sea ice changes over the past 2.2 kyr in Disko Bugt, West Greenland. arktos 4, 11.

Kolling, H.M., Stein, R., Fahl, K., Sadatzki, H., de Vernal, A., Xiao, X., 2020. Biomarker distributions in (sub)-Arctic surface sediments and their potential for sea-ice reconstructions. Geochemistry, Geophysics, Geosystems n/a, e2019GC008629.

Krawczyk, D.W., Witkowski, A., Moros, M., Lloyd, J.M., Hoyer, J.L., Miettinen, A., Kuijpers, A., 2017. Quantitative reconstruction of Holocene sea ice and sea surface temperature off West Greenland from the first regional diatom data set. Paleoceanography 32, 18-40.

Kremer, A., 2018a. The variability of sea ice in the Fram Strait throughout glacial-interglacial transitions of the Late Quaternary. University of Bremen. PhD dissertation.

Kremer, A., Stein, R., Fahl, K., Ji, Z., Yang, Z., Wiers, S., Matthiessen, J., Forwick, M., Lowemark, L., O'Regan, M., Chen, J., Snowball, I, 2018. Changes in sea ice cover and ice sheet extent

at the Yermak Plateau during the last 160 ka - Reconstructions from biomarker records. Quaternary Science Reviews 182, 93-108.

Krishnamurthy, R.V., Machavaram, M., Baskaran, M., Brooks, J.M., Champ, M.A., 2001. Organic Carbon Flow in the Ob, Yenisey Rivers and Kara Sea of the Arctic Region. Marine Pollution Bulletin 42, 726-732.

Kutzbach, J., Webb Ih, T., Roberts, N., Wright, H.E., Ruddiman, W., Street-Perrott, F., Bartlein, R., 1993. Global climates since the last glacial maximum, Vegetational, lake-level, and climatic history of the Near East and Southwest Asia. University of Minnesota Press New York, pp. 194-220.

Kwok, R., Spreen, G., Pang, S., 2013. Arctic sea ice circulation and drift speed: Decadal trends and ocean currents. 118, 2408-2425.

Lalande, C., Nothig, E.M., Bauerfeind, E., Hardge, K., Beszczynska-Moller, A., Fahl, K., 2016. Lateral supply and downward export of particulate matter from upper waters to the seafloor in the deep eastern Fram Strait. Deep-Sea Research Part I-Oceanographic Research Papers 114, 78-89.

Langner, M., Mulitza, S., 2019. Technical note: PaleoDataView – a software toolbox for the collection, homogenization and visualization of marine proxy data. Climate of the Past 15, 2067-2072.

Larsen, N.K., Strunk, A., Levy, L.B., Olsen, J., Bjørk, A., Lauridsen, T.L., Jeppesen, E., Davidson, T.A., 2017. Strong altitudinal control on the response of local glaciers to Holocene climate change in southwest Greenland. Quaternary Science Reviews 168, 69-78.

Lasher, G.E., Axford, Y., 2019. Medieval warmth confirmed at the Norse Eastern Settlement in Greenland. Geology 47, 267-270.

Laskar, J., Robutel, P., Joutel, F., Gastineau, M., Correia, A.C.M., Levrard, B., 2004. A long-term numerical solution for the insolation quantities of the Earth. Astronomy & Astrophysics 428, 261-285.

Lecavalier, B.S., Fisher, D.A., Milne, G.A., Vinther, B.M., Tarasov, L., Huybrechts, P., Lacelle, D., Main, B., Zheng, J., Bourgeois, J., Dyke, A.S., 2017. High Arctic Holocene temperature record from the Agassiz ice cap and Greenland ice sheet evolution. Proceedings of the National Academy of Sciences 114, 5952.

Lecavalier, B.S., Milne, G.A., Simpson, M.J.R., Wake, L., Huybrechts, P., Tarasov, L., Kjeldsen, K.K., Funder, S., Long, A.J., Woodroffe, S., Dyke, A.S., Larsen, N.K., 2014. A model of Greenland ice sheet deglaciation constrained by observations of relative sea level and ice extent. Quaternary Science Reviews 102, 54-84.

Ledu, D., Rochon, A., de Vernal, A., Barletta, F., St-Onge, G., 2010a. Holocene sea ice history and climate variability along the main axis of the Northwest Passage, Canadian Arctic. Paleoceanography 25, p. PA2213, 10.1029/2009PA001817.

Ledu, D., Rochon, A., de Vernal, A., St-Onge, G., 2008. Palynological evidence of Holocene climate change in the eastern Arctic: a possible shift in the Arctic oscillation at the millennial time scale. Canadian Journal of Earth Sciences 45, 1363-1375.

Ledu, D., Rochon, A., de Vernal, A., St-Onge, G., 2010b. Holocene paleoceanography of the northwest passage, Canadian Arctic Archipelago. Quaternary Science Reviews 29, 3468-3488.

Leu, E., Mundy, C.J., Assmy, P., Campbell, K., Gabrielsen, T.M., Gosselin, M., Juul-Pedersen, T., Gradinger, R., 2015. Arctic spring awakening – Steering principles behind the phenology of vernal ice algal blooms. Progress in Oceanography 139, 151-170.

Levac, E., De Vernal, A., Blake, W., 2001. Sea-surface conditions in northernmost Baffin Bay during the Holocene: palynological evidence. Journal of Quaternary Science 16, 353-363.

Leventer, A., 1998. The fate of Antarctic "sea ce diatoms" and their use as paleoenvironmental indicators. Antarctic Research Series, 73. 121-137.

Levy, L.B., Larsen, N.K., Davidson, T.A., Strunk, A., Olsen, J., Jeppesen, E.J.J.o.Q.S., 2017. Contrasting evidence of Holocene ice margin retreat, south-western Greenland. 32, 604.

Lewis, K.M., van Dijken, G.L., Arrigo, K.R., 2020. Changes in phytoplankton concentration now drive increased Arctic Ocean primary production. Science 369, 198-202.

Limoges, A., Ribeiro, S., Weckstrom, K., Heikkila, M., Zamelczyk, K., Andersen, T.J., Tallberg, P., Masse, G., Rysgaard, S., Norgaard-Pedersen, N., Seidenkrantz, M.S., 2018. Linking the Modern Distribution of Biogenic Proxies in High Arctic Greenland Shelf Sediments to Sea Ice, Primary Production, and Arctic-Atlantic Inflow. Journal of Geophysical Research-Biogeosciences 123, 760-786.

Lisiecki, L.E., Raymo, M.E., 2005. A Pliocene-Pleistocene stack of 57 globally distributed benthic delta O-18 records (vol 20, art no PA1003, 2005). Paleoceanography 20.

Ljungqvist, F.C., 2010. A New reconstruction of temperature variablity in the extra-Tropical Northern Hemisphere during the last two millennia. Geografiska Annaler Series a-Physical Geography 92A, 339-351.

Lloyd, J., Moros, M., Perner, K., Telford, R.J., Kuijpers, A., Jansen, E., McCarthy, D., 2011. A 100 yr record of ocean temperature control on the stability of Jakobshavn Isbrae, West Greenland. Geology 39, 867-870.

Lloyd, J.M., Kuijpers, A., Long, A., Moros, M., Park, L.A., 2007. Foraminiferal reconstruction of mid- to late-Holocene ocean circulation and climate variability in Disko Bugt, West Greenland. Holocene 17, 1079-1091.

Lloyd, J.M., Park, L.A., Kuijpers, B., Moros, M., 2005. Early holocene palaeoceanography and deglacial chronology of Disko Bugt, West Greenland. Quaternary Science Reviews 24, 1741-1755.

Lobbes, J.M., Fitznar, H.P., Kattner, G., 2000. Biogeochemical characteristics of dissolved and particulate organic matter in Russian rivers entering the Arctic Ocean. Geochimica Et Cosmochimica Acta 64, 2973-2983.

Locarnini, R. A., Mishonov, A. V, Antonov, J. I., Boyer, T. P., Garcia, H. E., Baranova, O. K., Zweng, M. M., Paver, C. R., Reagan, J. R., Johnson, D. R., Hamilton, M., and Seidov, D., 2013. WORLD OCEAN ATLAS 2013: Temperature Volume 1, edited by: Mishonov, A., Technical Ed., NOAA Atlas NESDIS 73.

Lochte, A.A., Repschlager, J., Seidenkrantz, M.S., Kienast, M., Blanz, T., Schneider, R.R., 2019. Holocene water mass changes in the Labrador Current. Holocene 29, 676-690.

Long, A.J., Roberts, D.H., 2002. A revised chronology for the 'Fjord Stade' moraine in Disko Bugt, west Greenland. Journal of Quaternary Science 17, 561-579.

Long, A.J., Roberts, D.H., 2003. Late Weichselian deglacial history of Disko Bugt, West Greenland, and the dynamics of the Jakobshavns Isbrae ice stream. Boreas 32, 208-226.

Long, A.J., Woodroffe, S.A., Roberts, D.H., Dawson, S., 2011. Isolation basins, sea-level changes and the Holocene history of the Greenland Ice Sheet. Quaternary Science Reviews 30, 3748-3768.

Macdonald, R.W., Sakshaug, E., Stein, R., 2004. The Arctic Ocean: Modern Status and Recent Climate Change, In: Stein, R. and Macdonald, R.W. (Eds.), The Organic Carbon Cycle in the Arctic Ocean. Springer-Verlag, Berlin, 6-21.

Manabe, S., Spelman, M.J., Stouffer, R.J., 1992. Transient Responses of a Coupled Ocean Armosphere Model to gradual changes of atmospheric CO2 .2. Seasonal Response. Journal of Climate 5, 105-126.

Mann, P.J., Eglinton, T.I., McIntyre, C.P., Zimov, N., Davydova, A., Vonk, J.E., Holmes, R.M., Spencer, R.G.M., 2015. Utilization of ancient permafrost carbon in headwaters of Arctic fluvial networks. Nature Communications 6, 7856.

Masse, G., Belt, S.T., Crosta, X., Schmidt, S., Snape, I., Thomas, D.N., Rowland, S.J., 2011. Highly branched isoprenoids as proxies for variable sea ice conditions in the Southern Ocean. Antarctic Science 23, 487-498.

Massé, G., Belt, S.T., Sicre, M.-A., 2010. Arctic sea ice: high resolution reconstructions, In conference: Iceland in the Central Northern Atlantic : hotspot, sea currents and climate change (May, 2010), Plouzané, France, https://hal.univ-brest.fr/hal-00482053/document.

Matero, I.S.O., Gregoire, L.J., Ivanovic, R.F., Tindall, J.C., Haywood, A.M., 2017. The 8.2 ka cooling event caused by Laurentide ice saddle collapse. Earth and Planetary Science Letters 473, 205-214.

Matthiessen, J., de Vernal, A., Head, M., Okolodkov, Y., Zonneveld, K., Harland, R., 2005. Modem organic-walled dinoflagellate cysts in arctic marine environments and their (paleo-) environmental significance. Paläontologische Zeitschrift 79, 3-51.

Mayewski, P.A., Rohling, E.E., Stager, J.C., Karlen, W., Maasch, K.A., Meeker, L.D., Meyerson, E.A., Gasse, F., van Kreveld, S., Holmgren, K., Lee-Thorp, J., Rosqvist, G., Rack, F., Staubwasser, M., Schneider, R.R., Steig, E.J., 2004. Holocene climate variability. Quaternary Research 62, 243-255.

McCave, I.N., Andrews, J.T., 2019. Distinguishing current effects in sediments delivered to the ocean by ice. II. Glacial to Holocene changes in high latitude North Atlantic upper ocean flows. Quaternary Science Reviews 223, 105902.

McPhee, M.G., Proshutinsky, A., Morison, J.H., Steele, M., Alkire, M.B., 2009. Rapid change in freshwater content of the Arctic Ocean. Geophysical Research Letters 36, L10602, 10610.11029/12009GL037525.

Melling, H., Gratton, Y., Ingram, G., 2001. Ocean circulation within the North Water Polynya of Baffin Bay. Atmosphere-Ocean 39, 301-325.

Melling, H., Gratton, Y., Ingram, G., Melling, H., Gratton, Y., and Ingram, G., 2010: Ocean circulation within the North Water polynya of Baffin Bay Ocean Circulation within the North Water Polynya of Baffin Bay, Atmosphere-Ocean, 39, 301–325, https://doi.org/10.1080/07055900.2001.9649683.

Meyers, P.A., 1994. Preservation of elemental and isotopic source identification of sedimentary organic matter. Chemical Geology 114, 289-302.

Meyers, P.A., 1997. Organic geochemical proxies of paleoceanographic, paleolimnologic, and paleoclimatic processes. Organic Geochemistry 27, 213-250.

Moller, H.S., Jensen, K.G., Kuijpers, A., Aagaard-Sorensen, S., Seidenkrantz, M.S., Prins, M., Endler, R., Mikkelsen, N., 2006. Late-Holocene environment and climatic changes in Ameralik Fjord, southwest Greenland: evidence from the sedimentary record. Holocene 16, 685-695.

Morison, J., Kwok, R., Peralta-Ferriz, C., Alkire, M., Rigor, I., Andersen, R., Steele, M., 2012. Changing Arctic Ocean freshwater pathways. Nature 481, 66-70.

Moros, M., Emeis, K., Risebrobakken, B., Snowball, I., Kuijpers, A., McManus, J., Jansen, E., 2004. Sea surface temperatures and ice rafting in the Holocene North Atlantic: climate influences on Northern Europe and Greenland. Quaternary Science Reviews 23, 2113-2126.

Moros, M., Jensen, K.G., Kuijpers, A., 2006. Mid- to late-Holocene hydrological and climatic variability in Disko Bugt, central West Greenland. Holocene 16, 357-367.

Moros, M., Lloyd, J.M., Perner, K., Krawczyk, D., Blanz, T., de Vernal, A., Ouellet-Bernier, M.-M., Kuijpers, A., Jennings, A.E., Witkowski, A., Schneider, R., Jansen, E., 2016. Surface and sub-surface multi-proxy reconstruction of middle to late Holocene palaeoceanographic changes in Disko Bugt, West Greenland. Quaternary Science Reviews 132, 146-160.

Mudie, P.T., Rochon, A., Prins, M. A., Soenarjo, D., Troelstra, S., R., L., E., Scott, D. B., Roncaglia, L. & Kuijpers, A., 2004. Late Pleistocene–Holocene marine geology of Nares Strait region: Palaeoceanography from foraminifera and dinoflagellate cysts, sedimentology and stable isotopes. Polarforschung 74, 69–183.

Müller, J., Masse, G., Stein, R., Belt, S.T., 2009. Variability of sea-ice conditions in the Fram Strait over the past 30,000 years. Nature Geoscience 2, 772-776.

Müller, J., Stein, R., 2014. High-resolution record of late glacial and deglacial sea ice changes in Fram Strait corroborates ice-ocean interactions during abrupt climate shifts. Earth and Planetary Science Letters 403, 446-455.

Müller, J., Wagner, A., Fahl, K., Stein, R., Prange, M., Lohmann, G., 2011. Towards quantitative sea ice reconstructions in the northern North Atlantic: A combined biomarker and numerical modelling approach. Earth and Planetary Science Letters 306, 137-148.

Müller, J., Werner, K., Stein, R., Fahl, K., Moros, M., Jansen, E., 2012. Holocene cooling culminates in sea ice oscillations in Fram Strait. Quaternary Science Reviews 47, 1-14.

Navarro-Rodriguez, A., Belt, S.T., Knies, J., Brown, T.A., 2013. Mapping recent sea ice conditions in the Barents Sea using the proxy biomarker IP25: implications for palaeo sea ice reconstructions. Quaternary Science Reviews 79, 26-39.

Nesje, A., Dahl, S.O., 2001. The Greenland 8200 cal. yr BP event detected in loss-on ignition profiles in Norwegian lacustrine sediment sequences. Journal of Quaternary Science 16, 155-166.

Nesje, A., Matthews, J.A., Dahl, S.O., Berrisford, M.S., Andersson, C., 2001. Holocene glacier fluctuations of Flatebreen and winter-precipitation changes in the Jostedalsbreen region, western Norway, based on glaciolacustrine sediment records. Holocene 11, 267-280.

Newton, A.M.W., Knutz, P.C., Huuse, M., Gannon, P., Brocklehurst, S.H., Clausen, O.R., Gong, Y., 2017. Ice stream reorganization and glacial retreat on the northwest Greenland shelf. Geophysical Research Letters 44, 7826-7835.

Not, C., Hillaire-Marcel, C., 2012. Enhanced sea-ice export from the Arctic during the Younger Dryas. Nature Communication 3, 10.1038/ncomms1658.

Notz, D., Stroeve, J., 2018. The Trajectory Towards a Seasonally Ice-Free Arctic Ocean. Current Climate Change Reports 4, 407-416.

Nöthig, E.M., Lalande, C., Fahl, K., Metfies, K., Salter, I., Bauerfeind, E., 2020. Annual cycle of downward particle fluxes on each side of the Gakkel Ridge in the central Arctic Ocean. Philosophical Transactions of the Royal Society a-Mathematical Physical and Engineering Sciences 378.

NSIDC, 2020. National Snow and Ice Data Center – Arctic Sea Ice News and Analysis.

Oppenheimer, M., 1998. Global warming and the stability of the West Antarctic Ice Sheet. Nature 393, 325-332.

Osterman, L.E., Nelson, A.R., 1989. Latest Quaternary and Holocene paleoceanography of the eastern Baffin Island continental-shelf, Canada - Banthic Foraminiferal Evidence Canadian Journal of Earth Sciences 26, 2236-2248.

Ouellet-Bernier, M.M., de Vernal, A., Hillaire-Marcel, C., Moros, M., 2014. Paleoceanographic changes in the Disko Bugt area, West Greenland, during the Holocene. Holocene 24, 1573-1583.

Patton, H., Hubbard, A., Andreassen, K., Auriac, A., Whitehouse, P.L., Stroeven, A.P., Shackleton, C., Winsborrow, M., Heyman, J., Hall, A.M., 2017. Deglaciation of the Eurasian ice sheet complex. Quaternary Science Reviews 169, 148-172.

Perner, K., Moros, M., Jennings, A., Lloyd, J.M., Knudsen, K.L., 2012. Holocene palaeoceanographic evolution off West Greenland. Holocene 23, 374-387.

Perner, K., Moros, M., Lloyd, J.M., Kuijpers, A., Telford, R.J., Harff, J., 2011. Centennial scale benthic foraminiferal record of late Holocene oceanographic variability in Disko Bugt, West Greenland. Quaternary Science Reviews 30, 2815-2826.

Perner, K., Moros, M., Snowball, I., Lloyd, J.M., Kuijpers, A., Richter, T.O., 2013. Establishment of modern circulation pattern at c. 6000 cal a BP in Disko Bugt, central West Greenland: opening of the Vaigat Strait. Journal of Quaternary Science 28, 480-489.

Peterson, B.J., Holmes, R.M., McClelland, J.W., Vorosmarty, C.J., Lammers, R.B., Shiklomanov, A.I., Shiklomanov, I.A., Rahmstorf, S., 2002. Increasing river discharge to the Arctic Ocean. Science 298, 2171-2173.

Philander, S.G., 2008. Ed., Encyclopedia of global warming and climate change, vol. 2, 3 vols. Los Angeles: SAGE, pp. 519-522.

Pieńkowski, A.J., Gill, N.K., Furze, M.F., Mugo, S.M., Marret, F., Perreaux, A., 2017. Arctic sea-ice proxies: Comparisons between biogeochemical and micropalaeontological reconstructions in a sediment archive from Arctic Canada. The Holocene 27, 665-682.

Polyak, L., Alley, R.B., Andrews, J.T., Brigham-Grette, J., Cronin, T.M., Darby, D.A., Dyke, A.S., Fitzpatrick, J.J., Funder, S., Holland, M., Jennings, A.E., Miller, G.H., O'Regan, M., Savelle, J., Serreze, M., St. John, K., White, J.W.C., Wolff, E., 2010. History of sea ice in the Arctic. Quaternary Science Reviews 29, 1757-1778.

Porter, S.E., Mosley-Thompson, E.S., 2011. Extracting a History of Baffin Bay Sea Ice Extent from West Central Greenland Ice Cores, AGU Fall Meeting Abstracts, 2011AGUFMPP43B1812P.

Randelhoff, A., Lacour, L., Marec, C., Leymarie, E., Lagunas, J., Xing, X., Darnis, G., Penkerc'h, C., Sampei, M., Fortier, L., D'Ortenzio, F., Claustre, H., Babin, M., 2020. Arctic mid-winter phytoplankton growth revealed by autonomous profilers. Science Advances 6, eabc2678.

Rasmussen, S.O., Andersen, K.K., Svensson, A.M., Steffensen, J.P., Vinther, B.M., Clausen, H.B., Siggaard-Andersen, M.L., Johnsen, S.J., Larsen, L.B., Dahl-Jensen, D., Bigler, M., Rothlisberger, R., Fischer, H., Goto-Azuma, K., Hansson, M.E., Ruth, U., 2006. A new Greenland ice core chronology for the last glacial termination. Journal of Geophysical Research-Atmospheres 111, D06102.

Reimer, P.J., Bard, E., Bayliss, A., Beck, J.W., Blackwell, P.G., Ramsey, C.B., Buck, C.E., Cheng, H., Edwards, R.L., Friedrich, M., Grootes, P.M., Guilderson, T.P., Haflidason, H., Hajdas, I., Hatte, C., Heaton, T.J., Hoffmann, D.L., Hogg, A.G., Hughen, K.A., Kaiser, K.F., Kromer, B., Manning, S.W., Niu, M., Reimer, R.W., Richards, D.A., Scott, E.M., Southon, J.R., Staff, R.A., Turney, C.S.M., van der Plicht, J., 2013. INTCAL13 and Marine13 radiocarbon age calibration curves 0-50,000 years cal BP Radiocarbon 55, 1869-1887.

Reimnitz, E., Dethleff, D., Nurnberg, D., 1994. Contrasts in Arctic shelf sea-ice regimes and some implications - Beaufort Sea versus Laptev Sea. Marine Geology 119, 215-225.

Ren, J., Jiang, H., Seidenkrantz, M.S., Kuijpers, A., 2009. A diatom-based reconstruction of Early Holocene hydrographic and climatic change in a southwest Greenland fjord. Marine Micropaleontology 70, 166-176.

Renssen, H., Seppä, H., Crosta, X., Goosse, H., Roche, D.M., 2012. Global characterization of the Holocene Thermal Maximum. Quaternary Science Reviews 48, 7-19.

Retamal, L., Bonilla, S., Vincent, W.F., 2008. Optical gradients and phytoplankton production in the Mackenzie River and the coastal Beaufort Sea. Polar Biology 31, 363-379.

Ribeiro, S., Sejr, M.K., Limoges, A., Heikkila, M., Andersen, T.J., Tallberg, P., Weckstrom, K., Husum, K., Forwick, M., Dalsgaard, T., Masse, G., Seidenkrantz, M.S., Rysgaard, S., 2017. Sea ice and primary production proxies in surface sediments from a High Arctic Greenland fjord: Spatial distribution and implications for palaeoenvironmental studies. Ambio 46, S106-S118.

Ribergaard, M.H., Olsen, S.M., Mortensen, J., 2008. Oceanographic Investigations off West Greenland 2007. In: Scientific Council Meeting, June 2008, NAFO SCR Doc. 08/3 Avaialble at: https://archive.nafo.int/open/sc/2008/scr08-003.pdf.

Rignot, E., Kanagaratnam, P., 2006. Changes in the velocity structure of the Greenland ice sheet. Science 311, 986-990.

Rigor, I.G., Wallace, J.M., Colony, R.L., 2002. Response of Sea Ice to the Arctic Oscillation. Journal of Climate 15, 2648-2663.

Risebrobakken, B., Dokken, T., Smedsrud, L.H., Andersson, C., Jansen, E., Moros, M., Ivanova, E.V., 2011. Early Holocene temperature variability in the Nordic Seas: The role of oceanic heat advection versus changes in orbital forcing. Paleoceanography 26, PA4206, 4210.1029/2011PA002117.

Robinson, N., Eglinton, G., Brassell, S.C., Cranwell, P.A., 1984. Dinoflagellate origin for sedimentary 4-alpha-methylsteroids and 5-alpha(H)-stanols. Nature 308, 439-442.

Rochon, A., de Vernal, A., Turon, J.L., Matthießen, J., Head, M.J., 1999. Distribution of recent dinoflagellate cysts in surface sediments from the North Atlantic Ocean and adjacent seas in relation to sea-surface parameters. American Association of Stratigraphic Palynologists Contribution Series 35, 1-146.

Roncaglia, L., Kuijpers, A., 2004. Palynofacies analysis and organic-walled dinoflagellate cysts in late-Holocene sediments from Igaliku Fjord, South Greenland. The Holocene 14, 172-184.

Rudels, B., Korhonen, M., Schauer, U., Pisarev, S., Rabe, B., Wisotzki, A., 2015. Circulation and transformation of Atlantic water in the Eurasian Basin and the contribution of the Fram Strait inflow branch to the Arctic Ocean heat budget. Progress in Oceanography 132, 128-152.

Rudels, B., Meyer, R., Fahrbach, E., Ivanov, V.V., Osterhus, S., Quadfasel, D., Schauer, U., Tverberg, V., Woodgate, R.A., 2000. Water mass distribution in Fram Strait and over the Yermak Plateau in summer 1997. Annales Geophysicae-Atmospheres Hydrospheres and Space Sciences 18, 687-705.

Sadler, H.E., 1976. Water, Heat, and Salt Transports though Nares Strait, Ellesmere Island. Journal of the Fisheries Research Board of Canada 33, 2286-2295.

Saini, J., Stein, R., Fahl, K., Weiser, J., Hebbeln, D., submitted. Holocene variability in sea ice and primary productivity in the Baffin Bay-Labrador Sea- A N-S transect study. (submitted to Boreas - International Journal of Quaternary Sciences on March, 26th, 2021).

Saini, J., Stein, R., Fahl, K., Weiser, J., Hebbeln, D., Hillaire-Marcel, C., de Vernal, A., 2020. Holocene variability in sea ice and primary productivity in the northeastern Baffin Bay. arktos 6, 55-73.

Sakshaug, E., 2004. Primary and secondary production in the Arctic seas. In: Stein, R., Macdonald, R.W. (Eds.), The Organic Carbon Cycle in the Arctic Ocean. Springer, Berlin 80, 57-82.

Sarnthein, M., Balmer, S., Grootes, P.M., Mudelsee, M., 2015. Planktic and benthic 14C reservoir ages for three ocean basins, calibrated by a suite of 14C plateaus in the glacial-to-deglacial Suigetsu atmospheric 14C-record. Radiocarbon 57, 129-151.

Schauer, U., Muench, R.D., Rudels, B., Timokhov, L., 1997. Impact of eastern Arctic shelf waters on the Nansen Basin intermediate layers. 102, 3371-3382.

Schefuß, E., Ratmeyer, V., Stuut, J.-B.W., Jansen, J.H.F., Sinninghe Damsté, J.S., 2003. Carbon isotope analyses of n-alkanes in dust from the lower atmosphere over the central eastern Atlantic. Geochimica et Cosmochimica Acta 67, 1757-1767.

Schmittner, A., Clement, A.C., 2002. Sensitivity of the thermohaline circulation to tropical and high latitude freshwater forcing during the last glacial-interglacial cycle. Paleoceanography 17, 7-1-7-12.

Schubert, C.J., Calvert, S.E., 2001. Nitrogen and carbon isotopic composition of marine and terrestrial organic matter in Arctic Ocean sediments:: implications for nutrient utilization and organic matter composition. Deep Sea Research Part I: Oceanographic Research Papers 48, 789-810.

Schubert, C.J., Stein, R., 1996. Deposition of organic carbon in Arctic Ocean sediments: terrigenous supply vs marine productivity. Organic Geochemistry 24, 421-436.

Schweinsberg, A.D., Briner, J.P., Miller, G.H., Bennike, O., Thomas, E.K., 2017. Local glaciation in West Greenland linked to North Atlantic Ocean circulation during the Holocene. Geology 45, 195-198.

Screen, J.A., Simmonds, I., 2010. The central role of diminishing sea ice in recent Arctic temperature amplification. Nature 464, 1334-1337.

Secher, K., 1980. Distribution of radioactive mineralisation in central West Greenland. Rapp. GrønlandsGeologiske Undersøgelse 100, 61–65.

Seidenkrantz, M.-S., 2013a. Benthic foraminifera as palaeo sea-ice indicators in the subarctic realm - examples from the Labrador Sea-Baffin Bay region. Quaternary Science Reviews 79, 135-144.

Seidenkrantz, M.S., Aagaard-Sorensen, S., Sulsbruck, H., Kuijpers, A., Jensen, K.G., Kunzendorf, H., 2007. Hydrography and climate of the last 4400 years in a SW Greenland fjord: implications for Labrador Sea palaeoceanography. Holocene 17, 387-401.

Seidenkrantz, M.S., Ebbesen, H., Aagaard-Sorensen, S., Moros, M., Lloyd, J.M., Olsen, J., Knudsen, M.F., Kuijpers, A., 2013b. Early Holocene large-scale meltwater discharge from Greenland documented by foraminifera and sediment parameters. Palaeogeography Palaeoclimatology Palaeoecology 391, 71-81.

Seidenkrantz, M.S., Roncaglia, L., Fischel, A., Heilmann-Clausen, C., Kuijpers, A., Moros, M., 2008. Variable North Atlantic climate seesaw patterns documented by a late Holocene marine record from Disko Bugt, West Greenland. Marine Micropaleontology 68, 66-83.

Serreze, M.C., Barrett, A.P., Slater, A.G., Steele, M., Zhang, J., Trenberth, K.E., 2007a. The large-scale energy budget of the Arctic. Journal of Geophysical Research-Atmospheres 112, 10.1029/2006JD008230.

Serreze, M.C., Barrett, A.P., Slater, A.G., Woodgate, R.A., Aagaard, K., Lammers, R.B., Steele, M., Moritz, R., Meredith, M., Lee, C.M., 2006. The large-scale freshwater cycle of the Arctic. Journal of Geophysical Research: Oceans 111, C11010, 11010.11029/12005JC003424.

Serreze, M.C., Barry, R.G., 2011. Processes and impacts of Arctic amplification: A research synthesis. Global and Planetary Change 77, 85-96.

Serreze, M.C., Holland, M.M., Stroeve, J., 2007b. Perspectives on the Arctic's shrinking sea-ice cover. Science 315, 1533-1536.

Serreze, M.C., Stroeve, J., 2015. Arctic sea ice trends, variability and implications for seasonal ice forecasting. Philosophical Transactions of the Royal Society a-Mathematical Physical and Engineering Sciences A 373, 10.1098/rsta.2014.0159.

Sheldon, C., Jennings, A., Andrews, J.T., Cofaigh, C.O., Hogan, K., Dowdeswell, J.A., Seidenkrantz, M.S., 2016. Ice stream retreat following the LGM and onset of the west Greenland current in Uummannaq Trough, west Greenland. Quaternary Science Reviews 147, 27-46.

Shemesh, A., Burckle, L.H., Froelich, P.N., 1989. Dissolution and Preservation of Antarctic diatoms and the effect on sediment thanatocoenoses. Quaternary Research 31, 288-308.

Sikes, E.L., Guilderson, T.P., 2016. Southwest Pacific Ocean surface reservoir ages since the last glaciation: Circulation insights from multiple-core studies. Paleoceanography 31, 298-310.

Simon, Q., Thouveny, N., Bourlès, D.L., Nuttin, L., Hillaire-Marcel, C., St-Onge, G., 2016. Authigenic 10Be/9Be ratios and 10Be-fluxes (230Thxs-normalized) in central Baffin Bay sediments during the last glacial cycle: Paleoenvironmental implications. Quaternary Science Reviews 140, 142-162.

Sinninghe Damsté, J.S., 2016. Spatial heterogeneity of sources of branched tetraethers in shelf systems: The geochemistry of tetraethers in the Berau River delta (Kalimantan, Indonesia). Geochim. Cosmochim. Acta 186, 13-31.

Sinclair, G., Carlson, A.E., Mix, A.C., Lecavalier, B.S., Milne, G., Mathias, A., Buizert, C., DeConto, R., 2016. Diachronous retreat of the Greenland ice sheet during the last deglaciation. Quaternary Science Reviews 145, 243-258.

Skinner, L.C., Primeau, F., Freeman, E., de la Fuente, M., Goodwin, P.A., Gottschalk, J., Huang, E., McCave, I.N., Noble, T.L., Scrivner, A.E., 2017. Radiocarbon constraints on the glacial ocean circulation and its impact on atmospheric CO2. Nature Communications 8, 16010.

Slabon, P., Dorschel, B., Jokat, W., Myklebust, R., Hebbeln, D., Gebhardt, C., 2016. Greenland ice sheet retreat history in the northeast Baffin Bay based on high-resolution bathymetry. Quaternary Science Reviews 154, 182-198.

Smik, L., Belt, S.T., Lieser, J.L., Armand, L.K., Leventer, A., 2016a. Distributions of highly branched isoprenoid alkenes and other algal lipids in surface waters from East Antarctica: Further insights for biomarker-based paleo sea-ice reconstruction. Organic Geochemistry 95, 71–80.

Smik, L., Cabedo-Sanz, P., Belt, S.T., 2016. Semi-quantitative estimates of paleo Arctic sea ice concentration based on source-specific highly branched isoprenoid alkenes: A further development of the PIP25 index. Organic Geochemistry 92, 63-69.

Solanki, S.K., Usoskin, I.G., Kromer, B., Schüssler, M., Beer, J., 2004. Unusual activity of the Sun during recent decades compared to the previous 11,000 years. Nature 431, 1084-1087.

Soltwedel, T., Bauerfeind, E., Bergmann, M., Bracher, A., Budaeva, N., Busch, K., Cherkasheva, A., Fahl, K., Grzelak, K., Hasemann, C., Jacob, M., Kraft, A., Lalande, C., Metfies, K.,

Nothig, E.M., Meyer, K., Queric, N.V., Schewe, I., Wlodarska-Kowalczuk, M., Klages, M., 2016. Natural variability or anthropogenically-induced variation? Insights from 15 years of multidisciplinary observations at the arctic marine LTER site HAUSGARTEN. Ecological Indicators 65, 89-102.

Sparkes, R.B., Selver, A.D., Bischoff, J., Talbot, H.M., Gustafsson, O., Semiletov, I.P., Dudarev, O.V., van Dongen, B.E., 2015. GDGT distributions on the East Siberian Arctic Shelf: implications for organic carbon export, burial and degradation. Biogeosciences 12, 3753-3768.

Spielhagen, R.F., Werner, K., Sorensen, S.A., Zamelczyk, K., Kandiano, E., Budeus, G., Husum, K., Marchitto, T.M., Hald, M., 2011. Enhanced Modern Heat Transfer to the Arctic by Warm Atlantic Water. Science 331, 450-453.

St-Onge, M.P., St-Onge, G., 2014. Environmental changes in Baffin Bay during the Holocene based on the physical and magnetic properties of sediment cores. Journal of Quaternary Science 29, 41-56.

Stein, R., 2008. Arctic Ocean Sediments: Processes, Proxies, and Paleoenvironment: Processes, Proxies, and Paleoenvironment. Elsevier, Amsterdam 2, 592 pp.

Stein, R., Fahl, K., 2000. Holocene accumulation of organic carbon at the Laptev Sea continental margin (Arctic Ocean): sources, pathways, and sinks. Geo-Marine Letters 20, 27-36.

Stein, R., Fahl, K., 2013. Biomarker proxy shows potential for studying the entire Quaternary Arctic sea ice history. Organic Geochemistry 55, 98-102.

Stein, R., Fahl, K., Schreck, M., Knorr, G., Niessen, F., Forwick, M., Gebhardt, C., Jensen, L., Kaminski, M., Kopf, A., Matthiessen, J., Jokat, W., Lohmann, G., 2016. Evidence for ice-free summers in the late Miocene central Arctic Ocean. Nature Communications 7: 11148, 10.1038/ncomms11148.

Stein, R., Fahl, K. and Müller, J., 2012. Proxy Reconstruction of Cenozoic Arctic Ocean Sea-Ice History – from IRD to IP25. Polarforschung, Bremerhaven, Alfred Wegener Institute for Polar and Marine Research & German Society of Polar Research 82 (1), 37-71

Stein, R., Grobe, H., Wahsner, M., 1994. Organic-carbon, carbonate, and clay mineral distributions in eastern central Arctic-Ocean surface sediments. Marine Geology 119, 269-285.

Stein, R., Korolov, S., 1994. Shelf-to-basin sediment transport in the eastern Arctic Ocean. Report on Polar Rresearch 144, 87-100.

Stein, R., Macdonald, R.W., 2004. Geochemical proxies used for organic carbon source identification in Arctic Ocean sediments. Berlin, 24-32.

Stein, R., MacDonald, R.W., 2004a. The Organic Carbon Cycle in the Arctic Ocean. Berlin: Springer, pp. 363.

Stein, R., Fahl, K., 2004a. The Kara Sea: Distribution, sources, variability and burial of organic carbon. In: Stein, R & Macdonald, R W (Eds.), The Organic Carbon Cycle in the Arctic Ocean, Springer-Verlag, Berlin, 213-237.

Stein, R., Fahl, K., 2004b. The Laptev Sea: Distribution, Sources, Variability and Burial of Organic Carbon , In: Stein, R. and Macdonald, R.W. (Eds.), The Organic Carbon Cycle in the Arctic Ocean. Springer-Verlag, Berlin.

Stern, H.L., Heide-Jorgensen, M.P., 2003. Trends and variability of sea ice in Baffin Bay and Davis Strait, 1953-2001. Polar Research 22, 11-18.

Stocker, T.F., Wright, D.G., 1991. Rapid transitions of the ocean's deep circulation induced by changes in surface water fluxes. Nature 351, 729-732.

Stroeve, J., Holland, M.M., Meier, W., Scambos, T., Serreze, M., 2007. Arctic sea ice decline: Faster than forecast. Geophysical Research Letters 34, L09501, 09510.01029/02007GL029703.

Stroeve, J., Notz, D., 2018. Changing state of Arctic sea ice across all seasons. Environmental Research Letters 13, 23.

Stroeve, J.C., Serreze, M.C., Holland, M.M., Kay, J.E., Malanik, J., Barrett, A.P., 2012. The Arctic's rapidly shrinking sea ice cover: a research synthesis. Climatic Change 110, 1005-1027.

Stuiver, M., 1961. Variations in radiocarbon concentration and sunspot activity. Journal of Geophysical Research (1896-1977) 66, 273-276.

Summons, R.E., Barrow, R.A., Capon, R.J., Hope, J.M., Stranger, C., 1993. The structure of a new C25 isoprenoid alkene biomarker from diatomaceous microbial communities. Australian Journal of Chemistry 46, 907-915.

Svendsen, J.I., Alexanderson, H., Astakhov, V.I., Demidov, I., Dowdeswell, J.A., Funder, S., Gataullin, V., Henriksen, M., Hjort, C., Houmark-Nielsen, M., Hubberten, H.W., Ingolfsson, O., Jakobsson, M., Kjaer, K.H., Larsen, E., Lokrantz, H., Lunkka, J.P., Lysa, A., Mangerud, J., Matiouchkov, A., Murray, A., Moller, P., Niessen, F., Nikolskaya, O., Polyak, L., Saarnisto, M., Siegert, C., Siegert, M.J., Spielhagen, R.F., Stein, R., 2004. Late quaternary ice sheet history of northern Eurasia. Quaternary Science Reviews 23, 1229-1271.

Syring, N., Stein, R., Fahl, K., Vahlenkamp, M., Zehnich, M., Spielhagen, R.F., Niessen, F., 2020. Holocene changes in sea-ice cover and polynya formation along the eastern North Greenland shelf: New insights from biomarker records. Quaternary Science Reviews 231, 106173.

ten Haven HL, Littke R, Rullkötter J, Stein R, DH, W., 1990 Accumulation rates and composition of organic matter in Late Cenozoic sediments underlying the active upwelling area off Peru. . In: Suess E, von Huene R et al. (eds) Proceedings of the Ocean Drilling Program, scientific results, vol 112. Ocean Drilling Program, College Station, p 591.

Tang, C.C.L., Ross, C.K., Yao, T., Petrie, B., DeTracey, B.M., Dunlap, E., 2004. The circulation, water masses and sea-ice of Baffin Bay. Progress in Oceanography 63, 183-228.

Tesi, T., Semiletov, I., Dudarev, O., Gustafsson, Ö., 2013. Sources, degradation and transport of terrigenous organic carbon on the East Siberian Arctic Shelf Seas, pp. EGU2013-8863.

Thomas, D.N., Dieckmann, G.S., 2010. Sea Ice (second ed.). Blackwell Publishing, Oxford., pp. 621.

Thomas, E.K., Briner, J.P., Ryan-Henry, J.J., Huang, Y.S., 2016. A major increase in winter snowfall during the middle Holocene on western Greenland caused by reduced sea ice in Baffin Bay and the Labrador Sea. Geophysical Research Letters 43, 5302-5308.

Thompson, D.W.J., Wallace, J.M., 1998. The Arctic Oscillation signature in the wintertime geopotential height and temperature fields. Geophysical Research Letters 25, 1297-1300.

Thorndike, A.S., 1986. Kinematics of Sea Ice, in: Untersteiner, N. (Ed.), The Geophysics of Sea Ice. Springer US, Boston, MA, pp. 489-549.

Tremblay, J.-É., Payne, C. D., Price, N. M., Gratton, Y., and Carmack, E. C., 2002. Impact of the large-scale Arctic circulation and the North Water Polynya on nutrient inventories in Baffin Bay, Journal of Geophysical Research, 107, 26-1–26-14, https://doi.org/10.1029/2000JC 000595.

Tremblay, J.-É., Anderson, L.G., Matrai, P., Coupel, P., Bélanger, S., Michel, C., Reigstad, M., 2015. Global and regional drivers of nutrient supply, primary production and CO2 drawdown in the changing Arctic Ocean. Progress in Oceanography 139, 171-196.

Trouet, V., Esper, J., Graham, N.E., Baker, A., Scourse, J.D., Frank, D.C., 2009. Persistent Positive North Atlantic Oscillation Mode Dominated the Medieval Climate Anomaly. Science 324, 78-80.

van Andel TH, H.G., Moore TC, 1975. Cenozoic history and paleoceanography of the Central Equatorial Pacific. Memoirs of the Geological Society of America.

Vare, L.L., Masse, G., Gregory, T.R., Smart, C.W., Belt, S.T., 2009. Sea ice variations in the central Canadian Arctic Archipelago during the Holocene. Quaternary Science Reviews 28, 1354-1366.

Vinther, B.M., Buchardt, S.L., Clausen, H.B., Dahl-Jensen, D., Johnsen, S.J., Fisher, D.A., Koerner, R.M., Raynaud, D., Lipenkov, V., Andersen, K.K., Blunier, T., Rasmussen, S.O., Steffensen, J.P., Svensson, A.M., 2009. Holocene thinning of the Greenland ice sheet. Nature 461, 385-388.

Vinther, B.M., Clausen, H.B., Johnsen, S.J., Rasmussen, S.O., Andersen, K.K., Buchardt, S.L., Dahl-Jensen, D., Seierstad, I.K., Siggaard-Andersen, M.L., Steffensen, J.P., Svensson, A., Olsen, J., Heinemeier, J., 2006. A synchronized dating of three Greenland ice cores throughout the Holocene. Journal of Geophysical Research-Atmospheres 111, D13102, 13110.11029/12005JD006921.

Volkman, J.K., 1986. A review of sterol markers for marine and terrigenous organic matter. Organic Geochemistry 9, 83-99.

Volkman, J.K., Barrett, S.M., Blackburn, S.I., Mansour, M.P., Sikes, E.L., Gelin, F., 1998. Microalgal biomarkers: A review of recent research developments. Organic Geochemistry 29, 1163-1179.

Volkman, J.K., Barrett, S.M., Dunstan, G.A., 1994. C25 and C30 Highly branched isoprenoid alkenes in laboratory cultures of 2 marine diatoms. Organic Geochemistry 21, 407-413.

Volkman, J.K., Barrett, S.M., Dunstan, G.A., Jeffrey, S.W., 1993. Geochemical significance of the occurence of dinosterol and other 4-methyl sterols in a marine diatom. Organic Geochemistry 20, 7-15.

Wacker, L., Fueloep, R.H., Hajdas, I., Molnar, M., Rethemeyer, J., 2013. A novel approach to process carbonate samples for radiocarbon measurements with helium carrier gas. Nuclear Instruments & Methods in Physics Research Section B-Beam Interactions with Materials and Atoms 294, 214-217.

Wadhams, P., 1992. Sea ice thickness distribution in the Greenland Sea and Eurasian Basin, May 1987. Journal of Geophysical Research: Oceans 97, 5331-5348.

Wagner, T., Zabel, M., Dupont, L., Holtvoeth, J., Schubert, C.J., 2004. Terrigenous Signals in Sediments of the Low Latitude Atlantic — Implications for Environmental Variations during the Late Quarternary: Part I: Organic Carbon, in: Wefer, G., Mulitza, S., Ratmeyer, V. (Eds.), The South Atlantic in the Late Quaternary: Reconstruction of Material Budgets and Current Systems. Springer Berlin Heidelberg, Berlin, Heidelberg, pp. 295-322.

Walsh, J.E., and W. L. Chapman, 2001. Twentieth-century sea ice variations from observational 897 data. Annals of Glaciology 33 (1): 444–448.

Wang, J., Mysak, L.A., Ingram, R.G., 1994. Interannual variability of sea-ice cover in Hudson bay, Baffin bay and the Labrador sea. Atmosphere-Ocean 32, 421-447.

Wang, M., Overland, J.E., 2012. A sea ice free summer Arctic within 30 years: An update from CMIP5 models. Geophysical Research Letters 39, L18501, 18510.11029/12012GL052868.

Wanner, H., Beer, J., Buetikofer, J., Crowley, T.J., Cubasch, U., Flueckiger, J., Goosse, H., Grosjean, M., Joos, F., Kaplan, J.O., Kuettel, M., Mueller, S.A., Prentice, I.C., Solomina, O., Stocker, T.F., Tarasov, P., Wagner, M., Widmann, M., 2008. Mid- to Late Holocene climate change: an overview. Quaternary Science Reviews 27, 1791-1828.

Wanner, H., Solomina, O., Grosjean, M., Ritz, S.P., Jetel, M., 2011. Structure and origin of Holocene cold events. Quaternary Science Reviews 30, 3109-3123.

Warren, C.R., 1992. Iceberg calving and the glacioclimatic record. Progress in Physical Geography: Earth and Environment 16, 253-282.

Wassmann, P., Carmack, E.C., Bluhm, B.A., Duarte, C.M., Berge, J., Brown, K., Grebmeier, J.M., Holding, J., Kosobokova, K., Kwok, R., Matrai, P., Agusti, S., Babin, M., Bhatt, U., Eicken, H., Polyakov, I., Rysgaard, S., Huntington, H.P., 2020. Towards a unifying pan-arctic perspective: A conceptual modelling toolkit. Progress in Oceanography 189, 102455.

Wassmann, P., Duarte, C.M., Agusti, S., Sejr, M.K., 2011. Footprints of climate change in the Arctic marine ecosystem. Global Change Biology 17, 1235-1249.

Weber ME, N.F., Kuhn G, Weidick M, 1997. Calibration and application of marine sedimentary physical properties using a multi-sensor core logger. Marine Geology 136:151-172.

Weijers, J.W.H., Schefuß, E., Kim, J.-H., Sinninghe Damsté, J.S., Schouten, S., 2014.

Wegner, C., Bennett, K.E., de Vernal, A., Forwick, M., Fritz, M., Heikkilä, M., Łącka, M., Lantuit, H., Laska, M., Moskalik, M., O'Regan, M., Pawłowska, J., Promińska, A., Rachold, V., Vonk, J.E., Werner, K., 2015. Variability in transport of terrigenous material on the shelves and the deep Arctic Ocean during the Holocene. Polar Research 34, 24964.

Weidick, A., Bennike, O., 2007. Quaternary glaciation history and glaciology of Jakobshavn Isbrae and the Disko Bugt region, West Greenland: A review. Geological Survey of Denmark and Greenland (GEUS) Bulletin, 38-39, https://doi.org/10.34194/geusb.v34114.34985.

Weiser, J., Titschack, J., Kienast, M., McCave, I.N., Lochte, A.A., Saini, J., Stein, R., Hebbeln, D., 2021. Atlantic water inflow to Labrador Sea and its interaction with ice sheet dynamics during the Holocene. Quaternary Science Reviews 256, 106833.

Weijers, J.W.H., Schefuß, E., Kim, J.-H., Sinninghe Damsté, J.S., Schouten, S., 2014. Constraints on the sources of branched tetraether membrane lipids in distal marine sediments. Organic Geochemistry 72, 14-22.

Werner, K., Mullner, J., Husum, K., Spielhagen, R.F., Kandiano, E.S., Polyak, L., 2016. Holocene sea subsurface and surface water masses in the Fram Strait - Comparisons of temperature and sea-ice reconstructions. Quaternary Science Reviews 147, 194-209.

Werner, K., Spielhagen, R.F., Bauch, D., Hass, H.C., Kandiano, E., 2013. Atlantic Water advection versus sea-ice advances in the eastern Fram Strait during the last 9 ka: Multiproxy evidence for a two-phase Holocene. Paleoceanography 28, 283-295.

Willemse, N.W., Tornqvist, T.E., 1999. Holocene century-scale temperature variability from West Greenland lake records. Geology 27, 580-584.

Wood, M., Rignot, E., Fenty, I., Menemenlis, D., Millan, R., Morlighem, M., Mouginot, J., Seroussi, H., 2018. Ocean-Induced Melt Triggers Glacier Retreat in Northwest Greenland. 45, 8334-8342.

Xiao, X., Fahl, K., Mueller, J., Stein, R., 2015. Sea-ice distribution in the modern Arctic Ocean: Biomarker records from trans-Arctic Ocean surface sediments. Geochimica Et Cosmochimica Acta 155, 16-29.

Yamamoto, M., Okino, T., Sugisaki, S., Sakamoto, T., 2008. Late Pleistocene changes in terrestrial biomarkers in sediments from the central Arctic Ocean. Organic Geochemistry 39, 754-763.

Young, N.E., Briner, J.P., 2015. Holocene evolution of the western Greenland Ice Sheet: Assessing geophysical ice-sheet models with geological reconstructions of ice-margin change. Quaternary Science Reviews 114, 1-17.

Yruela, I., Barbe, A., Grimalt, J.O., 1990. Determination of double-bond position and geometry in linear and highly branched hydrocarbons and fatty-acids from Gas-Chromatography Mass-Spectrometry of epoxides and diols generated by sterospecific resin hydration. Journal of Chromatographic Science 28, 421-427.

Yunda-Guarin, G., Brown, T.A., Michel, L.N., Saint-Béat, B., Amiraux, R., Nozais, C., Archambault, P., 2020. Reliance of deep-sea benthic macrofauna on ice-derived organic matter highlighted by multiple trophic markers during spring in Baffin Bay, Canadian Arctic. Elementa: Science of the Anthropocene 8, 047, https://doi.org/010.1525/elementa.2020.1047.

Yunker, M.B., Macdonald, R.W., Veltkamp, D.J., Cretney, W.J., 1995. Terrestrial and marine biomarkers in a seasonally ice-covered Arctic Estuary - Intergration of multivariate and biomarker approaches. Marine Chemistry 49, 1-50.

Zhang, J., Rothrock, D.A., 2003. Modeling Global Sea Ice with a Thickness and Enthalpy Distribution Model in Generalized Curvilinear Coordinates. Monthly Weather Review 131, 845-861.

Zreda, M., England, J., Phillips, F., Elmore, D., Sharma, P., 1999. Unblocking of the Nares Strait by Greenland and Ellesmere ice-sheet retreat 10,000 years ago. Nature 398, 139-142.
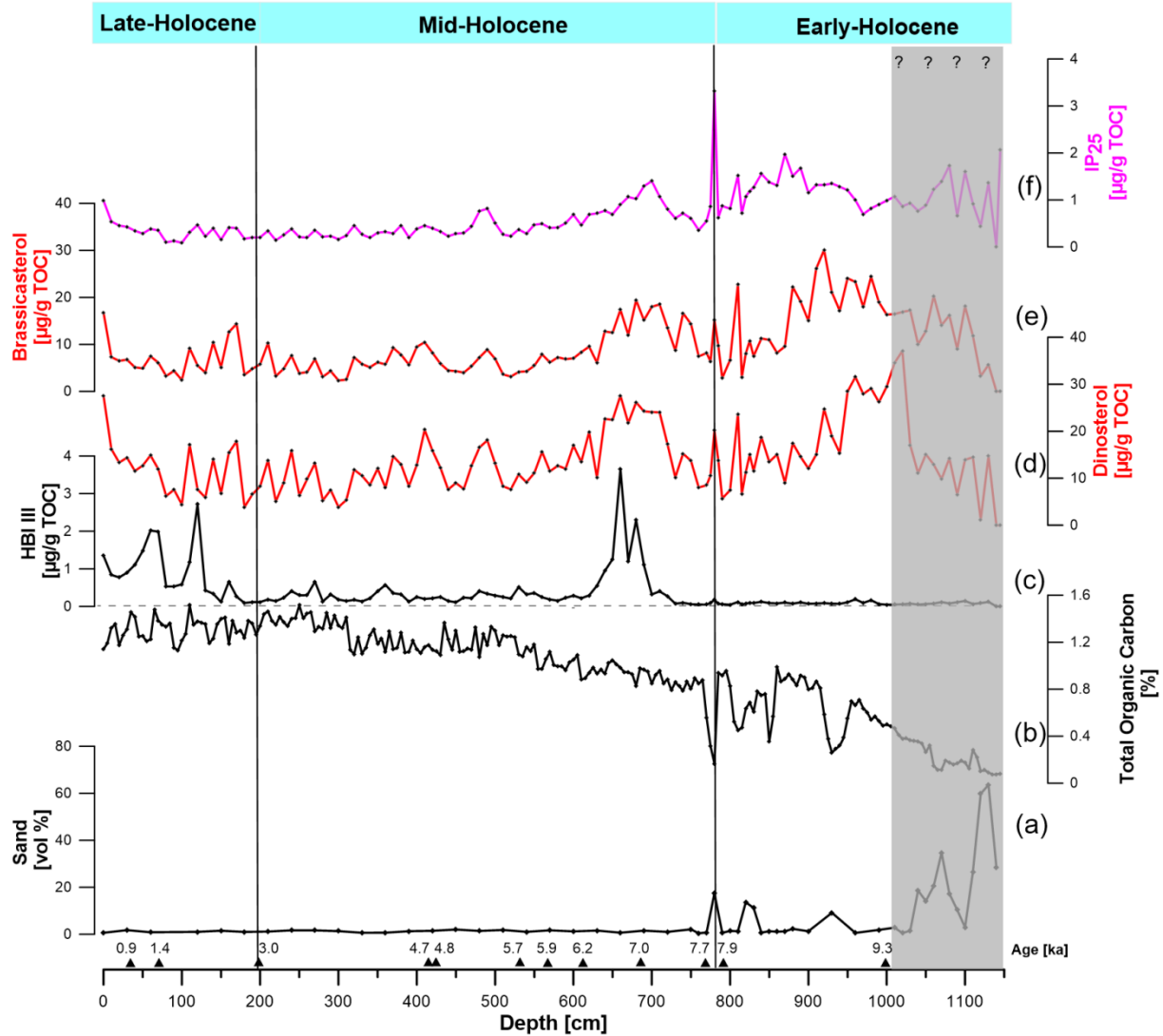
9   Supplementary Figures

Figure S4.1: Combined record of bulk parameters and biomarkers of Core GeoB19927-3 (a) Sand content [vol %], (b) Total organic carbon (TOC) content [%], (c) HBI III [µg/g TOC], (d) dinosterol [µg/g TOC], (e) brassicasterol [µg/g TOC] and (f) IP$_{25}$ [µg/g TOC]. Gray box marks the lower-most section of core, where the age model is extrapolated, and data have to be interpreted with caution. All plots are shown versus depth [cm]. Black solid triangles mark the AMS ^{14}C-datings [in ka].
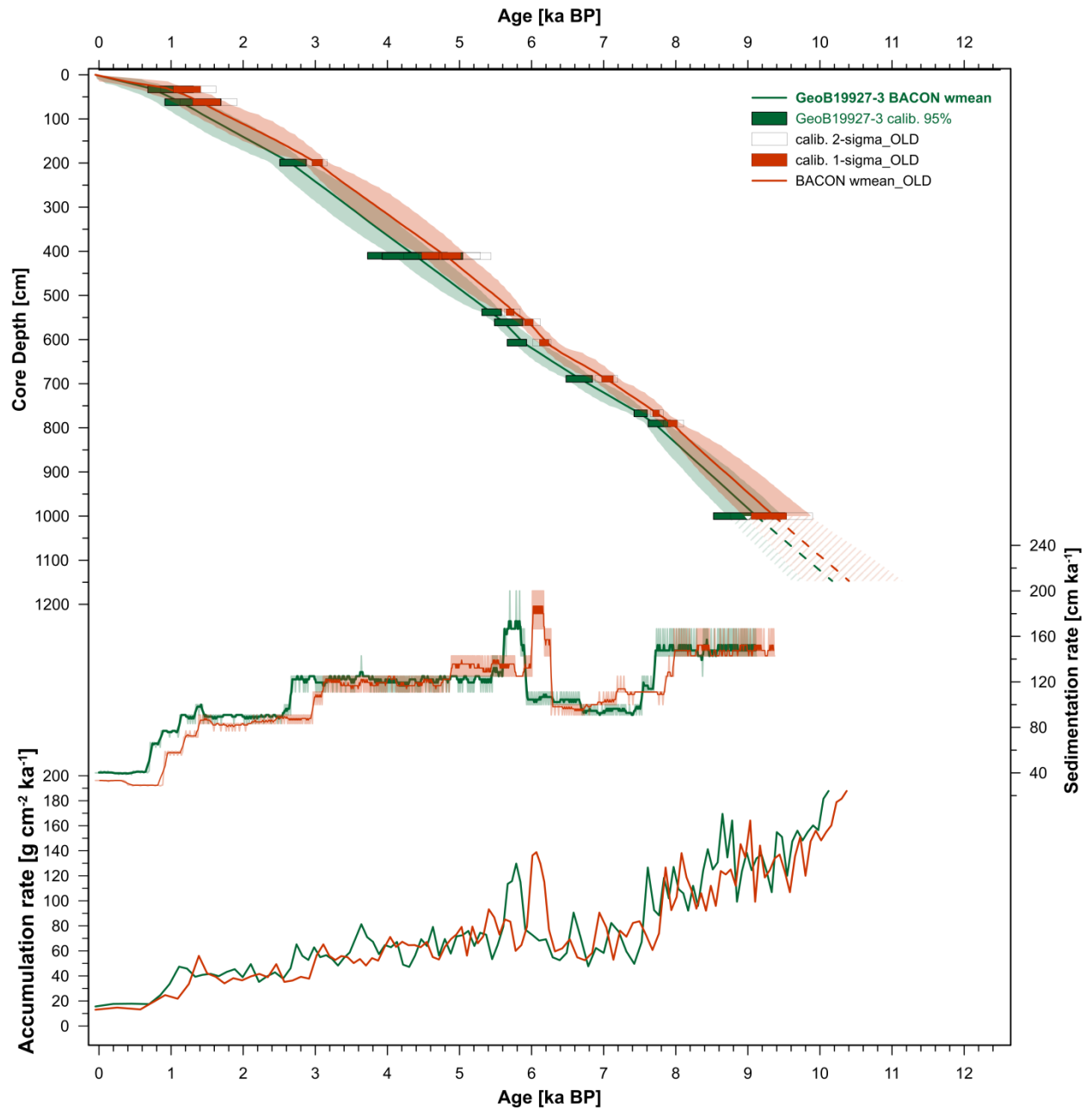
Figure S5.1: Comparison of GeoB19927-3 age-model determined by BACON (Saini et al., 2020) with that of updated PDV (Langner and Mulitza, 2019), which uses modelled reservoir ages (Butzin et al., 2017). Note, the updated age-model (shown in brown) used in this study is about 0.2 ka younger than previously shown by Saini et al. (2020).
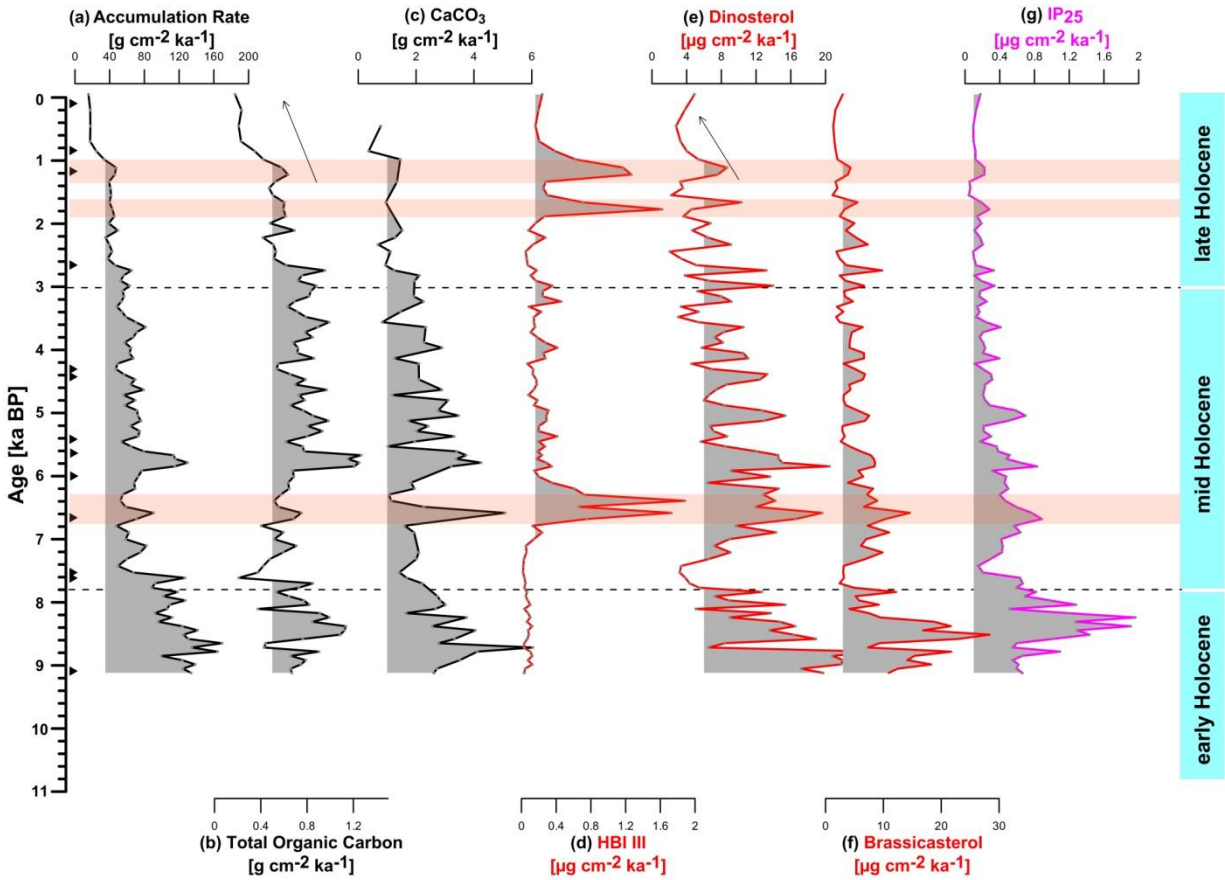
Figure S5.2: Downcore variations of core GeoB19927-3 based on Saini et al. (2020) (a) bulk accumulation rate, and accumulation rates of (b) total organic carbon, (c) CaCO$_3$ (this study), (d) Z-HBI III, (e) dinosterol, (f) brassicasterol, and (g) sea ice proxy IP$_{25}$. The orange box marks an ice-edge (IE) situations. All plots are shown versus age in 1000 years before present [ka BP].
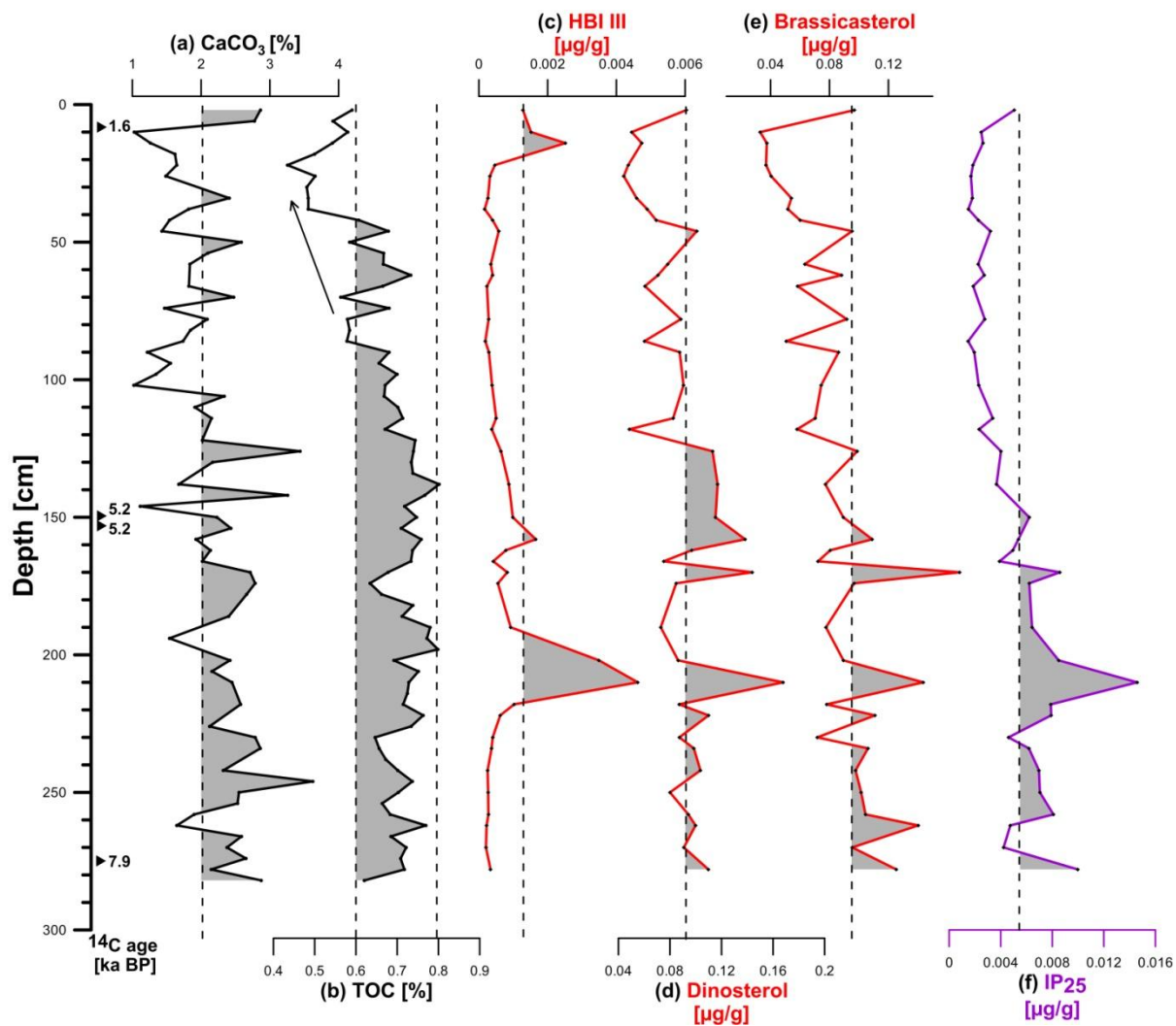
Figure S5.3: Combined record of core GeoB19948-3 (a) CaCO$_3$ content, (b) total organic carbon (TOC), (c) HBI III [µg/g], (d) dinosterol [µg/g], (e) brassicasterol [µg/g], and (f) sea ice proxy IP$_{25}$.
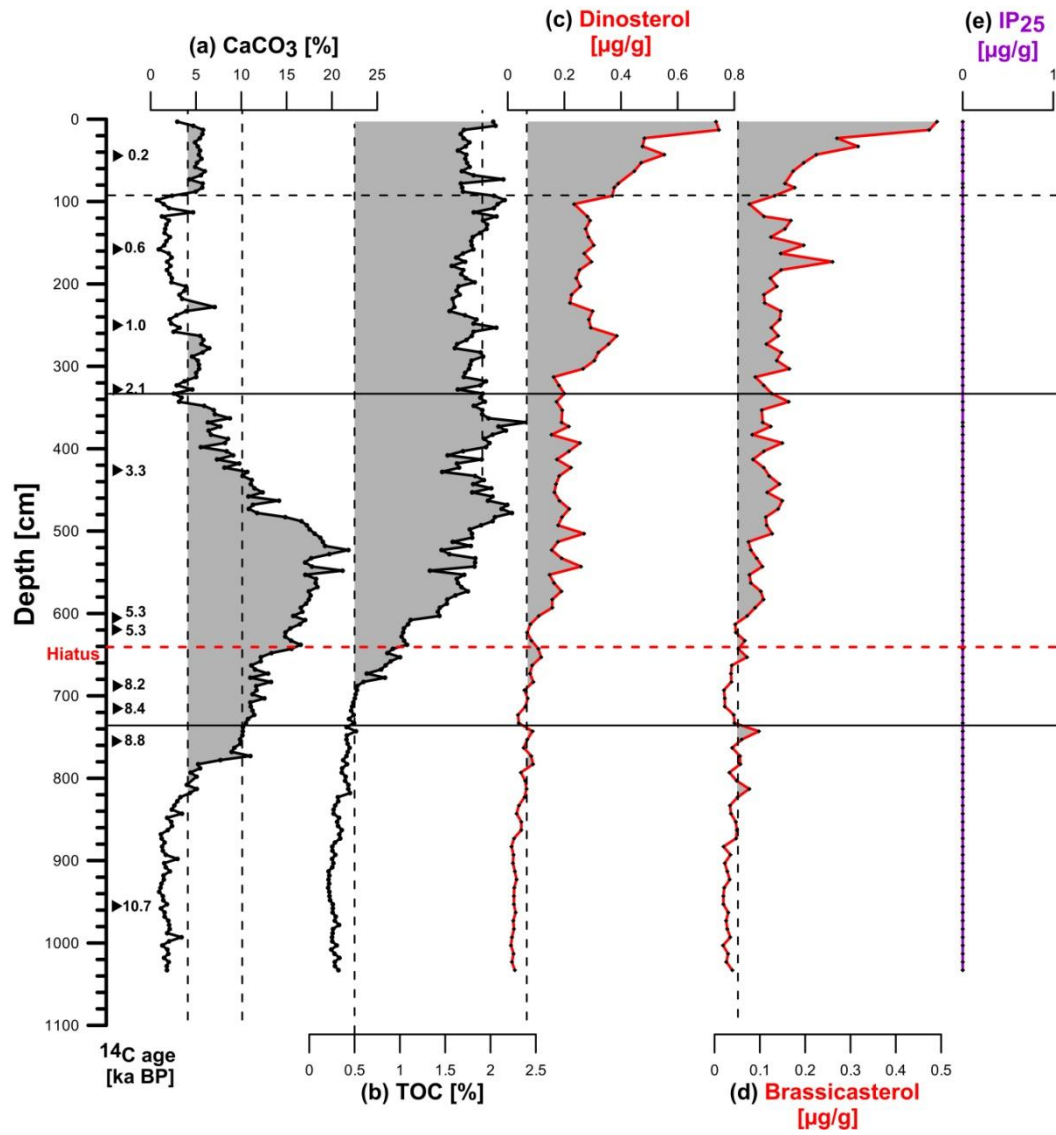
Figure S5.4: Combined record of core GeoB19905-1 (a) CaCO$_3$ content, (b) Total organic carbon (TOC), (c) dinosterol [µg/g], (d) brassicasterol [µg/g], and (e) sea ice proxy IP$_{25}$.